

INCORPORATION OF RHEOLOGICAL PROPERTIES INTO ICE SHEET FLOW MODELS

By

Wang, Wei Li

Submitted in fulfilment of the requirements for the degree of Doctor of Philosophy


Institute of Antarctic and Southern Ocean Studies (IASOS)

University of Tasmania

August, 2000

Declaration

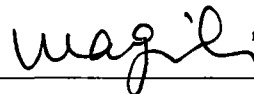
This thesis contains no material which has been accepted for a degree or diploma by the University of Tasmania or any other institution, except by way of background information that is duly acknowledged. To the best of my knowledge and belief, this thesis contains no material previously published or written by another person, expect where due acknowledgement is made in the text



Wang, Wei Li
August 2000

Authority of Access

This thesis may be available for loan and limited copying in accordance with the *Copyright Act 1968*.



Wang, Wei Li
August 2000

Abstract

In most current ice sheet models the rheological properties of ice are usually assumed to be either isotropic or some effects of anisotropy are taken into account by the use of a simple constant enhancement factor. Studies of ice cores have shown that in natural ice sheets approximately isotropic ice only exists at shallow depths typically less than several hundred metres. The large amounts of deeper ice have developed strong anisotropic crystal orientation fabrics. The results from both field and laboratory studies have indicated that the anisotropy due to flow-induced crystal orientations has a considerable effect on ice flow rate, therefore, the assumption of isotropic ice is no longer appropriate when anisotropy of the ice crystal fabric develops and we need to take account of the interaction between crystal orientation and rates of deformation. This project aims to incorporate into an ice sheet model the effect of ice fabric anisotropy on the flow of ice.

A model for anisotropic ice flow in a polar ice sheet is developed. It is based on laboratory measurements of ice rheology including ice cores and combined with borehole measurements in the ice sheet. In the model the shear flow of ice is enhanced as the ice passes through a range of stress regimes from predominantly vertical compression to predominantly vertical shear stress, as it flows down through the ice sheet. The enhanced flow, characterised by an increase in strain-rates compared to the secondary creep rate for isotropic ice, is primarily based on laboratory measurements of tertiary creep under combined compression and shear stresses.

To test this model two different flow lines in the Antarctic ice sheet have been studied. One flow line is from Law Dome which is an isolated ice cap with shallower and warmer ice. For comparison, the second, longer flow line, the I.A.G.P traverse line inland of Casey in the interior of East Antarctica, was studied to explore different conditions for deeper, colder ice and larger scale bedrock features. A simple application of the model to a number of boreholes with ice cores in Law Dome has been made, including a new borehole drilled in

Abstract

Law Dome Summit South where shear strain rates were measured as well as ice core fabrics through the 1200 m depth to the bed. In the study areas a large amount of glaciological work involving field surveys and ice core drilling provides sufficient data for model inputs and for model verification. The results from the model were compared with observations.

The implications of this work for other regions, including the whole Antarctic ice sheet, were also investigated.

It is concluded that in regions of high bedrock roughness the occurrence of a high shear layer of strongly anisotropic ice above the predominant bedrock perturbations needs to be taken into account.

Acknowledgements

I would like to thank my supervisors, Bill Budd and Roland Warner, for their guidance, encouragement, discussions and assistance during my research project, and especially to thank them for patiently reading the whole manuscript and making corrections and helpful suggestions. Without their advice and the theoretical insights they have taught me it would have been impossible to complete this project.

The acknowledgement is especially to Roland Warner for help in developing my computer skills and his help with solving programming problems. Two published papers (*Annals of Glaciology*, Vol. 27 and 29) were co-authored with Roland. The first paper (*Simulation of the influence of ice rheology on velocity profiles and ice sheet mass balance*, Wang and Warner, 1998) presented the preliminary studies which are reviewed in Chapter 4 and the second (*Modelling of anisotropic ice flow in Law Dome, East Antarctica*, Wang and Warner, 1999) included the part of the results from Chapter 6 of the thesis. The results presented in Chapter 8 are based on incorporating my ice flow scheme into a 3-D model of the whole Antarctic ice sheet, being developed by Roland. I thank him for making it simple to modify his program with a few new subroutines, and for his guidance in displaying the results.

Further thanks is due to Jo Jacka and Li Jun for access to detailed results of laboratory experiments, to Vin Morgan, Li Jun and Tas Van Ommen for providing the DSS borehole analysis data and the Law Dome Summit survey data prior to publication, and to Shavawn Donoghue for providing fabric parameter data for the Law Dome ice cores.

I am grateful for the award of an Australian Postgraduate Research award and additional scholarship founding from the Antarctic CRC.

IASOS and Antarctic CRC are thanked for providing the opportunity to undertake this work and the financial support to attend international symposia held in Hobart, in July 1997, and Lanzhou, China, in September 1998, when I presented the work published in the *Annals of Glaciology* papers.

I also like to thank Li Jun and Phoebe for understanding and support.

Contents

Declaration	ii
Authority of Access	ii
Abstract	iii
Acknowledgements	v
Contents	vi
List of Symbols	xi
List of Figures	xvi
List of Tables	xxi
1. INTRODUCTION	1
1.1. Antarctic Ice Sheet	1
1.2. Outline of the Problem	2
1.3. Outline of the Project	4
1.4. Synopsis of Thesis	6
2. ICE RHEOLOGY	11
2.1. Ice Flow and Rheology Model for Polycrystalline Ice	11
2.2. The Ice Rheological Variables	16
2.2.1. Stress	16
2.2.1.1. Stress Tensor and Stress Deviator Tensor	16
2.2.1.2. Invariants of Stress and Stress Deviator	19
2.2.1.3. Octahedral Stresses	21
2.2.2. Strain Rate	24
2.2.2.1. Strain	24
2.2.2.2. The Relation between Strain Rate and Velocity	24
2.2.2.3. Strain Rate Tensor	26
2.2.2.4. Invariants of Strain Rate	27
2.2.2.5. Octahedral Strain Rate	28
2.2.2.6. The Stress State for Different Stress Configurations	28
2.2.3. Ice Structure	30
2.2.3.1. Crystal Orientation Fabrics	30
2.2.3.2. Crystal Size	32

Contents

2.2.3.3. Impurities	33
2.2.3.4. Density	34
2.2.4. Temperature	35
2.3. Isotropic Temperature Dependent Flow Law	35
3. ANISOTROPIC ICE FLOW	39
3.1. Anisotropic Ice and its Effect on Ice Flow	39
3.2. Analysis of Anisotropic Ice and Flow Rates Observed from the Field	45
3.2.1. Law Dome	45
3.2.2. The Flow Line from Law Dome Summit to Cape Folger	48
3.2.3. Information on Ice Cores and Boreholes Drilled along the Flow Line	50
3.2.4. The Relationship of Enhancement Factor with Fabric	54
3.3. Laboratory Studies on Anisotropic Ice Flow	59
3.3.1. Deformation Tests on Ice from Different Ice Cores	59
3.3.2. Ice Flow Relations Derived from Ice Deformation Tests under Combined Shear and Compression stresses	61
3.4. Review of Previous Approaches to Modelling Anisotropic Ice Flow	66
3.4.1. Modelling of Anisotropic Ice Flow	66
3.4.1.1. Lile's Model	69
3.4.1.2. Lliboutry's Model	71
3.4.1.3. Azuma's Model	74
3.4.2. Modelling of Development of Crystal C-axis Orientation Fabrics	80
4. DEVELOPMENT OF AN ANISOTROPIC ICE FLOW MODEL	82
4.1. Introduction	82
4.2. Preliminary Studies	83
4.3. The Model Assumptions and Description	87
4.3.1. Stress Configurations and Driving Stress	88
4.3.2. The Flow Relations	91

Contents

4.3.2.1. Enhancement Factor Derived from Laboratory Experiments	94
4.3.2.2. Enhancement Factor based on Ice History	95
4.3.2.3. Temperature Dependent Parameters	96
4.3.3. Iterative Process	97
4.3.4. Bedrock Treatment	98
4.4. Numerical Methods and Calculations	100
4.4.1. Relative ζ -Coordinate	100
4.4.2. Finite Difference Method and Staggered Grid Points	103
4.4.3. Horizontal Velocity	104
4.4.3.1. Internal Velocity	104
4.4.3.2. Sliding Velocity	105
4.4.4. Vertical Strain Rate and Velocities	106
4.4.5. Balance Flux and Balance Velocity	110
4.4.6. Particle Trajectory and Age	111
4.4.7. Evolution of Compressive and Shear Strains	111
4.4.8. Temperature Distribution	112
4.4.8.1. Equation of heat Transfer in ζ -coordinate system	112
4.4.8.2. Boundary Conditions	113
4.4.8.3. Solution of the Steady State Equation of Heat Transfer	115
 5. AN ANALYSIS OF ANISOTROPIC ICE FLOW PROPERTIES AT THE DSS BOREHOLE, LAW DOME, ANTARCTICA	 117
5.1. Introduction	117
5.2. Background for the DSS Borehole	118
5.2.1. Law Dome Summit and DSS Ice Core Drilling	118
5.2.2. Borehole Measurements and Ice Core Studies	128
5.3. The Model Description	132
5.4. Results from the Model	137
5.5. Summary	139
 6. APPLICATION OF THE MODEL TO A FLOW LINE ON LAW DOME, ANTARCTICA	 141

Contents

6.1. Introduction	141
6.2. Model Input Data	142
6.3. Treatment of Basal Layers	144
6.4. Results from the Model Output	149
6.5. Comparison of the Model Results with Observations	156
6.5.1. Temperature Profiles	156
6.5.2. Shear Strain Rate Profiles	158
6.6. The Main Ice Flow Regions of the Law Dome Flow Line	160
6.7. Summary	162
7. APPLICATION OF THE MODEL TO AN I.A.G.P	
 FLOW LINE, WILKES LAND, ANTARCTICA	164
7.1. Introduction	164
7.2. I.A.G.P. Flow Line	166
7.2.1. Background of the I.A.G.P.	166
7.2.2. The I.A.G.P. Flow Line	166
7.3. Model Input Data	167
7.4. Results from the Model Output	170
7.4.1. Temperature and Enhancement	172
7.4.2. Stresses	173
7.4.3. Strains and age	173
7.4.4. Strain rates	176
7.4.5. Velocities	176
7.5. High Shear Layers	179
7.6. The Main Ice Flow Regions of the I.A.G.P Flow Line	181
7.7. Summary	185
8. INCORPORATION OF ANISOTROPIC RHEOLOGY	
 INTO WHOLE ANTARCTIC ICE SHEET MODEL	187
8.1. Model Input Data Sets	187
8.2. The Running of the Model and the Results	188
8.3. Comparison with the Results from the Flow Line Model along the I.A.G.P. Flow Line	196
8.4. Concluding Remarks	199

Contents

9. CONCLUSION AND FUTHER STUDIES	200
9.1. Summary and Conclusions	200
9.2. The Need for Further Studies	205
References	208
Appendix I. Ice Dynamics and Thermodynamics Equations	229
AI.1. Continuity Equation	229
AI.2. Equations of Motion	230
AI.3. Equation of Heat Transfer	231
Appendix II. Iterative Scheme for Calculation of Steady State Temperature Distributions	234

List of Symbols

Constants

a_s	A constant for sliding velocity.	$0.32 \times 10^3 \text{ m}^3 \text{ bar}^{-1} \text{ a}^{-1}$
E_c	Enhancement factor in compression only.	3
E_s	Enhancement factor in shear only.	6
g	Gravitational acceleration.	9.81 m s^{-2}
n	Flow law exponent.	3
P	Ice thickness adjustment for firn layer.	20 m
T_o	Triple point temperature of water.	273.16 K (0.01 °C)
β'	Constant for calculating pressure melting point.	$8.7 \times 10^{-4} \text{ K m}^{-1}$
γ_s	Surface temperature lapse rate.	0.01 °C/m
ρ	Density of ice.	918 kg m^{-3}
ρ_{ice}	Mean density of floating ice.	884 kg m^{-3}
ρ_{sea}	Density of sea water.	1027 kg m^{-3}

Variables

a_1, a_2, a_3	Direction cosines.	dimensionless
A_o	Temperature dependent coefficient for octahedral component.	$\text{bar}^{-3} \text{ yr}^{-1}$
A_{xz}	Temperature dependent coefficient for horizontal shear component.	$\text{bar}^{-3} \text{ yr}^{-1}$
B	Bedrock elevation.	m
$B(f, \Lambda)$	Interference component of the enhancement in Lile's model.	dimensionless

List of Symbols

c	Specific heat capacity.	$\text{m}^2 \text{yr}^{-2} \text{ }^\circ\text{C}^{-1}$
D	Ice thickness.	m
D^*	Ice thickness above buoyancy.	m
E	Surface elevation.	m
E_1, E_2, E_3	Invariants of strain rate tensor.	yr^{-1}
$E(\lambda_c)$	Enhancement factor as the function of compression fraction for octahedral component.	dimensionless
$E(\epsilon_{xz} / \epsilon_z)$	Enhancement factor as a function of strains.	dimensionless
$E(f, \Lambda)$	Octahedral enhancement factor in Lile's model.	dimensionless
f	Internal heating.	$\text{bar} \cdot \text{yr}^{-1}$
\bar{F}	Total mass flux.	$\text{m}^2 \text{yr}^{-1}$
F_{bal}	Balance flux.	$\text{m}^2 \text{yr}^{-1}$
F_{in}	Total mass inflow from any column of a flow line.	$\text{m}^2 \text{yr}^{-1}$
F_{out}	Total mass outflow from any column of a flow line.	$\text{m}^2 \text{yr}^{-1}$
$F(\lambda_c)$	Enhancement factor as a function of compression fraction for compression component.	dimensionless
$G(\lambda_c)$	Enhancement factor as a function of compression fraction for shear component.	dimensionless
$G(f, \Lambda)$	Geometric component of the enhancement in Lile's model.	dimensionless
G_{ij}	Geometrical tensor in Azuma's model.	dimensionless
I_1, I_2, I_3	Invariants of stress tensor.	$\text{bar}, \text{bar}^2, \text{bar}^3$
J_1, J_2, J_3	Invariants of stress deviator.	$\text{bar}, \text{bar}^2, \text{bar}^3$
k	Thermal conductivity.	$\text{kg m yr}^{-3} \text{ }^\circ\text{C}^{-1}$
K	Thermal diffusivity.	$\text{m}^2 \text{yr}^{-1}$
M	The net of accumulation and ablation.	m yr^{-1}

List of Symbols

\mathbf{M}	Symmetric fluidity matrix in Lliboutry's model.	dimensionless
N_x	Number of vertical grid point.	dimensionless
N_z	Number of horizontal grid point.	dimensionless
P	Hydrostatic pressure.	bar
\bar{q}	Heat flux vector.	
$S_{ij} (i,j=x,y,z)$	Stress deviator tensor.	
S_1, S_2, S_3	Principle stress deviators.	bar
S_x, S_y, S_z	Normal stress deviator components in x, y, z direction respectively.	bar
t	Time.	yr
T	Temperature.	$^{\circ}\text{C}$
T_{pmp}	Pressure melting point.	$^{\circ}\text{C}$
T_s	Surface temperature.	$^{\circ}\text{C}$
U, V, W	Velocity components (considering basal sliding) in x, y, z direction respectively.	m yr^{-1}
\vec{V}	Velocity vector.	m yr^{-1}
\bar{V}, \bar{U}	Depth-averaged horizontal velocity.	m yr^{-1}
V_{bal}	Balance velocity.	m yr^{-1}
V_i	Internal velocity.	m yr^{-1}
V_s	Basal sliding velocity.	m yr^{-1}
V_{surface}	Surface velocity.	m yr^{-1}
V_x, V_y, V_z	Velocity components (without basal sliding) in x, y, z direction respectively.	m yr^{-1}
x, y, z	The components in a Cartesian coordinates.	
Z	Vertical depth below the surface.	m

List of Symbols

α	Surface slope.	dimensionless
β	Bed slope.	dimensionless
$\epsilon_{ij} \begin{pmatrix} i,j=x,y,z \\ i \neq j \end{pmatrix}$	Shear strains.	dimensionless
$\epsilon_i \ (i=x,y,z)$	Normal strains.	dimensionless
$\dot{\epsilon}_e$	Effective shear strain rate.	yr^{-1}
$\dot{\epsilon}_o$	Octahedral shear strain rate.	yr^{-1}
$\dot{\epsilon}_{ij} \ (i,j=x,y,z)$	Strain rate tensor.	
δ_{ij}	Kronecker unit tensor.	
ψ	Shape function.	dimensionless
γ_g	Basal geothermal heat flux gradient in the ice.	K m^{-1}
$\dot{\gamma}_{ij} \begin{pmatrix} i,j=x,y,z \\ i \neq j \end{pmatrix}$	Shear strain rates.	yr^{-1}
λ	Polycrystalline fluidity in Lile's model.	dimensionless
Λ	Stress configuration parameter in Lile's model.	dimensionless
λ_c	Compression fraction.	dimensionless
λ_s	Shear fraction.	dimensionless
$\sigma_{ij} \ (i,j=x,y,z)$	Stress tensor.	
$\sigma_x, \sigma_y, \sigma_z$	Normal stress components in x, y, z direction respectively.	bar
$\sigma_1, \sigma_2, \sigma_3$	Principal stresses.	bar
σ_o	Octahedral normal stress.	Bar
τ_b	basal shear stress.	bar
$\tau_{ij} \begin{pmatrix} i,j=x,y,z \\ i \neq j \end{pmatrix}$	Shear stresses.	bar
τ_o	Octahedral shear stress.	bar

List of Symbols

τ_e	Effective shear stress.	bar
ω	Vertical velocity in ζ -coordinate.	dimensionless
$\dot{\omega}_{ij}$ (i,j=x,y,z)	Rotation rate tensor.	yr ⁻¹
ζ	Relative vertical coordinate	dimensionless

List of Figures

1.1. Map of Antarctica.	2
1.2. The study areas for the model applications.	5
2.1. Flow trajectories and a typical profile of horizontal velocity for an ice sheet flow line.	12
2.2. Proposed rheological model for polycrystalline ice.	14
2.3. Ice creep curve.	15
2.4. The stress components in Cartesian coordinates x, y, z .	16
2.5. Octahedron.	22
2.6. Ice crystal orientation fabrics for different stress configurations from laboratory studies and field observations from ice sheet.	31
3.1. Observed fabrics for horizontal section from the ice cores drilled in the Low Dome Ice Cape, East Antarctica.	40
3.2. Creep curves with compatible fabrics for initially isotropic ice.	41
3.3. Strain rate enhancement factor as a function of depth in the ice sheet.	42
3.4. Creep curves with compatible fabrics for initially isotropic and anisotropic ice in compression (a), and in shear (b), stress configurations.	44
3.5. Map of Law Dome showing surface and bedrock elevations.	46
3.6. Map of Law Dome showing surface accumulation and velocities.	47

List of Figures

3.7. The profile of surface and bedrock elevations from the Law Dome Summit to Cape Folger showing the boreholes.	49
3.8. Shear strain rate profiles with the fabric evolutions at BHQ, BHF, BHC1 and CHC2 boreholes.	52
3.9. The profiles of temperature, shear strain rate, enhancement factor and fabric parameter $\phi(1/4)$ at boreholes BHQ, BHF, BHC1 and BHC2.	56
3.10. The plot of the fabric parameter $\phi(1/4)$ as the function of enhancement factor obtained from the borehole analyses and ice deformation tests.	58
3.11. Creep curves for ice deformation tests in various combinations of compression and shear.	62
3.12. Plots of combined octahedral strain rate at minimum (isotropic) strain rate and at tertiary (anisotropic) strain rate as a function of λ_c (or λ_s).	65
3.13. Rheological parameters in Lliboutry's model.	74
3.14. Calculated flow-enhancement factors in Azuma's model.	77
3.15. Stress configurations and fabric development in a drainage basin of an ice sheet predicted by Azuma's model.	78
4.1. Comparison of the stress configurations in the model and laboratory experiments.	89
4.2. The ratio of enhancement factors for the shear component ($G(\lambda_c)$) to the compression component ($F(\lambda_c)$) is plotted as a function of the compression fraction (λ_c).	93
4.3. Comparison of the values of the temperature dependent coefficient from the Arrhenius relation and from the laboratory experiments.	97
4.4. The model structure.	99

List of Figures

4.5. The profile of an ice flow line.	100
4.6. Staggered grid points.	103
5.1. Location map of DSS borehole on Law Dome showing Glaciological data.	119
5.2. The Law Dome Summit survey grid with indications of Dome Summit A001 and the DSS borehole.	120
5.3. The colour maps with contours of surface elevation, bedrock elevation, ice thickness, surface slope and bedrock slope in the Law Dome Summit area.	121
5.4. The flow lines in the Law Dome Summit area.	124
5.5. A “wire mesh” perspective view of the surface and bedrock topography in the Law Dome Summit area	125
5.6. RES profile from the DSS borehole upstream to the Law Dome Summit A001.	126
5.7. The results from the borehole measurements at the DSS borehole.	130
5.8. The results from the ice core studies at the DSS borehole.	131
5.9. The profile of temperature, shear strain rates, enhancement factor and fabric parameter $\phi(1/4)$ at the DSS borehole.	133
5.10. The plot of fabric parameter ($\Phi(1/4)$) as a function of the enhancement factor (E), above the maximum shear strain rate and below the maximum shear strain rate.	135
5.11. Results from the model.	138
6.1. The model input data for the Law Dome flow line.	143
6.2. Surface and bedrock of the coastal end of the Dome – Folger line with indication of subsurface echoes.	145
6.3. Variables stress and strain rates in ice sheets.	148

List of Figures

6.4. Plots of results from the model based on $E(\lambda_c)$ and $E(\epsilon_{xz}/\epsilon_z)$ for the Law Dome flow line.	150
6.5. The flow and strain regimes for the law Dome flow line from the previous work and from the current work.	156
6.6. The temperature distribution from the model and the temperature profiles from the model and from the borehole observations.	157
6.7. Shear strain rate profiles from borehole inclination measurements and from the model results.	159
6.8. Profile of the transect from the summit of Law Dome to Cape Folger, showing the flow regions and crystal orientation fabrics measured from ice cores.	161
7.1. Map of region of Antarctica showing the location of the I.A.G.P line and the contours of surface elevation in meters.	165
7.2. Map showing smooth flow lines in the study area.	167
7.3. The model input data for the I.A.G.P flow line	168
7.4. Bedrock smoothing along the I.A.G.P flow line	169
7.5. Vertical profiles of temperature, strain rates, stresses and velocities at the distance of 300 km from the origin of the I.A.G.P flow line.	171
7.6. Contour plots of temperature, compression fraction and enhancement.	172
7.7. Contour plots of stresses.	174
7.8. Contour plots of strains, ice trajectories and isochrones.	175
7.9. Contour plots of strain rates.	177
7.10. Contour plots of horizontal and vertical velocities, and the profiles of balance velocity and the ratio of horizontal column average velocity to surface velocity	178
7.11. Comparison of the high shear layers.	180

List of Figures

7.12. The percentage of ice thickness and the depth above the bed of the high shear layer as a function of the envelope thickness and mean thickness along the I.A.G.P flow line	181
7.13. The ice flow regions for the I.A.G.P flow line	182
8.1. Map of surface, bedrock elevations, surface temperature and accumulation over the whole Antarctic ice sheet.	189
8.2. The distribution of balance fluxes over the whole Antarctic grounded ice sheet.	191
8.3. The cut-off depth (top) and the height of the cut-off layer (bottom) above the bedrock data set over the whole grounded Antarctic ice sheet.	193
8.4. Elevations of bedrock data set (top) and of cut-off layer (bottom) over the whole Antarctic ice sheet.	194
8.5. Dynamics flux (top) and the ratio (bottom) of the dynamics flux to balance flux over the whole Antarctic ice sheet.	195
8.6. The bedrock comparison along the I.A.G.P flow line.	197
8.7. Contour plots of temperature, enhancement factor, shear strain rate and the ration of shear strain rate to compression strain rate from the flow line model and 3-D model.	198
AI.1. The forces on a block of size $dx dy dz$.	230
AII.1. The scheme showing the heat horizontal advection	235

List of Tables

2.1.	Summary of stresses and strain rates in several common Stress configurations.	29
2.2.	Apparent activation energy for minimum creep rate at $\tau_0=1\text{bar}$ (octahedral) from -0.525 to -45°C .	36
3.1.	Summary of measured data at drilling sites of boreholes along the Dome Summit – Cape Folger line.	51
3.2.	Data for crystal orientation fabrics and enhancement factors resulting from simple shear tests.	61
4.1.	Enhancement factor as function of the ratio of shear strain to compressive strain.	85
4.2.	Temperature dependent coefficient values of octahedral and simple shear component.	96
5.1.	The geographical and physical parameters at DSS borehole drilling site.	127
7.1.	The parameters in the ice flow regions for the I.A.G.P. flow line.	183

Chapter 1

INTRODUCTION

1.1. Antarctic Ice Sheet

The Antarctic continent (Figure 1.1) is almost entirely covered by ice with an average elevation of 2113 metres and an average annual mean surface temperature of -35°C , making Antarctica the highest and coldest continent on the Earth. The world's lowest temperature of -89.2°C was recorded at the Soviet Antarctic station, Vostok (McWhirter, 1986). Antarctica holds the record as the windiest continent with wind speeds of up to 320 km/h. Antarctica is also the driest continent on the Earth with an average annual mean precipitation equivalent to just 15 cm of water, which is as low as in desert areas of the world.

The total area of Antarctica is $13.7 \times 10^6 \text{ km}^2$ (Radok and others, 1995). In winter with a band of sea ice surrounding its size is effectively doubled (Jacka, 1983) and reaches its maximum extent in September-October. For millions of years snow and ice have built up on the land, so that now 98% of the land is buried under a permanent ice sheet. The ice sheet holds almost 90% of the world's ice, $24.4 \times 10^6 \text{ km}^3$ in volume (Radok and others, 1995), which is about 70% of the world's known fresh water. It is estimated that if all the ice were to melt the sea level would rise by 65 to 70 metres, and that if the weight of the ice were removed the underlying rock of the Antarctic continent would rise isostatically by 700 to 1000 meters.

As the largest fresh water reservoir on the Earth, the formation and the evolution of Antarctic ice sheet play an important role in terms of heat budget, atmospheric circulation, sea level, oceanic physics and biology at the surface of the Earth, and the change of global climate and environment. The interior of the Antarctic ice

sheet preserves a continuous environmental record stretching back more than 400,000 years (Petit and others, 1999). A study of the present ice sheet helps us understand the dynamic processes governing its growth and retreat, its behaviour during the last glaciation period, and also provides further information on its response to possible future climate change and the role of the cryosphere in determining those changes.

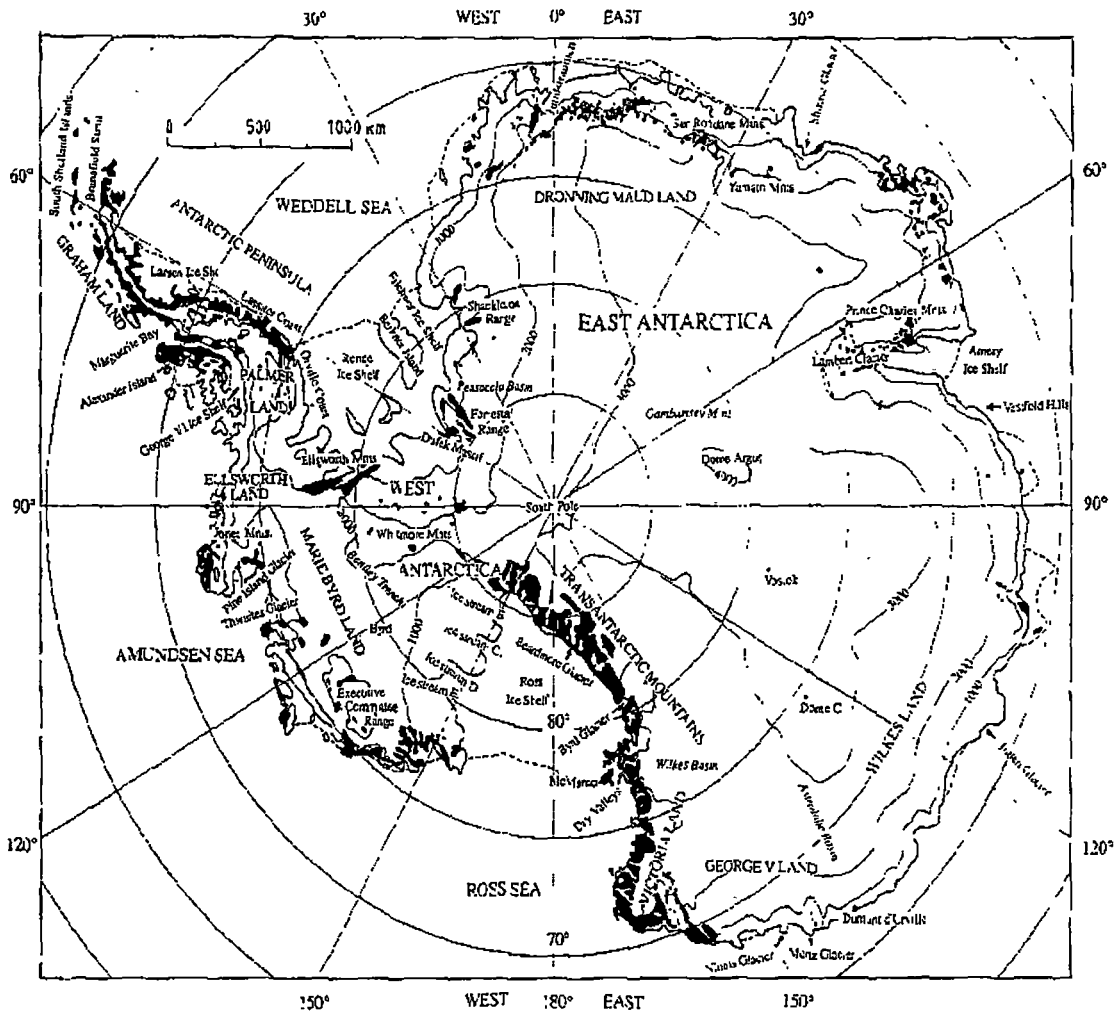


Figure 1.1. Map of Antarctica. (from Huybrechts, 1992).

1.2. Outline of the Problem

In an ice sheet the snow deposited on the surface undergoes a complicated densification process to form firn and eventually polycrystalline ice under its own weight. The flow of ice within the ice sheet is primarily due to internal

deformation generated by the non-hydrostatic stress field. This deformation creep flow is mainly dependent on temperature and stress. The flow of ice within the ice sheet not only produces a wide variety of large-scale structures such as crevasses, faults etc., but also changes of small-scale features of the ice such as the size, shape, and orientation of the crystals. It has been found from both field and laboratory results that as strain is accumulated with the flow of ice the crystals of ice with initially random orientation (isotropy) develop a preferred orientation (anisotropy), and that the bulk flow properties of the polycrystalline ice change during the course of deformation through feedback from the development of this anisotropy with recrystallisation.

Laboratory ice deformation experiments, measurement of bore-hole inclination profiles in large ice sheets, and studies of the mechanical properties of ice from those bore-holes, all indicate that tertiary deformation rates for shear can be up to an order of magnitude greater than the minimum creep rates for ice with randomly oriented crystals. This occurs once an anisotropic ice crystal fabric compatible with the dominant applied stress configuration has developed (e.g. Russell-Head and Budd, 1979; Jacka and Budd, 1989; Li and others, 1996).

Some uncertainty regarding the strength of enhancement of shear flow appropriate for ice sheet studies remains unresolved. Enhancements above the isotropic ice shear rates by factors of 6 to 10 or more are reported. There may also be a possible dependence of the magnitude of enhancement on the strength of the stress, and it is important to remember that laboratory experiments usually have not been performed at low stresses directly comparable to the situation in ice sheets.

In most current computer models of major ice sheets the rheological properties of ice are assumed to be isotropic. This is no longer appropriate when it is well known that anisotropy of the ice crystal fabric develops in the deeper parts of the ice sheet and we need to take account of the interaction between crystal orientation and deformation rates.

Some models include a constant enhancement factor, which is often regarded as an adjustable parameter. Clearly if ice sheet models are to provide reliable studies of evolving ice sheet geometry, their treatment of the flow of ice should be based on a proper understanding of ice rheology.

1.3. Outline of the Project

This project aims to incorporate the effect of the developing ice fabric anisotropy on the flow of ice into an ice sheet model.

In this thesis, a model for anisotropic ice flow in a polar ice sheet is developed. It is based on the combination of laboratory measurements of ice rheology with shear deformation rates measured in boreholes through the ice. In the model the shear flow of ice is enhanced as the ice passes through a range of stress regimes from predominantly vertical compression in the upper layers to predominantly horizontal shear stress, as it flows down through the ice sheet. The enhanced flow, characterised by an increase in strain-rates compared to the secondary creep rate for isotropic ice, is based primarily on laboratory measurements of tertiary creep under combined compression and shear stresses (Li and others, 1996), but is also guided by analyses of the shear rates observed in boreholes and the ice from the cores.

Two major complications must be addressed in extending the results of laboratory ice deformation experiments to the quantitative description of ice flow in ice sheets. The first is the development of anisotropic crystal fabrics with increasing strain, in response to applied stresses. The second is that the nature of flow in the regions near the base of ice sheets is rather uncertain, even though it is in this part of the ice column that ice sheet models typically develop much of the horizontal deformation velocity. In basal layers, where ice is usually at its warmest and deformation rates can be large, any deviations from the usual presumption of linearly increasing shear stress with depth produce large changes in estimates of shear strain-rate and consequently of horizontal velocity. As this project progressed it became clear that the implementation of a specific anisotropic ice flow law based on laboratory and field observations made it necessary to confront this question of flow in basal regions.

In this project a concept of an envelope topography, smoothing over the higher frequency bedrock roughness, will be used. This is based on observations, from boreholes and radar echo sounding, showing relatively smooth high shear layers

over rough bedrock features. The appropriate spatial scales for this smoothing deserve further examination.

The model has been tested on the Law Dome Summit to Cape Folger line, Law Dome, East Antarctica, where detailed information is available from an ice core and borehole through the thickness at DSS near the summit and considerable information exists for an approximate flow line from the summit to Cape Folger, including a number of other boreholes and ice cores. In this area a large amount of glaciological work involving field surveys and ice core drilling provides sufficient data for model inputs and for model verification. In particular the results from the model can be compared with observations. The model is then applied to an approximate flow line in the main Antarctic ice sheet in Wilkes Land where detailed bedrock, surface elevation and velocity information is available along a traverse line from near Vostok to Law Dome as shown in Figure 1.2.

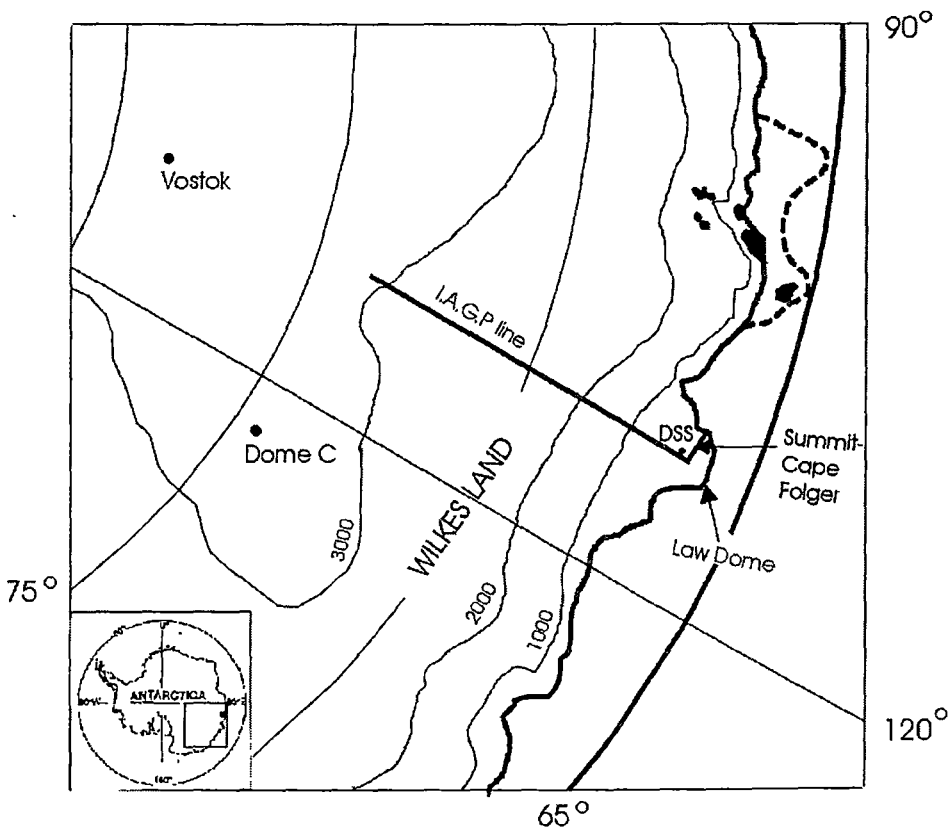


Figure 1.2. The study areas for the model applications. The I.A.G.P flow line and the Law Dome flow line (from Summit to Cape Folger) are indicated by the thick lines, and the DSS borehole site by the dot.

1.4. Synopsis of Thesis

In Chapter 1, a brief general description of the Antarctic ice sheet is given first of all and then it is followed by an outline of the problem and the present project.

Chapter 2 gives a review of ice rheology relevant to this project. In this chapter, some questions are addressed such as how large ice masses flow; what are the major factors which influence the flow and what are the relationships amongst those various ice rheological variables. The constitutive equation of ice (i.e. flow law) is described in detail for isotropic ice.

Chapter 3 describes the anisotropy of polycrystalline ice, and its effect on ice flow. After some general remarks, evidence of these phenomena from field observations is presented. Background material is presented about the Law Dome ice cap in East Antarctica and the ice cores and bore holes on the Summit to Cape Folger flow line. Then a brief presentation is made (in Section 3.2.4) of profiles of flow enhancement factors for four of these boreholes, using shear strain-rate profiles derived by other researchers from borehole inclination studies. These estimates of enhanced flow were made as part of this thesis project, using an isotropic version of the flow model that forms a major part of this thesis. They are presented within this review chapter to demonstrate the need to consider enhanced shear flow in ice sheets and to discuss the association of enhanced shear flow with anisotropic crystal fabrics. To demonstrate this association, the calculated enhancement factors are related to an analysis of crystal fabric data, produced by Donaghue (1999) from a range of crystal fabric measurements of the corresponding ice cores. For completeness, results of a similar enhancement factor profile analysis, taken as the first stage of detailed work in Chapter 5 for the Law Dome Summit South bore hole, are also presented at this point, together with corresponding ice crystal fabric data from Li (1995). Then some laboratory experiments for anisotropic ice flow are reviewed. This includes ice deformation tests carried out by the author as an intercomparison study on the flow properties of ice samples from ice cores from various ice caps around the world for an M. Sc. thesis (Wang, 1994). To study the connection between fabric parameters measured in that study for the unmodified ice cores, and any enhanced flow, the previous

strain-rate results (Wang, 1994) were used to calculate new estimates of enhancement for the present study, based on comparing minimum strain rates in those anisotropic ice core samples with corresponding strain rates in isotropic ice samples. A review of a number of numerical modelling studies, including modelling of anisotropic ice flow and modelling of development of crystal c-axis orientation fabrics, is also presented well. Three previous models describing anisotropic ice flow are chosen to discuss in detailed, they are Lile's model, Lliboutry's mode and Azuma's model. So far these models have not adequately included the co-evolution of changes in crystal size (number per unit volume) with the associated processes of recrystallisation as well as the interactions between crystals. The model developed in this thesis for relating the strain rate to strain, based on both laboratory studies and ice core results, inherently provides the basis for the evolution of the development of the statistical characteristics of the crystal structure including crystal size, orientation fabrics shape, and the statistical parameters of the distribution as a by product. This model is described in next Chapter.

Chapter 4 presents a parameterised anisotropic ice flow model developed in this thesis. It is based primarily on laboratory measurements of ice rheology, and includes the effect of anisotropic flow enhancement in tertiary creep as the ice progresses through a range of stress regimes as it passes through the ice sheet. Two different treatments of enhanced shear flow were studied. They were both incorporated into a steady state dynamic/thermodynamic ice sheet flow line model. These models – the ice dynamics and thermodynamics, and the enhancement parameter models – were written in MATLAB (<http://www.mathworks.com/>) by the author with the guidance of Roland Warner as part of this project. Unlike some models which deal with the evolution of crystal orientations and the response of the resulting polycrystalline material to stresses, strains and rotations at a microscopic or polycrystalline sample level, this model uses a more direct and simple way to parameterise empirically the strength of enhancement as it develops in shear flow, based on the laboratory observations of the process as a function of total strain and the comparisons with shear rates measured on ice core ice and in the boreholes. This project draws upon the

physical paradigm of evolving compatible crystal fabrics, in relation to laboratory deformation experiments, and to observations correlating ice core fabrics and bore hole inclinations, in developing a simple parameterisation of the enhancement of horizontal shear flow, but the aim of this project is not to model explicitly the details of fabric evolution. Although the crystallographic properties are not used directly in the model they provide a means to validate the model and allow to direct intercomparison with the analysis of results for individual boreholes and ice cores.

In **Chapter 5** the model is tested for the DSS drilling site on Law Dome, Wilkes Land, East Antarctica. The ice flow properties at the DSS borehole have been studied in this Chapter from a combination of data including the analysis of the crystal fabrics from the ice cores and observed shear rates measured in the boreholes. The shear strain rate profile from the model based on laboratory rheology for anisotropic ice under combined compression and shear provides reasonable agreement with the observations. The model presents a quantitative scheme for reduced enhancements and shear stresses near the bed of the borehole.

Chapter 6 shows the results from applying the model to the Dome Summit-Cape Folger line on Law Dome, Wilkes Land, East Antarctica. Comparing the results from the model with the observations from boreholes drilled on this line (mainly in the upper layers of the ice sheet), good agreement is found between the shear strain-rate profiles from the model and borehole inclination measurements.

Modifications to the treatment of the basal layers of the ice cap are required in order to match the observed surface velocities. In these lower regions reductions in both the enhancement of shear flow and shear stress appear to be required to match the observed lower strain rates, and this suggests that more attention needs to be given to the dynamics near the base of ice sheets as the ice flows over the irregularities of the bed.

Chapter 7 shows the results from the application of the model to a longer transect in Wilkes Land, East Antarctica, which was surveyed as part of the International Antarctic Glaciological Project (I.A.G.P.) in Wilkes Land, East Antarctica. Compared with the Law Dome flow line (Chapter 6), this I.A.G.P. line has the features of a much larger scale with a longer flow line (~600 km compared to

~100km) deeper (4000 m compared to 1000 m) and colder (below -50 °C compared to about -20 °C at the surface) ice, and reaching faster ice flow (60 m a⁻¹ compared to 10 m a⁻¹ in surface velocity). The basal layers were treated in the same way as the studies for the Law Dome flow line in order to match the observed surface velocities. The longer line gave an opportunity to further explore the concept of an envelope bedrock.

Based on the stress configurations and the magnitudes of strains and strain rates, resulting from the model, the ice flow regions for the I.A.G.P. line are divided into five typical crystallographic flow regions which are the firm zone, the compression zone, the transition zone, the shear zone and the basal ice. The predicted evolution of the fabric development is shown in each ice flow region.

The thickness of basal ice in the I.A.G.P line is similar to the amount found in the Law Dome flow line. The ice at the bed over most of the I.A.G.P line appears to be near to the pressure melting point, indicating that some loss of ice by melting may be occurring which also may need to be taken into account in refining the model.

Chapter 8 shows the results from a whole Antarctic ice sheet model with incorporation of anisotropic rheology. The scheme for including the octahedral stress in the shear flow law, and for calculating the enhancement effect of anisotropic ice flow developed in Chapter 4, and the simple treatment of flow in basal regions used in Chapters 6 and 7 were reformulated as new FORTRAN subroutines and incorporated into a three dimensional steady state thermomechanical model of the whole Antarctic ice sheet, recently developed by Roland Warner at the Antarctic CRC. This model was then applied to provide first indications of the effect of the anisotropic rheology scheme over the whole continent at 20 km resolution.

Chapter 9 presents conclusions from the work and recommendations for further studies.

This is followed by the **References** appearing in this thesis.

At the end of the thesis there are two appendices:

Appendix I reviews the ice thermodynamics equations, including the continuity equation, the equations of motion and the equation of heat transfer, as used in the ice sheet modelling;

Appendix II describes the iterative scheme for the calculation of steady state temperature distributions.

Chapter 2

ICE RHEOLOGY

2.1. Ice Flow and Rheological Model for Polycrystalline Ice

The problem of how large, apparently solid, masses of ice can flow has been studied for a several centuries. By the 18th century it was correctly recognised that gravity was the main cause of the ice mass motion down slope (Paterson, 1994). However it was still seriously debated to what extent that movement consisted of ice deformation or of the ice sliding over its bed. It is, now, clearly known that the movement of ice sheets (or glaciers) may consist of two components – internal deformation as a result of stresses produced by its own weight with its given geometry and sliding over the underlying bedrock particularly where the basal ice is at or near the melting point. The internal deformation of ice is due to the plastic flow generated by the non-hydrostatic stress field.

Figure 2.1 represents an idealised ice sheet profile. Ice flows along those particle paths (dashed lines) through a range of stress regimes from predominantly compression near the surface to predominantly shear stress near the base. In the accumulation zone the ice near the surface is vertically compressed and spreads out in other directions. The ice near the bottom is dominated by steadily increasing horizontal shear. Figure 2.1 also shows an idealised horizontal velocity profile. Total horizontal velocity U consists of an internal velocity component (V_i) and basal sliding component (V_s) (see Section 4.4.3).

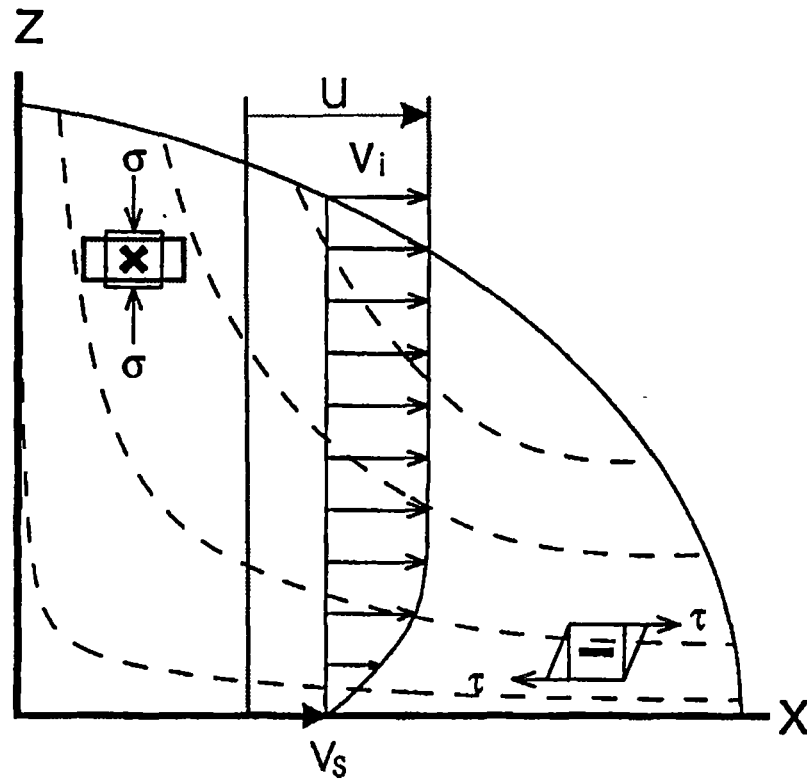


Figure 2.1. Flow trajectories and a typical profile of horizontal velocity (U), consisting of a internal velocity (V_i) and basal sliding (V_s) components, for an ice sheet flow line, together with indications of the two different stress regimes, moving from the predominant vertical compressive stress (σ) near the surface to predominantly horizontal shear (τ) nearer the bed.

Some understanding of the mechanism of ice flow has been reached by the application of modern ideas in solid state physics and metallurgy. It was realised that, since ice is a polycrystalline solid, it might be expected to deform in a way similar to other polycrystalline solids such as metals, rather than a homogeneous viscous fluid. Laboratory experiments confirmed that ice does indeed behave like some crystalline metals at temperatures not far below their melting point in particular a non-linear flow law was observed.

Polycrystalline ice can be made in the laboratory as an aggregate of randomly oriented grains of single ice crystals. A similar random orientated aggregate is

expected to form as snow crystals compact under their own weight to form glacial ice. Since the orientation of the crystals is random, polycrystalline ice can, for many purposes, be regarded on the larger scale as an isotropic material. As has been determined for hexagonal ice single crystals, polycrystalline ice may be considered to be an elastic, viscoelastic or viscoplastic body, depending on the physical processes under consideration. For single crystals the shear rate on basal planes is about 2 orders of magnitude high than other forms of deformation of the crystal (e.g. Steinemann, 1958; Wakahama, 1967; Glen and Hones, 1967; Jones and Glen, 1968; Higashi, 1969; Homer and Glen, 1978). In a polycrystalline aggregate single crystals usually deform by glide on the basal planes otherwise recrystallisation may take place. A rheological model for polycrystalline ice (Budd and Jacka, 1989; Jacka, 1987) is shown in Figure 2.2. The corresponding ice creep curves are also shown in Figure 2.3. The general features of the creep curves are as follows:

Section A-B: there is at first an initial *instantaneous elastic* impulse strain and it is *fully recoverable*;

Section B-C: after the elastic impulse, the initial **primary creep**, with decreasing strain rate ($\dot{\epsilon} < 0$), occurs up to about 0.1% strain. This stage of creep is largely *anelastic* i.e. it has *time dependent recoverable* strain if the load is removed;

Section C-D: at strains great than about 0.1%, $\dot{\epsilon}$ increases till, at about 1.0% strain, it reaches a value of zero ($\dot{\epsilon} = 0$) where strain rate reaches a minimum ($\dot{\epsilon} = \dot{\epsilon}_{\min}$) at the same time. This stage of the creep curve has been labelled **secondary creep**, which represents *irrecoverable* plastic creep;

Section D-E: beyond the minimum, strain rates increase ($\dot{\epsilon} > 0$) to a maximum ($\dot{\epsilon} = \dot{\epsilon}_{\max}$) at about 10% strain. This stage of the creep curve is labelled **accelerating creep**

Section E-F: the maximum strain rate is maintained, and it is considered to be time independent (provided the sample geometry and stress distribution are preserved) and is labelled here steady state **tertiary creep**.

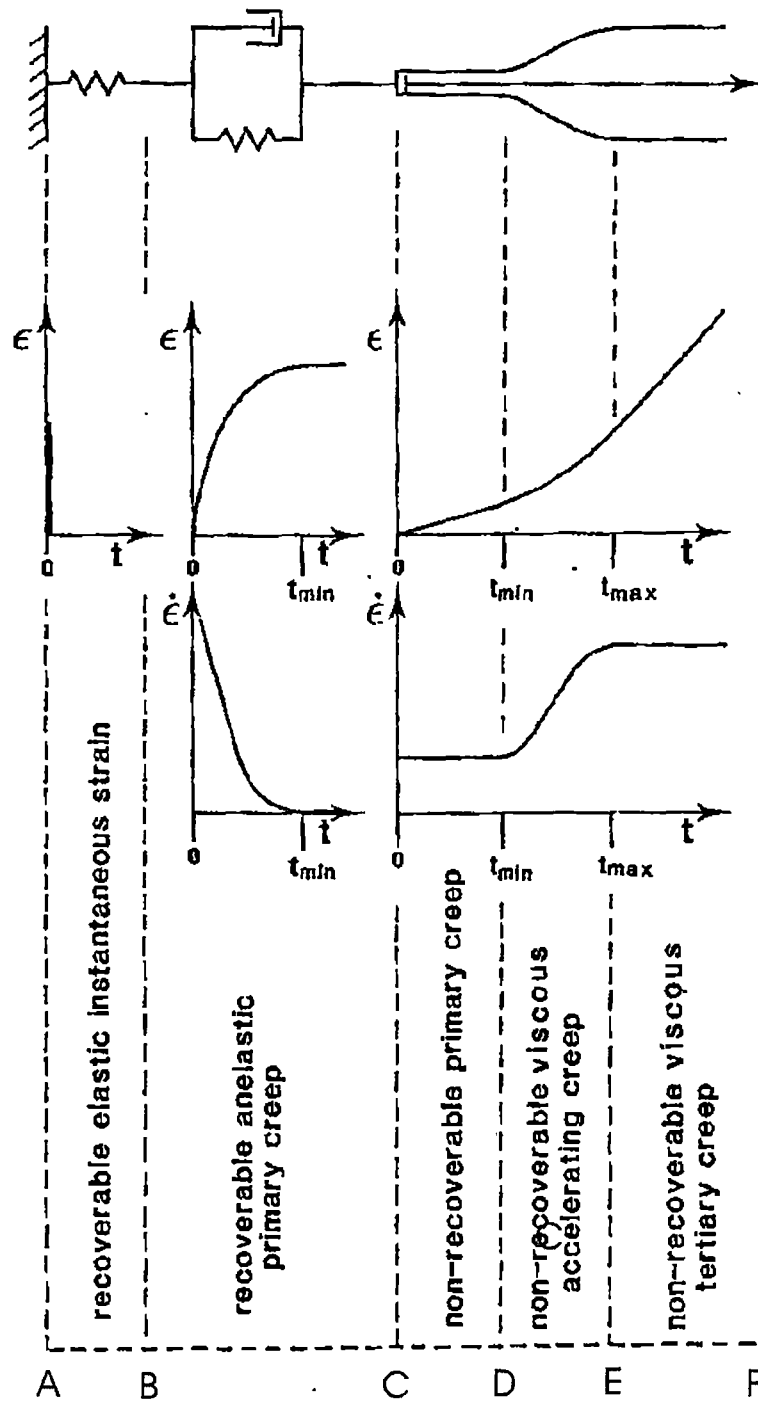


Figure 2.2. Proposed rheological model (with a simple mechanical analogue depicted) for polycrystalline ice (from Jacka, 1987).

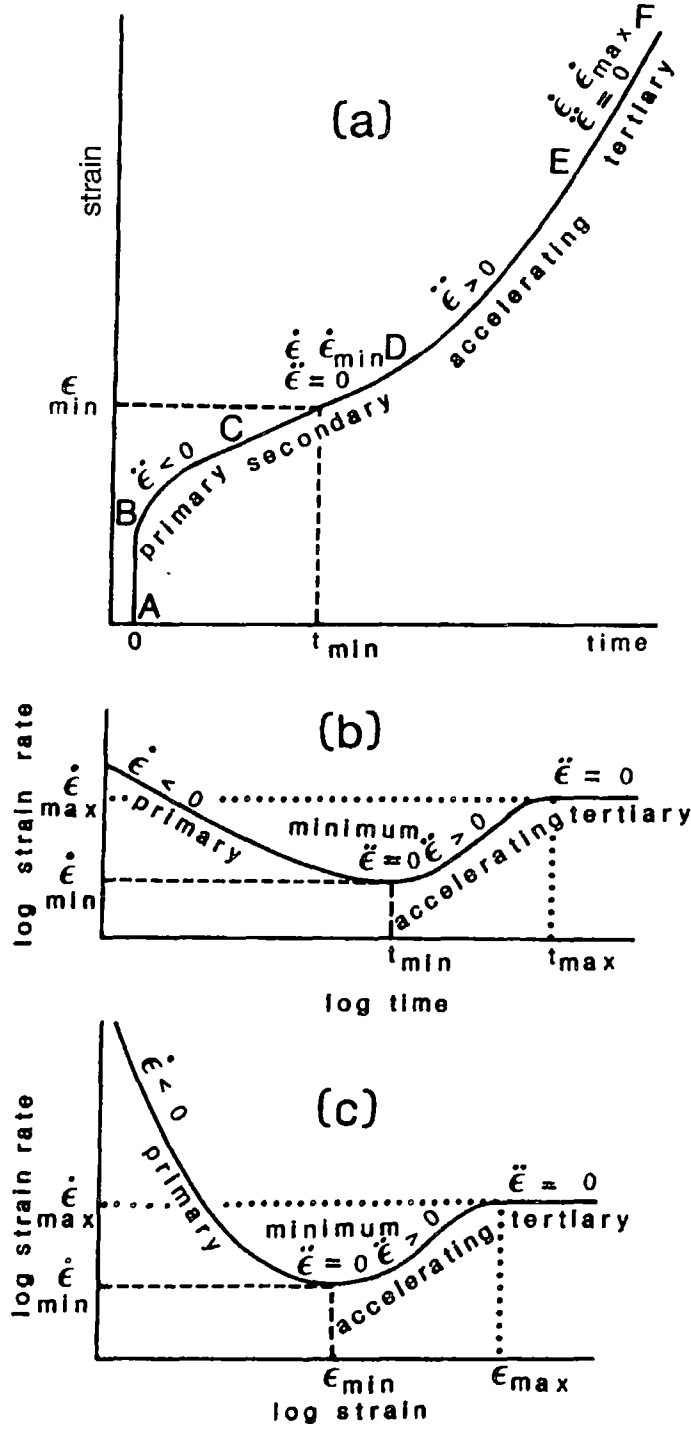


Figure 2.3. Ice creep curve. (a) an idealised creep curve for ice shows the various stages of strain ϵ versus time t . (b) The corresponding log strain rate $\dot{\epsilon}$ versus log time plot is shown indicating the minimum and “steady state” tertiary strain rates. (c) The corresponding log strain rate versus log strain shows the same features (from Budd and Jacka, 1989).

2.2. The Ice Rheological Variables

Flow of ice is influenced by many factors. The most important of them are stress, temperature, and ice structure. This section gives a review of these rheological variables and of their effects on ice flow.

2.2.1. Stress

2.2.1.1. Stress Tensor and Stress Deviator Tensor

In three-dimensional system (Jaeger, 1969), the state of stress at any point in a medium can be described by nine stress components, for example in Cartesian coordinates x, y, z (Figure 2.4) they are

$\sigma_x, \sigma_y, \sigma_z, \tau_{xy}, \tau_{yx}, \tau_{yz}, \tau_{zy}, \tau_{xz}, \tau_{zx}$.

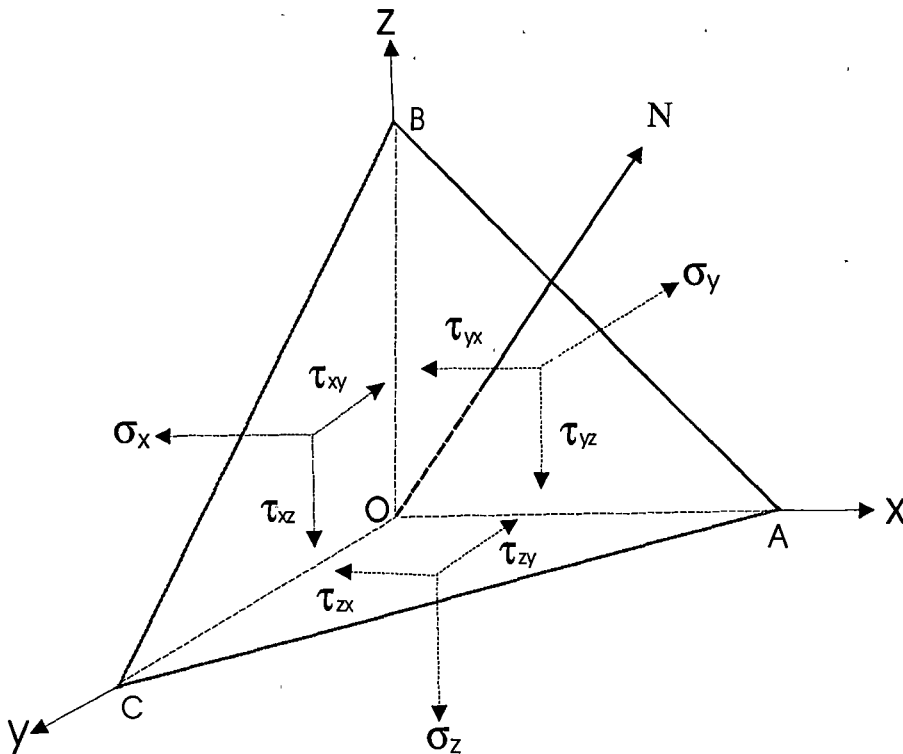


Figure 2.4. The stress components in Cartesian coordinates x, y, z . σ_x, σ_y and σ_z are normal stresses, and $\tau_{xy}, \tau_{yx}, \tau_{yz}, \tau_{zy}, \tau_{xz}$ and τ_{zx} are shear stresses. N is the normal direction of the ABC plane.

These stresses can be regarded as giving rise to the various forces on the faces of a unit cube of material, with edges oriented along the coordinate axes. In any

given physical situation their magnitudes are dependent on the directions of the coordinates. The stress components in a new coordinate system, as known from the theory of elasticity, can be obtained from the old ones by a coordinate transform. The aggregate of these nine components having this transform relation is called the “*stress tensor*”.

Using the notation σ_{ij} ($i, j = x, y, z$) to express the stress tensor, we have components labelled by the direction of the applied force (rows) and by the direction of the normal to the plane to which the force is applied (column).

$$\sigma_{ij} = \begin{bmatrix} \sigma_x & \tau_{xy} & \tau_{xz} \\ \tau_{yx} & \sigma_y & \tau_{yz} \\ \tau_{zx} & \tau_{zy} & \sigma_z \end{bmatrix} \begin{array}{l} \text{--- x direction} \\ \text{--- y direction (2.2.1)} \\ \text{--- z direction} \end{array}$$

|

|

|

y-z plane

x-z plane

x-y plane

This is a second-rank tensor. For steady uniform motion, forces must be balanced. Thus, to ensure that there is no tendency for the unit in Figure 2.4 to rotate, it is necessary that $\tau_{xy} = \tau_{yx}$, $\tau_{xz} = \tau_{zx}$ and $\tau_{yz} = \tau_{zy}$, so that only six independent components are needed to specify the stress at a point and the stress tensor is symmetric. Referring to three mutually perpendicular directions (principal axes 1, 2 and 3) in which the stress is purely normal the stress tensor can be represented in the form

$$\sigma_{ij} = \begin{bmatrix} \sigma_1 & & \\ & \sigma_2 & \\ & & \sigma_3 \end{bmatrix}, \quad (2.2.2)$$

where, σ_1 , σ_2 and σ_3 are called the *principal stresses*.

The mean value of the normal stresses at a point is given by

$$P = \frac{1}{3}(\sigma_x + \sigma_y + \sigma_z) \text{ or } P = \frac{1}{3}(\sigma_1 + \sigma_2 + \sigma_3). \quad (2.2.3)$$

For a hydrostatic situation P may be taken as equal to the hydrostatic pressure. If the normal stresses are expressed in the form

$$\begin{aligned}\sigma_x &= P + (\sigma_x - P) \\ \sigma_y &= P + (\sigma_y - P) \\ \sigma_z &= P + (\sigma_z - P).\end{aligned}\tag{2.2.4}$$

Equation 2.2.1 becomes

$$\sigma_{ij} = \begin{bmatrix} P & 0 & 0 \\ 0 & P & 0 \\ 0 & 0 & P \end{bmatrix} + \begin{bmatrix} \sigma_x - P & \tau_{xy} & \tau_{xz} \\ \tau_{yx} & \sigma_y - P & 0 \\ \tau_{zx} & \tau_{zy} & \sigma_z - P \end{bmatrix}.\tag{2.2.5}$$

The first term on the right hand side is the spherical tensor representing the hydrostatic pressure and the second term is *stress deviator*.

The spherical tensor can be written as

$$\begin{bmatrix} P & 0 & 0 \\ 0 & P & 0 \\ 0 & 0 & P \end{bmatrix} = P \delta_{ij},\tag{2.2.6}$$

where kronecker δ is

$$\delta_{ij} = \begin{cases} 1 & i=j \\ 0 & i \neq j \end{cases}.\tag{2.2.7}$$

Therefore δ_{ij} can be represented by the unit tensor

$$\delta_{ij} = \begin{bmatrix} 1 & 0 & 0 \\ 0 & 1 & 0 \\ 0 & 0 & 1 \end{bmatrix}.\tag{2.2.8}$$

As P is a normal stress, it contributes only to the normal stresses, and not to the shear stresses, i.e. the deviatoric shear stresses are the same as their nondeviatoric components, but the deviatoric normal stresses may be very different from the total normal stresses. Subtracting the hydrostatic pressure P from the stress tensor yields the stress deviator tensor

$$S_{ij} = \sigma_{ij} - P \delta_{ij} = \begin{bmatrix} S_x & S_{xy} & S_{xz} \\ S_{yx} & S_y & S_{yz} \\ S_{zx} & S_{zy} & S_z \end{bmatrix} = \begin{bmatrix} S_x & \tau_{xy} & \tau_{xz} \\ \tau_{yx} & S_y & \tau_{yz} \\ \tau_{zx} & \tau_{zy} & S_z \end{bmatrix}. \quad (2.2.9)$$

It has been known that the stress spherical tensor represents the state of hydrostatic pressure and that if the small compressibility is neglected the ice deformation is caused by the stress deviators rather than by hydrostatic pressure.

The results of Rigsby (1958) for the effects of hydrostatic stress on ice deformation indicate that the compressibility and change in deformation rate can be neglected provided the temperature is expressed in terms of the difference from pressure melting point under those stress conditions.

2.2.1.2. Invariants of Stress and Stress Deviator

In Figure 2.4, assuming the vector stresses represent the components of the stresses on the tetrahedrons, consider the plane defined by the triangle ABC, with unit normal N. Three direction cosines (a_1 , a_2 and a_3) of the normal (N) have the relation of

$$a_1^2 + a_2^2 + a_3^2 = 1 \quad (2.2.10)$$

and the vector stresses along the axes of x, y and z are

$$\begin{aligned} X_n &= \sigma_x a_1 + \tau_{xy} a_2 + \tau_{xz} a_3 \\ Y_n &= \tau_{yx} a_1 + \sigma_y a_2 + \tau_{yz} a_3 \\ Z_n &= \tau_{zx} a_1 + \tau_{zy} a_2 + \sigma_z a_3. \end{aligned} \quad (1.2.11)$$

The normal stress on ABC is

$$\sigma_n = X_n a_1 + Y_n a_2 + Z_n a_3. \quad (2.2.12)$$

The components of the normal stress σ_n at the directions of x, y and z-axes can be resolved as

$$\begin{aligned} X_n &= \sigma_n a_1 \\ Y_n &= \sigma_n a_2 \\ Z_n &= \sigma_n a_3. \end{aligned} \quad (2.2.13)$$

Using Equation 2.2.12 in Equation 2.2.13 gives

$$(\sigma_x - \sigma_n) a_1 + \tau_{xy} a_2 + \tau_{xz} a_3 = 0$$

$$\tau_{yx} a_1 + (\sigma_y - \sigma_n) a_2 + \tau_{yz} a_3 = 0$$

$$\tau_{zx} a_1 + \tau_{zy} a_2 + (\sigma_z - \sigma_n) a_3 = 0. \quad (2.2.14)$$

the combined Equations 2.2.14 can be satisfied simultaneously only if their determinant vanishes; that is, when

$$\begin{vmatrix} \sigma_x - \sigma_n & \tau_{xy} & \tau_{xz} \\ \tau_{yx} & \sigma_y - \sigma_n & \tau_{yz} \\ \tau_{zx} & \tau_{zy} & \sigma_z - \sigma_n \end{vmatrix} = 0. \quad (2.2.15)$$

Equation 2.2.15 is of the third degree in σ_n . Its three roots are the principal stresses ($\sigma_1, \sigma_2, \sigma_3$). Expanding the above determinant gives

$$\sigma_n^3 - I_1 \sigma_n^2 - I_2 \sigma_n - I_3 = 0, \quad (2.2.16)$$

in which the coefficients have the following values:

$$I_1 = \sigma_x + \sigma_y + \sigma_z$$

$$I_2 = -\sigma_x \sigma_y - \sigma_y \sigma_z - \sigma_z \sigma_x + \tau_{xy}^2 + \tau_{yz}^2 + \tau_{zx}^2$$

$$I_3 = \sigma_x \sigma_y \sigma_z + 2\tau_{xy} \tau_{yz} \tau_{zx} - \sigma_x \tau_{yz}^2 - \sigma_y \tau_{zx}^2 - \sigma_z \tau_{xy}^2. \quad (2.2.17)$$

If the direction of the axes of x, y and z are changed the values of the six components of stress will be expected to change, but coordinate invariance requires that the principal stresses (the roots of Equation 2.2.15) must retain the same values. The coefficients of Equation 2.2.16 therefore are not changed. I_1, I_2, I_3 can also be expressed in terms of principal stresses

$$I_1 = \text{tr}(\sigma) = \sigma_1 + \sigma_2 + \sigma_3$$

$$I_2 = \frac{1}{2} \text{tr}(-\sigma^2) = -\sigma_1 \sigma_2 - \sigma_2 \sigma_3 - \sigma_3 \sigma_1$$

$$I_3 = \frac{1}{3} \det(\sigma) = \sigma_1 \sigma_2 \sigma_3. \quad (2.2.18)$$

I_1 , I_2 , and I_3 are independent of the choice of the x , y and z - axes and are called *invariants* of the stress tensor.

Similarly, the invariants of the stress deviator can be written in terms of the six independent components of the stress deviator

$$\begin{aligned} J_1 &= S_x + S_y + S_z = 0 \\ J_2 &= - S_x S_y - S_y S_z - S_z S_x + \tau_{xy}^2 + \tau_{yz}^2 + \tau_{zx}^2 \\ J_3 &= S_x S_y S_z + 2\tau_{xy} \tau_{yz} \tau_{zx} - S_x \tau_{yz}^2 - S_y \tau_{zx}^2 - S_z \tau_{xy}^2. \end{aligned} \quad (2.2.19)$$

Or in terms of principal stress deviators

$$\begin{aligned} J_1 &= \text{tr} (S) = S_1 + S_2 + S_3 = 0 \\ J_2 &= \frac{1}{2} \text{tr} (- S^2) = - S_1 S_2 - S_2 S_3 - S_3 S_1 \\ J_3 &= \frac{1}{3} \det (S) = S_1 S_2 S_3. \end{aligned} \quad (2.2.20)$$

2.2.1.3. Octahedral Stresses

If OA , OB and OC in Figure 2.4 represent unit vectors along the principal axes 1,2 and 3, the plane ABC is called the *octahedral plane*. Eight such planes can form an *octahedron* shown in Figure 2.5.

Octahedral stresses are the resultant stresses on an octahedron, associate with the principal axes, and are unaffected by any rotation of the coordinate axes (Jaeger, 1969). The octahedral plane makes the same angle with the three principal directions, so N , the normal to the plane has direction cosines

$$\begin{aligned} a_1^2 + a_2^2 + a_3^2 &= 3 a^2 = 1 \\ a &= a_1 = a_2 = a_3 = \sqrt{\frac{1}{3}}. \end{aligned} \quad (2.2.21)$$

Then, we may obtain the octahedral normal stress as

$$\sigma_o = (\sigma_1 a_1^2 + \sigma_2 a_2^2 + \sigma_3 a_3^2) = \frac{1}{3} (\sigma_1 + \sigma_2 + \sigma_3) = \frac{1}{3} I_1, \quad (2.2.22)$$

and octahedral shear stress

$$\begin{aligned}
 \tau_o &= \{(\sigma_1^2 a_1^2 + \sigma_2^2 a_2^2 + \sigma_3^2 a_3^2) - (\sigma_1 a_1^2 + \sigma_2 a_2^2 + \sigma_3 a_3^2)^2\}^{1/2} \\
 &= \left\{ \frac{2}{9} (\sigma_1^2 + \sigma_2^2 + \sigma_3^2 - (\sigma_1\sigma_2 + \sigma_2\sigma_3 + \sigma_3\sigma_1)) \right\}^{1/2} \\
 &= \left\{ \frac{2}{9} (I_1^2 - 3I_2) \right\}^{1/2}.
 \end{aligned} \tag{2.2.23}$$

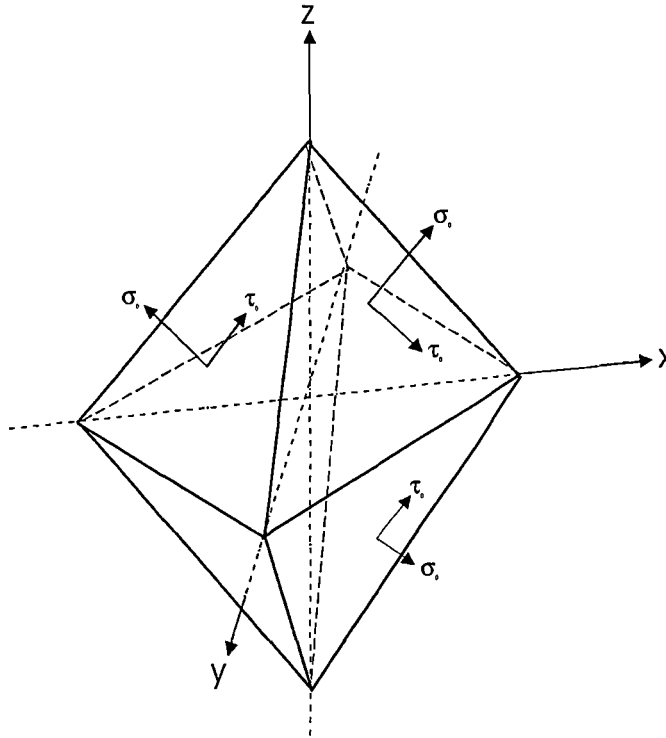


Figure 2.5. Octahedron. σ_o and τ_o indicate the octahedral normal stress and octahedral shear stress.

Due to symmetric nature of the octahedron with respect to the principal axes, the magnitudes of the shear stresses on each face of the octahedron are equal. The same is here for the normal stresses.

By using first and second invariants of the stress tensor (Equations 2.2.18) the octahedral stresses can be expressed in the terms of the six components of stress in Cartesian coordinates as following

$$\sigma_o = \frac{1}{3} (\sigma_x + \sigma_y + \sigma_z) \quad (2.2.24)$$

$$\begin{aligned} \tau_o &= \left\{ \frac{2}{9} \{ (\sigma_x + \sigma_y + \sigma_z)^2 - 3(\sigma_x \sigma_y + \sigma_y \sigma_z + \sigma_z \sigma_x - \tau_{xy}^2 - \tau_{yz}^2 - \tau_{zx}^2) \} \right\}^{1/2} \\ &= \frac{1}{3} \{ (\sigma_x - \sigma_y)^2 + (\sigma_y - \sigma_z)^2 + (\sigma_z - \sigma_x)^2 + 6(\tau_{xy}^2 + \tau_{yz}^2 + \tau_{zx}^2) \}^{1/2}. \end{aligned} \quad (2.2.25)$$

Rearranging the above equation, τ_o will be expressed in the terms of the second invariant of the stress deviator (Equation 2.2.20) in the form of

$$\tau_o = \sqrt{\frac{2}{3} J_2} = \sqrt{\frac{1}{3} S_{ij} S_{ij}}, \quad (2.2.26)$$

$$\text{since } J_2 = \frac{1}{2} \sum_{ij} S_{ij} S_{ij}.$$

These equations permit the computation of the octahedral stress without the inconvenience of first determining the three principal stresses. It is noted here that the effective shear stress, τ_e defined by Nye (1953) and used in his form of the flow law is related to the octahedral shear stress, τ_o by Nye

$$\tau_e = \sqrt{\frac{3}{2}} \tau_o. \quad (2.2.27)$$

The octahedral normal stress is in fact the hydrostatic pressure and not considered in deformation calculations. The octahedral shear stress is important because it contains the second invariant of the stress deviator which for isotropic ice is assumed to be the only stress parameter affecting the flow of ice (see flow law in section 2.3.3). Also the octahedral shear stress may be regarded as a useful measure of the stress magnitude since it is equal to the root mean square of the principal stress deviators.

2.2.2. Strain Rate

The strain rate ($\dot{\epsilon}$) is defined as the change of strain (ϵ) with the time (t), i.e.

$$\dot{\epsilon} = \frac{d\epsilon}{dt} \quad (2.2.28)$$

2.2.2.1. Strain

In a three dimensional system, if the displacements of a point moving from P to P' in the x-, y- and z-directions are \bar{X} , \bar{Y} and \bar{Z} respectively, the normal strain in the x-direction at P is defined as

$$\epsilon_x = \frac{\partial \bar{X}}{\partial x}, \quad (2.2.29)$$

this definition is suitable for small (infinitesimal) strains. When calculating strains from measurements, the total strain is normally not infinitesimal. If strains are infinitesimal, the total strain (i.e. *natural strain* or *logarithmic strain*) is then the sum of the infinitesimal strains (Jaeger, 1969). The relation between the *natural strain* (δ) and the *nominal strain* (ϵ) is

$$\delta = \ln (1 + \epsilon), \quad (2.2.30)$$

when deformation is small $\delta \sim \epsilon$.

The shear strain may be defined as one half the angular decrease in an initially drawn right angle and has the form of

$$\epsilon_{xz} = \frac{1}{2} \left(\frac{\partial \bar{X}}{\partial z} + \frac{\partial \bar{Z}}{\partial x} \right). \quad (2.2.31)$$

Similarly there are nine components of strain and the other seven of them can be written in corresponding forms. The strain tensor is a second rank tensor and is symmetric, too, because from the definition $\epsilon_{xy} = \epsilon_{yx}$, $\epsilon_{xz} = \epsilon_{zx}$ and $\epsilon_{yz} = \epsilon_{zy}$.

2.2.2.2. The Relation between Strain Rate and Velocity

According to the definition of the strain rate, the normal strain rate in the x-direction is the change of strain in the x-direction with the time as

$$\dot{\epsilon}_x = \frac{d\epsilon_x}{dt} = \frac{d}{dt} \frac{\partial \bar{X}}{\partial x}, \quad (2.2.32)$$

assuming V_x is the velocity in the x-direction and $V_x = \frac{dx}{dt}$, we obtain

$$\dot{\epsilon}_x = \frac{\partial V_x}{\partial x}, \quad (2.2.33)$$

similarly, if V_y and V_z are the velocities in the y- and z-directions, and $V_y = \frac{dy}{dt}$,

$V_z = \frac{dz}{dt}$, the relations for the other strain rate components with velocities can be

expressed bellow:

normal strain rates are:

$$\dot{\epsilon}_y = \frac{\partial V_y}{\partial y} \quad (2.2.34)$$

$$\dot{\epsilon}_z = \frac{\partial V_z}{\partial z}, \quad (2.2.35)$$

shear strain rates are:

$$\begin{aligned} \dot{\epsilon}_{xz} &= \frac{1}{2} \left(\frac{\partial V_x}{\partial z} + \frac{\partial V_z}{\partial x} \right) \\ \dot{\epsilon}_{yz} &= \frac{1}{2} \left(\frac{\partial V_y}{\partial z} + \frac{\partial V_z}{\partial y} \right) \\ \dot{\epsilon}_{xy} &= \frac{1}{2} \left(\frac{\partial V_x}{\partial y} + \frac{\partial V_y}{\partial x} \right). \end{aligned} \quad (2.2.36)$$

Thus, the expression of strain rates in the suffix notation is

$$\dot{\epsilon}_{ij} = \frac{1}{2} \left(\frac{\partial V_i}{\partial x_j} + \frac{\partial V_j}{\partial x_i} \right). \quad (2.2.37)$$

When $i=j$ it represents the normal strain rate, while for $i \neq j$ it represents shear strain rate, so this formulation represents both shear and normal strain rates or all the components of the strain rate tensor.

In general, shear results in rotations which do not change the size and shape of volume element. Similarly, the rotation rate tensor represents the rigid body rotation part of the motion and is given by

$$\dot{\omega}_{ij} = \frac{1}{2} \left(\frac{\partial V_i}{\partial x_j} - \frac{\partial V_j}{\partial x_i} \right). \quad (2.2.38)$$

This is an antisymmetric tensor because $\dot{\omega}_{ij} = -\dot{\omega}_{ji}$, and has only these independent near zero compounds. If $\dot{\omega}_{ij} = 0$ for all i and j , the flow is considered as irrotational. This does not mean that there is no differential rotation of parts within the body but as a whole the rigid body rotation is zero.

2.2.2.3. Strain Rate Tensor

Similar to the stress, the strain rate tensor ($\dot{\epsilon}_{ij}$) at a point can be expressed in terms of strain rate components

$$\dot{\epsilon}_{ij} = \begin{bmatrix} \dot{\epsilon}_x & \dot{\epsilon}_{xy} & \dot{\epsilon}_{xz} \\ \dot{\epsilon}_{yx} & \dot{\epsilon}_y & \dot{\epsilon}_{yz} \\ \dot{\epsilon}_{zx} & \dot{\epsilon}_{zy} & \dot{\epsilon}_z \end{bmatrix} \quad \text{or} \quad \dot{\epsilon}_{ij} = \begin{bmatrix} \dot{\epsilon}_x & \frac{\gamma_{xy}}{2} & \frac{\gamma_{xz}}{2} \\ \frac{\gamma_{yx}}{2} & \dot{\epsilon}_y & \frac{\gamma_{yz}}{2} \\ \frac{\gamma_{zx}}{2} & \frac{\gamma_{zy}}{2} & \dot{\epsilon}_z \end{bmatrix}, \quad (2.2.39)$$

or in terms of principal components

$$\dot{\epsilon}_{ij} = \begin{bmatrix} \dot{\epsilon}_1 & 0 & 0 \\ 0 & \dot{\epsilon}_2 & 0 \\ 0 & 0 & \dot{\epsilon}_3 \end{bmatrix}. \quad (2.2.40)$$

Using the relation of the strain rate components with the velocity gradients (section 2.2.2.1), the tensor of velocity gradients can be expanded into a symmetrical tensor and an antisymmetrical tensor ($\dot{\omega}_{ij}$), and the symmetrical tensor in turn can be expressed as the sum of a spherical tensor ($\dot{\epsilon}_m$) and a deviator (γ_{ij})

$$\frac{\partial V_i}{\partial x_j} = \begin{bmatrix} \dot{\epsilon}_m & 0 & 0 \\ 0 & \dot{\epsilon}_m & 0 \\ 0 & 0 & \dot{\epsilon}_m \end{bmatrix} + \begin{bmatrix} \dot{\epsilon}_x - \dot{\epsilon}_m & \frac{\gamma_{xy}}{2} & \frac{\gamma_{xz}}{2} \\ \frac{\gamma_{yx}}{2} & \dot{\epsilon}_y - \dot{\epsilon}_m & \frac{\gamma_{yz}}{2} \\ \frac{\gamma_{zx}}{2} & \frac{\gamma_{zy}}{2} & \dot{\epsilon}_z - \dot{\epsilon}_m \end{bmatrix} + \begin{bmatrix} 0 & \dot{\omega}_{xy} & \dot{\omega}_{xz} \\ \dot{\omega}_{yx} & 0 & \dot{\omega}_{yz} \\ \dot{\omega}_{zx} & \dot{\omega}_{zy} & 0 \end{bmatrix} \quad (2.2.41)$$

As the ice deformation is assumed incompressible, i.e. the first term on the right hand side of equation 2.2.41 is

$$\dot{\epsilon}_m = \frac{1}{3}(\dot{\epsilon}_x + \dot{\epsilon}_y + \dot{\epsilon}_z) = 0, \quad (2.2.42)$$

the strain rate tensor is therefore a deviator tensor. The second term is the deformation rate tensor and represents a pure distortion, and third term is the rotation rate tensor.

2.2.2.4. Invariants of Strain Rate

The strain rate tensors also have three corresponding invariants to those given for stress. They are

$$\begin{aligned} E_1 &= \text{tr}(\dot{\epsilon}) = \dot{\epsilon}_1 + \dot{\epsilon}_2 + \dot{\epsilon}_3 \\ &= \dot{\epsilon}_x + \dot{\epsilon}_y + \dot{\epsilon}_z, \\ E_2 &= \frac{1}{2} \text{tr}(-\dot{\epsilon}^2) = -\dot{\epsilon}_1\dot{\epsilon}_2 - \dot{\epsilon}_2\dot{\epsilon}_3 - \dot{\epsilon}_3\dot{\epsilon}_1 \\ &= -\dot{\epsilon}_x\dot{\epsilon}_y - \dot{\epsilon}_y\dot{\epsilon}_z - \dot{\epsilon}_z\dot{\epsilon}_x + \gamma_{xy}^2 + \gamma_{yz}^2 + \gamma_{zx}^2, \\ E_3 &= \frac{1}{3} \text{tr}(\dot{\epsilon}) = \dot{\epsilon}_1\dot{\epsilon}_2\dot{\epsilon}_3 \\ &= \dot{\epsilon}_x\dot{\epsilon}_y\dot{\epsilon}_z + 2\gamma_{xy}\gamma_{yz}\gamma_{zx} - \dot{\epsilon}_x\gamma_{yz}^2 - \dot{\epsilon}_y\gamma_{zx}^2 - \dot{\epsilon}_z\gamma_{xy}^2, \end{aligned} \quad (2.2.43)$$

where, $\dot{\epsilon}_i$ ($i=1,2,3$) represent principal strain rates, $\dot{\epsilon}_i$ and γ_{ij} ($i, j=x, y, z$) are components of strain rates.

2.2.2.5. Octahedral Strain Rate

As for the case of stresses, strain rates on an octahedron aligned with the principal axes (see Section 2.2.1.3) are called the octahedral strain rates. By the analogy with the octahedral stress case, the octahedral normal strain rate is zero (incompressibility) and octahedral shear strain rate is

$$\dot{\epsilon}_o = \frac{1}{3} \{ (\dot{\epsilon}_x - \dot{\epsilon}_y)^2 + (\dot{\epsilon}_y - \dot{\epsilon}_z)^2 + (\dot{\epsilon}_z - \dot{\epsilon}_x)^2 + 6(\dot{\gamma}_{xy}^2 + \dot{\gamma}_{yz}^2 + \dot{\gamma}_{zx}^2) \}^{\frac{1}{2}}. \quad (2.2.44)$$

It can be also expressed as

$$\dot{\epsilon}_o = \sqrt{\frac{1}{3} \dot{\epsilon}_{ij} \dot{\epsilon}_{ij}}, \quad (2.2.45)$$

and has the relation with effective shear strain rate given by

$$\dot{\epsilon}_e = \sqrt{\frac{3}{2}} \dot{\epsilon}_o. \quad (2.2.46)$$

2.2.2.6. The Stress State for Different Stress Configurations

As described in the previous section 2.1, in an ice sheet on the large scale where perturbations in the longitudinal stresses are ignored and, for locations where transverse shear stresses are small, the combination of stresses varies from vertical compression dominated in the upper part, to shear dominated in the deeper parts. Therefore, the ice deforms from vertical compression near to surface to horizontal shear near bottom in an ice sheet. The expressions of stresses and strain rates in several common stress configurations which can be set up in a mechanical testing laboratory are summarised in Table 2.1. These involve the stress tensor, the hydrostatic pressure, the stress deviator tensor, the strain rate, the octahedral and effective shear stresses, and the octahedral and effective shear strain rates.

Chapter 2. Ice Rheology

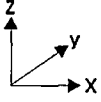
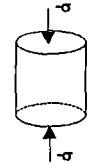
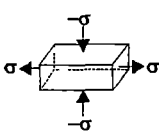
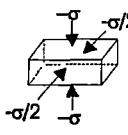
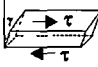
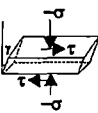
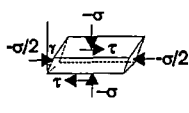
stress state 	Stress tensor σ_{ij}	Hydrostatic pressure P	Stress deviator tensor S_{ij}	Strain rate tensor $\dot{\epsilon}_{ij}$	Octahedral and effective shear stress and strain rate $\tau_o \tau_e \dot{\epsilon}_o \dot{\epsilon}_e$
(a) compression I 	$\begin{pmatrix} 0 & 0 & 0 \\ 0 & 0 & 0 \\ 0 & 0 & -\sigma \end{pmatrix}$	$-\sigma/3$	$\begin{pmatrix} \sigma/3 & 0 & 0 \\ 0 & 0 & 0 \\ 0 & 0 & -2/3\sigma \end{pmatrix}$	$\begin{pmatrix} \dot{\epsilon}/2 & 0 & 0 \\ 0 & \dot{\epsilon}/2 & 0 \\ 0 & 0 & -\dot{\epsilon} \end{pmatrix}$	$\tau_o = \frac{\sqrt{2}}{3}\sigma$ $\tau_e = \frac{1}{\sqrt{3}}\sigma$ $\dot{\epsilon}_o = \frac{1}{\sqrt{2}}\dot{\epsilon}$ $\dot{\epsilon}_e = \frac{\sqrt{3}}{2}\dot{\epsilon}$
(b) compression II 	$\begin{pmatrix} \sigma & 0 & 0 \\ 0 & 0 & 0 \\ 0 & 0 & -\sigma \end{pmatrix}$	0	$\begin{pmatrix} \sigma & 0 & 0 \\ 0 & 0 & 0 \\ 0 & 0 & -\sigma \end{pmatrix}$	$\begin{pmatrix} \dot{\epsilon} & 0 & 0 \\ 0 & 0 & 0 \\ 0 & 0 & -\dot{\epsilon} \end{pmatrix}$	$\tau_o = \sqrt{\frac{2}{3}}\sigma$ $\tau_e = \sigma$ $\dot{\epsilon}_o = \sqrt{\frac{2}{3}}\dot{\epsilon}$ $\dot{\epsilon}_e = \dot{\epsilon}$
(c) compression III 	$\begin{pmatrix} 0 & 0 & 0 \\ 0 & -\sigma/2 & 0 \\ 0 & 0 & -\sigma \end{pmatrix}$	$-\sigma/2$	$\begin{pmatrix} \sigma/2 & 0 & 0 \\ 0 & 0 & 0 \\ 0 & 0 & -1/2\sigma \end{pmatrix}$	$\begin{pmatrix} \dot{\epsilon} & 0 & 0 \\ 0 & 0 & 0 \\ 0 & 0 & -\dot{\epsilon} \end{pmatrix}$	$\tau_o = \frac{1}{\sqrt{6}}\sigma$ $\tau_e = \frac{1}{2}\sigma$ $\dot{\epsilon}_o = \sqrt{\frac{2}{3}}\dot{\epsilon}$ $\dot{\epsilon}_e = \dot{\epsilon}$
(d) simple shear 	$\begin{pmatrix} 0 & 0 & \tau \\ 0 & 0 & 0 \\ \tau & 0 & 0 \end{pmatrix}$	0	$\begin{pmatrix} 0 & 0 & \tau \\ 0 & 0 & 0 \\ \tau & 0 & 0 \end{pmatrix}$	$\begin{pmatrix} 0 & 0 & \dot{\gamma}/2 \\ 0 & 0 & 0 \\ \dot{\gamma}/2 & 0 & 0 \end{pmatrix}$	$\tau_o = \sqrt{\frac{2}{3}}\tau$ $\tau_e = \tau$ $\dot{\epsilon}_o = \sqrt{\frac{2}{3}}\dot{\gamma}$ $\dot{\epsilon}_e = \dot{\gamma}$
(e) Unconfined combination 	$\begin{pmatrix} 0 & 0 & \tau \\ 0 & 0 & 0 \\ \tau & 0 & -\sigma \end{pmatrix}$	$-\sigma/3$	$\begin{pmatrix} \sigma/3 & 0 & \tau \\ 0 & \sigma/3 & 0 \\ \tau & 0 & -2/3\sigma \end{pmatrix}$	$\begin{pmatrix} \dot{\epsilon}/2 & 0 & \dot{\gamma}/2 \\ 0 & 0 & 0 \\ \dot{\gamma}/2 & 0 & -\dot{\epsilon} \end{pmatrix}$	$\tau_o = \frac{\sqrt{2}}{3}\sqrt{\sigma^2 + 3\tau^2}$ $\tau_e = \frac{1}{\sqrt{3}}\sqrt{\sigma^2 + 3\tau^2}$ $\dot{\epsilon}_o = \sqrt{\frac{2}{3}}\sqrt{\frac{\dot{\epsilon}^2}{4} + \dot{\gamma}^2}$ $\dot{\epsilon}_e = \sqrt{\frac{3}{4}\dot{\epsilon}^2 + \dot{\gamma}^2}$
(f) confined combination 	$\begin{pmatrix} -\sigma/2 & 0 & \tau \\ 0 & 0 & 0 \\ \tau & 0 & -\sigma \end{pmatrix}$	$-\sigma/2$	$\begin{pmatrix} 0 & 0 & \tau \\ 0 & \sigma/2 & 0 \\ \tau & 0 & -1/2\sigma \end{pmatrix}$	$\begin{pmatrix} 0 & 0 & \dot{\gamma}/2 \\ 0 & \dot{\epsilon} & 0 \\ \dot{\gamma}/2 & 0 & -\dot{\epsilon} \end{pmatrix}$	$\tau_o = \sqrt{\frac{2}{3}}\sqrt{\frac{\sigma^2}{4} + \tau^2}$ $\tau_e = \sqrt{\frac{\sigma^2}{4} + \tau^2}$ $\dot{\epsilon}_o = \sqrt{\frac{2}{3}}\sqrt{\dot{\epsilon}^2 + \dot{\gamma}^2}$ $\dot{\epsilon}_e = \sqrt{\dot{\epsilon}^2 + \dot{\gamma}^2}$

Table 2.1. Summary of stresses and strain rates in several common stress configurations. (a) unconfined compression; (b) transverse confined compression; (c) longitudinally confined compression; (d) simple shear; (e) unconfined combination of shear and compression; (f) longitudinally confined combination of shear and compression.

2.2.3. Ice Structure

The explicit effect of ice structure on ice flow is usually neglected in most flow laws used in ice sheet modelling. In this section, several parameters commonly considered to be the most important for their effect on the flow of ice are discussed.

2.2.3.1. Crystal Orientation Fabric

Crystal orientation fabrics represent the distribution of the directions of the c-axes of the ice crystals in space. For example, in a horizontal section of ice a central single maximum pattern or fabric indicates that the c-axes of most of the crystals are near to vertical and the irregular basal planes are near to horizontal. C-axes of individual crystals can be measured with a Rigsby Stage (Langway, 1958), or an automatic fabric analyzer (Russell-Head, personal communication) using optical polarization properties associated with the c-axes direction.

A large number of experimental results have shown that the various crystal orientation fabric patterns found in the natural ice sheets can be produced in the laboratory by deforming ice samples through the application of a similar dominant stress configuration to a similar total strain, at the same temperature. Unconfined uniaxial compression (Figure 2.6a) produces a small circle girdle fabric with c-axes clustered in a ring (girdle) centered on the compression axis (Jacka and Maccagnan, 1984; Gao and Jacka, 1987). This type of fabric occurs frequently in the upper zones of the ice thickness in natural ice sheets where the ice deformation is dominated by a net vertical compression (Jacka and Gao, 1989) with uniform extension in both horizontal directions. Vertical compression with horizontal extension confined to one dimension (approximately plane strain) (Figure 2.6b) produces 2 maxima centered in the plane of deformation at a similar angle to the vertical (Budd and Matsuda, 1974). The upper ice fabrics may be expected to typically vary between these two cases depending on the transverse strain rate. Simple shear initially develops a fabric with two maxima (Figure 2.6c) but, due to rotation, this changes to a single maximum (Figure 2.6d) in the direction perpendicular to the plane of shear, provided the deformation continues to large strain (Bouchez and Duval, 1982; Kamb, 1972; Gao and others, 1989).

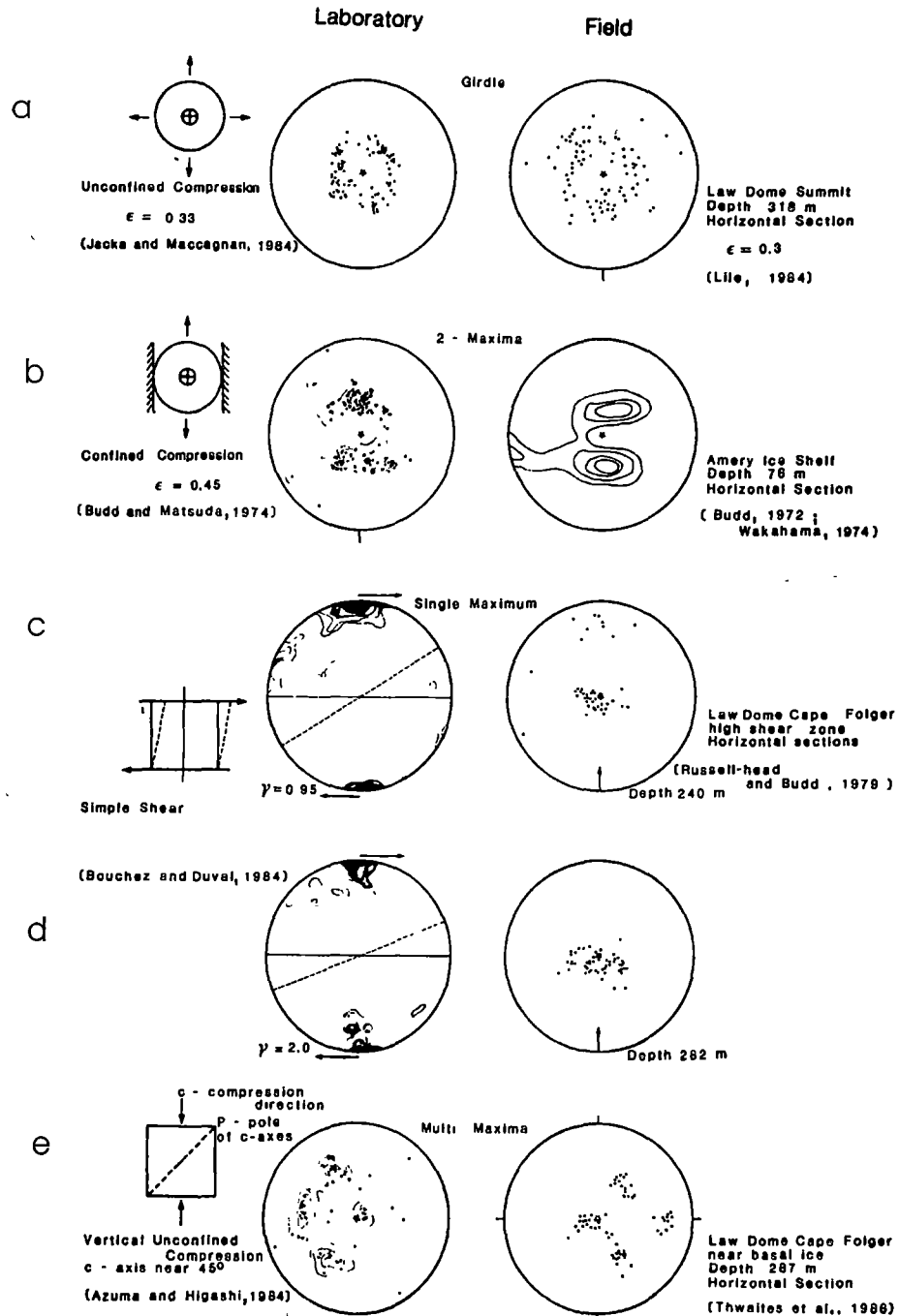


Figure 2.6. Ice crystal orientation fabrics for different stress situations from laboratory studies and field observations from ice sheets. (a) Unconfined uniaxial vertical compression giving a small circle girdle. (b) Confined vertical compression and longitudinal extension giving two stable maxima. (c) Simple shear developing stages with secondary maximum. (d) Simple shear later stages with a single maximum. (e) Multiple 4-maxima fabric produced from a single maximum by compression. (from Budd and Jacka, 1989).

In the large polar ice sheets, single maximum fabrics, associated with fine crystals, generally exist around the third quarter of the depth where strong horizontal shear deformation dominates (e.g. Gow and Williamson, 1976; Herron and Langway, 1982; Hooke and Hudleston, 1981). A multiple-maxima fabric pattern (Figure 2.6e) is sometimes exhibited in the ice near the base of ice sheets particularly where the ice temperature is warmer than -10°C (e.g. Gow and Williamson, 1976; Matsuda and Wakahama, 1978; Kamb and Shreve, 1963; Xie 1985). This ice often consists of large crystals consistent with the higher temperatures and possibly low deformation rates for the ice in which it is found. Comparable fabric patterns have also been developed in the laboratory deformation under combined compression and shear stresses (Li, unpublished; Li and others, 1996). A study of the a -axes directions in large crystal multi maximum fabric ice by Matsuda and Wakahama (1978) indicated that this type of ice may be characteristic of twinning. Russell-Head and Budd (1979) found this type of ice had a similar shear rate to randomly oriented laboratory ice. The effect of crystal fabric on ice flow and the development of ice crystal orientations with the ice flow will be discussed in Chapter 3.

2.2.3.2. Crystal Size

The study of crystal size distributions in ice sheets can also provide information on the past history of the ice or on its current conditions depending on the stress, temperature and the rates of crystal growth and deformation.

In natural ice sheets it has been widely found that crystal size varies with depth and also with distance along an ice sheet (Gow and Williamson, 1976; Herron and others, 1985; Li and others, 1985, 1988; Xie, 1985; Duval and Lorius, 1980; Kamb, 1963; Young and others, 1985; Nartita and others, 1978, 1986). Some measurements from ice cores have shown a strong relationship between crystal size, microparticle concentration and fabric, i.e. smaller crystals are coincident with higher microparticle concentrations and stronger fabrics. The contrast with clean ice is especially strong for ice from the time of the glacial maximum (Hooke and Hudleston, 1980; Hooke and others, 1988; Dahl-Jensen and Gundestrup,

1987; Herron and Langway, 1982; Thompson, 1977; Thompson and Mosley-Thompson, 1981; Morgan and others, 1998).

The results from laboratory experiment have shown that the initial crystal size in laboratory-made randomly orientated ice does not effect ice minimum strain rate while the ice flow to tertiary strain induces a steady state crystal size dependent on the stress and temperature (Jacka, 1984; Wang, 1994; Li, 1995).

2.2.3.3. Impurities

The impurities in polar ice sheets include insoluble and soluble matter. The insoluble impurities consist mainly of “dust”, i.e. particles in the size range 0.1 to 2 μm , which are of continental origin, and are transported to the ice sheets by wind. The soluble impurities comprise predominantly sodium, calcium and magnesium, and chloride, nitrate and sulphate ions. In both hemispheres, sodium and chloride come mainly from sea salt. Sulphate ions come mainly from sulphuric acid produced by oxidation of dimethylsulphide emitted at the ocean surface by biogenetic activity in Antarctica (Langway and others, 1988) and in the Northern Hemisphere (Herron and Langway, 1985). Major volcanic eruptions can produce significant increases in concentrations of sulphuric and hydrochloric acid, but these peaks are limited to two to three years after each event (Hammer, 1980). The source of nitrate is neutral nitrate salt and nitric acid which is most probably formed by tropical or mid-latitude lightning and transported with water vapour to Antarctica (Legrand and Delmas, 1986,1988). Their source is unknown in the Northern Hemisphere (Herron, 1982).

Some laboratory results show that for high concentrations of insoluble impurities the strain rates may decrease with increased concentrations (Hooke and others, 1972; Ting, 1983). The results reported by Budd and Jacka (1989) show very little effect of sand content in ice (at -18°C , 1.3 bars octahedral stress in compression) up to concentrations of about 15% by volume. Some field measurements show enhanced flow rates in dirty basal ice (Shoji and Langway, 1984) or in basal amber coloured ice (Holdsworth and Bull, 1970; Anderton, 1974). However in these field situations it is also necessary to take account of

possible crystal orientation and size effects. The effect of insoluble impurities on strain rate for low concentrations is still a subject of ongoing research. For example, recent experiments (Li, personal communication) on laboratory-made ice containing dust up to 0.8% by volume, at temperatures varying from -0.2°C to -13°C and octahedral shear stress between 2 bar and 5 bar, in compression and simple shear stress configurations respectively have shown a slightly slower flow tendency.

Some laboratory experiments have suggested that there may be effects of concentrations of the soluble impurities on ice flow rates. Dahl-Jensen and Gundestrup (1987) attributed the enhanced deformation rate of Wisconsin ice in the Dye 3 borehole primarily to the high concentration of chloride and sulphate ions and dust. Fisher and Koerner (1986) ascribed the enhanced flow observed in the Agassiz Ice Cap to high concentrations of calcium and dust. It is usually considered that two forms of chemical impurities can effect the flow of ice if present in high enough concentration. These are trace concentrations of some dopants such as fluoride or ammonia (Glen and Jones, 1967; Jones and Glen, 1969) and relatively larger concentrations of more common natural chemicals such as sea salt (Glen, 1974, 1975).

The results from ice deformation tests (Wang, 1994) examining the tertiary strain rate and impurity concentrations failed to find any significant difference between the flow rates of Wisconsin and Holocene ice from these ice cores, despite significant variations in the impurity concentrations. On the other hand these experiments showed that the ice crystal orientation fabrics had a strong effect on the deformation rate.

2.2.3.4. Density

Densities in an ice sheet vary with depth. In firn layers densities change from about 0.4 Mg m^{-3} (snow) to 0.82 Mg m^{-3} (bubble close off). Beyond the value of 0.82 Mg m^{-3} the densities increase slowly due to compression of the bubbles to a maximum about of 0.93 Mg m^{-3} (Paterson, 1994). Studies of density have shown that the creep rate tends to decrease with increasing density in the range of 0.65 Mg m^{-3} to 0.83 Mg m^{-3} (Mellor and Smith, 1966). Only small changes in the

creep rate occur with further the changes of density when the density is greater than 0.82 Mg m^{-3} (Gao, unpublished; Jacka, 199x; Budd and Jacka, 1989). Since the firm layer is a small fraction of the total depth in ice sheet, the density effects on strain rates may be neglected for large scale ice sheet modelling.

2.2.4. Temperature

The temperature distribution in an ice sheet results from the interaction of several processes, such as, the surface mean temperature, the accumulation at the surface, ice thickness, the geothermal heat, basal melting, conduction, advection associated with ice movement and the deformational generation of heat within the ice. The present variation of temperature with depth in polar ice sheets provides information about past variations of surface temperature (Paterson, 1994). In an ice sheet the change of snow to ice and the deformation rate of ice are dependent on temperature. Laboratory tests (Lile, 1984) have shown a linear thermal coefficient of expansion for ice of approximately $5 \times 10^{-5} \text{ }^{\circ}\text{C}^{-1}$, i.e. a $1 \text{ }^{\circ}\text{C}$ change in temperature will cause a change of 5×10^{-5} in thermal strain.

2.3. Isotropic Temperature Dependent Flow Law

Fundamental to all theoretical treatment of ice flow is the flow law of ice, i.e. the relation between strain rate and the stress that produces it. Based on mechanical experiments on randomly oriented polycrystalline ice (Glen, 1955a; Steinemann, 1954), Glen (1955) found that the secondary (minimum) strain rate varied as a power of the stress, suggesting an empirical power law representation of the form

$$\dot{\epsilon} = A \sigma^n \quad (2.3.7)$$

Where $\dot{\epsilon}$ is the strain rate, σ is the applied stress. The exponent n is generally accepted as a constant with a mean value of 3 (e.g. Glen, 1958; Budd, 1968; Hooke, 1981; Budd and Jacka; 1989). The sufficient A is observed to depend strongly in temperature. The value of A is proposed to vary, with temperature according to the Arrhenius relation (Paterson, 1994)

$$A(T) = A' \exp(-Q/RT) \quad (2.3.8)$$

Where A' is independent of temperature, R is the gas constant ($8.314 \text{ J mol}^{-1} \text{ K}^{-1}$), Q the activation energy for creep which varies with temperature and has a mean value of about 60 kJ/mol when $T < -10^\circ \text{C}$ and about 139 kJ/mol when $T > -10^\circ \text{C}$, but which increases rapidly approaching the melting point reaching values over 300 kJ/mol above -1°C (Budd and Jacka, 1989) as shown in Table 2.2.

Temperature ($^\circ \text{C}$)	-0.525	-1.5	-3.5	-7.5	-15	-25	-35	-45
Activation energy (kJ mol^{-1})	500	300	200	124	77	66	71	73

Table 2.2. Apparent activation energy for minimum creep rate at $\tau_o=1\text{bar}$ (octahedral) from -0.525 to -45°C . (modified from Budd and Jacka, 1989).

In order to express the stress dependence of the flow law for ice in a more general form Glen (1958) examined the relationship between the stress and strain rate tensors. Assuming isotropic polycrystalline ice for which the strain rate depends only on stress, he started with a general form in terms of the stress tensor (σ_{ij}) as

$$\dot{\epsilon}_{ij} = A(I_1, I_2, I_3) \delta_{ij} + B(I_1, I_2, I_3) \sigma_{ij} + C(I_1, I_2, I_3) \sigma_{ik} \sigma_{kj} \quad (2.3.9)$$

or in terms of deviatoric stress tensor (S_{ij}) as (assuming the summation convention applies for repeated suffixes)

$$\dot{\epsilon}_{ij} = A(J_2, J_3) \delta_{ij} + B(J_2, J_3) S_{ij} + C(J_2, J_3) S_{ik} S_{kj} \quad (2.3.10)$$

where ϵ_{ij} is strain rate tensor, the suffixes i and j can take any of the values 1, 2 or 3 and so give the various components of the two tensors, kronecker $\delta_{ij} = 1$ if $i = j$ and $\delta_{ij} = 0$ if $i \neq j$, and A , B and C are scalar functions of the invariants of the stress tensor I_1 , I_2 and I_3 , or of the invariants of the deviatoric stress tensor J_2 and J_3 only, J_1 being zero (see Section 2.2.1). Then he made following three assumptions to reform this complex relation to a more simple expression.

Assumption I: incompressibility.

If it is assumed that the density of ice remains constant during flow, i.e. ice is incompressible, Equation 2.3.10 can be written as

$$\dot{\epsilon}_{ii} = A(J_2, J_3) \delta_{ii} + B(J_2, J_3) S_{ii} + C(J_2, J_3) S_{ik} S_{ki} = 0. \quad (2.3.11)$$

Since $S_{ii}=0$, $\delta_{ii}=3$, and $J_2=1/2 S_{ik}S_{ki}$ (see Section 2.2.1), Equation 2.3.11 becomes

$$A(J_2, J_3) = -\frac{1}{3} C(J_2, J_3) S_{ik} S_{ki} = -\frac{2}{3} C(J_2, J_3) J_2. \quad (2.3.12)$$

Substituting the above relation in to equation 2.3.10 gives

$$\dot{\epsilon}_{ij} = -\frac{2}{3} C(J_2, J_3) J_2 \delta_{ij} + B(J_2, J_3) S_{ii} + C(J_2, J_3) S_{ik} S_{ki}. \quad (2.3.13)$$

This is the most general form that the relation between stress and strain rate can have under the assumption I. This relation contains two arbitrary functions of two variables which can not be determined from any laboratory experiment under simple single stress configurations, for example compression tests. To obtain a simpler form of the flow relation further assumptions are required.

Assumption II: proportionality of strain rate and stress deviator components.

A further assumption was made by Nye (1957) that the components of strain rate are proportional to the components of the stress deviator. This assumption implies that the principal strain rates are proportional to the principal stress deviators and it can be written (assuming none of S_1, S_2, S_3 are zero)

$$\frac{\dot{\epsilon}_1}{S_1} = \frac{\dot{\epsilon}_2}{S_2} = \frac{\dot{\epsilon}_3}{S_3}. \quad (2.3.14)$$

Substituting for $\dot{\epsilon}_1, \dot{\epsilon}_2$ and $\dot{\epsilon}_3$ from Equation 2.3.12 we have

$$\begin{aligned} & -\frac{2}{3} C(J_2, J_3) \frac{J_2}{S_1} + B(J_2, J_3) + C(J_2, J_3) S_1 \\ & = -\frac{2}{3} C(J_2, J_3) \frac{J_2}{S_2} + B(J_2, J_3) + C(J_2, J_3) S_1 \\ & = -\frac{2}{3} C(J_2, J_3) \frac{J_2}{S_3} + B(J_2, J_3) + C(J_2, J_3) S_3 \end{aligned} \quad (2.3.15)$$

Subtracting from each of these expressions to remove $B(J_2, J_3)$ and dividing by $C(J_2, J_3)$ providing it is not zero gives

$$-\frac{2}{3} \frac{J_2}{S_1} + S_1 = -\frac{2}{3} \frac{J_2}{S_2} + S_2 = -\frac{2}{3} \frac{J_2}{S_3} + S_3. \quad (2.3.16)$$

It is obvious that this equation is not true when $S_1=1$, $S_2=-1$ and $S_3=0$. Thus the assumption that $C(J_2, J_3)$ is not zero must be false, and Equation 2.3.13 can be reduced to

$$\dot{\epsilon}_{ij} = B(J_2, J_3) S_{ij}. \quad (2.3.17)$$

Assumption III: dependence of flow on second invariants only.

This assumption in fact removes the influence of the anisotropy of the stress configuration from the flow rates. (It had already been assumed that the flow properties of the material were isotropic, Equation 2.3.9). With this assumption we can reduce Equation 2.3.13 further to

$$\dot{\epsilon}_{ij} = B(J_2) S_{ij}. \quad (2.3.18)$$

For the laboratory results given above with the power law flow with index $n=3$ the commonly used isotropic form of the flow law can be expressed as

$$\dot{\epsilon}_{ij} = A(T) \tau_o^2 S_{ij} \quad (2.3.19)$$

since $\tau_o^2 = \frac{2}{3} J_2$ (Equation 2.2.26).

It should be noticed that this simpler form of relation between strain rate and the stress tensors is only for isotropic ice and not appropriate for anisotropic ice. The flow relation for anisotropic ice as is relevant to ice sheets, will be discussed in Chapter 3 and Chapter 4 of the thesis.

Chapter 3

ANISOTROPIC ICE FLOW

In this chapter the anisotropy of polycrystalline ice and its effect on ice flow are discussed. The relationship between the enhancement factor and the fabric parameter for strength of c-axis verticality, $\phi(1/4)$, is investigated by the analysis of the anisotropic ice and flow rates observed from several boreholes and ice cores drilled in Law Dome, Antarctica. A review of a number of laboratory experiments and numerical modelling studies, including modelling of anisotropic ice flow and modelling of development of crystal c-axis orientation fabric, is presented.

3.1 Anisotropic Ice and its Effect on Ice Flow

Polycrystalline ice described in the previous section (Section 2.3) was mainly considered as an ice aggregate consisting of fine-grained randomly oriented crystals forming a statistically homogeneous and isotropic material. In large ice sheets this type of isotropic ice only occurs to relatively shallow depths, typically less than several hundred metres. The large amounts of deeper ice have highly anisotropic crystal structures which are the result of continuous deformation to large strains involving several processes such as crystal rotation, recrystallisation and crystal growth (Steinemann, 1954, 1958; Budd, 1972; Rigsby, 1972; Gow and Williamson, 1976; Budd and Jacka, 1989; Alley, 1988, 1992).

Figure 3.1 shows an example of the development of a sequence of anisotropic ice fabrics as observed through an ice core obtained from the borehole (BHC1, see Section 3.2 for detail) in the Law Dome ice cap, East Antarctica.

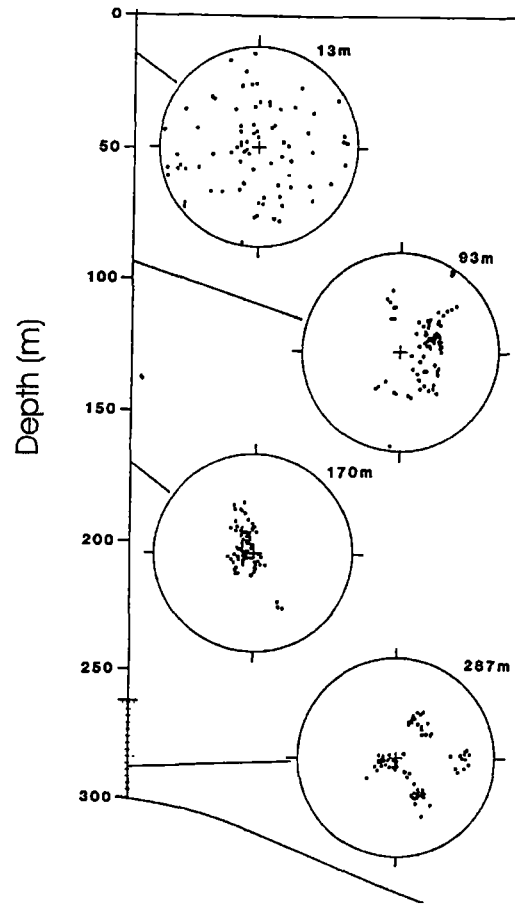


Figure 3.1. Observed fabrics for horizontal sections from the ice core drilled in the Law Dome Ice Cape, East Antarctica. (from Thwaites and others, 1984).

It is seen that near the surface the crystal fabric is approximately random. A broad maximum gradually develops with increasing depth, and then tends towards the central axis. As shear strain accumulates, this fabric pattern develops into a strong central maximum. A multi-maximum or diamond pattern appears at the bottom, which is considered to be the result of stress relaxation and annealing under relative warmer temperatures in the basal portion of the ice cap (Etheridge, 1989; Thwaites and others, 1984; Han and Young, 1988; Xie and others, 1991). The analysis by Matsuda and Wakahama (1978) indicates that this large crystal basal

ice may also be associated with twinning. The similar evolution of the fabrics has been found from Antarctica (Thwaites and others, 1984; Xie, 1985; Li, 1995; Young and others, 1998), Greenland (Herron and others, 1985; Thorsteinsson, 1996) and other ice masses (Fisher and Koerner, 1986).

A number of field and laboratory studies of ice deformation have indicated that crystallographic anisotropy plays an important role in the flow of ice. The anisotropy due to flow-induced crystal orientations has a most significant effect on the ice flow rate in natural ice masses (e.g. Russell-Head and Budd, 1979; Budd and Jacka, 1989; Wang, 1994).

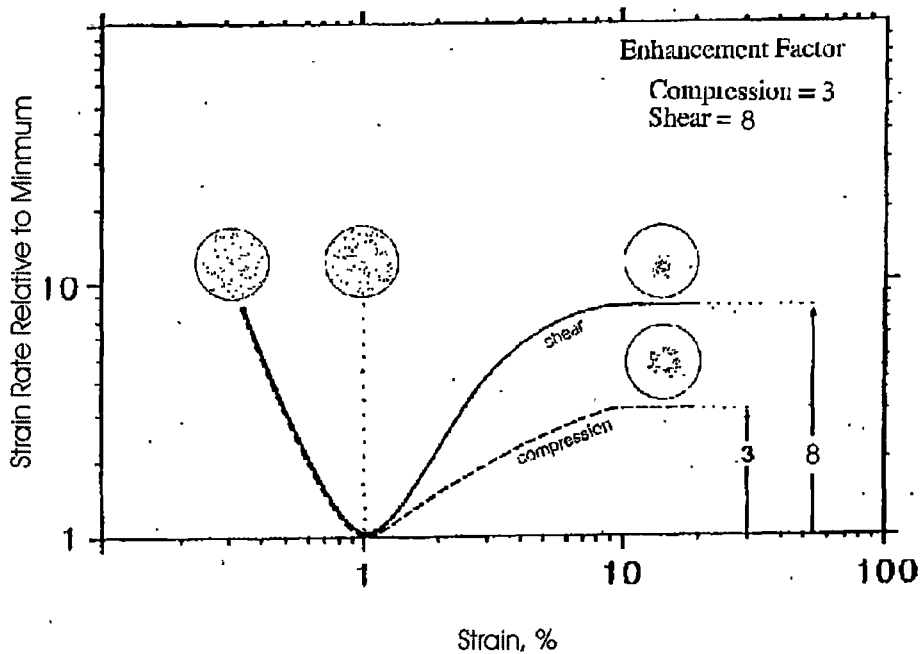


Figure 3.2. Creep curves with compatible fabrics for initially isotropic ice. Octahedral shear strain rates versus strain for initially isotropic ice going through to tertiary strain by which stage well developed anisotropy is established. The shear rate enhancement above minimum is about 8 compared to that for compression of about 3. (modified from Budd and Jacka, 1989).

As summarised in Figure 3.2, laboratory ice creep tests on initially randomly orientated polycrystalline ice subjected to constant stress indicate that the minimum strain rate is attained at about 1% octahedral shear strain. Beyond this, and associated with the development of the anisotropic fabric in the ice sample, the strain rate increases. This can be considered as an enhancement of

strain rate above the minimum strain rate as a function of strain, and is observed over a range of stresses and temperatures. The enhanced strain rate approaches an asymptote beyond about 10-20% octahedral shear strain, with an enhancement factor of about 3 for uniaxial compression and about 6 to 10 for simple shear (Budd and Jacka, 1989; Li and others, 1996).

The work of Russell-Head and Budd (1979), relating Antarctic bore-hole shear measurements (BHF, see Section 3.2 for detail) to long-term shear deformation experiments on anisotropic ice samples from the ice cores obtained from that borehole, demonstrated the existence of enhanced flow at deeper levels in the ice sheet (Figure 3.3).

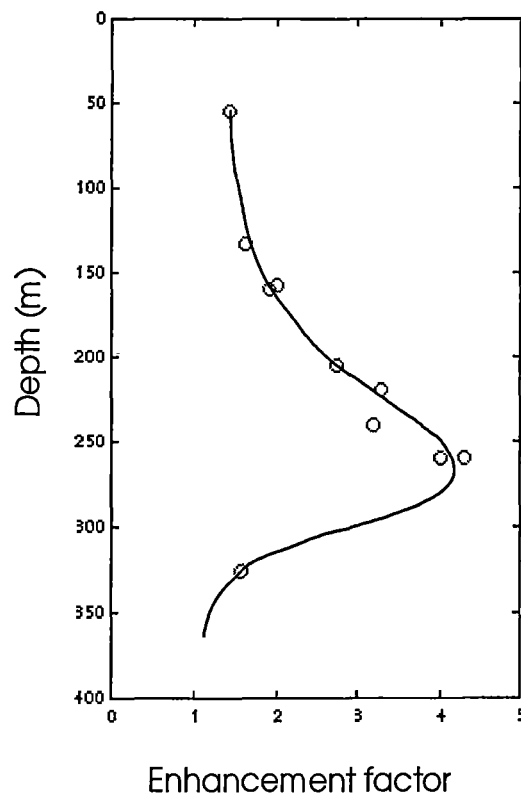


Figure 3.3. Strain rate enhancement factor as a function of depth in the ice sheet, from a combination of laboratory deformation studies of the ice core samples, and changes in inclination of the borehole with depth, from BHF on Law Dome. (from Russell-Head, 1979).

Deformation tests on polycrystalline ice with a developed crystal orientation fabric have shown that the creep rate is enhanced when the preferred orientation fabric is

compatible with the stress configuration. For example a single maximum pattern is compatible with a shear stress configuration where the shear stress is applied across the plane normal to the maximum and a small circle girdle pattern is compatible with a symmetrical axial compressive stress configuration. Therefore, it is said that the single maximum fabric is an “easy glide” crystal orientation fabric for shear and the small circle girdle fabric for compression in the respective compatible orientations. Recent laboratory experiments (Li and Jacka, 1998) have shown that for shear the fabric which is compatible with compression (i.e. a small circle girdle pattern) is an easier glide crystal orientation fabric than the uniform distribution and this pattern facilitates enhanced flow by a factor of about 2.5 over the minimum flow rate for a random fabric. In Figure 3.4, we can see that with the progression of strain, the ice deformation tends to reach a constant steady state (tertiary) flow rate. The path to steady state flow is dependent upon the relationship between stress configuration and crystal orientation fabric pattern. Ice with an initial c-axis fabric pattern compatible with the applied stress configuration (i.e. “easy glide”) reaches the steady state tertiary flow rate (for initially isotropic ice) directly, without passing through a minimum creep stage (curves i). In contrast the flow of ice with an initially “hard glide” fabric (such as a single maximum fabric in compression in the direction of the fabric maximum) has a minimum strain rate (curve a iii) lower than that of the isotropic ice for compression (curve a ii). Figure 3.4 (b) shows the result of an example of the small circle girdle from compression giving higher shear rates (b iii) than the isotropic ice as mentioned above (b ii). This is because the mean angle of the girdle fabric from the compression (25° - 30°) tends to have the basal planes of the crystals more favourable for horizontal shear than those of the isotropic ice.

The clear relationship between the preferred orientation of c-axes and the strain rates has been demonstrated by many laboratory experiments (Lile, 1978; Russell-head and Budd, 1979; Duval and Le Gac, 1982; Azuma and Higashi, 1984; Gao, 1989; Wang, 1994) and by borehole tilting measurements (Shoji and Langway, 1984; Russell-Head and Budd, 1979; Gundestrup and Hansen, 1984; Morgan and others, 1998). The main results is that the tertiary flow rates and crystal

anisotropy develop together with strain and this will be used for the basis of the anisotropic ice flow model developed here.

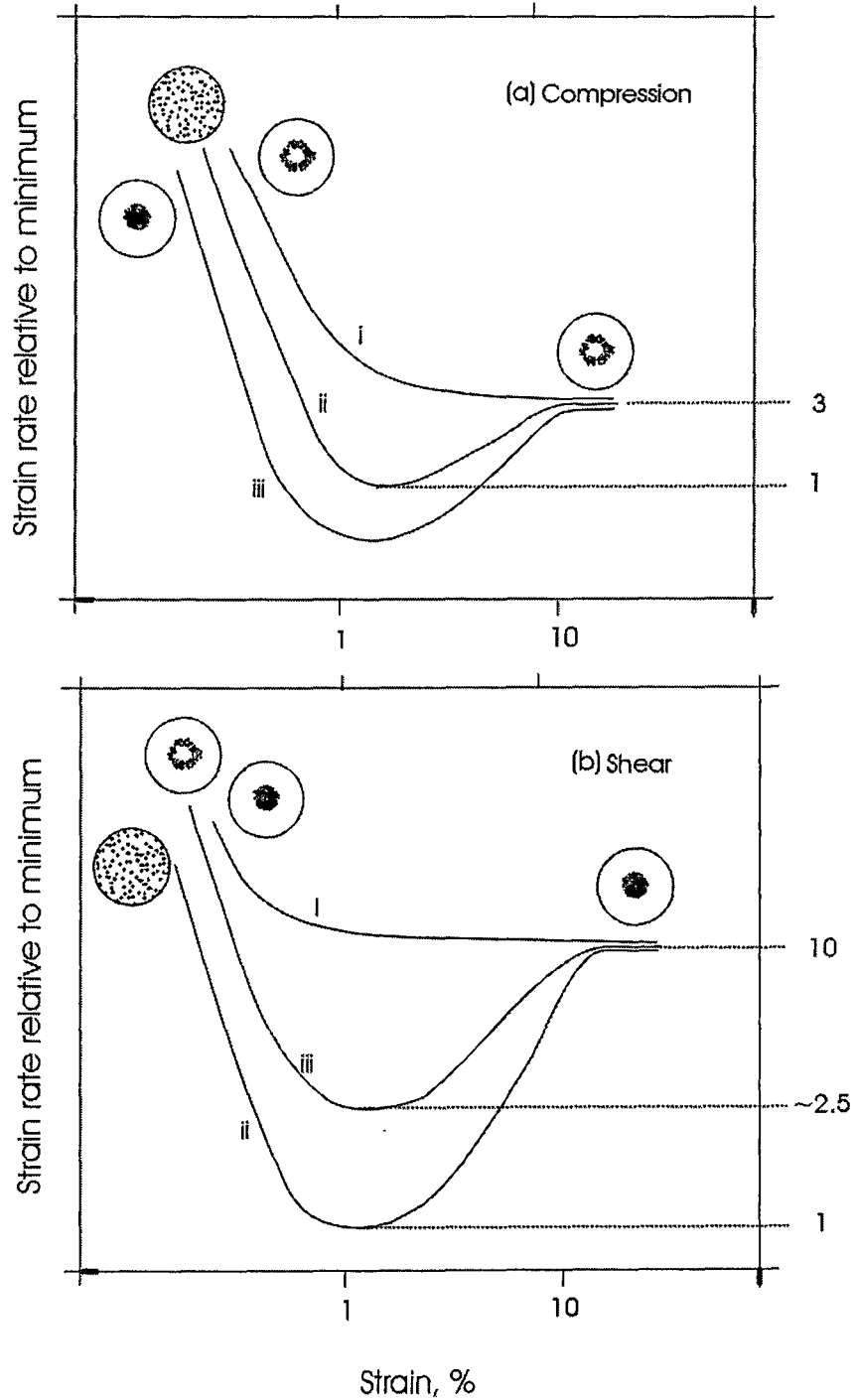


Figure 3.4. Creep curves with compatible fabrics for initially isotropic and anisotropic ice in compression (a) and in shear (b) stress configurations.

3.2 Analysis of Anisotropic Ice and flow Rates Observed from the Field

Following the work of Russell-Head and Budd (1979), relating the enhancement factor with the crystal fabrics at a borehole (BHF) drilled in Law Dome, East Antarctica, a new analysis of enhanced flow and relation between enhancement factors and fabrics at other boreholes drilled near BHF along a traverse line from Law Dome Summit to Cape Folger are presented here. First some background information on Law Dome is presented to provide the context for the flow line with the boreholes.

3.2.1 Law Dome

Law Dome (Figure 1.2 and Figure 3.5), previously referred to as Wilkes Ice Cap (Budd 1970), is a small local ice cap, about 200 km in diameter, adjoining the main Antarctic ice sheet in Wilkes Land between longitudes 110 °E and 116 °E. The ice cap is approximately circular with a surface elevation of 1389 m at the summit, 66°44' S, 112°50' E. It is separated from the main Antarctic ice sheet by the divergence of two large glaciers which define its borders to the south. To the north, Law Dome is surrounded by the ocean. Its flow pattern can therefore be studied in isolation from the main Antarctic ice sheet.

The ice flow from the main East Antarctic ice sheet diverges around the southern side of Law Dome, exiting to the sea via the steep-sided trench which connects the Vanderford and Totten glaciers. In regards to the long term history of the Law Dome ice cap, there is evidence from the oxygen isotope analysis of the deeper ice at Cape Folger (Budd and Morgan, 1977), and from the glacial geomorphology of the Windmill Islands (Cameron, 1964) to suggest that prior to 10000 years ago, Law Dome was more extensive but not completely covered by the main Antarctic ice sheet. Since then, the Antarctic ice has retreated and Law Dome has become an ice cap near to a balanced state with its present configuration and with a largely independent flow regime.

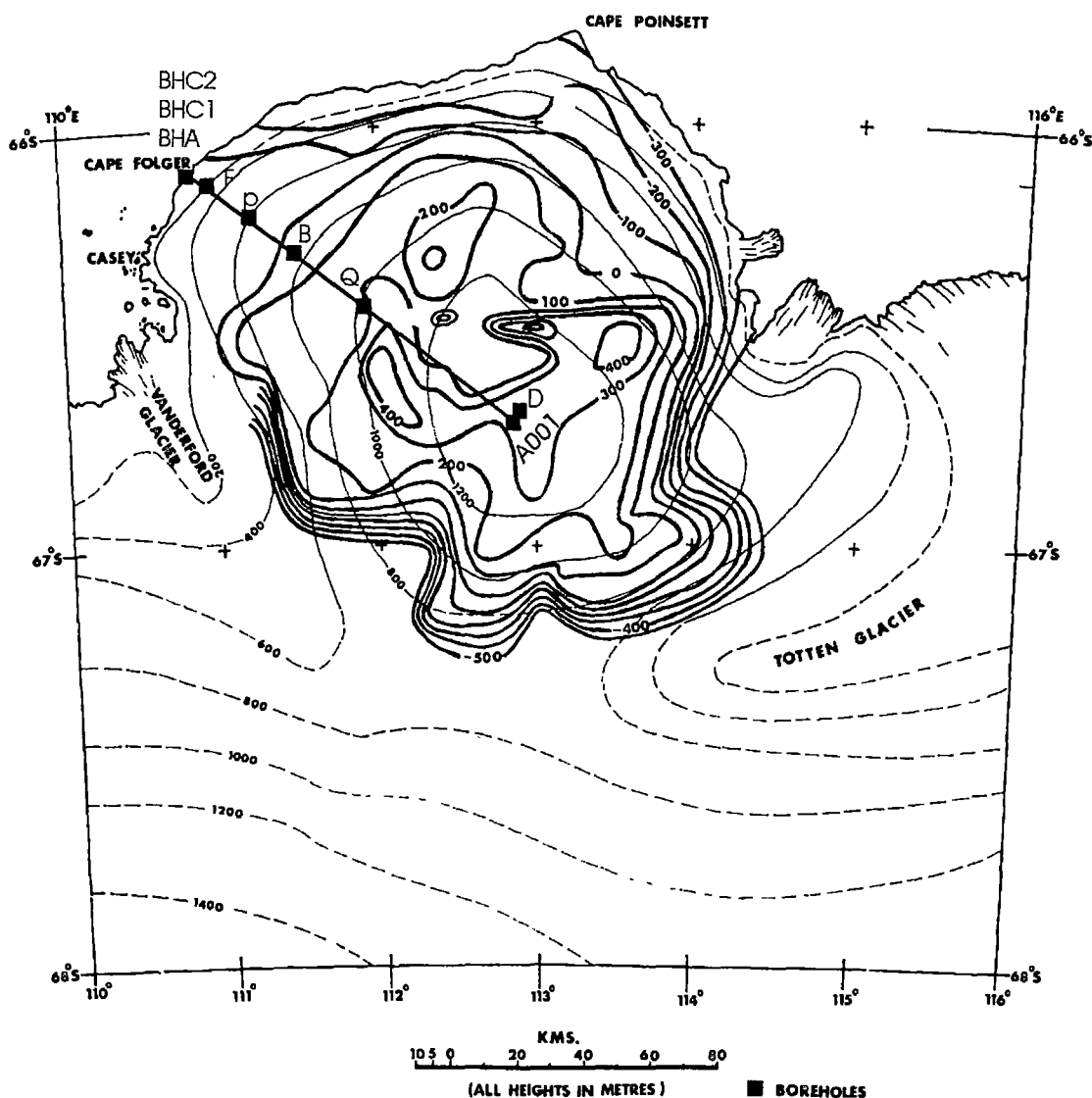


Figure 3.5. Map of Law Dome showing surface (thin line) and bedrock (thick line) elevations. The traverse route From Dome Summit to Cape Folger and the locations of borehole site are also shown. (modified from Budd and others, 1976).

Near the centre of Law Dome, ice thickness exceeds 1200 m. The bedrock (Figure 3.5) is irregular and has several high points where elevation exceeds 400 m above sea level. The average bedrock elevation is about 300 m near the centre of Law Dome (which is a high point in both surface and bedrock) and falls away to several hundred metres below sea level at the northern seaward boundary.

Ice velocity increases from the summit towards the coast. On the west side, measured values increase from zero at the summit to about 10 m yr^{-1} near Cape Folger. Ice velocity tends to be smaller in the south-west quadrant and increases towards the east and along the northern coastline. The largest values of ice velocity occur in the north-east and towards the east the measured values are mainly in the range of 0 to 50 m yr^{-1} and exceed 100 m yr^{-1} towards the coast. Some ice surface velocity vectors selected from the 1966 triangulation survey measurements (Pfitzner, 1980) are shown in Figure 3.6.

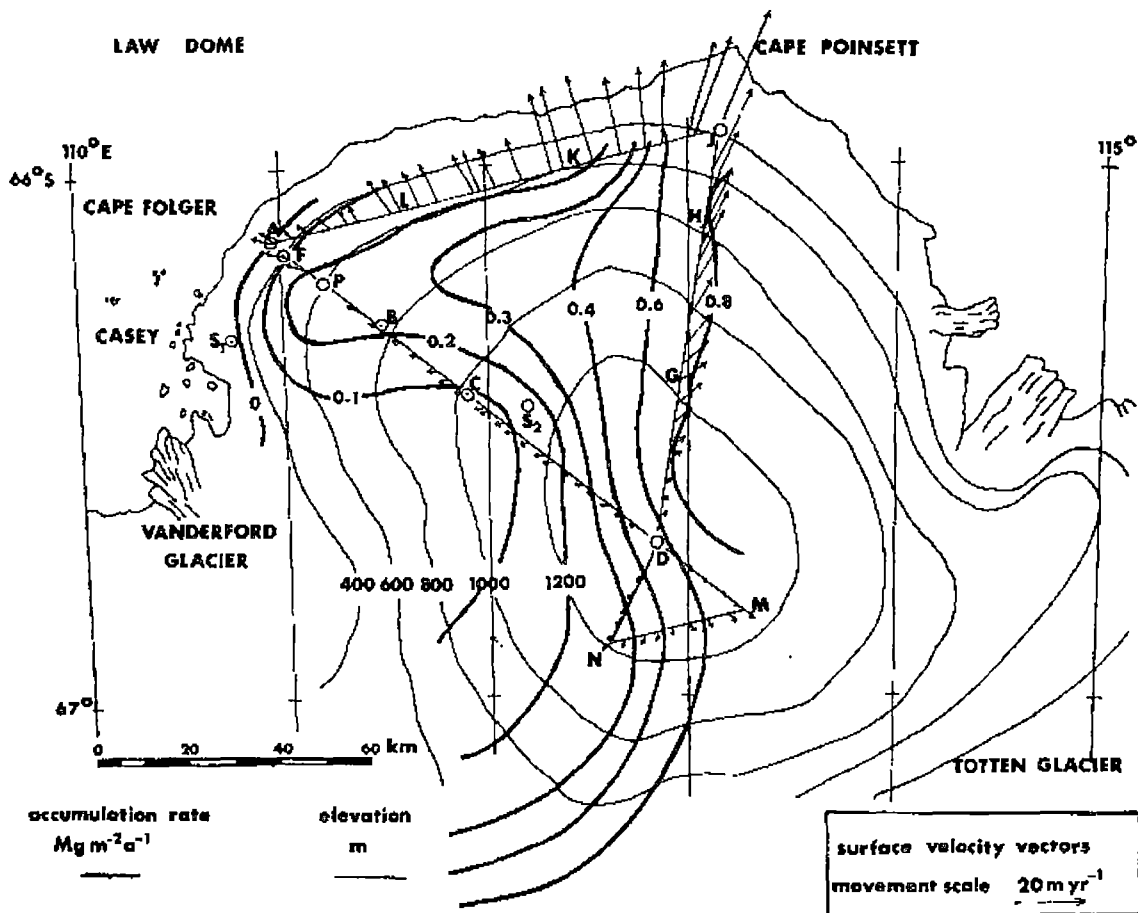


Figure 3.6. Map of Law Dome showing surface accumulation (bold contours) and velocities. (from Budd and others, 1976).

Surface accumulation data (Budd and Morgan, 1977; Hamley and others, 1986; Xie and others, 1989) shows that the strong gradient in accumulation increases from west to east. The largest values of accumulation rate are found on the east side, with extreme values in the south-east and on the Totten Glacier, while the smallest values are found in the south-west quadrant. The distribution of accumulation rate on Law Dome is also shown in Figure 3.6.

Mean annual surface temperature varies approximately linearly with elevation over a narrow range from -9°C to -22°C (Xie and others, 1989). The characteristic surface lapse rate for Law Dome is $1.02^{\circ}\text{C}/100\text{ m}$, for elevations above 400 m (Cameron, 1964), but for the data from the northern half of Law Dome the surface lapse rate is $0.95^{\circ}\text{C}/100\text{ m}$ (Xie and others, 1989). Melt is rare above 400 m and the typical deposited snow crystal size in the net accumulation at the surface is about 0.3 mm.

Law Dome is an accessible and conveniently located ice cap which is well suited to modelling studies. Data collection is continuing and, in addition to the interest in ice core drilling, includes surface ice velocity measurements which are being extended and improved using satellite Doppler and GPS positioning equipment. Because of the isolated and roughly symmetrical nature of this ice cap, it is also of interest as an analogue of the larger main East Antarctic ice sheet. It is small enough to be studied in detail but large enough to exhibit the main general features of large ice masses.

3.2.2 The Flow Line from Law Dome Summit to Cape Folger

Since the 1950's, a large amount of glaciological work has been carried out to determine the physical characteristics of Law Dome. This work has involved many field surveys, including firn and ice core drilling. Surveys undertaken on over-snow traverses provided information on the surface physical characteristics of the ice cap including its shape, mass budget and surface flow velocity.

Analyses of snow and firn cores provide data on the distribution of physical properties in the near surface layer and the processes which determine those properties. Analyses of deep ice cores provide data on the internal properties of the ice cap and its dynamics. Other analyses can be made on the firn and ice cores

in order to investigate past changes of climate and to reconstruct changes of the ice sheet extent and the development of the ice cap over time. A brief history of glaciological research on Law Dome up to 1993 has been summarised by Hamley (1987) and Li (1995).

The survey line from the summit of Law Dome to Cape Folger on the coast and ice core drilling sites along this line are shown in Figures 3.5 and 3.7.

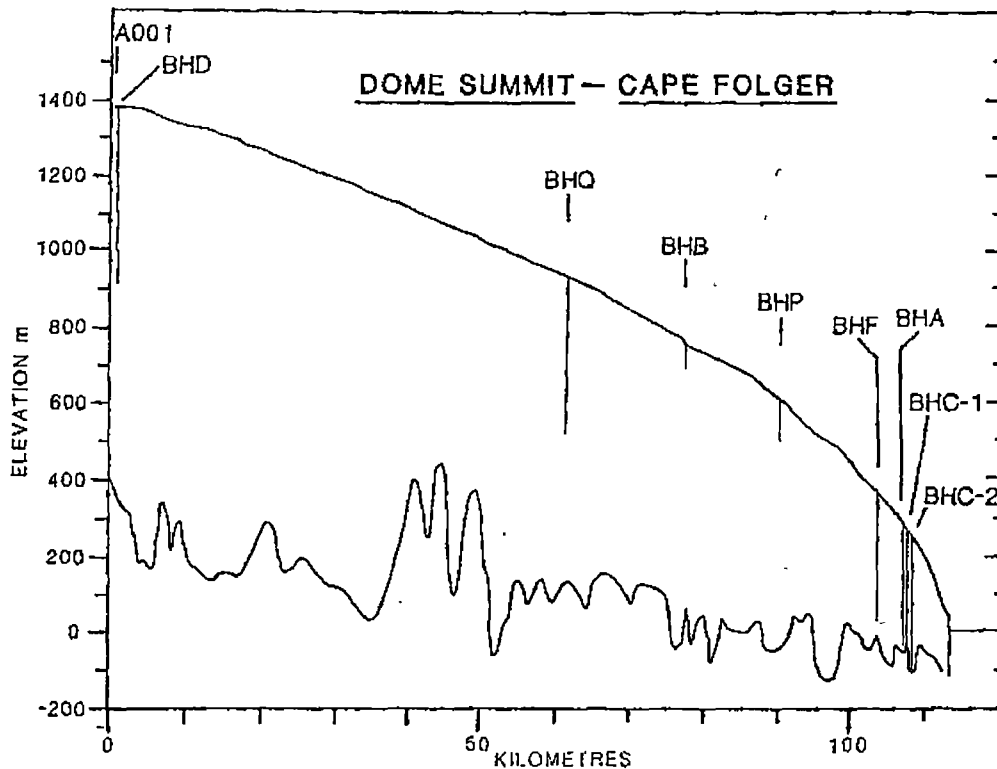


Figure 3.7. The profile of surface and bedrock elevations from the Law Dome Summit to Cape Folger showing the boreholes. (from Hamley and others, 1986)

Surveys undertaken during surface traverses have collected the data of the surface elevation, ice thickness, surface accumulation, surface temperature and surface flow velocity (Carter, 1976; Pfitzner, 1980). The results from measurements of those borehole inclinations (Russell-Head and Budd, 1979; Russell-Head, 1979; Etheridge, 1989) and analyses of ice cores (Wakahama, 1974; Russell-Head and Budd, 1979; Russell-Head, 1979; Thwaites and others, 1984; Xie, 1985; Li and others, 1988; Jacka and Budd, 1989; Gao, 1989; Jacka and Gao, 1989) have

provided a great deal of background information about the internal properties of the ice and its dynamics. All this information makes this survey line an ideal approximate flow line for modelling the relation between anisotropy and ice dynamics. The results from the application of the model of anisotropic ice rheology developed in the next chapter to this flow line from Dome Summit to Cape Folger are shown in Chapter 6. Here a summary of the main observations from the region are presented.

3.2.3 Information on Ice Cores and Boreholes Drilled along the Flow Line

Nine ice cores were drilled along the line from the summit to Cape Folger (Figures 5.5 and 5.7). BHA, BHC1 and BHC2 were drilled to near bedrock towards the coast. The borehole deformation was measured for BHQ, BHF, BHC1 and BHC2 (Etheridge, 1989; Russell-Head and Budd, 1979). The temperature profile was measured for all boreholes (Budd and others, 1976; Etheridge, 1989). Measured values of some physical parameters at the borehole sites are summarised in Table 3.1.

BHQ is about midway along the Summit to Cape Folger line in an area above rough bedrock with a large bedrock rise about 12 km approximately up-stream. BHC1 was drilled on a bedrock rise about 4 km down-stream from BHF, while BHC2 was drilled above a bedrock hollow 350 m further down-stream.

Figure 3.8 shows the profiles of borehole deformation with corresponding crystal orientation fabrics for BHQ, BHF, BHC1 and BHC2 boreholes. The features of borehole deformation and fabric evolution are described below:

(a). BHQ

As shown in Figure 3.8a, from the surface to about 100 m, where the shear strain rate is small, crystal structure is characterised by steady growth with depth of approximately equal-sized crystals with regular polygonal shape and near-random c-axis fabrics. Thus in this upper ice layer the crystal orientation structure has not been significantly modified by ice deformation and is mainly controlled by the

surface weather conditions which set the temperature in the firn which primarily controls the growth rate of the crystals.

Borehole Name	A001	BHD	BHQ	BHB	BHP	BHF	BHA	BHC1	BHC2
Date Drilled	1969	1977	1977	1972	1972	1974	1969	1982	1982
Latitude (S)	66°43' 13"	66°43' 13"	66°23' 00"	66°18' 07"	66°13' 48"	66°09' 06"	66°07' 57"	66°07' 50"	66°07' 43"
Longitude (E)	112°5' 10"	112°50' 10"	111°43' 34"	111°27' 42"	111°13' 54"	111°00' 40"	110°56' 40"	110°56' 17"	110°56' 10"
Site Elevation (m)	1389.7	1380	297	773	610	360	274	261	249
Ice Thickness (m)	1370	1200	850	700	500	385	364	305	350
Borehole Depth (m)	385	475	419	73	113	348	320	300	345
Depth of LGM (m)	-	-	-	-	-	310	270	260	305
Surface Accumulation (kg m ⁻² yr ⁻¹) (ice m yr ⁻¹)	600 0.64	650 0.63	65 0/093	140 0.18	180 0/18	80 0.17	160 0.086	60 0.086	? 0.086
Surface Velocity (m yr ⁻¹)	0*	0.36*	4.1*	4.8*	7.5*	9.1*	10.4*	9.6	9.4
Surface Slope*	0.002	0.002	0.008	0.011	0.013	0.023	0.023	0.023	0.023
Bedrock Slope*	0.048	0.053	0.025	0.056	0.022	0.011	0.012	0.013	0.015
Surface Temperature (°C)	-22	-22	-16	-16	-14	-12	-12	-12	-12
Borehole Basal Temp. (°C)	-	-	-	-	-	-2.53	-	-0.97	-0.54
Borehole Basal temperature gradient (°Cm ⁻¹)	-	-	-	-	-	0.033	-	0.05	0.038
References of ice core studies	5, 6, 9, 17	2, 5, 12	3, 7, 10, 11,	-	-	13, 14, 20	1, 17	3, 8, 16, 18, 19	2, 3, 7, 15, 19,
1.Budd,1972;2.3.Etheridge,1985;1989;4. Etheridge andMcCray,1985;5. Gao,1989;6. Gao and Jacka,1989;7. Han and Young ,1988;8..Huang, and others,1988;9. Jacka and Budd,1989; 10. Li,199511. Li and others,1988; 12.Morgan and McCray,1985;13. Russell-Head,1979;14.Russell-Head and Budd,1979;15.Thwarites and others, 1984;16. Wang,1994;17.Warkahama,1974; 18.19.Xie,1985;1989;20. Young and others,1985.									

Table 3.1. Summary of measured data at drilling site of boreholes along the Law Dome Summit – Cape Folger line. The symbol * indicates that the value is taken from the model input (Figure 6.1). (based on Morgan, personal communication)

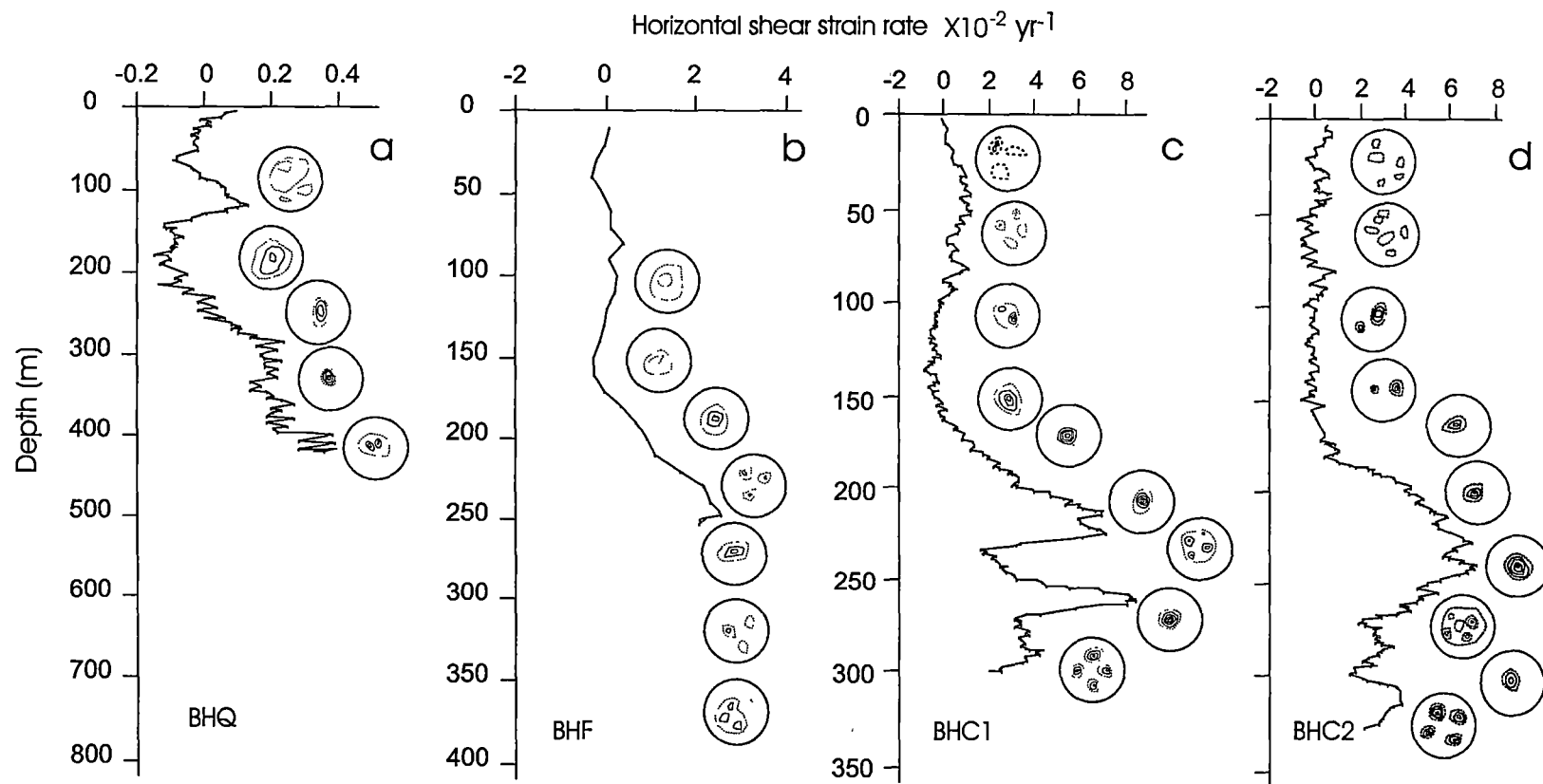


Figure 3.8. Shear strain rate profiles with the fabric evolutions at (a) BHQ borehole (Etheridge, 1989; Li, 1995), (b) BHF borehole (Russell-Head, 1979; Young and others, 1985), (c and d) BHC1 and BHC2 boreholes (Etheridge, 1989; Xie, 1989).

Over the depth of about 100 to 200m, the crystals become complicated in shape and grow with larger variations associated with the development of preferred c-axis orientation fabrics towards a weak small circle girdle pattern. This indicates that ice deformation has become significant for the development of crystal structure below about 100 m.

Below about 200 m the shear strain rate increases with depth significantly. The fabric patterns exhibit the development of a strong single maximum in response to the large shear strain accumulated over a long time interval (Li, 1995).

(b). BHF

The borehole inclination logging for BHF (Figure 3.8b), unfortunately, does not extend to the bedrock or even to the base of the hole. However, some restriction (upper limit) can be placed on the average shear rate from the lowest depth measured in the borehole down to the bedrock, which indicated that the shear strain rate cannot continue to increase through the remaining levels (Russell-Head and Budd, 1979).

On the basis of the crystal structures of BHF, Russell-Head (1979) delineated the ice core into three distinct sections. The upper section (0 – 175 m) is characterized by medium-sized crystals of ice exhibiting fabrics of the girdle type; the lower-central section (175 – 284 m) is characterized by smaller-sized crystals exhibiting fabrics of the vertical single-maximum type; and the basal section (285 – 385 m) is characterized by large-crystal ice exhibiting fabrics of the multiple maxima type.

(c). BHC1

The BHC1 shear strain rate profile (Figure 3.8c) reveals two bands of enhanced flow indicating an upper shear zone at ~200 to 235 m depth and a lower shear zone at ~250 to 275 m. The Holocene/Wisconsin boundary occurs in the upper shear zone at ~225m. The lower shear zone therefore is entirely Wisconsin age ice.

The orientation fabrics for BHC1 show the four basic types of pattern found in ice cores in the general region where horizontal shear deformation is dominant, the ice is relatively thin, and is flowing over a rough bedrock. In the upper levels of

the core a near-random fabric gradually concentrates toward a small circle girdle with increasing depth. As shear strain accumulates, this fabric pattern develops into a strong central single maximum (170 m) extending to 230 m. Below 230 m the ice develops a multi-maxima fabric which usually occurs in the warmer ice near the base of the ice cap (Thwaites and others, 1984).

(d). BHC2

Features similar to those of BHC1 are seen in the shear strain rate profile of BHC2 (Figure 3.8d). Two high shear zones are again apparent although at slightly different levels and with a smoother structure than in BHC1. The lower zone in BHC2, located in Wisconsin age ice, also has significantly lower shear rates than in BHC1, possibly because BHC2 is in a bedrock trough. The surface velocity at the two locations differs very little.

The general pattern of c-axis variation in BHC2 is also similar to that in BHC1. Fabric develops from a random fabric near the surface through a small circle girdle at about 90 m depth and a well developed vertical single maximum extending to 250 m, to multi-maxima fabrics near the base (Thwaites and others, 1984).

3.2.4 The Relationship of Enhancement Factor with Fabric

In the analysis of the extent of ice flow enhancement in the BHF borehole Russell-Head and Budd (1979) noted a relation between the enhancement factor associated with the shear strain rate and the crystal orientation fabric in the ice core. They found that the shear enhancement was related to the strength of the concentration of the ice crystal fabric around a single direction normal to the shear plane. The fabric parameter $\phi(1/4)$, defined as the half-apex angle of the core containing 25% of the c-axes in a sample of polycrystalline ice, was used to quantify the fabric concentration. This indicates that enhancement might be obtained directly from a given fabric for the compatible stress configuration; therefore it is worth studying further.

In this section the corresponding analyses are carried out for the four boreholes on the Law Dome Summit to Cape Folger line, using the strain rate profiles presented

in the previous section. The relationship between the calculated enhancement factors and the crystal fabric anisotropy is then discussed using fabric data from Donoghue (1999). A quantitative estimate of enhancement of shear strain rate requires as a reference the “background” isotropic ice “minimum” creep rate.

As temperature profiles are available for these boreholes, “unenhanced” strain rate profiles could be calculated using the simple temperature dependant flow law of Equation 2.3.7, together with the usual isotropic shallow ice approximate treatment of ice sheet flow- taking the shear stress τ_{xz} as $\rho g \alpha Z$ in terms of the ice density ρ , the acceleration due to gravity g , the depth Z and the surface slope α and modelling the shear strain rate as

$$\dot{\epsilon}_{xz} = \frac{2}{3} A_o(T) (\rho g \alpha Z)^3 \quad (3.2.1)$$

where the octahedral stress has been approximated by neglecting the compressive stresses. The model for anisotropic ice flow presented in the next chapter contains some other improvements to this simple treatment in addition to the enhancement of the flow. It includes an estimation of τ_o that includes the influence of the vertical compressive stresses in the ice sheet.

For consistency, that model has been used here, without its flow enhancement features, to estimate the strain rates that could prevail in the absence of anisotropy, as a basis for calculating the enhancement factors for these four boreholes.

A more detailed analysis is presented in Chapter 5 to relate the detailed borehole inclination logging and ice crystal fabric orientation data available for the Law Dome Summit South (DSS) borehole and ice core, and a detailed explanation of the computational steps used is provided there. The motive for presenting these enhancement profiles and their relationships to crystal fabrics here is to establish before moving on to describe the model, the need to address the enhanced shear flow in ice sheets, and the association with the anisotropic crystal structure.

Figure 3.9 shows the results of the studies for four boreholes (BHQ, BHF, BHC1 and BHC2) drilled along the flow line from the Law Dome Summit to Cape Folger (Figures 3.5 and 3.7). The enhancements at these boreholes have been calculated in the same manner as for the DSS borehole following **Step1** to **Step3**

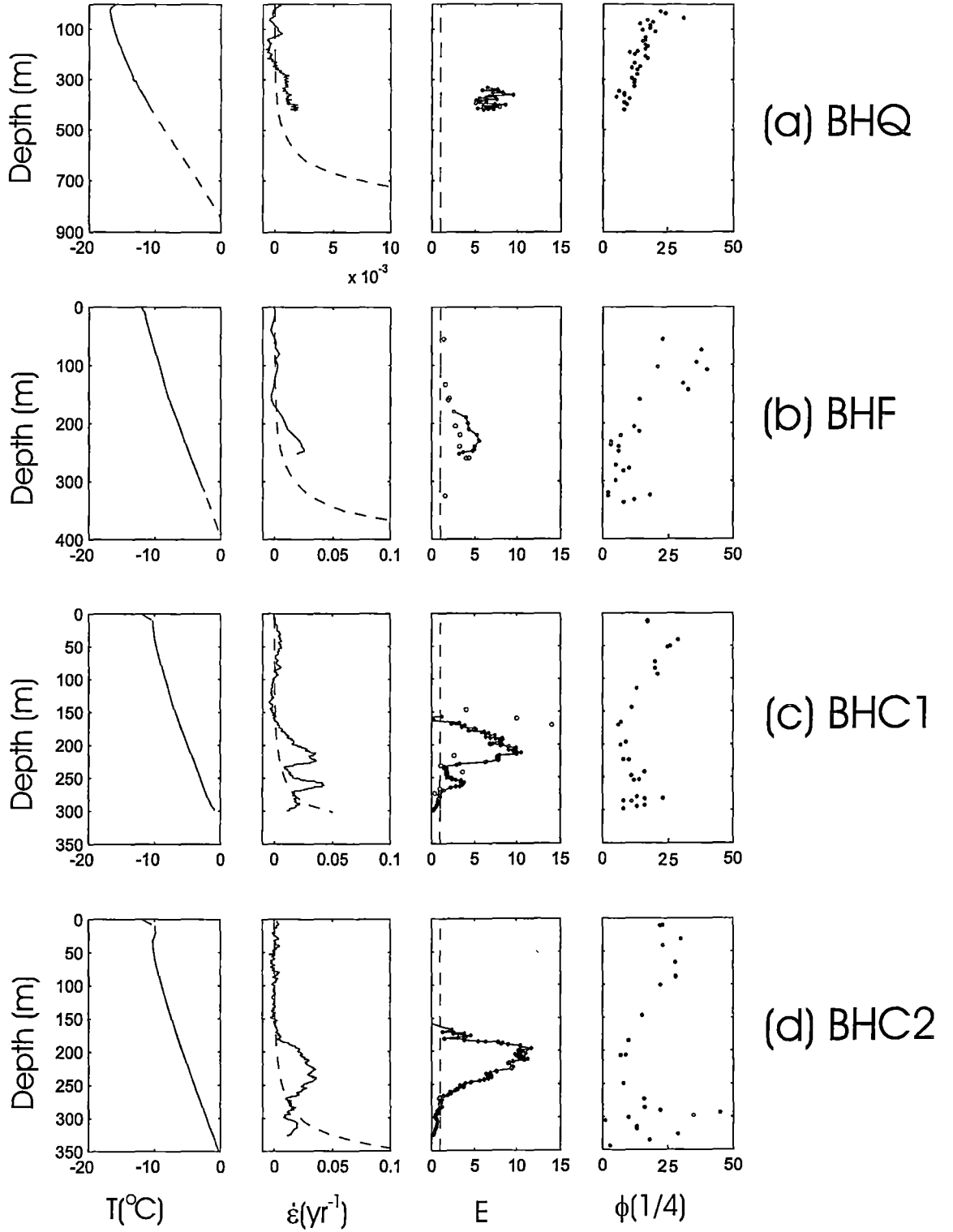


Figure 3.9 (see next page)

Figure 3.9. The profiles of (i). temperature T (solid line from the observations and dashed line from the extrapolation); (ii). shear strain rate $\dot{\epsilon}$ (solid line from the observations (Figure 3.8) and dashed line for isotropic ice calculated from the model and the isotropic laboratory ice tests); (iii). enhancement factor E calculated as the ratio of the observed strain rate to the calculated strain rate for isotropic ice and shown from the depth of the start of enhancement ("*" from the model calculations and "o" from ice deformation tests on BHF and BHC1 ice cores, dashed line is 1); and (iv). fabric parameter $\phi(1/4)$ (half-apex angles of the cones containing 25% of the c-axes) at boreholes BHQ, BHF, BHC1 and BHC2. Borehole temperature and deformation rate data from Etheridge (1989) and Russell-Head (1979) and fabric parameter data from Donoghue (1999).

as described in detail in Section 5.3. The temperature profiles for those boreholes which did not reach the bed are extrapolated from the bottom of the boreholes. The results of estimating enhancement factors from ice deformation tests on corresponding ice cores (BHF from Figure 3.3 - Russell-Head 1979) and BHC1 from Table 3.2) are also shown (as circles) for comparison.

It should be mentioned that enhancements in the BHF, BHC1 and BHC2 boreholes (Figure 3.9) all reach their maximum values above the depths of the maximum shear strain rate, which is consistent with the DSS borehole results (Chapter 5). This indicates that near the bed the enhancements reduce earlier than the shear strain rates. For example, at the DSS borehole (treated in detail in Chapter 5) the enhancements reduce at about 961 m depth while shear strain rates begin to decrease at about 1003 m. The $\phi(1/4)$ profiles presented in Figure 3.9 show a strong correlation with the enhancement where the results in Figure 3.9 are combined with data from laboratory deformation experiments.

Figure 3.10 summarises the relation between the enhancement factors for shear and fabric strength $\phi(1/4)$, from these borehole inclination studies (as labelled) and from laboratory ice deformation tests on anisotropic ice core samples. The results from the borehole studies (from Figure 3.9) are only shown for the depths between the start of enhancement and the maximum enhancement so that the effect of the reduced shear stress near the bed can be avoided. The results from the laboratory

simple shear tests on anisotropic ice (all denoted with the symbol of “x”) are taken from Table 3.2. The results from the earlier studies of Russell-Head and Budd (1979) for BHF borehole based on the deformation experiments are shown by the dashed line. Some results from the analysis in Chapter 5 of the DSS borehole (from Figure 5.10) are also presented for completeness.

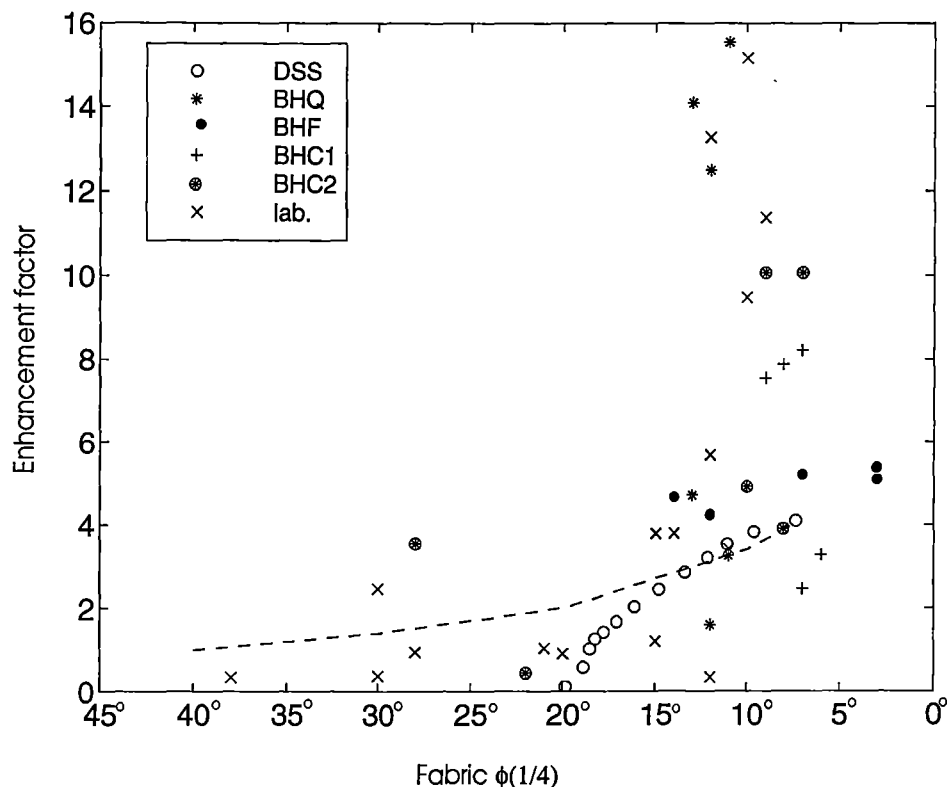


Figure 3.10. The plot of the fabric parameter $\phi(1/4)$ as the function of enhancement factor obtained from the borehole analyses and ice deformation tests.

Generally, horizontal shear enhancement increases with the strengthening of fabric tendency towards a near vertical single maximum. The high values of enhancement measured in the laboratory have considerable scatter and uncertainty dependent on the sample geometry and the exact relation between the orientation of the single maximum of the anisotropic samples and the plane of shear in the rig (Wang, 1994). There is no significant enhancement when fabric parameter $\phi(1/4)$ is greater than about $\sim 30^\circ$. As $\phi(1/4)$ reduces from $\sim 20^\circ$ to $\sim 10^\circ$ and below, the enhancement increases from values around 2 to about 8. As $\phi(1/4)$ decreases,

particularly below 15° , individual borehole studies and the laboratory experiments show some trend for rapidly increasing enhancement, but the compilation also displays a range of values from 4 to ~ 16 . It should be mentioned that for the borehole studies (except DSS) the estimates of the fabric parameter for very strong fabrics i.e. $\phi(1/4)$ less than 10° are not very accurate, because they were measured from the fabric diagrams of the original ice core thin sections using a digitizer, and for $\phi(1/4)$ less than 10° it is hard to see how many points lie near the centre of the graphic (Donoghue, 1999).

While there is considerable scatter in the compilation in Figure 3.10, the example of DSS, where detailed, accurate crystallographic work has been done, suggests that further experimental work along such lines might lead to a relationship which could be used to predict the enhancement that would be obtained for simple shear given the single maximum fabric strength normal to the shear plane, as expressed by a measure of central tendency such as the angle $\phi(1/4)$. For studies of flow in ice sheets this would still leave us with the task of modelling the evolution of crystal fabrics.

3.3 Laboratory Studies on Anisotropic Ice Flow

3.3.1 Deformation Tests on Ice from Different Ice Cores

Among a large number of other laboratory experimental studies of ice flow (Budd and Jacka, 1989), Wang (1994) made a comprehensive investigation of crystal anisotropic and possible impurity effects on ice flow properties based on a series of laboratory analyses and deformation tests on isotropic laboratory ice and ice from a number of different ice cores.

These experiments were carried out both in uniaxial compression and in simple shear configurations, at 0.2 MPa octahedral shear stress and -5°C on ice core samples which included samples deposited as snow during both the Wisconsin and Holocene periods. Samples for testing were selected from ice cores of Dye 3 in South Greenland, AGZ 77, in the Agassiz Ice Cap, Ellesmere Island, Canada

and BHC1, Law Dome Ice Cap, East Antarctica, with the aim of determining the relative flow rates for anisotropic ice compared with isotropic ice and for finding the reasons for different flow rates between the ice from different climate periods. Differential flow rates had been reported for the ice from different depths in the ice cores, based on field measurements of borehole closure and inclination change.

The experiments, in two different stress configurations, gave complementary results. With the progression of strain (see Figure 3.4), the deformation of the samples tended to reach a constant steady state (tertiary) flow rate which resulted in an approach to steady rate crystal size and fabric pattern compatible with the stress configuration. The path to steady state flow was dependent upon the relationship between the stress configuration and the initial crystal orientation fabric pattern. Ice with a c-axis fabric pattern compatible with the applied stress configuration (small circle girdle pattern for compression and single maximum pattern for shear) reached steady state flow directly (after primary creep), without passing through a significant minimum creep stage. Examination of the tertiary strain rate and impurity concentrations failed to find any significant difference between the tertiary flow rates of Wisconsin and Holocene ice, despite significant variations in the impurity concentrations. The experimental results show that the initial crystal size and the presence of impurities (in the concentrations found in the different ice samples) seem not to affect the ice flow rates at the temperature and stress tested. The ice flow rates are found to be determined mainly by crystal orientation fabric pattern. It was concluded therefore, that the more rapid flow measured in some field projects for the Wisconsin ice is primarily due to enhanced crystal orientation strength.

Some fabric statistical parameters (Wang, 1994) measured from tested samples are summarised in Table 3.2. The enhancement factors which in this case are calculated as the ratio of minimum strain rate of the (anisotropic) sample to the minimum strain rate for isotropic ice from the simple shear tests, are also included in Table 3.2. This modified measure of enhancement is used in order to be able to relate it to the unmodified anisotropic crystal fabric. The fabric parameter $\phi(1/4)$

versus enhancement factor has been plotted with the results obtained from the analysis of the boreholes in Figure 3.10.

Sample number	Fabric Description	μ	σ	$\phi(1/4)$	$\phi(1/2)$	E
AGZ 77-225A	weak maximum	27	16	15	22	1.2
AGZ 77-225B	weak maximum	33	20	20	26	0.9
AGZ 77-229	single maximum	25	17	15	21	3.8
AGZ 77-230	single maximum	19	11	12	18	5.7
BHC1-73B	central trend	21	9	14	21	4.0
BHC1-79C	central trend	19	15	10	15	9.5
BHC1-84B	central trend	21	10	12	20	13
BHC1-108D	?	48	26	30	35	2.5
BHC1-116D	multi maximum	26	7	21	25	1.0
BHC1-121B	multi maximum	36	26	11	28	3.4
BHC1-134D	?	58	29	28	71	1.0
BHC1-138C	multi maximum	46	46	30	40	0.4
Dye 3-T338	girdle	52	17	38	57	0.3
Dye 3-T1556	central trend	23	20	12	13	0.3
Dye 3-T1763	single maximum	17	9	10	16	15
Dye 3-T1922	single maximum	16	11	9	14	11

Table 3.2. Data for crystal orientation fabrics and enhancement factors resulting from simple shear tests. μ and σ indicate mean angle and standard deviation of the c-axis crystals to the vertical, and $\phi(1/4)$ and $\phi(1/2)$ the half-apex angles of the cones containing 25% and 50% of the c-axes. E is enhancement factor, the ratio of minimum strain rate of the sample to the minimum strain rate for isotropic ice (fabric data taken from Wang, 1994).

3.3.2 Ice Flow Relations Derived from Ice Deformation Tests under Combined Shear and Compression Stresses

Li and others (1996) performed a range of laboratory ice deformation tests with combined compression and shear stress configurations at a constant temperature of -2.0 °C. The test samples were laboratory-prepared finegrained polycrystalline ice with initially randomly oriented ice crystals. Experiments were carried out for

various combinations of shear and compression with shear stress ranging from 0 to 0.49 MPa and compressive stress ranging from 0 to 0.98 MPa but such that for every experiment, the octahedral shear stress was 0.4 MPa. They found that with constant octahedral stress (root mean square of the principal stress deviators), the *minimum* isotropic octahedral shear strain rate has no dependence on stress configuration (Figure 3.11). This result is in support of the hypothesis that isotropic ice flow is dependent on the second invariant alone, of the stress tensor. This fundamental assumption has been used to provide a general description of ice flow behaviour independent of the stress configuration (e.g. Nye, 1953; Glen, 1958; Budd, 1969). Most laboratory studies of ice deformation to determine the flow properties of ice relevant to ice sheet flow have concentrated on either simple shear or unconfined compression tests. Some experiments such as Steinemann (1954) and Kamb (1972) have studied combined compression and shear by the use of hollow cylindrical samples which were deformed by vertical axial compression and torsion for horizontal shear simultaneously. These experiments provided very useful results for the development of crystal orientation fabrics in these combined stress situations but have not been sufficient to provide a clear indication of the dependence of the flow properties on the combined stress conditions, particularly in steady state tertiary flow where the new ice fabrics are well developed.

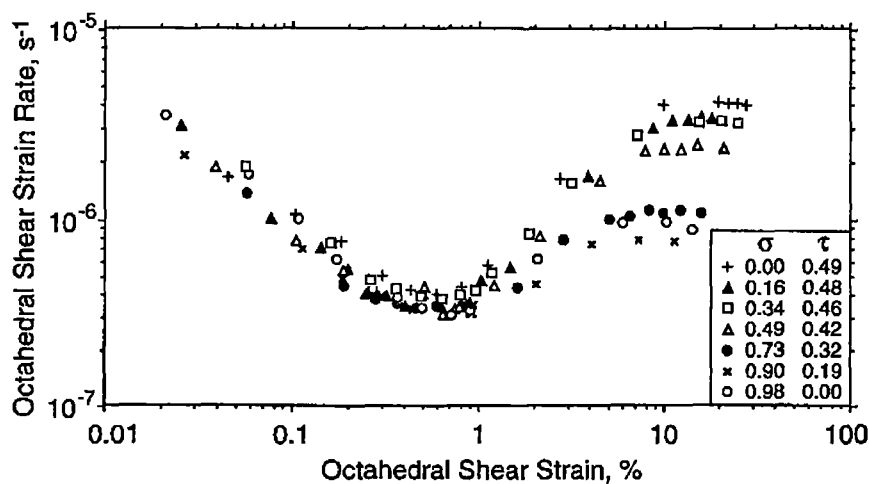


Figure 3.11. Creep curves (log-log plots of octahedral strain rate as a function of octahedral strain) for ice-deformation tests in various combinations of compression and shear. The combined octahedral stress for all tests was 0.4 Mpa. The test temperature was -2.0°C . (from Li and others, 1996).

Li and Jacka (1996) carried out further experiments with a variety of ratios of shear to compression, and including a range of octahedral stress magnitudes, thus allowing examination of the power law exponent. Octahedral shear stresses ranged between 0.2 and 0.8 MPa. All tests were run to beyond minimum creep. Results show that isotropic minimum octahedral shear strain rate increases with increasing octahedral shear stress according to the power flow law with an exponent of 3. This octahedral strain rate stress relation is in good agreement with that obtained from the simple stress configurations, providing support for the fundamental assumption (Nye, 1953; Glen, 1958) that the isotropic octahedral ice flow rate is dependent only on the second invariant alone, of the stress tensor.

For *tertiary* (anisotropic) ice flow, the octahedral strain rate is stress configuration dependent as a consequence of the developed crystal orientation fabric, which is also stress configuration dependent, and which develops with strain, rotation and recrystallization. The results from Li and others (1996) indicate that the enhancement factor for steady state tertiary octahedral shear strain rate depends on the "shear or compression fractions". The "shear fraction" (λ_s) and the "compression fraction" (λ_c) of the octahedral shear stress were defined (Li and others, 1996) respectively as

$$\lambda_s = \frac{2\tau}{\sqrt{\sigma^2 + 4\tau^2}} \quad (3.3.1)$$

and

$$\lambda_c = \frac{\sigma}{\sqrt{\sigma^2 + 4\tau^2}} \quad (3.3.2)$$

for the stress configuration involving longitudinally confined vertical compression combined with horizontal shear

$$\sigma_{ij} = \begin{bmatrix} -\sigma/2 & 0 & \tau \\ 0 & 0 & 0 \\ \tau & 0 & -\sigma \end{bmatrix} \quad (3.3.3)$$

where σ_{ij} is stress tensor, $\sigma_z = -\sigma$ is applied vertical compressive stress, $\tau_{xz} = \tau$ is the horizontal shear stress, while $\sigma_x = -\sigma/2$ arises from confining the horizontal extension to the transverse (y) direction (see Li and others, 1996, for details).

These fractions, which differ from Λ , the generalised stress configuration parameter of Lile (1984, 1987) since they explicitly relate to the configuration for simple shear (see Section 3.4.1.1), vary from 0 to 1 and 1 to 0 respectively as the stress situation varies from purely confined simple compression ($\tau = 0$) to purely simple shear ($\sigma = 0$), and are simply symmetrically related by

$$\lambda_s^2 = 1 - \lambda_c^2 \quad (3.3.4)$$

The octahedral shear strain rates for minimum (secondary flow with still isotropic ice) and for tertiary flow (with well developed fabrics) were presented as a function of the shear and compression fractions by Li and others (1996) as shown here in Figure 3.12. These results indicate that the minimum octahedral shear strain rate remains unchanged for all combinations of the level of shear versus the level of compression (for the fixed octahedral stress of 0.4 MPa). For the tertiary anisotropic strain rates Figure 3.12 provides a measure of the enhancement factor which was found to vary from ~3 for compression alone (with zero shear) to ~10 for shear alone (with zero compression). Based on these experimental data a flow law in terms of octahedral values for anisotropic ice was represented by incorporating a variable enhancement factor, E dependent on the degree of shear or compression. Thus the octahedral shear strain rate for anisotropic ice $\dot{\epsilon}_{ot}$ has the relation with the octahedral shear stress τ_o given by

$$\dot{\epsilon}_{ot} = EA\tau_o^n, \quad (3.3.5)$$

where A is the temperature rate parameter for minim creep in isotropic ice and n is about 3.

If E_c and E_s are the respective enhancement factors for compression and shear alone, then the enhancement factor for the combined stress situation (3.3.3), E_{λ_c} with compression fraction, λ_c is given by (using the straight line fit in Figure 3.12)

$$E(\lambda_c) = E_s \left(\frac{E_c}{E_s} \right)^{\lambda_c}, \quad (3.3.6)$$

with $E_c = \sim 3$ and $E_s = \sim 10$.

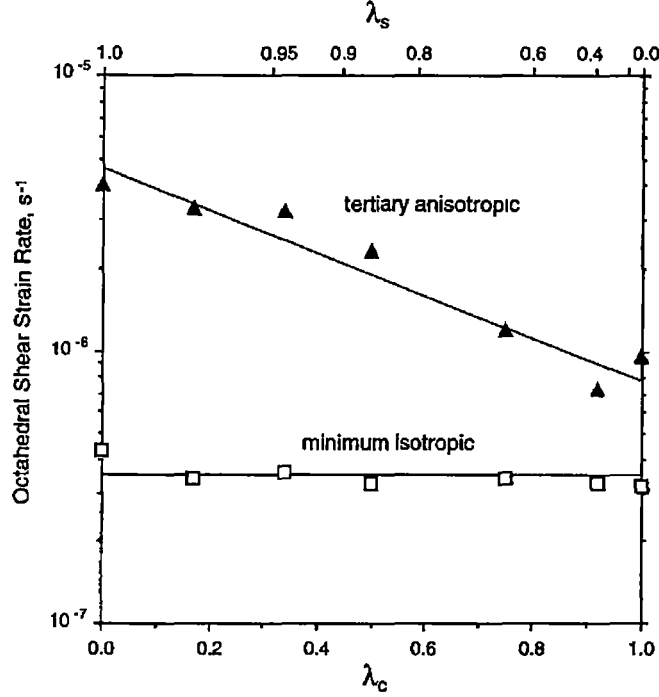


Figure 3.12. Plots of combined octahedral strain rate at minimum (isotropic) strain rate and at tertiary (anisotropic) strain rate (log scale) as a function of compression fraction λ_c (linear scale). Corresponding values of shear fraction λ_s are also shown. The minimum octahedral strain rates (for isotropic ice) are relatively constant, whereas the tertiary rates (with strongly developed fabrics) give enhancements relative to minimum of about a factor of 3 for compression to about a factor of 10 for shear. The combined octahedral stress for all tests was 0.4 Mpa. The test temperature was -2.0°C . (from Li and others, 1996).

Based on a more extensive set of experimental data, Budd and others (in preparation) and Warner and others (1999) made a comprehensive examination of tertiary flow rates for individual component strain rates. The conventional Glen-Nye flow law predicts an increase in component strain rates, for increases in the other component stress, through the corresponding increase in the octahedral shear stress. They found instead that the increase in tertiary compression rates from increasing shear stress is greater than the Glen-Nye law prediction, whereas the

influence on tertiary shear rates of increasing compressive stress was less (Warner and others; 1999, Fig.1). A possible generalisation of the flow relations providing a reasonable quantitative fit to their results was proposed as:

$$\dot{\epsilon}_{xz} = \frac{2}{3} k_o \alpha (\alpha^2 S_{xz}^2 + \beta^2 S_{zz}^2) S_{xz} \quad (3.3.7)$$

$$\dot{\epsilon}_{zz} = \frac{2}{3} k_o \beta (\alpha^2 S_{xz}^2 + \beta^2 S_{zz}^2) S_{zz}, \quad (3.3.8)$$

where $\alpha = E_s^{1/3}$ and $\beta = E_c^{1/3}$ are taken as constants. Here k_o is temperature rate parameter in octahedral values and corresponds to the value of A in Equation 3.3.5, S_{xz} and S_{zz} are shear and compression stress deviators respectively. These flow relations contain both the direct influence of combined stresses expected from a non-linear flow law and the enhancement that are partially related to the development in tertiary flow of “compatible” ice crystal orientation fabrics (the “induced anisotropy”)(Warner and others, 1999).

3.4 Review of Previous Approaches to Modelling Anisotropic Ice Flow

3.4.1 Modeling of Anisotropic Ice Flow

Within the last decade there has been increasing interest in numerical modelling of the flow of ice sheets. Such models have been used for predicting the response of ice sheets to climatic variations, for developing time scales for deep ice cores from Greenland and Antarctica, and for a understanding the development and decay of Pleistocene ice sheets. One of the problems, which affect the results of the models, is the type of flow law (i.e. constitutive relation for ice) which is used in the model, and the values of the various parameters in the relation.

Fundamental to understanding the dynamics of ice sheets is the rheological flow law for ice, that is, the constitutive relation of strain rate to the stress that produces it. Most ice sheet models use a form of Glen’s flow law (Equation 2.3.18). The theoretical considerations of Glen’s flow law are based on the assumption that ice

consists of fine-grained randomly oriented polycrystals representing a statistically homogeneous and isotropic material. In natural ice sheets the simple isotropic form of polycrystalline ice only exists at shallow depths, typically less than several hundred metres. The large amounts of deeper ice have developed strong anisotropic crystal orientation fabrics. The anisotropy due to flow-induced crystal orientations has a large effect on the ice flow rate (see Section 2.2.3), therefore, Glen's simple flow law is not appropriate when anisotropy of the ice crystal fabric develops in the deeper parts of ice sheet, allowing the ice to flow possibly an order of magnitude more rapidly than it would for isotropic ice.

Some attempts have been made to describe the anisotropic ice flow by incorporating the effects of anisotropy into the constitutive relation (flow law). There are usually two kinds of approach for this. One approach, a simpler procedure accounting for anisotropic effects, is by modifying Glen's flow law by introducing an enhancement factor (Russell-Head and Budd, 1979; Kostecka and Whillans, 1988; Reeh, 1988; Schoot and others, 1992, 1996; Huybrechts, 1992). The enhancement factor, defined as the ratio of the strain rate for anisotropic ice to the strain rate for isotropic ice, can be derived from laboratory experiments (Russell-Head and Budd, 1979; Baker, 1981, 1982; Jacka and Budd, 1989; Li and others, 1996; Budd and others, in preparation; Warner and others, in press) or also from field observations (Russell-Head and Budd, 1979; Dahl-Jensen, 1985; Shoji and Langway, 1984, 1988). Some authors use a Schmid factor instead of the enhancement factor (Azuma, 1995; Dahl-Jensen and others, in press; Miyamoto and others, in press). The Schmid factor is determined from the crystal c-axis orientations (Azuma, 1995). Another approach is by establishing a new theoretical expression for the constitutive relation which includes anisotropy. (Johnson, 1977; Lile, 1978; Lliboutry and Duval, 1985; Van der Veen and Whillans, 1990; Lliboutry, 1993; Azuma and Goto-Azuma, 1996).

Analyses such as those as Johnson (1977) extend the form of the flow relations from the isotropic Glen form discussed in Section 2.3, to an anisotropic form by using new tensor invariants constructed from the stress deviator and a preferred direction (unit vector \hat{m}) associated with the material structure in relation to the stress.

Flow relations of this type, selecting the vertical direction for \hat{m} , were applied by Van de Veen and Whillans (1990) to an analysis of the ice flow leading to the Dye3 borehole, in an attempt to model the strain rate profile measured by the Gundestrup and Hanson (1984) and to explain the enhancement factor for shear strain calculated by Dahl-Johnson (1985).

In quite a different approach Paterson (1994) used Johnson's flow relations, choosing as the preferred direction (\hat{m}) the direction of the single maximum axis of an ice core fabric, in his analysis of the compression experiments made by Shoji and Langway (1984) on ice from Dye3, which applied the compression at various angles to the fabric orientation.

The other approaches require knowledge of the variation of the crystal c-axis orientation throughout the ice sheet and of the validation of the theoretical predictions of the behaviour of the ice in natural ice masses. There are two well-known extreme hypotheses in polycrystalline deformation. One is the Sachs model (1928) which assumes that the stress on each grain is equal to the applied stress, and the other is the Taylor model (1938) which assumes that the strain throughout the polycrystalline sample is uniform so that the strain in each grain is equal to the bulk strain. Real polycrystalline behaviour probably exists between these two extreme hypotheses.

Some work on this aspect has recently been presented at a *workshop on ice rheology and anisotropy* which was held in Grindelwald, Switzerland (Dahl-Jensen and Morland, 1997)

In the following sections three examples of previous models for anisotropic ice flow are chosen to discuss the problem in more detail. They are Lile's original model, which also provides a reminder that many microscopic models do not discuss interactions between crystals, Lliboutry's model, which has been applied to several recent studies of idealised ice sheet flow in flow line models, and the model presented by Azuma and Goto-Azuma which includes explicit sums over crystal aggregates. These three models develop their own constitutive relations for anisotropic polycrystalline ice.

The usual approach to obtaining anisotropic flow relations from a microscopic description of the highly anisotropic behaviour of the individual grains in polycrystalline ice involves either simulations with explicit summations over aggregates of individual crystal c-axes, or the parameterisation of the distribution of c-axes using an orientation distribution function, f , depicting the volume fraction per steradian of a continuum aggregate of crystals of total volume V , representing c-axes orientated within an elementary solid angle $d\Omega$, defined by the longitude and latitude coordinates

$$f(\theta, \varphi) = \frac{1}{V} \frac{dV}{d\Omega}.$$

3.4.1.1 Lile's Model

Following Weertman's (1963) lead, Lile (1978, 1984) made the first quantitative study of the effect of a preferred c-axis orientation fabric on the flow rate of ice. He considered a linear rheology. Based on assumption that the stress on each grain is equal to the applied stress and that the basal glide rate is linearly proportional to the resolved basal shear stress, he considered an ice aggregate as a collection of interconnected crystals. These crystals were treated as deforming independently by basal glide but with the bulk flow rate being influenced by the "interference" between crystal grains, which Lile related to the mean square of the difference between the strain rate for an individual grain and the strain rate of the aggregate. He then established a model relating the deformation rate of an anisotropic polycrystal aggregate to that of an isotropic polycrystal aggregate, developed in terms of an enhancement factor applied to the bulk isotropic fluidity in the flow law.

In Lile's flow law the relation of strain rate tensor ($\dot{\epsilon}_{ij}$) to the deviatoric stress tensor (S_{ij}) for anisotropic ice flow is expressed in terms of the polycrystalline fluidity λ :

$$\dot{\epsilon}_{ij} = \lambda S_{ij}, \quad (3.4.1)$$

where

$$\lambda = \lambda(J_2, J_3, f, T) \quad (3.4.2)$$

is a scalar function of the second (J_2) and third (J_3) deviatoric stress invariants (see Section 2.2.1), temperature T , and crystallography represented by the orientation distribution function f .

From the relationship between the various stresses when dependence on J_2 is eliminated from J_3 by scaling the components of S_{ij} to an octahedral value of $2^{1/6}$ (see Lile, 1978, for details), a stress configuration parameter, Λ , is introduced and defined as

$$\Lambda = \frac{\tau_3 - \tau_1}{\tau_2} \quad \text{or} \quad \Lambda = \frac{-3 S_2}{S_1 - S_3}, \quad (3.4.3)$$

where, τ_1 , τ_2 and τ_3 are the principal shear stresses and S_1 , S_2 and S_3 the principal deviatoric stresses (see Section 2.2.1). Λ is non-dimensional and independent of the second deviatoric stress invariant while retaining the symmetry and unity limits exhibited by the normalized form of the third deviatoric stress invariant. It ranges from +1 for uniaxial tension ($S_2 = S_3 = -\frac{1}{2} S_1$) to -1 for uniaxial

compression ($S_1 = S_2 = -\frac{1}{2} S_3$) with 0 for simple shear ($S_2 = 0$ and $S_3 = -S_1$).

Specification of the independent physical invariants, octahedral shear stress (τ_o) and the stress configuration parameter (Λ), together with the orientation of the principal axes of stress is sufficient to define an arbitrary deviatoric stress situation.

Replacing J_2 and J_3 by Λ in Equation 3.4.2, the polycrystalline **fluidity** becomes

$$\lambda = \lambda(\Lambda, f, T). \quad (3.4.4)$$

Lile found that two aggregates differing only with regard to their orientation fabrics and deforming under identical conditions of temperature, stress situation, etc. If one is isotropic, the ratio of their octahedral deformation rates ($\dot{\epsilon}_o$) defined as octahedral enhancement factor is

$$E(f, \Lambda) = \frac{\dot{\epsilon}_o(f, \Lambda)}{\dot{\epsilon}_o(f')} = \frac{\lambda_o(f, \Lambda)}{\lambda_o(f')} = B(f, \Lambda)G(f, \Lambda), \quad (3.4.5)$$

where $B(f, \Lambda)$ is the interference component of the enhancement, and $G(f, \Lambda)$ is the geometric component of the enhancement, and both involve integrations over the crystal orientation, where the orientation distribution function weights the various products of individual crystal strain rates, and these in turn involve the relationship between the individual crystal axes and the stress configuration described by the parameters (see Lile, 1978, for details). The above equation provides a flow law for an arbitrary orientation fabric and state of stress through application of the enhancement factor E to the flow law for an isotropic aggregate.

To compare the results from the model calculation with the observations, ice deformation tests on anisotropic ice, taken from ice cores from Law Dome, East Antarctica, were carried out in uniaxial compression ($\Lambda = -1$) and simple shear ($\Lambda = 0$) respectively (Lile, 1978; 1984). The enhancements calculated from the model using the measured orientation fabric, stress configuration and tilt orientation of the specimen as inputs show a close agreement with the observed enhancements from experiments (see Table 1, Lile, 1978). Lile's results were useful to compare the flow rates for low stress in early primary creep which follows approximately linear stress dependence rheology. The formulation is not appropriate for the cubic stress dependence of tertiary flow. The model also does not address the problem of the development of the anisotropic crystal structure in the ice sheet. While only the influence of different fabrics and stress configurations, i.e. the anisotropic aspect interference, was considered, this work represents one of the early contributions to describing the influence of interactions between the crystals. This is clearly an important topic since even well aligned polycrystalline samples deform far more slowly than single crystal deformation rates.

3.4.1.2 Lliboutry's Model

Lliboutry (1987b) derived an anisotropic power law depending on seven rheological parameters which are determined from the polycrystal fabric, under the assumptions that the stress is uniform and there is no energy dissipation at

grain boundaries. Lliboutry (1993) extended his model to a polynomial flow law by adding a Newtonian dissipation potential, which increases the number of the rheological parameters to ten. These ten rheological parameters depend on 2 temperature-dependent parameters and on the 4 first even moments of the c-axes distribution.

From the flow relation for the deformation rate ($\dot{\gamma}_b$) of an single crystal in terms of the resolved shear stress (τ_b) on its basal plane

$$\dot{\gamma}_b = \varphi_b \tau_b + B_b \tau_b^3 \quad (3.4.6)$$

where φ_b and B_b are temperature parameters, the anisotropic constitutive law in Lliboutry's model, is expressed by the relation between bulk strain rate ($\dot{\gamma}$) and applied deviatoric stress (S) as

$$\dot{\gamma} = M S \quad (3.4.7)$$

or

$$\begin{bmatrix} \dot{\gamma}_d \\ \dot{\gamma}_{ax} \\ \dot{\gamma}_4 \\ \dot{\gamma}_5 \\ \dot{\gamma}_6 \end{bmatrix} = \begin{bmatrix} \varphi_{\perp} & \sqrt{3}C(s_4^2 - s_d^2) & 0 & 0 & 0 \\ \sqrt{3}C(s_4^2 - s_d^2) & \varphi_{ax} & -2\sqrt{3}Cs_5s_6 & 0 & 0 \\ 0 & -2\sqrt{3}Cs_5s_6 & \varphi_{\parallel} + 2\sqrt{3}Cs_d s_{ax} & 0 & 0 \\ 0 & 0 & \varphi_{\parallel} - 2\sqrt{3}Cs_d s_{ax} & -2\sqrt{3}Cs_{ax}s_4 & 0 \\ 0 & 0 & 0 & -2\sqrt{3}Cs_{ax}s_4 & \varphi_{\perp} \end{bmatrix} \begin{bmatrix} s_d \\ s_{ax} \\ s_4 \\ s_5 \\ s_6 \end{bmatrix}, \quad (3.4.8)$$

where \mathbf{M} is a **symmetric fluidity** matrix. In a right-handed Cartesian coordinate system when the z-axis is an axis of rotational symmetry, the subscripts of 4, 5 and 6 denote the y-z plane, x-z plane and x-y plane, respectively; and subscripts d and ax denote normal directions reduced from the x, y and z three directions by the incompressibility of ice (see Lliboutry, 1993, for details). The parameters in the matrix \mathbf{M} have the relations reflecting the two terms in the single crystal flow law (Equation 3.4.8) as:

$$\begin{bmatrix} \varphi_{ax} \\ \varphi_{\perp} \\ \varphi_{\parallel} \end{bmatrix} = \begin{bmatrix} \psi_{ax} \\ \psi_{\perp} \\ \psi_{\parallel} \end{bmatrix} + \begin{bmatrix} B_{ax} & A_{ax\perp} & A_{\parallel ax} \\ A_{ax\perp} & B_{\perp} & A_{\perp\parallel} \\ A_{\parallel ax} & A_{\perp\parallel} & B_{\parallel} \end{bmatrix} \begin{bmatrix} s_{ax}^2 \\ \tau_{\perp}^2 \\ \tau_{\parallel}^2 \end{bmatrix}, \quad (3.4.9)$$

where (ψ_i, B_j, A_{kl}, C) ($i, j, l, k = ax, \perp, \parallel$) are the 10 rheological parameters. The subscripts of \perp and \parallel denote the values are normal or shear components, respectively. The ψ_i are proportional to ψ_b , while B_j and A_{kl} are proportional to B_b , with the proportionality factors consisting of integrations involving the orientation distribution and represent the interaction of the fabric and the applied stresses. For the rotational symmetric case $f(\theta, \phi)$ depends only on the angle θ . ψ_b and B_b are temperature parameters (independent of the fabric) which can be obtained from Budd and Jacka (1989) for $n=3$ and Castelnau and others (1996a) for $n=1$ (Mangeney and others, 1996). In this case, the fabric is described by a somewhat different function $V(\theta)$ for the distribution of c-axes orientations; $V(\theta)$ represents the volume of grains for which the angle between the c-axis and the in situ vertical direction is larger than θ . As a simple parameterisation Lliboutry took

$$V(\theta) = \cos^v \theta \quad (3.4.10)$$

where v expresses the strengthening of the fabric. The 10 rheological parameters can then be expressed as a function of a parameter $\theta_{1/2}$ (corresponding to the $\phi(1/2)$ fabric parameter discussed earlier) which is linked to the exponent v to give $V(\theta_{1/2}) = 1/2$; $\theta_{1/2} = 60^\circ$ for isotropic ice and a zero value corresponds to the case where all c-axes align exactly with the in situ vertical direction (Figure 3.13). From Equations 3.4.8 and 3.4.9 we can see that the shear strain rates in the x-z and y-z plans $\dot{\gamma}_4$ and $\dot{\gamma}_5$ respectively contain the cubic flow law terms $B_{\parallel} \tau_{\parallel}^2 S_4$ and $B_{\parallel} \tau_{\parallel}^2 S_5$: and from Figure 3.13 it is clear that B_{\parallel} not only dominates the flow relations by an order of magnitude for fabrics with a strong single maximum compatible with shear stresses such as S_4 and S_5 , but also that there is an enhancement in B_{\parallel} approaching $35/8$ compared with isotropic fabrics.

This flow law has been applied to solve the force balance equations for the steady flow of a viscous, incompressible, anisotropic fluid with a fixed (Mangeney and others, 1996) and a free surface (Mangeney and others, 1997) for a flow line under isothermal conditions, and for investigating the shallow ice approximation for

anisotropic ice (Mangeney and Califano, 1998). Although this provides a useful approach to deal with anisotropic ice flow it needs to be tested more fully against laboratory determined anisotropic flow rates, this scheme also does not address the evolution of the crystallographic structure within the ice sheet.

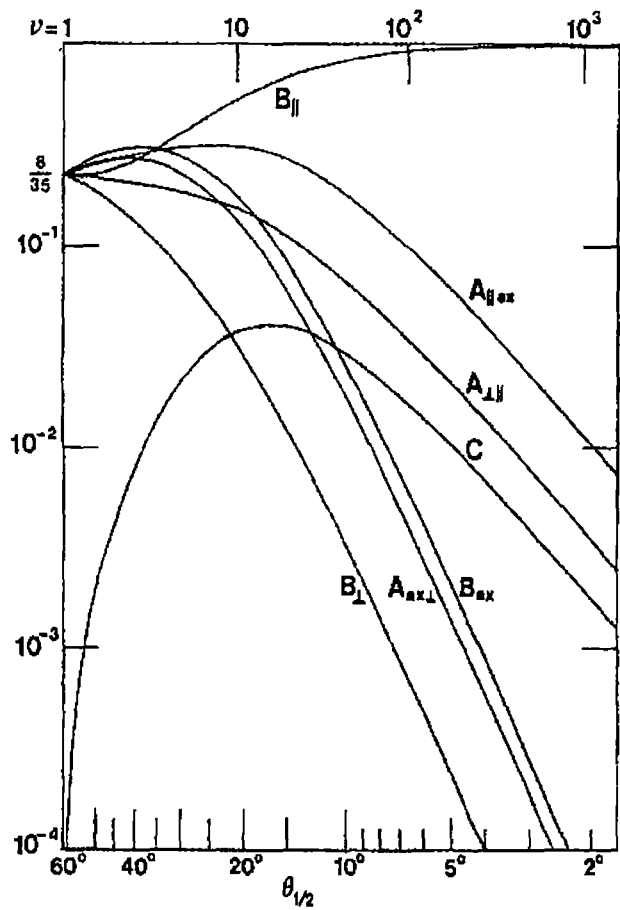


Figure 3.13. Rheological parameters in Lliboutry’s model (from Lliboutry, 1993). Taking B_b as unit, the relative volume of crystals whose c -axis deviates from the axis of rotational symmetry by more than θ is assumed to be $V(\theta)=\cos^3 \theta$. The median of θ is given at the bottom.

3.4.1.3 Azuma’s Model

From uniaxial compressive deformation tests on individual crystals of different orientation, a relationship for the c -axis orientation, strain rate and stress for individual grains was derived (Azuma, 1995). Based on this relationship a flow law of polycrystalline ice with arbitrary c -axis orientation fabrics was derived and

expressed in terms of the principal-axes coordinate system (Azuma, 1994) and in the x-y-z coordinate system (Azuma and Goto-Azuma, 1996). This model takes the approach of summing the contribution of individual crystals. It has been applied to aggregates of crystals produced to fit particular orientation distribution functions, and to thin section fabrics from ice cores. It does not require any assumption of symmetries.

To derive this flow law expressed in the x-y-z coordinate system (Azuma and Goto-Azuma, 1996), several assumptions were made:

- (1) Individual grains deform only by basal glide.
- (2) The basal glide of each grain takes place in the maximum shear-stress direction on the basal plane when the macroscopic stresses act on the grain.
- (3) A larger stress acts on a grain surrounded by softly oriented grains than that surrounded by stiffly oriented grains and a larger stress acts on the stiffer grain, i.e. the stresses on an individual grain are related to the bulk stress by

$$\sigma_{g\ ij} = \frac{G_{ij}^L}{G_{ij}^g} \sigma_{ij}. \quad (3.4.11)$$

where G^g is a grain geometric tensor, relating the individual crystal c-axis orientation to the macroscopic stress situation, and the “local” geometric tensor G^L involves a average over grains in the neighbourhood of the grain (g).

- (4) Shear strain rate and shear stress on basal planes of single ice crystals are related by a power-law equation (Weertman, 1983).
- (5) The macroscopic strain rate component of the aggregate is equal to the averaged value on all the grains in the aggregate of the strain rate components of individual grains.

In Azuma and Goto-Azuma (1996) the further approximation was made of replacing the local averaging of the grain geometric tensor G_{ij}^g in assumption (3) with the average the whole aggregate.

In this flow law model, the strain rate tensor ($\dot{\epsilon}_{ij}$) is related to the stress tensor (σ_{ij}) by a bulk **geometrical tensor** (G_{ij}):

$$\dot{\epsilon}_{ij} = \beta G_{ij}^{\text{sym}} \tau^n, \quad \tau = G_{ij} \sigma_{ij}, \quad i, j = x, y, z \quad (3.4.12)$$

where, G_{ij} and G_{ij}^{sym} are averages over the aggregate grain geometrical tensors discussed below, σ_{ij} is the applied (macroscopic) stress, n is a constant value of 3, and β is a parameter dependent on temperature and possibly impurity concentration and other variables but independent of stress configuration.

The grain geometrical tensor, G_{ij}^g , is defined as

$$G_{ij}^g = m_i c_j \quad (3.4.13)$$

and for grain and bulk tensors

$$G_{ij}^{\text{sym}} = \frac{1}{2}(G_{ij} + G_{ij}^T), \quad (3.4.14)$$

where c_j is the unit vector parallel to the c -axis of the grain, and m_i is the unit vector of the glide direction on the basal plane and can be determined from assumption (2) with the stress tensor σ_{ij} and the unit vector c_j (see Azuma and Goto-Azuma, 1996, for details). Hence, the geometrical tensor G_{ij} can be calculated with the c -axis fabric data and the stress configuration. For example, when uniaxial compression or simple shear act on ice with a random fabric ice (isotropic ice), the stress tensor σ_{ij} and the G_{ij} tensors become:

$$\sigma_{ij}^{\text{comp}} = \begin{pmatrix} 0 & 0 & 0 \\ 0 & 0 & 0 \\ 0 & 0 & -\sigma \end{pmatrix} \quad G_{ij}^{\text{comp.}} = \begin{pmatrix} 1/6 & 0 & 0 \\ 0 & 1/6 & 0 \\ 0 & 0 & -1/3 \end{pmatrix}$$

and

$$\sigma_{ij}^{\text{shear}} = \begin{pmatrix} 0 & 0 & \sigma \\ 0 & 0 & 0 \\ \sigma & 0 & 0 \end{pmatrix} \quad G_{ij}^{\text{shear}} = \begin{pmatrix} 0 & 0 & 3/10 \\ 0 & 0 & 0 \\ 3/10 & 0 & 0 \end{pmatrix}.$$

In Equation 3.3.1, the stress tensor σ_{ij} can be replaced by the deviatoric stress tensor S_{ij} , as $G_{xx} + G_{yy} + G_{zz} = 0$. This flow law demonstrates the direction-dependent mechanical properties of anisotropic ice. For each c -axis distribution

the tensor G_{ij} can be calculated by Equation 3.4.13 for a given stress field σ_{ij} .

Then the strain rate tensor $\dot{\epsilon}_{ij}$ can be obtained from Equation 3.4.12.

Figure 3.14 shows the enhancement factor, the ratio of the strain rate for anisotropic ice with a developed crystal orientation distributions to that for isotropic ice, with a random crystal orientation distribution, calculated by this flow law (Azuma and Goto-Azuma, 1996). The angle ϕ for the single maximum fabric shows the standard deviation of the zenith angles of c-axes. For the small circle girdle pattern, the c-axes are distributed so that the zenith angle of each c-axis should be $\phi \pm 5^\circ$. The enhancement factor of the horizontal shear deformation for a single maximum (HS(SM)) increases to a value of about 8 as the angle ϕ decreased. On the other hand, the enhancement factor of the vertical compression for a single maximum (VC(SM)) decreases to zero as the angle ϕ decreases. In the case of a small circle girdle, the enhancement factor for the vertical compression (VC(SCG)) approaches a value of 5 as ϕ approaches 45° and decreases to zero as ϕ moves away from it. These theoretical calculations agree reasonably well with the laboratory experimental results (Budd and Jacka, 1989).

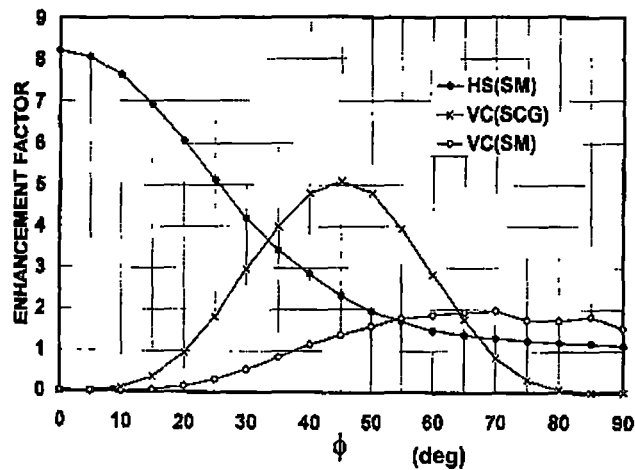


Figure 3.14. Calculated flow enhancement factors by Azuma's model (from Azuma and Goto-Azuma, 1996). HS(SM) indicates the enhancement factor for horizontal shear deformation of a single-maximum fabric ice. VC(SM) designates the enhancement factor for the vertical compression of a single-maximum fabric ice. VC(SCG) is that for the vertical compression of a small-circle girdle.

This flow law has been used to simulate fabric development in ice sheets by considering crystal lattice rotation only (Azuma, 1994). Qualitatively estimating the stress field from the topography of the ice sheet three typical ice flow regimes were derived as shown in Figure 3.15. In the flow regions A and B, where the stress fields may be uniaxial compression or pure shear, Azuma proposed that the c-axes align vertically with depth and form a broad single maximum or two maxima at the middle depth in the ice sheet, which is then followed by the development of a strong single maximum pattern in the flank region owing to the increase in simple shear with depth. In the flow region C, where the stress fields may be uniaxial extension or pure shear, the development of a great circle girdle or a two-maxima pattern is predicted at the middle depth. Such a great circle girdle would be altered to a strong single maximum at great depth due to the increase in simple shear with depth.

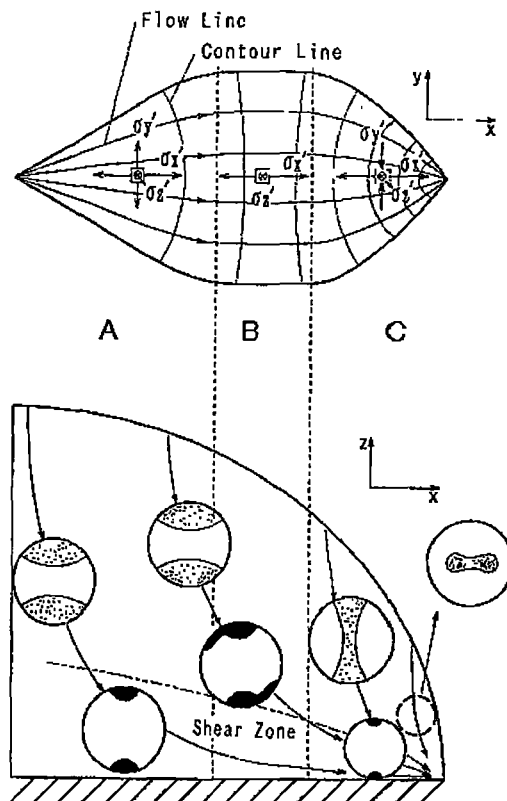


Figure 3.15. Stress configurations and fabric development predicted by Azuma's model at a drainage in an ice sheet (from Azuma, 1994). A=divergent flow region; B=parallel flow region; C=convergent flow region.

This theoretical flow relation has been improved by including the parameterisation for a recrystallization effect (Azuma, 1997). Dahl-Jensen (1997) used this microscopic (crystal based) theory to calculate theoretical anisotropic viscosities for fabrics with a transverse symmetry. These anisotropic viscosities were used in a macroscopic constitutive equation for materials with transverse isotropy analogous to that formulated by Johnson (1977). This flow law has been applied to the Dye 3 borehole, South Greenland (Azuma and Goto-Azuma, 1996; Thorsteinsson and others, 1999). Thorsteinsson and others (1999) concluded that the fabric alone could not account for the enhanced deformation in the upper part of the lower 250 m of glacial ice or the reduced strain rate in the lower part by Azuma's theories. Thorsteinsson and others (1999) suggested that an impurity factor should be included in the constitutive relations. However the results obtained from the intercomparison study of ice core shear and compression rates by Wang (1994) indicated that the similarity of flow rates for the tertiary strain rates irrespective of the impurity content did not favour an impurity based exploration.

Although Azuma's model provides a useful approach to both the evolution of the ice crystal structure and the flow properties of anisotropic ice there are some notable discrepancies with results from laboratory studies and also with the fabrics observed in the ice cores from Law Dome. In particular the laboratory results of Russell-Head and Budd (1979), Wang (1994) and Li (1995) show a sharper increase in enhancement factor with decreasing fabric parameter ϕ ($1/4$). Also in both laboratory experiments and ice core observations (Jacka, 1987; Budd and Jacka, 1989) the development of the vertical single maximum and high tertiary flow rates with horizontal shear appear to occur largely over the first 20% shear strain compared with the larger strains involved in the Azuma model.

This suggests that at this stage the direct empirical approach of moving enhancement to flow based on the laboratory studies together with ice core and borehole measurements will provide the most appropriate scheme for ice sheet modelling.

3.4.2 Modeling of Development of Crystal C-axis Orientation Fabrics

There has also been work on the complementary task of modelling the development of crystal fabrics in flowing ice, since realistic simulation of ice sheet flow would also require a model to predict the ice fabrics when age, past strains, temperatures, and maybe other factors, such as dust or salt content, are known.

Azuma and Higashi (1985) first gave a simple model for uniaxial compression which considers each crystal in the aggregate as an isolated crystal subject to a basal shear strain proportional to the overall strain and to geometrical constraints. An extension was then made to cover uniaxial tension (Fujita and others, 1987; Alley, 1988), pure shear and simple shear (Alley, 1988). This model has been improved to predict the development of preferred c-axis orientation with increasing strain in an ice sheet when a given stress condition is applied (Azuma, 1994).

So far these models do not give the steady state girdle fabric for continuing unconfined compression as observed from the laboratory experiments and for appropriate field situations e.g. the central zones of ice shelves (Budd, 1972).

Models based on the hypothesis of a uniform stress state in the polycrystal have been proposed by Van der Veen and Whillans (1994) and Castelnau and Duval (1994). The work of Van der Veen and Whillans (1994) incorporates recrystallization in their simulation and the evolution of crystal axes under cumulative strain. They simulated recrystallization by removing some crystals whose cumulative strain differed from the aggregate value by more than a threshold amount, and replaced them with new crystals oriented for easy glide.. This enabled them to simulate the development of girdle fabrics under uniaxial compression.

In order to get closer to the physical mechanisms involved at the grain scale, Castelnau and others (1996a; 1996b) have used a powerful viscoplastic self-consistent (VPSC, Hutchinson, 1976) model (Molinari and others, 1987; Lebensohn and Tome, 1993; 1994) to simulate fabric formation and evolution in

polar ice. This model considers each grain as a heterogeneous inclusion embedded in a homogeneous matrix which can exhibit any kind of anisotropy. It is assumed that the ice single crystal deforms by slip on the basal plane and in the prismatic and pyramidal planes.

Some models have been outlined (Meysonnier and Philip, 1996 and Svendsen and Hutter, 1996) which aim at a simultaneous evolution of a parameterisation of the crystal fabric via an orientation distribution function and calculation of the corresponding variables describing the mechanical deformation of the ice. Applications have been made for transverse isotropic fabrics in the simple configurations of uniaxial tension and compression (Meysonnier and Philip, 1996) and simple shear (Svendsen and Hutter, 1996) with qualitatively encouraging results.

So far these models have not adequately included the co-evolution of changes in crystal size (number per unit volume) with the associated processes of recrystallisation as well as the interactions between crystals. The treatment of anisotropic ice flow developed in this thesis in relating the strain rate to strain, based on both laboratory studies and ice core results, inherently also gives the evolution of the development of the statistical characteristics of the crystal structure including crystal size, orientation fabrics shape, and the statistical parameters of the distribution as a byproduct. Although the crystallographic properties are not used directly in the flow line model they provide a means to validate the model and allow direct intercomparison for the analysis of results for individual boreholes and ice cores.

Chapter 4

DEVELOPMENT OF AN ANISOTROPIC ICE FLOW MODEL

4.1. Introduction

In this chapter a model for anisotropic ice flow is developed. To incorporate the effect of ice fabric anisotropy on the flow of ice into an ice sheet model some modellers have simply applied an “enhancement factor” to the relationship between stress and strain rate measured in the laboratory as a constant rescaling factor uniform throughout the ice sheet. Instead of treating the details of the twin questions of the evolution of crystal orientations and the response of the resulting polycrystalline material to stresses at a microscopic level (see Section 3.4), the approach developed here is to use a more direct and simple way to parameterise empirically the strength of enhancement as it develops in shear flow, based on the laboratory observations of the process. This inherently includes the effect of development of the anisotropic fabrics along with the changes in strain rate with strain. Although the success of theoretical work on the flow of ice is a heartening confirmation of the assumptions made, laboratory tests provide the best foundation for our knowledge of the behaviour of ice (Glen, 1958; Budd and Jacka, 1989). This project draws for guidance upon the physical paradigm of evolving compatible crystal fabrics, in relation to laboratory deformation experiments, and to observations correlating ice core fabrics and bore hole shear

rates, in developing the simple parameterisation of the enhancement of horizontal shear flow, but the aim of this project is not to explicitly model the details of fabric evolution.

4.2. Preliminary Studies

The model described in this section is from a preliminary study, as part of the project, to incorporate into ice sheet models the enhanced ice flow which arises from the development of anisotropic ice crystal fabrics which are compatible with the flow conditions. In this model anisotropic rheology is incorporated into a steady state ice sheet flow model via an enhancement factor for shear flow. This enhancement factor depends on the strain history of the ice. It is based on laboratory studies of ice deformation, together with ice core studies, and is determined in the model by iteratively (see Section 4.5) calculating shear and compression strains along ice flow trajectories and feeding these back into the anisotropic ice flow law. This model has been applied to calculate the ratio of depth averaged velocity to surface velocity from an idealised flow line of a large ice sheet in a study which examined the influence of enhanced horizontal shear flow at depth in ice sheets on velocity profiles and consequently on ice-flux measurements (Wang and Warner, 1998).

As described in Section 3.1, laboratory ice creep tests on initially randomly orientated polycrystalline ice subjected to constant stress indicate that the minimum strain rate is attained at about 1% octahedral shear strain. Beyond this, and associated with the development of the anisotropic fabric in the ice sample, the strain rate increases. This can be considered as an enhancement of strain rate above the minimum strain rate as a function of strain, and is observed over a range of stresses and temperatures. The enhanced strain rate approaches an asymptote beyond about 10-20% octahedral shear strain, with an enhancement factor of about 3 for uniaxial compression and about 6-10 for simple shear. The experiments show that accumulated strain provides a natural parameter to describe the development of the enhancement factor from 1 at 1% strain to 10 beyond 10-20% strain for shear flow.

In this preliminary model, longitudinal stresses are neglected for the large scale flow (horizontal scales greater than about 10 ice thickness) and the shear stress τ_{xz} is taken as the driving stress, $\tau_{xz} = \rho g \alpha Z$, in terms of the ice density ρ , the acceleration due to gravity g , the depth Z and the surface slope α where these values also represent large scale averages. The relation between shear strain rate ($\dot{\epsilon}_{xz}$) and shear stress (τ_{xz}) includes an enhancement factor E which is a function of the shear (ϵ_{xz}) and compression (ϵ_z) strains accumulated in the ice,

$$\dot{\epsilon}_{xz} = E(\epsilon_{xz}, \epsilon_z) A(T) \tau_{xz}^3 \quad (4.2.1)$$

with the temperature dependent coefficient $A(T)$ (see Section 4.3.2.2) describing the flow relationship at the minimum creep rate for isotropic ice.

For initially isotropic ice the developing enhancement under continued constant shear stress is easily described as a function of the cumulative strain as discussed above. A slightly more complicated situation arises in ice sheets.

The ice deformation in the upper part of an ice sheet is dominated by vertical compression while in the deeper parts the deformation is dominated by steadily increasing shear. Even though the ice sheet model dynamics neglects compressive stresses and are driven by horizontal shear stress (τ_{xz}), the dependence of crystal fabrics on the stress configuration and strain history must be taken into account, varying from development towards a fabric compatible with vertical compression in the upper regions to the development towards a fabric compatible with horizontal shear as the ice flows downwards and outwards.

To address this complication, the enhancement factor $E(\epsilon_{xz}, \epsilon_z)$ is taken to be a function of the ratio of shear strain to compressive strain, $r = \epsilon_{xz}/\epsilon_z$, rather than a function of the shear strain alone, as might be appropriate for a laboratory shear alone experiment starting with isotropic ice. This enables us to ensure that the enhancement factor is kept at unity until shear strain overtakes vertical compressive strain. In ice sheets this occurs at depths where the shear strain greatly exceeds 1%, and while shear strain thereafter increases rapidly with depth, vertical compressive strain changes only slowly. Using the ratio of strains thus provides a convenient way to rescale the dependence on shear strain to ensure that

the developing enhancement of ice flow under sustained shear comes into play only once the shear compatible fabric has overwritten any compressive fabrics. This approach was based on the assumption that the shear flow of the ice whose fabric is vertical compatible with compression proceeds at the secondary minimum creep rate for isotropic ice under horizontal shear. This assumption has been used because of the absence of laboratory data on the shear deformation of ice with a fully developed small circle girdle fabric at the time the model was developed. Since then, these kinds of laboratory experiments have been carried out and the results do not completely support the above assumption. An improved model that will be described in the section 4.3 has taken this into account.

Strain Ratio ($\epsilon_{xz} / \epsilon_z$)	Enhancement Factor (E)
< 1	1
1 ~ 3	($\epsilon_{xz} / \epsilon_z$) ^{1/log₁₀ 3}
3 ~ 100	10
100 ~ 1000	1000 / ($\epsilon_{xz} / \epsilon_z$)
> 1000	1

Table 4.1. Enhancement factor $E(\epsilon_{xz}/\epsilon_z)$ as a function of the ratio of horizontal shear strain (ϵ_{xz}) to vertical compressive strain (ϵ_z).

In this initial study a simple parameterisation for the enhancement factor E as a function of the shear strain to the compressive strain has been used. The enhancement factor $E(\epsilon_{xz}/\epsilon_z)$ displayed in Table 4.1 increases from 1 to a maximum of 10 (adopted from laboratory results for shear) as the ratio of shear strain to compressive strain increases from 1 to 3 and is kept unchanged until the strain ratio r reaches 100. Russell-Head and Budd (1979) observed that very near

the base of the ice sheet the shear strain rate can fall to low values. This decline may owe something to disruption of shear compatible fabrics due to the influence of varying longitudinal stresses which would reduce the enhancement factor, but may also involve a decrease in shear stress and not be solely due to crystallographic effects. It may reflect relatively stagnant or obstructed ice below the highest shear zone, which may be related to the large-scale bedrock roughness which in general might not be well defined by ice thickness sounding.

Accordingly in this model it was decided not to carry the enhancement of shear flow all the way to the local mean bedrock, and for the preliminary study a reduction in the enhancement factor commenced once the strain ratio exceeded 100 and enhancement was progressively returned to unity as the strain ratio increases from 100 to 1000. This prescription is somewhat arbitrary but is motivated by the idea that a high shear layer may form some distance above the large scale average bedrock in real ice sheets, where the shear may be relatively undisturbed by the influence of irregular bedrock topography peaks and the corresponding induced local longitudinal stresses on the flow. As we see that the major effects of this treatment of enhancement are a rapid increase in strain-rate where enhancement sets in, and then nearer the bedrock a competition between decreasing enhancement and the rising influence of higher temperatures. In other studies the parameterisation of the reduction of enhancement near the base of the ice sheet has also been investigated as a function of distance from the bedrock. The vertical length scale for such a reduction in enhancement (perhaps as a proxy for reducing shear stress) should presumably be characteristic of the amplitude of those bedrock undulations which occur within a horizontal distance corresponding to the assumptions of the shallow ice approximation, rather like a smoothing envelope over the bedrock bumps with a length scale of several ice thicknesses. An example (see Figure 6.3) showing the reduction in local shear stress near the bed for ice flow over irregular bedrock near Cape Folger was given by Budd and Jacka (1989), from results of a finite element model study by Budd and Rowden-Rich (1985).

These preliminary model studies revealed that for temperature dependent ice rheology the shear strain overtakes the compressive strain at compressive strains

which are often in excess of 50%. With the benefit of hindsight it may be that in such circumstances full enhancement would be reached even more rapidly than as described by the parameterization in Table 4.1. This preliminary model already showed that enhancement develops over a relatively narrow transition zone, indicating that even a conservative estimate of the shear needed to establish a fully developed compatible anisotropic crystal fabric produces striking modifications to strain rate profiles.

4.3. The Model Assumptions and Description

In the preliminary study (Section 4.2) a simple dependence of enhancement of the shear flow on ice flow history was introduced, through the ratio of shear strain to compression strain, giving enhanced shear flow (compared to minimum creep rates) only after the shear strain becomes substantially dominant. Recent experiments have shown that when horizontal shear stress is applied to ice which has a fabric compatible with vertical compression (i.e. small circle girdle pattern), the secondary shear flow is already ~ 2.5 times faster than minimum strain-rates for isotropic ice (Li and Jacka, 1998; see Figure 3.4b). This indicates that for shear the fabric which is compatible with compression is an easier glide crystal orientation fabric than the uniform distribution and this pattern facilitates enhanced flow by a factor of 2.5 over the minimum flow rate for a random fabric. This result implies that there is a delay of enhancement in the scheme prescribed for the preliminary model (Section 4.2).

Here the model is improved by the use of a different enhancement scheme which is more directly linked to the laboratory experiments of Li and others (1996) involving combined shear and compression stresses. In this steady state dynamic and thermodynamic flow line model, the basic assumption of the treatment of enhanced flow is that ice is always in tertiary flow, with the ice crystal fabric always compatible with the current stress configuration. This assumption ignores any delay in the crystal fabric responding (becoming compatible with) the *in situ* applied stresses. It therefore represents the most rapid response possible of flow enhancement to stress conditions. The laboratory experiments indicate that

increasements of about 10% strain are enough to establish a close approximation to a compatible fabric in tertiary flow from a prior configuration (Budd and Jacka 1989; Li and others, 1996; Li and Jacka, 1998). The combination of stresses in an ice sheet in general varies from compression dominated in the upper part of ice sheet to shear dominated in the deeper parts. Since this model involves the relative magnitudes of shear and compression stresses, the influence of the compressive stress on shear strain rates has been also included by retaining the octahedral stress in the shear component of the flow relations. This has a direct influence on the shear strain rates in the upper regions of the ice sheet.

This is the form of the anisotropic flow model that is applied to two different flowlines (Chapter 6 and Chapter 7), one borehole drilling site (Chapter 5) and in a trial application to a model of the whole Antarctic ice sheet in Chapter 9 in this thesis.

4.3.1. Stress Configurations and Driving Stress

In this flow line model an initial assumption is made to consider flow entirely constrained to a vertical section in steady state balance. In this case it is assumed that

$$\dot{\epsilon}_y = -\dot{\epsilon}_{xy} = \dot{\epsilon}_{yz} = 0 \quad (4.3.1.1)$$

and

$$\dot{\epsilon}_x = -\dot{\epsilon}_z, \quad (4.3.1.2)$$

where x is in the line of flow and z in vertical. The model would be readily generalised to include a prescribed transverse extension with $\dot{\epsilon}_y \neq 0$. For the present version the corresponding stress configuration is shown in Figure 4.1 (companied with laboratory experiment case), so that the laboratory results (Li and others, 1996) can be directly used in this model, even though they addressed the converse case of $\dot{\epsilon}_x = 0$ and $\dot{\epsilon}_y = -\dot{\epsilon}_z$ in the experiments.

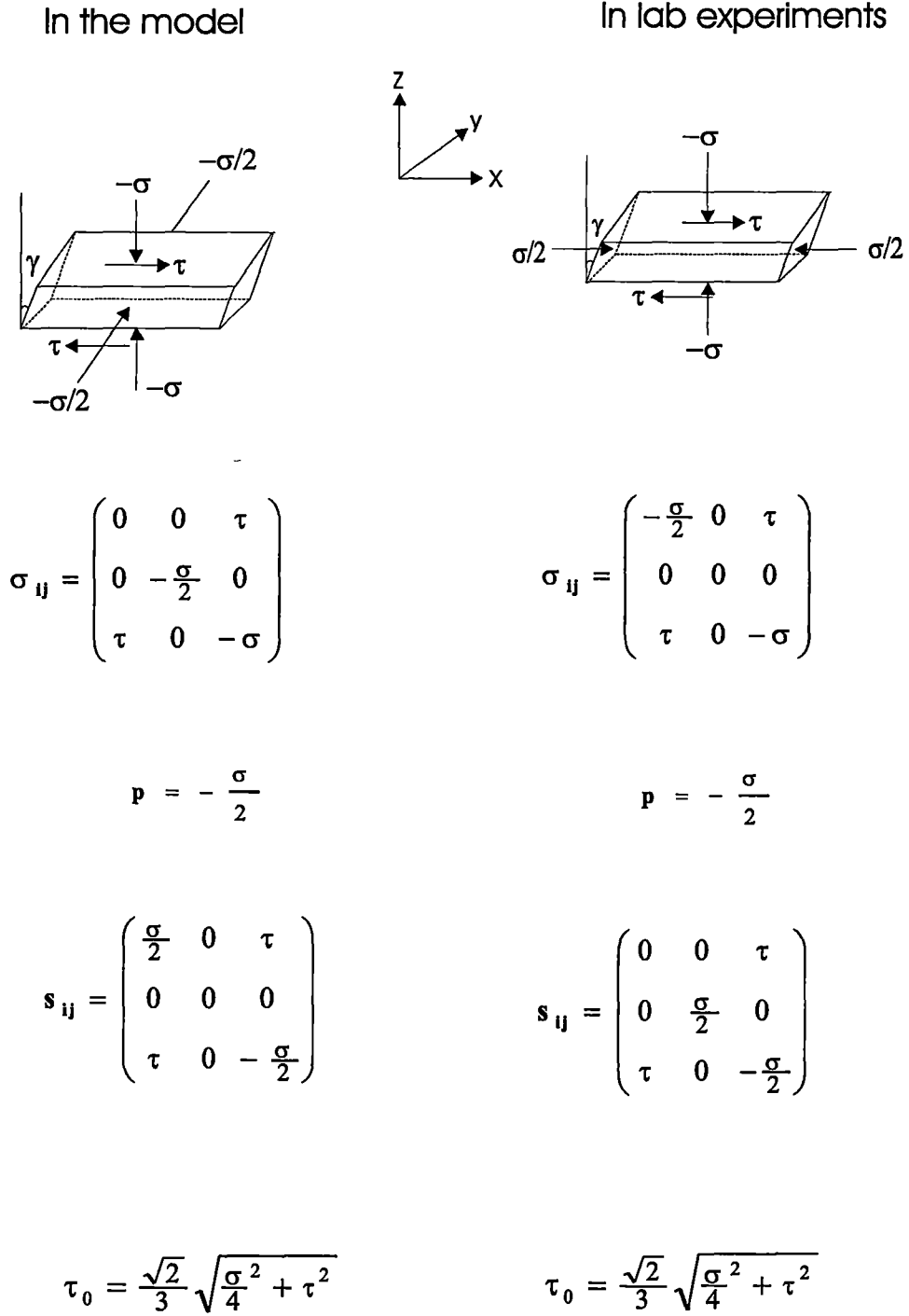


Figure 4.1. Comparison of the stress configurations in the model (left side) and laboratory experiment (right side) under confined combination of compression (σ) and shear (τ) stresses. Also shown are the stress tensor (σ_{ij}), hydrostatic pressure (P), stress deviator tensor (S_{ij}) and octahedral stress (τ_0).

Then the equations of motion (Appendix I) reduce to

$$\frac{\partial \sigma_x}{\partial x} + \frac{\partial \tau_{xz}}{\partial z} = 0 \quad (4.3.1.3)$$

$$\frac{\partial \sigma_y}{\partial y} = 0 \quad (4.3.1.4)$$

$$\frac{\partial \tau_{xz}}{\partial x} + \frac{\partial \sigma_z}{\partial z} = -\rho g \quad (4.3.1.5)$$

in a Cartesian coordinate system (Figure 4.5) with the x-y plane parallel to the geoid and the z-axis pointing vertically upwards ($z=0$ at sea level, $z=E$ at surface and $z=B$ at bed).

The relation between stress (σ_i) and deviatoric stress (S_i) is

$$S_i = \sigma_i - P, \quad i = x, y, z \quad (4.3.1.6)$$

where the hydrostatic pressure is given by

$$P \approx \rho g (E - z),$$

where E is the surface elevation (4.3.1.7)

ρ is the density of ice and g the acceleration due to gravity.

Replacing stresses with stress deviators, Equations (4.3.1.3), (4.3.1.4) and (4.3.1.5) become

$$\frac{\partial S_x}{\partial x} + \frac{\partial P}{\partial x} + \frac{\partial \tau_{xz}}{\partial z} = 0 \quad (4.3.1.8)$$

$$\frac{\partial P}{\partial y} = 0 \quad (4.3.1.9)$$

$$\frac{\partial \tau_{xz}}{\partial x} + \frac{\partial S_z}{\partial z} + \frac{\partial P}{\partial z} = -\rho g \quad (4.3.1.10)$$

Integration of Equation (4.3.1.10) from the surface, E , to a depth, z , gives

$$-P(z) = \int_z^E (-\rho g - \frac{\partial S_z}{\partial z} - \frac{\partial \tau_{xz}}{\partial x}) dz = -\rho g (E - z) - \int_z^E \frac{\partial \tau_{xz}}{\partial x} dz - S_z \Big|_z^E \quad (4.3.1.11)$$

substituting (4.3.1.11) into (4.3.1.8) and integrating again from the surface to z yields

$$\tau_{xz} = \rho g \frac{\partial E}{\partial x} (E - z) + \int_z^E \int_{z'}^E \frac{\partial^2 \tau_{xz}}{\partial x^2} dz' dz + \frac{\partial S_z(E)}{\partial x} (E - z). \quad (4.3.1.12)$$

In the above equation, the second and third terms on the right hand side are considered smaller compared with the first term. The second term on the right (Budd, 1970a; 1971; 1975) may be termed the *variational stress* since it represents the resistance of the ice to a *varying stress gradient* in the line of motion. It is usually associated with curved particle paths. For slowly varying stresses or long wave fluctuations it becomes negligible (irrespective of the magnitude of τ_{xz}) but for short-wave fluctuations it becomes very important. Budd (1968) indicated that for variations of wavelength about four times the ice thickness or shorter this term should be considered.

By neglecting the last two terms in Equation (4.3.1.12) the shear stress as the driving stress in the model is then calculated in

$$\tau_{xz} = \rho g \alpha (E - z) \quad (4.3.1.13)$$

where α is the surface slope. Equation (4.3.1.13) implies that the large scale smoothed ice flow is driven primarily by large scale gradients in the surface elevation. If the surface were to be perfectly horizontal, there would be no large scale driving force and hence no ice flow without longitudinal stresses, but this is not generally the case in natural ice sheets.

4.3.2. The Flow Relations

In the model that is the main focus of this thesis the flow law is based directly on the laboratory experiments by Li and others (1996), discussed in Section 3.3.2. Those experiments, involving combined shear and confined compression stresses, showed an anisotropic rheology which they summarised by a flow relation, expressed in terms of octahedral values of stress and strain-rate, for the strain-rate in tertiary creep $\dot{\epsilon}_o$:

$$\dot{\epsilon}_o = E(\lambda_c) A_o(T) \tau_o^3 \quad (4.3.2.1)$$

involving an enhancement factor $E(\lambda_c)$ which is a function of the compression fraction (λ_c) and the temperature dependent flow coefficient $A_o(T)$ that describes the octahedral minimum creep rate. The compression fraction is defined as the function of shear stress (τ_{xz}) and compressive stress deviator (S_z) in

$$\lambda_c = \frac{S_z}{\sqrt{\tau_{xz}^2 + S_z^2}}. \quad (4.3.2.2)$$

Once the isotropic condition implicit in Glen's flow law no longer applies, a single relation between the octahedral stresses and strain-rates no longer suffices to describe the flow law. For our model, we consider the flow relations for components of shear and compression as follows

$$\dot{\epsilon}_{xz} = G(\lambda_c) A_o(T) \tau_o^2 \tau_{xz} \quad (4.3.2.3)$$

$$\dot{\epsilon}_z = F(\lambda_c) A_o(T) \tau_o^2 S_z, \quad (4.3.2.4)$$

where $G(\lambda_c)$ and $F(\lambda_c)$ are enhancement factors of shear and compression component, respectively.

The octahedral shear stress is taken as

$$\tau_o = \sqrt{\frac{2}{3}(\tau_{xz}^2 + S_z^2)}, \quad (4.3.2.5)$$

on the assumption made in Section 4.3.1 that the ice flow corresponds to a confined vertical compression stress combined with a horizontal shear stress.

While it is assumed $\tau_{xz} = \rho g \alpha (E - z)$, S_z is not defined and so λ_c is related to the strain rates by taken the ratio of (4.3.2.3) to (4.3.2.4)

$$\lambda_c = \frac{\dot{\epsilon}_z}{\sqrt{\frac{F^2}{G^2} \dot{\epsilon}_{xz}^2 + \dot{\epsilon}_z^2}} \quad (4.3.2.6)$$

Using Equations (4.3.2.3) and (4.3.2.4) to obtain an expression for τ_o which is substituted back into Equation (4.3.2.3) yields a cubic equation for the shear strain rate $\dot{\epsilon}_{xz}$:

$$\dot{\epsilon}_{xz}^3 - \frac{2}{3}G(\lambda_c)A_o(T)\tau_{xz}^3\dot{\epsilon}_{xz}^2 - \frac{2}{3}G(\lambda_c)^3/F(\lambda_c)^2 A_o(T)\tau_{xz}^3\dot{\epsilon}_z^2 = 0 \quad (4.3.2.7)$$

in terms of the compression fraction λ_c , the shear stress τ_{xz} and the vertical strain rate $\dot{\epsilon}_z$. This equation can be solved iteratively (Section 4.3.3) for the shear strain rate $\dot{\epsilon}_{xz}$, which can be integrated to provide the horizontal velocity in the usual way (see Section 4.4.3). The vertical strain-rates can be calculated from the horizontal velocities using the incompressibility of ice. From Equations (4.3.2.3) and (4.3.2.4) $G(\lambda_c)$ approaches $E(\lambda_c)$ as λ_c tends to zero, while $F(\lambda_c)$ approaches $E(\lambda_c)$ as λ_c tends to one. When the shear strain rate is much larger than the compression strain rate, Equation 4.3.2.7 simplifies to the usual relation

$$\dot{\epsilon}_{xz} = \frac{2}{3}G(\lambda_c)A_o(T)\tau_{xz}^3 \quad (4.3.2.8)$$

where $G(\lambda_c)$ then corresponds to the enhancement for shear alone.

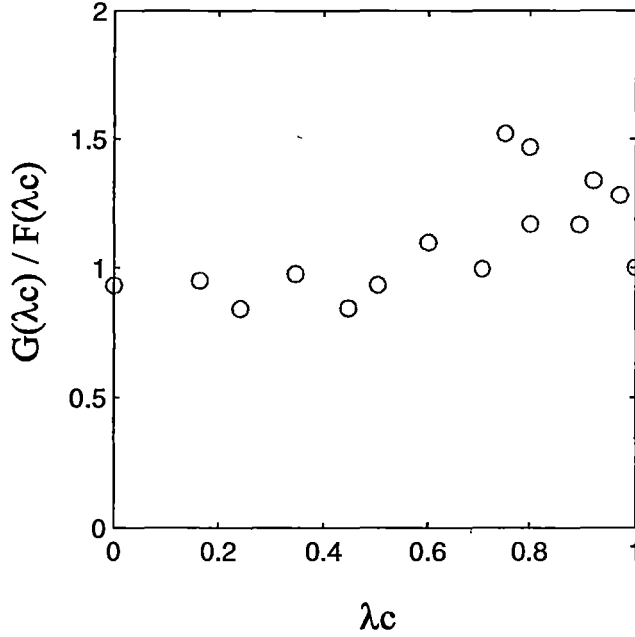


Figure 4.2. The ratio of enhancement factors in the shear component ($G(\lambda_c)$) to the compression component ($F(\lambda_c)$) is plotted as a function of the compression fraction (λ_c). (The data come from Li and Jacka, personal communication).

The results of laboratory combined stress experiments (Li and Jacka, personal communication) for individual components of the stress and strain-rate tensors, show that the ratio $G(\lambda_c)/F(\lambda_c)$ is of order unity (Figure 4.2). There appears to be a gradual trend for the ratio $G(\lambda_c)/F(\lambda_c)$ to fall slowly as shear dominance increases, but this is not important in determining the shear strain rate. Accordingly for the present model we simplified Equation 4.3.2.6 by taking $G(\lambda_c) = F(\lambda_c) = E(\lambda_c)$ to obtain

$$\dot{\epsilon}_{xz}^3 - \frac{2}{3}E(\lambda_c)A_o(T)\tau_{xz}^3(\dot{\epsilon}_{xz}^2 + \dot{\epsilon}_z^2) = 0 \quad (4.3.2.9)$$

and used the parameterisation of Li and others (1996) for $E(\lambda_c)$ described in next section.

4.3.2.1. Enhancement Factor Derived from Laboratory Experiments

The enhancement factor for shear $G(\lambda_c)$ and compression $F(\lambda_c)$ are simplified to be equal to $E(\lambda_c)$ in this model. Li and others (1996) described the way the enhancement factor for $\dot{\epsilon}_o$ in tertiary flow varies between E_s and E_c , the respective enhancement factors for shear or compression alone, (they took $E_s = 10$ and $E_c = 3$) by

$$E(\lambda_c) = E_s \left(\frac{E_c}{E_s} \right)^{\lambda_c} \quad (4.3.2.10)$$

in terms of the compression fraction λ_c , which is defined in Equation 4.3.2.2 and can be calculated from shear ($\dot{\epsilon}_{xz}$) and compressive ($\dot{\epsilon}_z$) strain rates as

$$\lambda_c = \frac{\dot{\epsilon}_z}{\sqrt{\dot{\epsilon}_{xz}^2 + \dot{\epsilon}_z^2}}. \quad (4.3.2.11)$$

The compression fraction varies from 1 to 0 as the stress situation varies from purely confined compression (shear stress $\tau_{xz} = 0$) to simple shear (compressive deviatoric stress $S_z = 0$).

In the calculations presented in the remaining Chapters of this thesis, the form of the enhancement factor, $E(\lambda_c)$, suggested by Li and others (1996) (4.3.2.10) above was retained with $E_c=3$, but taking $E_s=6$. This reduction in the maximum enhancement of shear strain rates is based on the studies of the DSS borehole (Chapter 5) and Law Dome flow line (Chapter 6). It reflects the remaining uncertainty as to how representative the laboratory enhancement results are for flow under the stress levels encountered in ice sheets as discussed in Chapter 3. The model applications made for Chapter 5 and Chapter 6 showed that by taking the enhancement varying from 3 to 6 the modeled shear strain rate profiles have a good match with the borehole strain-rate measurements (Figure 5.11(a) and Figure 6.7) and the modeled temperature profiles (Figure 6.6, the basal geothermal heat flux gradient is 0.035 K m^{-1}) showed better agreement with the borehole measurements than the calculations made (not presented in the thesis for reasons of space) taking enhancement varying from 3 to 10 and the basal geothermal heat flux gradient of 0.02 K m^{-1} . The higher basal geothermal heat flux gradient of 0.035 K m^{-1} was chosen for the flow line calculations presented, based on the borehole measurements (see Table 3.1) and it led to better agreement using a lower enhancement (see Equation 4.3.2.9).

4.3.2.2. Enhancement Factor based on Ice History

For comparison, the enhancement factor $E(\epsilon_{xz}/\epsilon_z)$ from the preliminary studies mentioned in Section 4.2 and displayed in Table 4.1, containing the history of the ice, is also employed in place of $E(\lambda_c)$ in Equation (4.3.2.9) in the study of the Law Dome flow line in Chapter 6. In that set of calculations $E(\epsilon_{xz}/\epsilon_z)$ is calculated using Table 4.1, with ϵ_{xz}/ϵ_z being evaluated along the flow trajectories. For this work the original range of enhancements from the preliminary model was retained, increasing from 1 to a maximum of 10 (adopted from laboratory results for shear) as the ratio of shear strain (ϵ_{xz}) to compressive strain (ϵ_z) increases from 1 to 3. As well as exploring possible differences in the onset of enhancement these parallel calculations also provide a comparison using a higher maximum enhancement factor. Unlike the preliminary studies (Wang and Warner 1998) the final two rows of Table 4.1 are not required as the modelling in Chapter 6

involves a different approach to the possible reduction of enhancement near the base of the ice sheet.

4.3.2.3. Temperature Dependent Parameters

The temperature dependent coefficient $A(T)$ (Table 4.2) is based on laboratory experiments (corresponding to the octahedral shear stress of 0.1 MPa) summarised by Budd and Jacka (1989). In our model this table was used to interpolate $A(T)$ using logarithmically. The values of octahedral (A_o) and simple shear (A_{xz}) have the relation (Budd and Jacka, 1989) of

$$A_{xz} = \frac{2}{3} A_o. \quad (4.3.2.12)$$

Temperature (°C)	0	-1	-2	-5	-10	-20	-30	-40	-50
A_{xz} ($\text{bar}^{-3} \text{ yr}^{-1}$)	2.94 $\times 10^{-1}$	1.43 $\times 10^{-1}$	8.62 $\times 10^{-2}$	3.15 $\times 10^{-2}$	1.09 $\times 10^{-2}$	2.70 $\times 10^{-3}$	7.57 $\times 10^{-4}$	1.68 $\times 10^{-4}$	3.15 $\times 10^{-4}$
A_o ($\text{bar}^{-3} \text{ yr}^{-1}$)	4.41 $\times 10^{-1}$	2.15 $\times 10^{-1}$	12.93 $\times 10^{-2}$	4.73 $\times 10^{-2}$	1.64 $\times 10^{-2}$	4.05 $\times 10^{-3}$	11.36 $\times 10^{-4}$	2.52 $\times 10^{-4}$	4.73 $\times 10^{-4}$

Table 4.2. Temperature dependent coefficient values of octahedral (A_o) and simple shear (A_{xz}) component.

According to Arrhenius relation (Paterson, 1994) the value of $A(T)$ varies with temperature (T) as

$$A(T) = A' \exp\left(-\frac{Q}{RT}\right), \quad (4.3.2.13)$$

where A' is independent of temperature, R is the gas constant ($8.314 \text{ J mol}^{-1} \text{ K}^{-1}$), Q the activation energy for creep. With the following values for A' and Q (Huybrechts, 1992):

$$\begin{array}{lll} T < -10 \text{ }^{\circ}\text{C} & A' = 1.14 \times 10^{-5} \text{ pa}^{-3} \text{ yr}^{-1} & Q = 60 \text{ kJ mol}^{-1} \\ T \geq -10 \text{ }^{\circ}\text{C} & A' = 5.47 \times 10^{10} \text{ pa}^{-3} \text{ yr}^{-1} & Q = 139 \text{ kJ mol}^{-1}, \end{array}$$

the values of $A(T)$ are plotted in Figure 4.3 together with the values of $A_{xz}(T)$ used in our model. Figure 4.3 shows little difference between these two sets of data which has also been indicated by Huybrechts (1992, Figure 4.3).

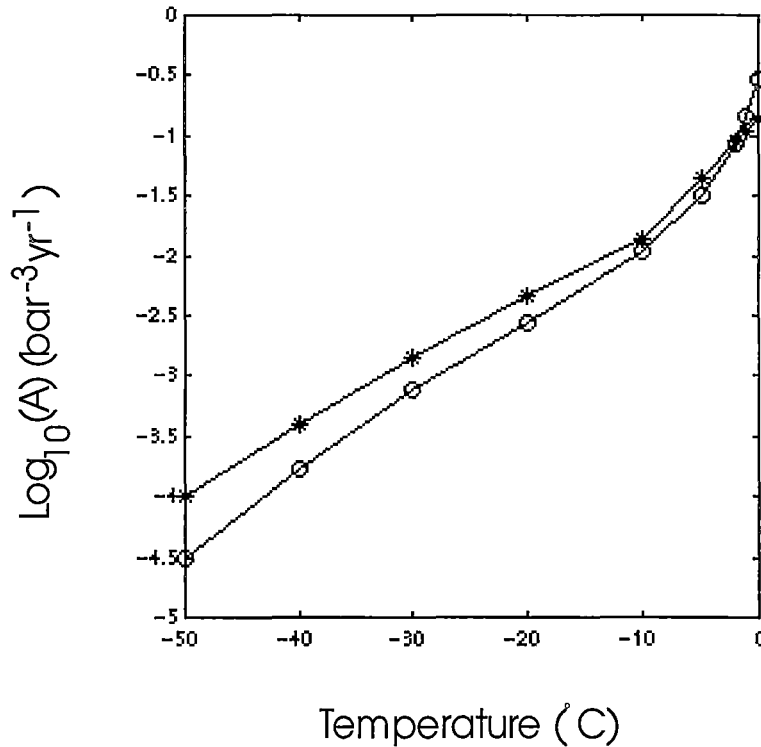


Figure 4.3. Comparison of the *temperature dependent coefficient values from the Arrhenius relation (Equation 4.3.2.12) indicated by the symbol (*) and from the laboratory experiments (A_{xz}) used in our model indicated by the symbol (o).*

4.3.3. Iterative Process

In this model the strain-rates are determined by solving Equation (4.3.2.8) through an iterative process (Figure 4.4). The steady state temperature distribution in the

ice sheet and the enhancement factor distribution were treated alternately. For fixed enhancement factors ($E(\lambda_c)$), the heat equation was solved for the steady state temperature distribution (Section 4.4.8). This temperature distribution was then used to calculate new shear strain-rates and so update the velocities (see Sections 4.4.3 and 4.4.4). New temperatures were calculated and this process was repeated until the temperature distribution converged. For a fixed temperature distribution ($A_o(T)$), the enhancement factors were determined using the compression fractions (λ_c) calculated in terms of shear and compressive strain rates. This enhancement factor distribution was then used to calculate new shear strain-rates. The horizontal velocities were then updated and new vertical strain-rates determined, allowing an updating of the enhancement factor.

4.3.4. Bedrock Treatment

Two major complications must be addressed in extending the results of laboratory ice deformation experiments to the quantitative description of ice flow in ice sheets. The first is the development of anisotropic crystal fabrics with increasing strain, in response to applied stresses. The second is that the nature of flow in the regions near the base of ice sheets is rather uncertain, even though it is in this part of the ice column that ice sheet models typically develop much of the horizontal deformation velocity. In basal layers, where ice is usually at its warmest and deformation rates can be large, any deviations from the usual presumption of increasing shear stress with depth produce large increases in the computed shear strain-rate and consequently of horizontal velocity.

In this project a concept of an envelope topography, smoothing over the higher frequency bedrock roughness, will be used. This is based on the combination of observations, from boreholes and radar echo sounding, showing relatively smooth and continuous high shear layers with the appearance of enveloping over the rough bedrock features. The appropriate spatial scales for the representation of this smoothing in the model require further examination.

Longitudinal averaging of surface slopes and ice thickness could be done following the approach of Kamb and Echelmeyer (1986) however the simpler

methods employed here are more appropriate because of the uncertainties associated with bedrock variations across the flow direction

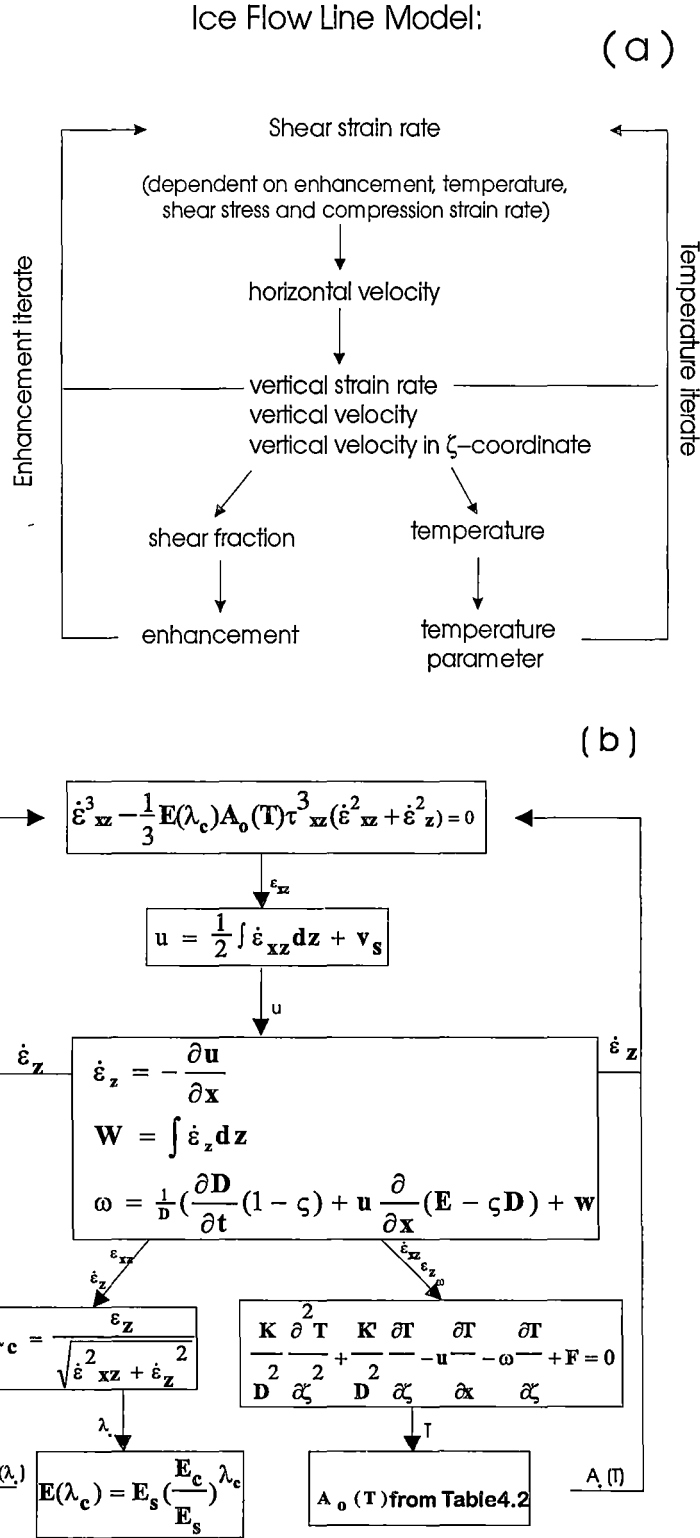


Figure 4.4. The model structure.

of the ice will generally not coincide with grid points. This problem may be reasonably overcome by transforming the vertical coordinate z to a new vertical coordinate ζ .

The relation between z and ζ is

$$\zeta = \frac{E - z}{D} \quad \text{or} \quad z = E - \zeta D \quad (4.4.1.1)$$

and

$$\frac{\partial \zeta}{\partial z} = -\frac{1}{D} \quad (4.4.1.2)$$

where $D=E-B$ is the ice thickness, E is the surface elevation, and B is the bedrock elevation. ζ is dimensionless and varies from 0 at surface ($z = E$) to 1 at the base of the ice ($z = B$). The transformation of an orthogonal system (x, y, z, t) into a non-orthogonal system (x, y, ζ, t) was introduced to ice sheet modelling (Budd and others, 1971; Jenssen, 1977; Funk and others, 1994) based on analogy to the σ -coordinate system developed by Phillips (1957) for numerical weather forecasting.

The partial derivatives of a scalar dependent variable S in (x, y, z, t) system and in (x, y, ζ, t) system have the general relations (see e.g. Haltiner and Williams, 1980)

$$\begin{aligned} \left. \frac{\partial S}{\partial r} \right|_z &= \left. \frac{\partial S}{\partial r} \right|_\zeta - \frac{\partial S}{\partial \zeta} \frac{\partial \zeta}{\partial z} \frac{\partial z}{\partial r} \\ &= \left. \frac{\partial S}{\partial r} \right|_\zeta + \frac{1}{D} \frac{\partial S}{\partial \zeta} \frac{\partial}{\partial r} (E - \zeta D), \quad r = x, y, \text{ or } t \end{aligned} \quad (4.4.1.3)$$

$$\begin{aligned} \left. \frac{\partial S}{\partial z} \right|_z &= \frac{\partial S}{\partial \zeta} \frac{\partial \zeta}{\partial z} \\ &= -\frac{1}{D} \frac{\partial S}{\partial \zeta} \end{aligned} \quad (4.4.1.4)$$

$$\left. \frac{\partial^2 S}{\partial z^2} \right|_z = \frac{1}{D^2} \frac{\partial S}{\partial \zeta} \quad (4.4.1.5)$$

where the subscript z and ζ denote (x, y, z, t) system and (x, y, ζ, t) system respectively.

Using the two-dimensional divergence

$$\nabla_z = \nabla_\zeta = \frac{\partial}{\partial x} \hat{i} + \frac{\partial}{\partial y} \hat{j}, \quad (4.4.1.6)$$

Equation 4.4.1.3 can be written as

$$\begin{aligned} \nabla_z S &= \nabla_\zeta S - \frac{\partial S}{\partial \zeta} \frac{\partial \zeta}{\partial z} \nabla_\zeta z \\ &= \nabla_\zeta S + \frac{1}{D} \frac{\partial S}{\partial \zeta} \nabla_\zeta (E - \zeta D) \end{aligned} \quad (4.4.1.7)$$

or

$$\begin{aligned} \bar{\nabla}_z \cdot \bar{\nabla} &= \bar{\nabla}_\zeta \cdot \bar{\nabla} - \frac{\partial \bar{\nabla}}{\partial \zeta} \frac{\partial \zeta}{\partial z} \cdot \nabla_\zeta z \\ &= \bar{\nabla}_\zeta \cdot \bar{\nabla} + \frac{1}{D} \frac{\partial \bar{\nabla}}{\partial \zeta} \cdot \nabla_\zeta (E - \zeta D) \end{aligned} \quad (4.4.1.8)$$

for a vector dependent variable $\bar{\nabla}$ in the x, y plane.

When $r = t$, the result is

$$\left. \frac{\partial S}{\partial t} \right|_\zeta = \left. \frac{\partial S}{\partial t} \right|_z + \frac{\partial S}{\partial \zeta} \frac{\partial \zeta}{\partial z} \frac{\partial z}{\partial t} \Big|_\zeta \quad (4.4.1.9)$$

the total derivative in ζ -coordinates is

$$\frac{dS}{dt} = \left. \frac{\partial S}{\partial t} \right|_\zeta + \bar{\nabla} \cdot \bar{\nabla}_\zeta S + \omega \frac{\partial S}{\partial \zeta} \quad (4.4.1.10)$$

where $\bar{\nabla}$ is the horizontal velocity henceforth,

$$\omega = \frac{d\zeta}{dt} \quad (4.4.1.11)$$

is the vertical velocity in the ζ system and S can be a scalar or a vector.

In the (x, y, ζ, t) system, velocity and temperature are calculated at the levels formed by dividing the ice thickness into certain bands. These bands could be

divided evenly (e.g. Budd and others, 1971; Jenssen, 1977; Mavrakakis, 1992) or unevenly with higher concentration towards the base of the ice (Huybrechts, 1992). 100 evenly spaced bands are used in the model described here.

4.4.2. Finite Difference Method and Staggered Grid Points

In the model, partial differential equations are solved using the finite-difference method. A staggered grid finite-difference scheme in the ζ -coordinate system is employed (MacAyeal, 1996).

Considering a rectangular domain in x, ζ space, where i, j denote the index numbers of a grid point with N_x, N_z the total number along the respective axes, the variables calculated at the grid points are shown in Figure 4.6.

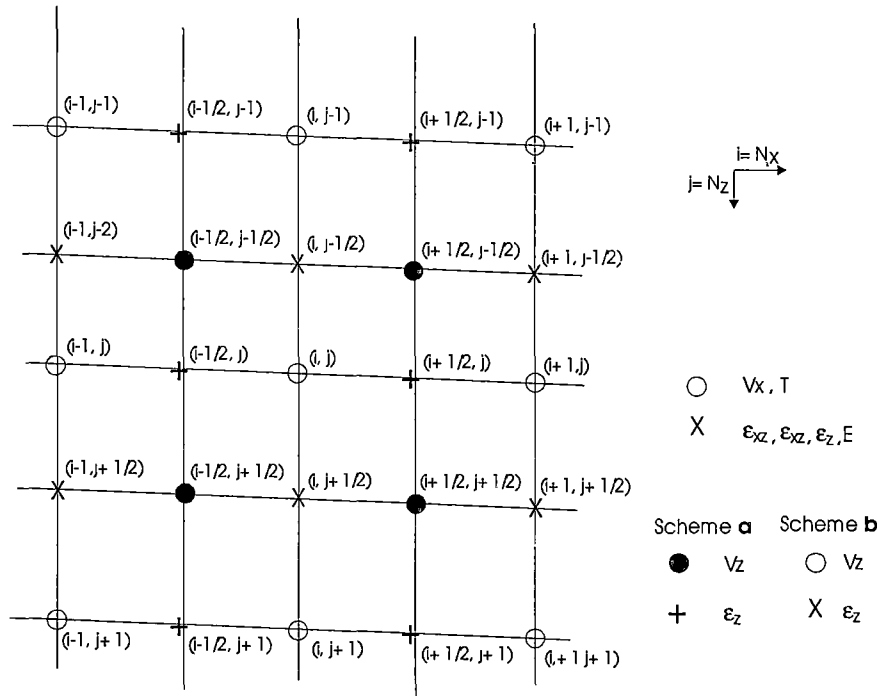


Figure 4.6. Staggered grid points, showing the locations of the values of horizontal (V_x) and vertical (V_y) velocities, shear ($\dot{\epsilon}_{xz}$) and compressive ($\dot{\epsilon}_z$) strain rates, shear (ϵ_{xz}) and compressive (ϵ_z) strains, enhancement factor (E), and temperature (T). Scheme a and scheme b means V_z and $\dot{\epsilon}_z$ are calculated by the longitudinal strain rates and by the shape function approaches, respectively (see Section 4.4.4). i and j denote the index numbers of a grid point. N_x and N_z are the total numbers of the grid points in the horizontal and vertical directions.

4.4.3. Horizontal Velocity

Since the movement of the ice sheet is caused by internal deformation of ice and basal sliding over bedrock, the horizontal velocity (U) along the flow direction for grounded ice consists of two components, i.e. an internal deformational part (V_i) and a basal sliding (V_s), as

$$U = V_i + V_s. \quad (4.4.3.1)$$

The sliding is expected only where the basal ice is at or near the melting point. In the case of the basal ice frozen on bedrock where the basal temperature is lower than pressure melting point, there is no sliding at the base of the ice so that the horizontal velocity is equal to the internal ice velocity, as given in section 4.4.3.1. The sliding velocity formulation is given in section 4.4.3.2.

4.4.3.1. Internal Velocity

From the relations between the strain rate and velocity components (Section 2.2.2.1), we have

$$\dot{\epsilon}_{xz} = \frac{1}{2} \left(\frac{\partial V_x}{\partial z} + \frac{\partial V_z}{\partial x} \right), \quad (4.4.3.2)$$

where $\dot{\epsilon}_{xz}$ is the shear strain rate determined from the flow law (Section 4.3), V_x is the horizontal velocity along the flow direction and V_z is the vertical velocity. Here, V_x is the internal velocity (V_i) which is a function of depth with a maximum value at the surface and zero at the bedrock. The second term on the right hand of Equation 4.4.3.2 is usually neglected by assuming $\partial V_z / \partial x \ll \partial V_x / \partial z$, i.e. that horizontal variations in the profile of the vertical velocity are small. For a given shear strain rate the internal velocity at any depth is here computed by integrating Equation 4.4.3.2 with respect to z ,

$$V_i = V_x = \frac{1}{2} \int_{\text{bed}}^z \dot{\epsilon}_{xz} dz = -\frac{D}{2} \int_1^\zeta \dot{\epsilon}_{xz} d\zeta, \quad (4.4.3.3)$$

where

$$dz = d(E - \zeta D) = -D d\zeta, \quad (4.4.3.4)$$

4.4.3.2. Sliding Velocity

When the temperature of the basal layers reaches the melting point, basal melt water is formed and basal sliding may occur. The sliding law - the relation between basal velocity, shear stress, water pressure, and the characteristics of the bedrock - is the basal boundary condition in the analysis of the flow of glaciers (or ice sheets) with the basal ice at melting point. Establishing a sliding law is one of the major current unsolved problems in glacier physics (Paterson, 1994).

Since Hopkins (1845, 1849) first studied steady sliding velocities as a function of slope, many attempts have been made to derive sliding velocities from various geometric aspects of glaciers and ice sheets (e.g. Weertman, 1964; Budd, 1976; Budd and others, 1979, 1984; Lliboutry, 1979, 1987; Bindshadler, 1983)

The form of the empirical equation used in the model described here is adopted from Budd and others (1984). The basal sliding velocity (V_s) is

$$V_s = a_s \frac{\tau_b}{D^{*2}}, \quad (4.4.3.5)$$

where a_s is a constant dependant mainly on bed roughness and taken here as $0.32 \times 10^3 \text{ m}^3 \text{ bar}^{-1} \text{ a}^{-1}$ (Note: it is 5×10^3 in Budd's model for West Antarctica) for matching the observations from Law Dome, East Antarctica (see Chapter 6), τ_b ($=\rho g \alpha D$) is the basal shear stress, and D^* is ice thickness above buoyancy and is determined by

$$D^* = E - aD + b, \quad (4.4.3.6)$$

with

$$a = 1 - \frac{\rho_{ice}}{\rho_{sea}} \quad \text{and} \quad b = -P \frac{\rho_{ice}}{\rho_{sea}}$$

here ρ_{ice} ($= 885 \text{ kg m}^{-3}$) is the density of floating ice, ρ_{sea} ($= 1027 \text{ kg m}^{-3}$) is the density of sea water, and P ($=20 \text{ m}$) is a factor used to account for the surface firm layer of lower density so that the surface elevation for the equivalent solid ice thickness is reduced by P . In hindsight it should be noted that the lower density for floating ice (from Jenssen, 1988) includes the effect of the firm which is

accounted for by the 20m adjustment. However since floating ice has not been treated here this correction is not relevant to the present context.

4.4.4. Vertical Strain Rate and Velocities

Two approaches to calculating vertical strain rate and velocities in terms of horizontal velocity were explored in this project: (a) the direct approach from the longitudinal strain rates using incompressibility and (b) from an approximation combining incompressibility and continuity, using the shape function from the horizontal velocity profile. The latter scheme is based on the assumption that the shape of the horizontal-velocity/depth profile varies only slowly with x . This section will describe the vertical strain rate ($\dot{\epsilon}_z$) and the vertical velocities in z -coordinates (W) and in ζ -coordinates (ω) calculated from both approaches.

If U , V and W are the velocities for the x , y and z directions, respectively, the incompressibility of ice gives:

$$\frac{\partial U}{\partial x} + \frac{\partial V}{\partial y} + \frac{\partial W}{\partial z} = 0 \quad \text{or} \quad \dot{\epsilon}_x + \dot{\epsilon}_y + \dot{\epsilon}_z = 0. \quad (4.4.4.1)$$

The definition of the vertical velocity in the z -coordinate is

$$W = \frac{dz}{dt}, \quad (4.4.4.2)$$

using equations (4.4.1.1) and (4.4.1.10) to transform it to the ζ -coordinate system and considering U is the only horizontal velocity component in this flow line model :

$$\begin{aligned} W = \left. \frac{dz}{dt} \right|_z &= \left. \frac{\partial z}{\partial t} \right|_{\zeta} + \bar{V} \cdot \bar{\nabla}_{\zeta} z + \omega \frac{\partial z}{\partial \zeta} \\ &= \frac{\partial D}{\partial t} (1 - \zeta) + U \frac{\partial}{\partial x} (E - \zeta D) - \omega D \end{aligned} \quad (4.4.4.3)$$

where $\omega = \frac{d\zeta}{dt}$ is called *relative vertical velocity in ζ -coordinates*. ∇_{ζ} is a two dimensional del operator in the (x, y, ζ, t) system and is expressed in Equation

(4.4.1.6). (Here $\frac{\partial E}{\partial t} = \frac{\partial D}{\partial t}$ is assumed by neglecting the change of bedrock elevation with time).

Taking the derivative of the vertical velocity W (Equation (4.4.4.3)) with depth z yields the vertical strain rate as:

$$\dot{\epsilon}_z = \left. \frac{\partial W}{\partial z} \right|_z = -\frac{1}{D} \frac{\partial W}{\partial \zeta} = \frac{1}{D} \left(\frac{\partial D}{\partial t} - \frac{\partial U}{\partial \zeta} \frac{\partial}{\partial x} (E - \zeta D) + U \frac{\partial D}{\partial x} \right) + \frac{\partial \omega}{\partial \zeta}. \quad (4.4.4.4)$$

Therefore, among these three variables of W , ω and $\dot{\epsilon}_z$, if any of them is known, the other two can be obtained from equations (4.4.4.3) and (4.4.4.4).

(a) From the longitudinal strain rates

Using this approach, the vertical strain rate $\dot{\epsilon}_z$ is computed from the longitudinal strain rates first and then vertical velocities W and ω are calculated in turn.

In the model, one of the flow conditions (Section 4.3.1) is $\dot{\epsilon}_y = 0$. This condition combined with incompressibility (4.4.4.1) implies $\dot{\epsilon}_z = -\dot{\epsilon}_x$, i.e.

$$\dot{\epsilon}_z = -\dot{\epsilon}_x = -\left. \frac{\partial U}{\partial x} \right|_z = -\left. \frac{\partial U}{\partial x} \right|_{\zeta} - \frac{1}{D} \frac{\partial U}{\partial \zeta} \frac{\partial}{\partial x} (E - \zeta D), \quad (4.4.4.5)$$

reflecting the non-orthogonal nature of the ζ -coordinate system.

The vertical velocity W can be obtained by integrating $\dot{\epsilon}_z$ through the whole column

$$W = \int_{\text{bed}}^z \dot{\epsilon}_z dz = -D \int_1^{\zeta} \dot{\epsilon}_z(\zeta) d\zeta \quad (4.4.4.6)$$

with the boundary condition of zero vertical velocity at the bed (no basal sliding). If there is basal sliding, then there should be horizontal at vertical components of basal sliding velocity related by the bedrock slope. Basal melting would also produce a small downward velocity to the ice at the bedrock. Then ω can be obtained from Equation (4.4.4.3).

(b) From the shape function

As mentioned above this approach is based on an assumption that the shape of the horizontal-velocity/depth profile varies only slowly with x . Using this approach (Budd and Jenssen, 1989; Mavraklis, 1992), ω is computed first and then W and $\dot{\epsilon}_z$ in turn. This approximate approach is especially advantageous for column profile calculations, for example, it is used for the DSS borehole studies (Chapter 5). The process is described below.

It is assumed that the horizontal velocity (U) can be expressed as

$$U = \psi \bar{U}, \quad (4.4.4.7)$$

where \bar{U} is the average horizontal velocity in the column

$$\bar{U} = \frac{1}{D} \int_{\text{bed}}^{\text{surface}} U(z) |dz| \text{ or } \bar{U} = \int_0^1 U(\zeta) |d\zeta|, \quad (4.4.4.8)$$

and ψ is a function of depth which gives the shape of the horizontal velocity curve as a function of the relative depth ζ . It is assumed that ψ changes only slowly from one column to another so $\partial\psi/\partial x$ is close to zero (at the bedrock and ice surface it is exactly zero) and so in ζ -coordinates

$$\left. \frac{\partial U}{\partial x} \right|_{\zeta} = \psi \left. \frac{\partial \bar{U}}{\partial x} \right|_{\zeta} + \bar{U} \left. \frac{\partial \psi}{\partial x} \right|_{\zeta} \approx \psi \left. \frac{\partial \bar{U}}{\partial x} \right|_{\zeta}. \quad (4.4.4.9)$$

The continuity equation for the evolution of the thickness D of the ice column is

$$\frac{\partial D}{\partial t} + \vec{\bar{V}}_z \cdot (D \vec{\bar{V}}) = M \quad (4.4.4.10)$$

where M is net of accumulation and ablation, and $\vec{\bar{V}}$ is the column averaged horizontal velocity vector. For the flow line U is only the horizontal velocity component. Since this equation is independent of z (or ζ) the above equation is easily converted to ζ -coordinates for the model described here:

$$\frac{\partial D}{\partial t} + \frac{\partial}{\partial x} (D \bar{U}) = M. \quad (4.4.4.11)$$

By neglecting term $\frac{\partial V}{\partial y}$, the incompressibility equation (4.4.4.1) becomes

$$\left. \frac{\partial U}{\partial x} \right|_z + \left. \frac{\partial W}{\partial z} \right|_z = 0. \quad \text{or} \quad \dot{\epsilon}_x + \dot{\epsilon}_z = 0 \quad (4.4.4.12)$$

Converting it to the ζ -coordinate system, by utilising Equations (4.4.4.4) and (4.4.4.5), yields

$$\left. \frac{\partial U}{\partial x} \right|_{\zeta} + \frac{1}{D} \left(\frac{\partial D}{\partial t} + \frac{\partial U}{\partial \zeta} \frac{\partial}{\partial x} (E - \zeta D) \right) + \frac{\partial \omega}{\partial \zeta} = 0 \quad (4.4.4.13)$$

By introducing the shape function ψ (Equation (4.4.4.7)) and the approximation (4.4.4.9) the above equation becomes

$$\frac{\partial \bar{U}}{\partial x} = -\frac{1}{\psi} \left(\frac{\partial \omega}{\partial \zeta} + \frac{1}{D} \left(\frac{\partial D}{\partial t} + U \frac{\partial D}{\partial x} \right) \right) \quad (4.4.4.14)$$

Expanding $\frac{\partial}{\partial x} (D\bar{U})$ in Equation (4.4.4.11) to $\bar{U} \frac{\partial D}{\partial x} + D \frac{\partial \bar{U}}{\partial x}$ and then substituting for $\frac{\partial \bar{U}}{\partial x}$ from Equation (4.4.4.14):

$$\frac{\partial \omega}{\partial \zeta} = \frac{1}{D} (\psi - 1) \frac{\partial D}{\partial t} - \frac{M\psi}{D} \quad (4.4.4.15)$$

Replacing ζ by $(1-\xi)$ and integrating the above equation from bedrock ($\xi=0$) to the general ξ :

$$\omega = \frac{1}{D} (1 - \zeta - v) \frac{\partial D}{\partial t} + \frac{Mv}{D} \quad (4.4.4.16)$$

where

$$v = \int_0^{\xi} \psi \, d\xi \quad (4.4.4.17)$$

Since the quantity ψ may be computed from a flow law, v is also a determinable function of depth. This expression is particularly useful for steady state modelling where $\partial D / \partial t = 0$.

Once ω is obtained from Equation (4.4.4.16), the vertical velocity W and vertical strain rate $\dot{\epsilon}_z$ can be then computed using Equations (4.4.4.3) and (4.4.4.4).

4.4.5. Balance Flux and Balance Velocity

The balance flux and balance velocity are calculated based on the assumption of a steady state balanced ice sheet and use the of the equation of continuity for a column:

$$\frac{\partial D}{\partial t} + \vec{\nabla} \cdot \vec{F} = M. \quad (4.4.5.1)$$

where D is the ice thickness, \vec{F} the total mass flux and M the net of accumulation and ablation (Budd and Warner, 1996)

Under balance conditions (i.e. steady state) $\frac{\partial D}{\partial t}$ is zero, then the divergence of total mass flux must be equal to the net of accumulation and ablation. The flux divergence (Figure 4.3) is

$$\vec{\nabla} \cdot \vec{F} = \frac{F_{\text{out}} - F_{\text{in}}}{\Delta x} \quad (4.4.5.2)$$

where F_{out} is the total mass outflow from any column of a flow line and F_{in} is the total mass inflow, Δx is the distance between these two columns.

Balance flux can be expressed as:

$$F_{\text{bal}} = F_{\text{in}} + M \cdot \Delta x. \quad (4.4.5.3)$$

The corresponding balance velocity (representing a depth averaged velocity) is then simply F_{bal} / D . Using Equations 4.4.5.1 – 4.4.5.3, the balance velocity is

$$V_{\text{bal}} = \frac{F_{\text{in}} + M \cdot \Delta x}{D} \quad (4.4.5.4)$$

Balance velocities are very useful in their own right. By comparing them with actual measured velocities a direct check can be made on the present state of balance, provided an estimate of the ratio of surface velocity to column average velocity i.e. $\psi(\zeta=0)$ can be made.

4.4.6. Particle Trajectory and Age

Combined with the ages of the ice the trajectories give a clear picture of the history of the ice. The trajectories provide the means of relating the properties of the ice at a certain depth in an ice core to the source region and deposition time of that ice. The age horizons provide one possible interpretation for internal radar echoes and thereby evidence for or against unsteady changes undergone by the ice sheet in the past (Budd and others, 1982).

From the definition of horizontal velocity ($U = \frac{dx}{dt}$) and vertical velocity

($W = \frac{dz}{dt}$) in (x, y, z, t) system, particle trajectories of the ice at the vertical depth below the surface, Z , at a certain distance x_i along the flow line are determined by

$$Z(x_i) = \int_{x_0}^{x_i} \frac{W(x', z(x'))}{U(x', z(x'))} dx', \quad (4.4.6.1)$$

and the corresponding time needed for following the particle trajectory

$$t(x_i, Z(x_i)) = \int_{x_0}^{x_i} \frac{1}{U(x', Z(x'))} dx'. \quad (4.4.6.2)$$

These two equations define the age of the ice anywhere in the ice sheet by following the particle trajectories from the surface.

4.4.7. Evolution of Compressive and Shear Strains

In the model, accumulated compressive strain (ϵ_z) and shear strain (ϵ_{xz}) are calculated following particle trajectories by

$$\epsilon_{xz}(x_i, Z(x_i)) = \int_0^t \dot{\epsilon}_{xz}(x_i, Z(x_i)) dt(x_i, Z(x_i)) = \int_0^{x_i} \frac{\dot{\epsilon}_{xz}(x_i, Z(x_i))}{U(x_i, Z(x_i))} dx. \quad (4.4.7.1)$$

$$\epsilon_z(x_i, Z(x_i)) = \int_0^t \dot{\epsilon}_z(x_i, Z(x_i)) dt(x_i, Z(x_i)) = \int_0^{x_i} \frac{\dot{\epsilon}_z(x_i, Z(x_i))}{U(x_i, Z(x_i))} dx \quad (4.4.7.2)$$

where $Z(x_i)$ is the vertical depth below the surface at a certain distance x_i along the flow line.

Compressive strain calculated from Equation (4.4.7.2) is in fact an *instantaneous* strain (i.e. *natural strain* or *logarithmic strain*). In order to compare with the shear strain, the compressive strain is converted from the natural strain (ϵ_z) to the actual strain (ϵ_z') by (see Section 2.2.2.1)

$$\epsilon_z' = e^{\epsilon_z} - 1. \quad (4.4.7.3)$$

ϵ_z' varies from 0 to 1.

4.4.8. Temperature Distribution

4.4.8.1. Equation of Heat Transfer in ζ -coordinate System

The full equation of heat transfer within an ice sheet (see Appendix I) is

$$\frac{dT}{dt} = \frac{k}{\rho c} \nabla^2 T + \frac{1}{\rho c} \bar{\nabla} k \cdot \bar{\nabla} T + \frac{f}{\rho c} \quad (4.4.8.1)$$

where $\frac{dT}{dt}$ is the change in temperature (T) with time (t) following the motion of ice, k the thermal conductivity, ρ the density of ice, c the specific heat for ice, and f is internal heating assumed to be mainly from shear deformation.

Simplifications made in the above equation include the use of a constant density and the omission of melting and refreezing processes in the variable density firn layer. Furthermore, horizontal conduction in an ice sheet can be disregarded as temperature gradients in the horizontal directions are usually small compared to the vertical gradient (Mavraklis, 1989; 1992), thus ∇T (or $\nabla^2 T$) can safely be replaced by $\frac{\partial T}{\partial z}$ (or $\frac{\partial^2 T}{\partial z^2}$). In addition the thermal conductivity is assumed to be a linear function of temperature, $\frac{\partial k}{\partial T} = k'$, so Equation 4.4.8.1 may be reduced to

$$\frac{dT}{dt} = \frac{k}{\rho c} \frac{\partial^2 T}{\partial z^2} + \frac{1}{\rho c} \frac{\partial k}{\partial T} \left(\frac{\partial T}{\partial z} \right)^2 + \frac{f}{\rho c}. \quad (4.4.8.2)$$

To convert it to the ζ -coordinate system, according to (4.4.1.10) the left hand side becomes

$$\left. \frac{dT}{dt} \right|_z = \left. \frac{\partial T}{\partial t} \right|_{\zeta} + \vec{V} \cdot \vec{\nabla}_{\zeta} T + \omega \frac{\partial T}{\partial \zeta}, \quad (4.4.8.3)$$

where \vec{V} is the horizontal velocity vector $\{U, V\}$ and $\omega = \frac{d\zeta}{dt}$ is the vertical velocity in the ζ -coordinate. Using (4.4.1.4) and (4.4.1.5) the right hand side can be expressed in ζ -coordinate system as

$$\left. \frac{k}{\rho c} \frac{\partial^2 T}{\partial z^2} \right|_z + \left. \frac{1}{\rho c} \frac{\partial k}{\partial T} \left(\frac{\partial T}{\partial z} \right)^2 \right|_z + \left. \frac{f}{\rho c} \right|_z = \frac{1}{D^2} \frac{k}{\rho c} \frac{\partial^2 T}{\partial \zeta^2} + \frac{1}{D^2} \frac{1}{\rho c} \frac{\partial k}{\partial T} \left(\frac{\partial T}{\partial \zeta} \right)^2 + \left. \frac{f}{\rho c} \right|_{\zeta}. \quad (4.4.8.4)$$

The combination of (4.4.8.3) and (4.4.8.4) yields

$$\left. \frac{\partial T}{\partial t} \right|_{\zeta} = \frac{1}{D^2} \frac{k}{\rho c} \frac{\partial^2 T}{\partial \zeta^2} + \frac{1}{D^2} \frac{1}{\rho c} \frac{\partial k}{\partial T} \left(\frac{\partial T}{\partial \zeta} \right)^2 - \vec{V} \cdot \vec{\nabla}_{\zeta} T - \omega \frac{\partial T}{\partial \zeta} + \frac{f}{\rho c}. \quad (4.4.8.5)$$

Considering the steady state ($\partial T / \partial t = 0$), the equation of heat transfer in the ζ -coordinate system used in the model is

$$\frac{1}{D^2} \frac{k}{\rho c} \frac{\partial^2 T}{\partial \zeta^2} + \frac{1}{D^2} \frac{1}{\rho c} \frac{\partial k}{\partial T} \left(\frac{\partial T}{\partial \zeta} \right)^2 - \vec{V} \cdot \vec{\nabla}_{\zeta} T - \omega \frac{\partial T}{\partial \zeta} + \frac{f}{\rho c} = 0 \quad (4.4.8.6)$$

This equation is based on the assumption of steady state temperature ($\partial T / \partial t = 0$) and a steady state ice mass ($\partial D / \partial t = 0$). In this equation, heat transfer is considered to result from vertical diffusion (first and second terms), horizontal and vertical advections (third and fourth terms), and internal deformation heating (fifth term).

4.4.8.2. Boundary Conditions

Two boundary conditions must be specified before equation 4.4.8.6 can be solved.

(1). Upper boundary:

In the model applications (Chapter 6 and Chapter 7), the temperature at the surface along the flow line is taken from observations.

(2). Lower boundary:

(i). Basal heating:

At the base, the ice sheet gains heat from both the geothermal heat flux and sliding friction due to the motion of the column. These heat flux contributions can most easily be incorporated in the basal temperature gradient:

$$\left. \frac{\partial T}{\partial z} \right|_b = \gamma_g + \frac{\tau_b V_s}{k} \quad (4.4.8.7)$$

where γ_g is the geothermal heat flux expressed as a temperature gradient in the basal ice, τ_b is the basal shear stress, V_s the basal sliding velocity and k the thermal conductivity.

(ii). Basal pressure melting point:

At the base, the temperature cannot exceed the pressure melting point. If the temperature is at pressure melting point then either melting or freezing of existing melting water could be occur. In the model, this is treated by the condition that if melting or freezing occurs the base temperature is set to the pressure melting point. The pressure melting point (T_{pmp}) is given by (Paterson, 1994, p212)

$$T_{pmp} = T_0 - \beta' P \quad (4.4.8.8)$$

where $T_0 = 273.16 \text{ K} = 0.01 \text{ }^\circ\text{C}$ is the triple-point temperature of water, $\beta' = 8.7 \times 10^{-4} \text{ K m}^{-1}$ and $P \approx \rho g (E - z)$ is the hydrostatic pressure. This relation varies with the impurity (air) content and properties of the ice (Paterson, 1994; Budd and others, 1982). In the model, using the above relation the pressure melting point is calculated by taking the ice density of 918 kg m^{-3} and the gravitational acceleration of 9.81 ms^{-2} and expressed in the units of $^\circ\text{C}$ as follows:

$$T_{pmp} = -0.00087 (E - z) \quad (4.4.8.9)$$

where E is the surface elevation and z is the vertical coordinate for the ice above the bed in the ice sheet.

4.4.8.3. Solution of the Steady State Equation of Heat Transfer

In this flow line model it is assumed $\dot{\epsilon}_y = 0$ (see section 4.3.1), thus the horizontal advection term ($\vec{V} \cdot \vec{\nabla}_\zeta T$) in Equation 4.4.8.6 will be replaced by $U \frac{\partial T}{\partial x}$, then

Equation 4.4.8.6 can be written in

$$\frac{K}{D^2} \frac{\partial^2 T}{\partial \zeta^2} + \frac{K'}{D^2} \left(\frac{\partial T}{\partial \zeta} \right)^2 - U \frac{\partial T}{\partial x} - \omega \frac{\partial T}{\partial \zeta} + F = 0 \quad (4.4.8.10)$$

where (see Mavrakakis, 1992, appendix 4)

$$\text{specific heat: } c = (2091 + 7.237T) \times 10^{15} \text{ m}^2 \cdot \text{yr}^{-2} \cdot ^\circ\text{C}^{-1}$$

$$\text{density of ice: } \rho = 918 \text{ kg} \cdot \text{m}^{-3}$$

$$\text{thermal conductivity: } k = (700.3 - 3.345T) \times 10^{20} \text{ kg} \cdot \text{m} \cdot \text{yr}^{-3} \cdot ^\circ\text{C}^{-1}$$

$$\text{thermal diffusivity: } K = \frac{k}{\rho c} = 36.27 - 0.3996T \text{ m}^2 \cdot \text{yr}^{-1}$$

$$K' = \frac{1}{\rho c} \frac{\partial k}{\partial T} = -\frac{1}{5.739 + 0.01986T}$$

internal heating f is assumed mainly from shear deformation, so that it can be calculated from shear strain rate ($\dot{\epsilon}_{xz}$) and shear stress (τ_{xz}) as $f = 2 \dot{\epsilon}_{xz} \tau_{xz}$,

$$\text{thus } F = \frac{f}{\rho c} = \frac{2\tau_{xz}\dot{\epsilon}_{xz}}{\rho c}.$$

For any column of ice (except at the ice divide) the temperature distribution can be calculated from Equation 4.4.8.10 by solving the following system linear equation for levels $j=2, N_z-1$:

$$a(T_{j+1} - 2T_j + T_{j-1}) + b(T_{j+1} - T_{j-1}) + cT_j = d \quad (4.4.8.11)$$

where the subscript refers to points in the column: $j=1$ at the ice surface and $j = N_z$ at the bedrock, N_z is the number of vertical levels formed by dividing ice thickness into certain bands (see Section 4.4.1), and

$$a = \frac{K}{(D \Delta \zeta)^2}$$

$$b = \frac{K'}{(2D \Delta\zeta)^2} (T_{j+1} - T_{j-1}) - \frac{\omega}{2\Delta\zeta}$$

$$c = \frac{U}{\Delta x}$$

$$d = -F - \frac{U}{\Delta x} T_j^{\text{upstream}}.$$

The boundary conditions are: (1) at the surface, $T_1 = T_{\text{observation}}$, (2) at the base, with

a known base temperature gradient $\left. \frac{\partial T}{\partial z} \right|_{N_z}$ or the pressure melting temperature as

appropriate. The final equation for the gradient boundary condition, the equation comes from the calculation of the basal temperature gradient using a three-point one-sided difference scheme in the ζ -coordinate:

$$\left. \frac{\partial T}{\partial \zeta} \right|_{N_z} = -D \left. \frac{\partial T}{\partial z} \right|_{N_z} = \frac{3T_{N_z} - 4T_{N_z-1} + T_{N_z-2}}{2\Delta\zeta}. \quad (4.4.8.12)$$

Since K , K' and b are all functions of T , Equations 4.4.8.11-4.4.8.12 form a set of non-linear equations and so an iterative scheme (Appendix II) is used to reach the solutions of the temperature distribution. Because upwind differences for were used the horizontal advection of temperature, the solution of successive temperature profiles down the flow line simply draws on the knowledge of the previously calculated profiles.

Chapter 5

AN ANALYSIS OF ANISOTROPIC ICE FLOW PROPERTIES AT THE DSS BOREHOLE, LAW DOME, ANTARCTICA

5.1. Introduction

An anisotropic ice flow model has been developed in this thesis in Chapter 4. The results from the applications of the model to two different flow lines in East Antarctica will be shown in Chapter 6 and Chapter 7. In this Chapter, the anisotropic ice flow properties at the Dome Summit South (DSS) borehole near the summit of Law Dome, East Antarctica, will be studied by applying this model to one vertical column of ice. DSS is not only the deepest borehole (about 1200 m deep) drilled in Law Dome (see Section 3.2.1) but also one that has complete observations from the borehole along with physical and chemical results from ice core analyses. Based on these detailed data a further study of the ice flow properties at the DSS borehole provides information about the internal dynamics of ice in Law Dome.

The borehole inclination measurements have shown reduced shear strain rates near the bedrock. It has been concluded here that this reduction cannot be entirely accounted for by the change in ice flow properties and therefore is probably due to the combination of both reduced shear stress, as a consequence of the influence of longitudinal stresses and reduced enhancement associated with the change from the strong shear fabrics to ice with fabrics less well aligned for shear. In the

applications of the model to the flow lines (Chapters 6 and 7), we do not know quantitatively how these different processes are responsible for this reduction in strain rate, so we experimented with the model by applying a more gradual “discount” (reduction) directly to the shear strain rates in the lower levels to produce a match to the observed surface velocities. This is because the observed surface velocity varies very smoothly over the domain whereas the ice thickness and bedrock elevations vary greatly. This means that this high variability near the base is accommodated primarily below the high shear zone. In this Chapter a quantitative account of the reduced enhancements and shear stresses near the bed of the borehole are examined.

5.2. Background for the DSS Borehole

5.2.1. Law Dome Summit and DSS Ice Core Drilling

After 20 years of drilling and analysis of ice cores up to 500 m depth in Law Dome, a 1200 m deep ice core - Dome Summit South (DSS) - was drilled at a location 4.6 km South-Southwest of the summit of Dome (Figure 5.1) during 1987-1993 summer seasons by Australia National Antarctic Research Expeditions (ANARE).

The drilling site was selected to give optimum conditions for a detailed study of climatic and other changes which might have occurred over at least the last 25000 years and possible interrelations between those changes. Law Dome Summit is a region of near zero horizontal ice flow where the basal ice has an age now thought to be in excess of 100,000 years. An ice core from the surface to bedrock at Law Dome summit can therefore provide data on the history of the ice sheet and climatic changes over this time period (Hamley and others, 1986; Etheridge, 1990; Morgan and others, 1997).

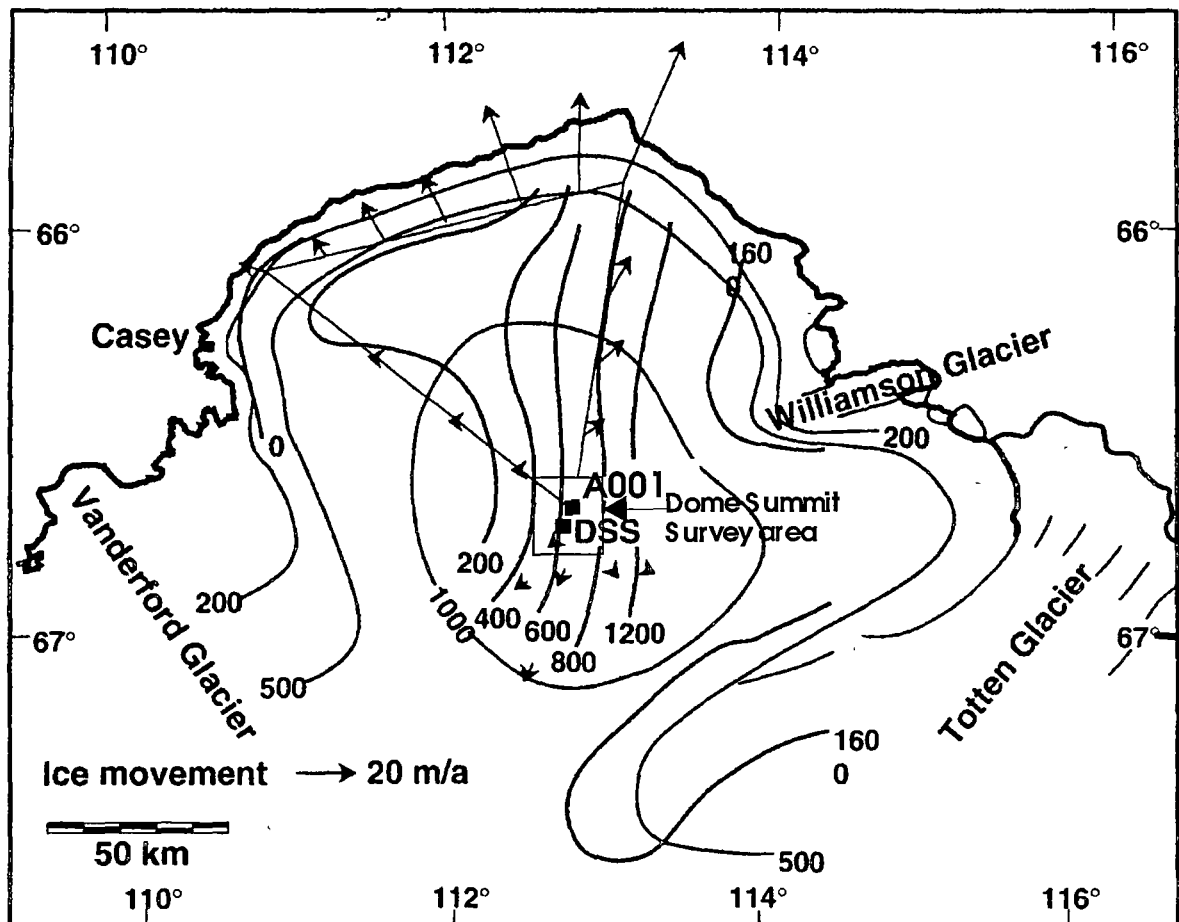


Figure 5.1. Location map of the DSS borehole on Law Dome showing Glaciological data. Surface elevation contours are light lines. Accumulation contours in kg m^{-2} are the heavier lines. Measured surface velocities are indicated by arrows of scale length. The Dome Summit survey grid is centred on A001. (modified from Morgan and others, 1997).

To enable the selection of the DSS drilling site a detailed bedrock and surface topographic survey was conducted over an area of 100 km^2 with 1 km grid spacing centred on A001 at Law Dome summit. The survey grids (Morgan, personal

communication) including later extensive work are shown in Figure 5.2 by the array of small dots (excluding those encircled).

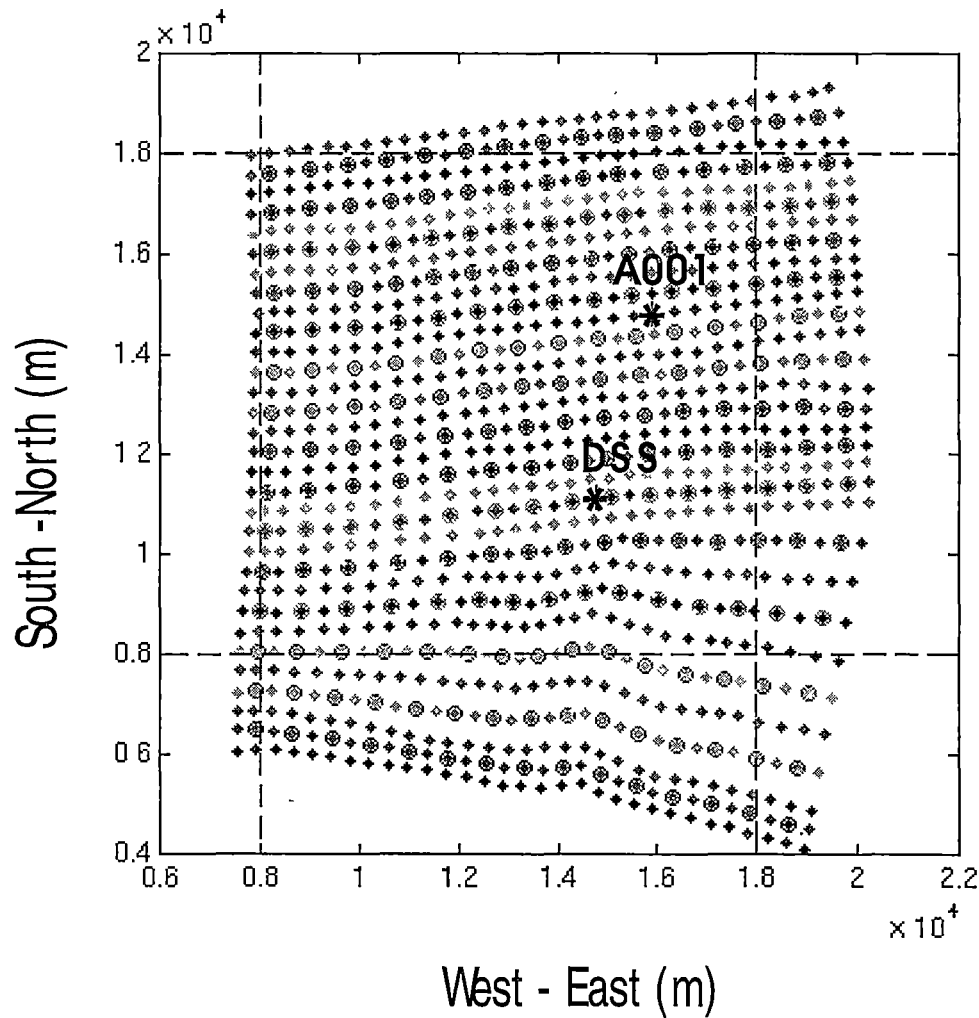


Figure 5.2. The Law Dome Summit survey grid with indications of the Dome Summit A001 and the DSS borehole. (data from Morgan, personal communication).

Here, for the convenience of calculation, the missing points in the survey grids in Figure 5.2 were interpolated from their eight neighbouring points and are indicated in Figure 5.2 by the symbols of dots with a ring. Then the grids within

the dashed line box were further interpolated onto an even spaced grid (north-south - east-west) with 125 m interval grid spacing.

Figure 5.3 shows contour maps of surface elevation (a), bedrock elevation (b), ice thickness (c), surface slope (d) and bedrock slope (e), calculated from on the evenly spaced grids within the dashed line box in Figure 5.2.

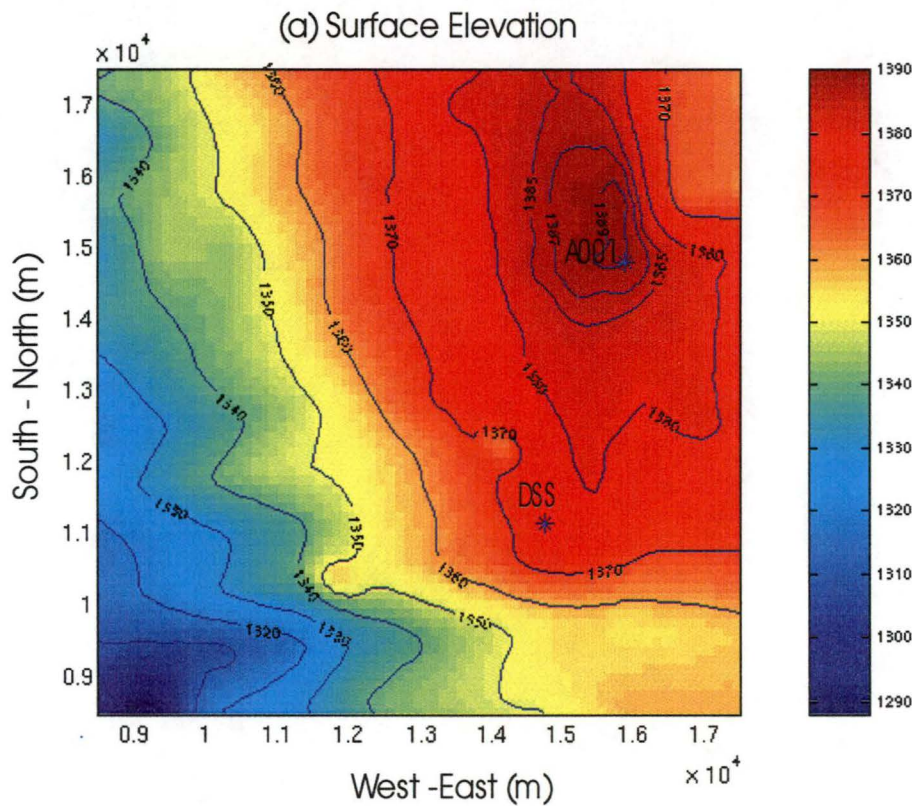


Figure 5.3. The colour maps with contours of surface elevation (a), bedrock elevation (b), ice thickness (c), surface slope (d) and bedrock slope (e), calculated based on the even spacing grids within the dashed line box in Figure 5.2. For (d) and (e), the colour map is in log scale. (re-gridded from data of surface elevation, bedrock elevation and ice thickness from Morgan, personal communication).

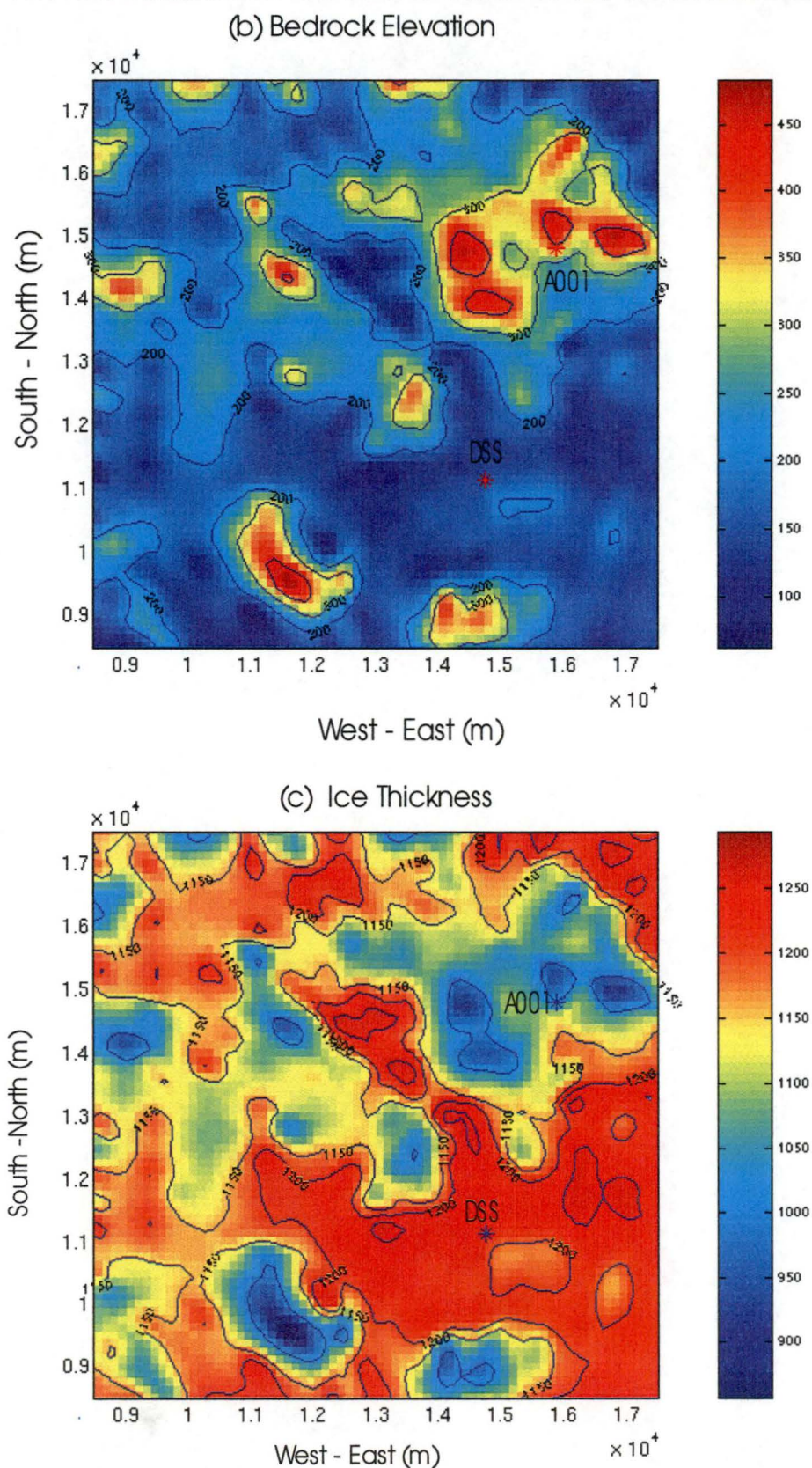


Figure 5.3. (continued)

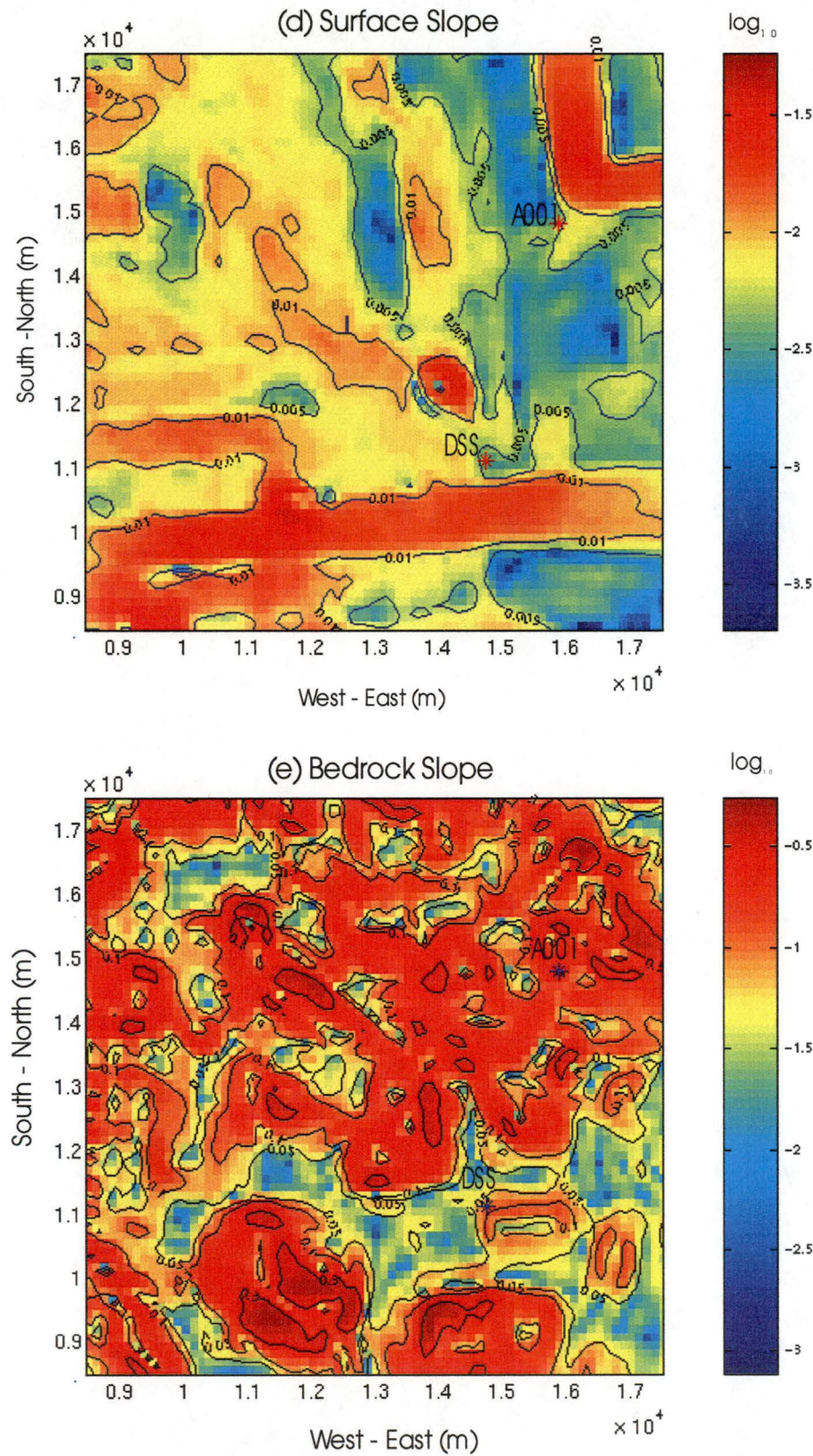


Figure 5.3. (continued)

The flow lines in the Law Dome Summit area (inside of dashed line box in Figure 5.2) were generated (Figure 5.4) on the assumption that ice flows downhill in the direction perpendicular to the surface elevation contours using the more smoothed surface elevation (also shown in Figure 5.4) with the 125 m even spacing grids. Figure 5.4 shows a region of ice flow divergence near the DSS site, indicating that any study of the flow line from the Dome Summit towards the DSS site needs to take transverse flow into account.

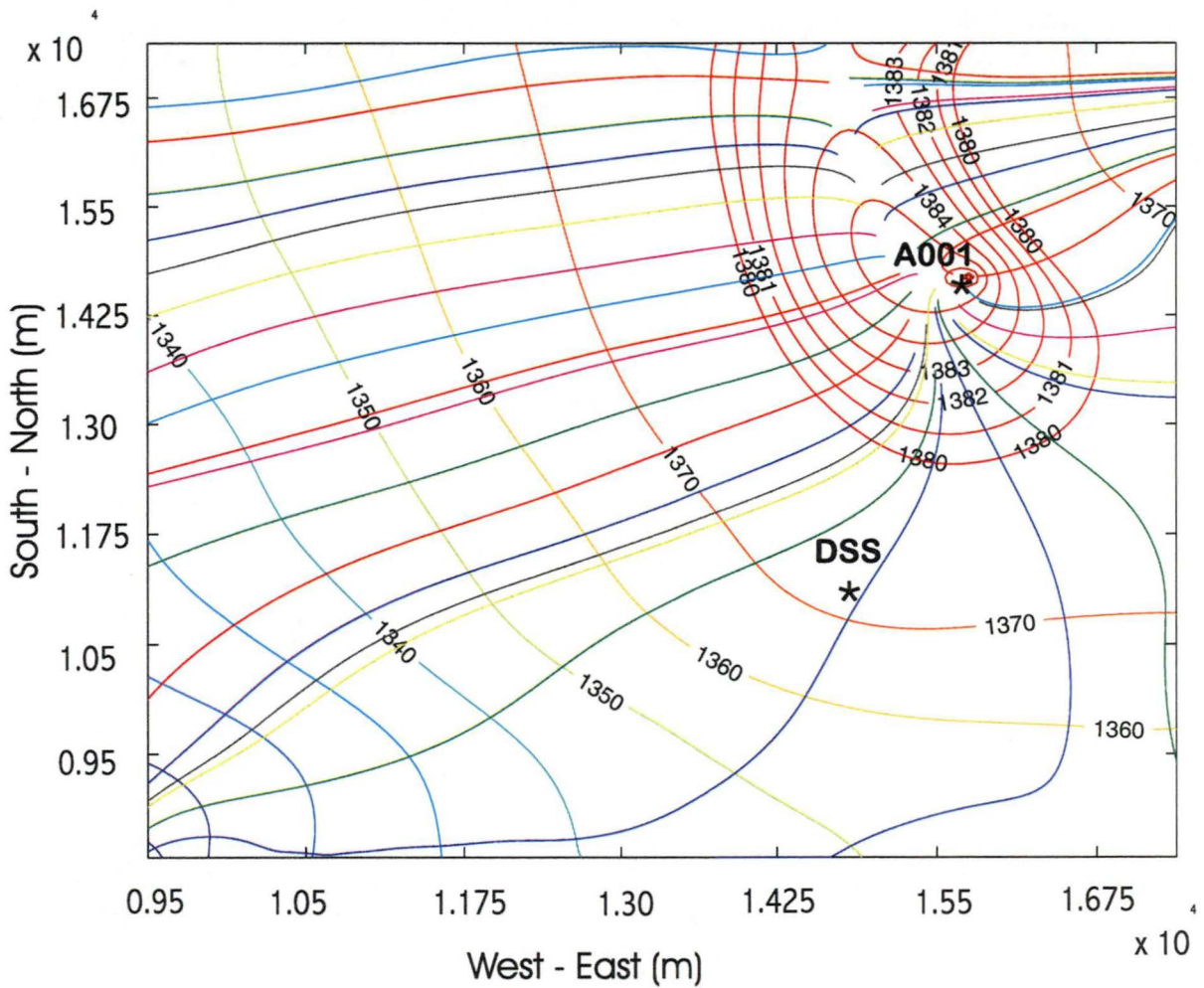


Figure 5.4. The flow lines in the Law Dome Summit area. Also shown are the smoothed surface elevation contours.

The aim of the drilling at DSS was to exploit the special characteristics of Law Dome summit area, i.e. low surface temperature and high accumulation rate near an ice divide, to obtain a high-resolution ice core for climatic/environmental studies of the Holocene and the changes from the Last Glacial Maximum (LGM). Using Radar Echo Sounding (RES) to identify areas where laminar within-ice echoes extended to the greatest depth, the DSS site was selected to be near to the summit (and ice divide) but in an area of relatively level bedrock as shown in Figures 5.5 and 5.6.

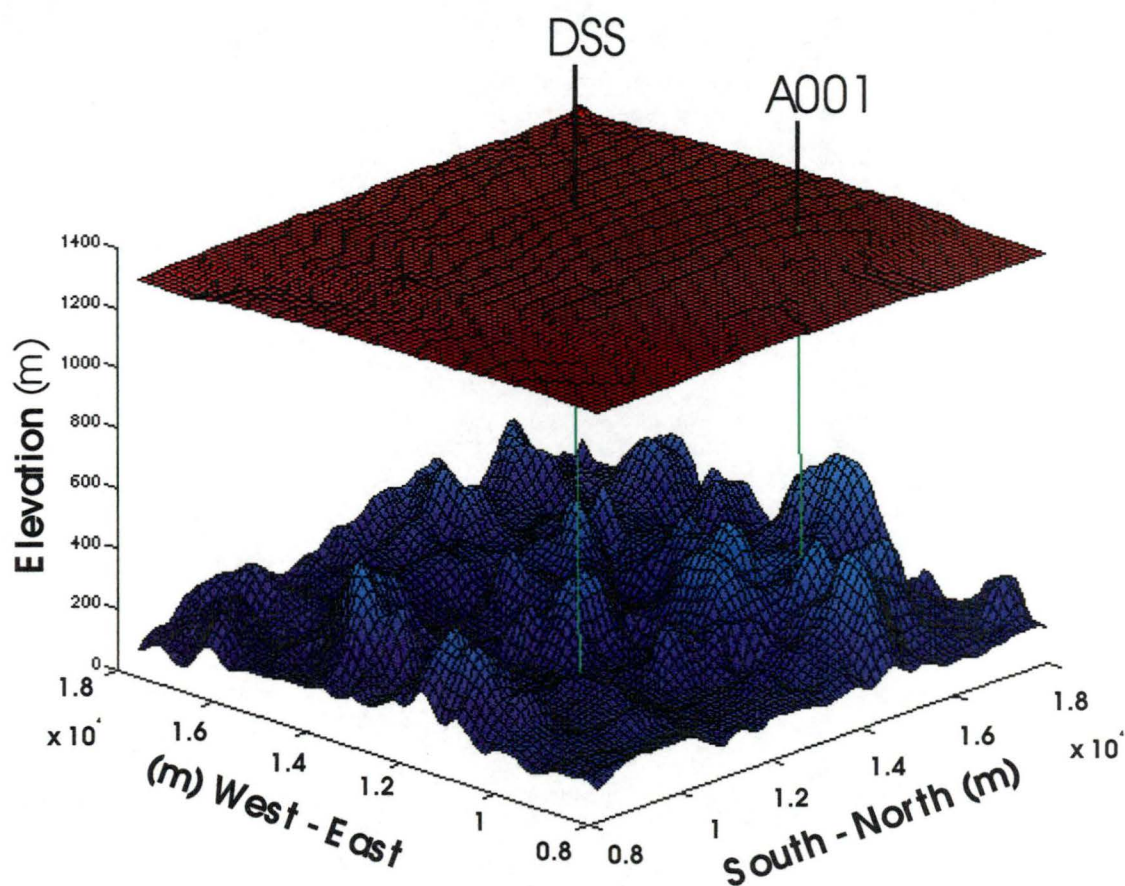


Figure 5.5. A “wire mesh” perspective view of the surface and bedrock topography in the Law Dome Summit area (inside of the dashed line box in Figure 5.2) with locations of the sites of the Dome Summit A001 and the DSS borehole, is drawn based on the evenly spaced grid.

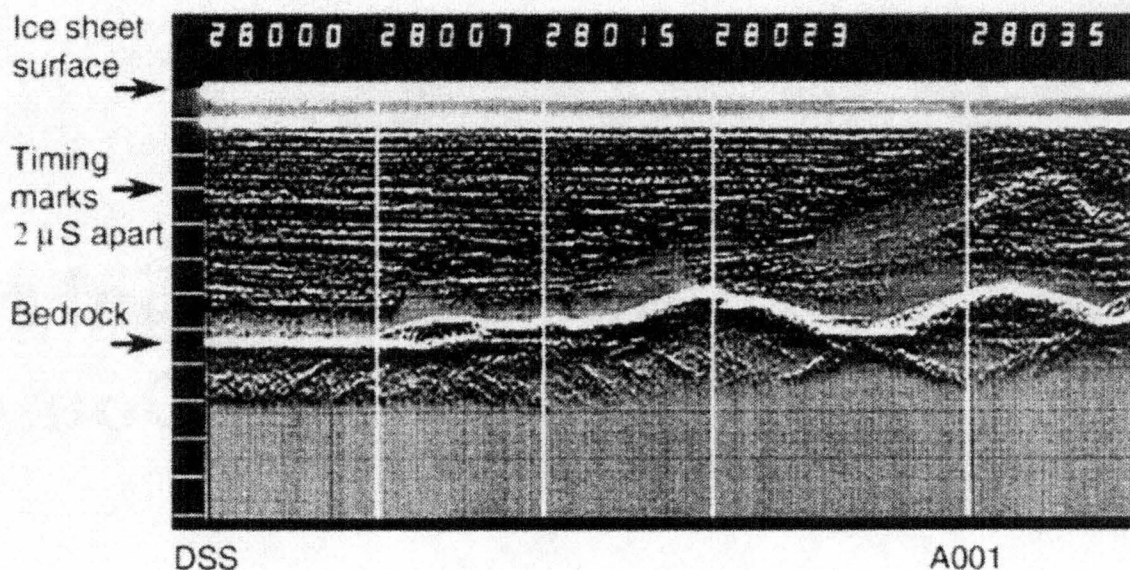


Figure 5.6. Radar Echo Sounding (RES) profile from the DSS borehole on the left going upstream to the Law Dome Summit A001. (from Morgan and others, 1997). Note that the lowest strong internal echo from the R.E.S. corresponds to the maximum shear layer observed in the DSS borehole.

The main ice sheet characteristics at the DSS drilling site relevant to this borehole and core study are summarised in Table 5.1. The depth of ice measured by RES is 1220 m (Morgan and others, 1997). The relatively high surface accumulation rate of 0.69 m yr^{-1} is a mean value over the past 50 years (Morgan and others, 1997). The annual mean surface temperature is -21.8°C and there is no evidence of the occurrence of surface melting in the summer months (Morgan and others, 1997). The temperature at the bottom of the borehole is -6.9°C with a basal temperature gradient in the ice of $0.034^\circ\text{C m}^{-1}$. The values of the local slopes of the surface and the bedrock are taken from Figure 5.3d and Figure 5.3e. The mean values of ice thickness, surface slope and bedrock slope are obtained by averaging points over 11 km of the 1 km spaced grid points (i.e. about 10 times of the ice thickness at DSS) from Figure 5.3.

Table 5.1. *The geographical and physical parameters at the DSS borehole drilling site (modified from Morgan and others, 1997).*

Latitude	66°46'11" S
Longitude	112°48'25" E
Distance from dome summit	4.68 km at 195 °
Surface elevation	1370 m
Ice thickness by RES, (D)	1220 ± 25 m
Mean ice thickness	1174 (averaged over 11 km, ~10D)
Borehole depth	1195.6m below the 1987-88 surface
Depth of LGM	1133 m
Mean annual temperature	-21.8 °C
Temperature at bottom of borehole	-6.9 °C
Borehole basal temperature gradient	0.034 °C m ⁻¹
Mean accumulation rate (last 50 years)	0.69 m yr ⁻¹
Surface velocity (from GPS)	2.04 ± 0.11 m yr ⁻¹
Local surface slope	0.005
Mean surface slope	0.0079 (averaged over 11 km, ~10D)
Local bedrock slope	0.05
Mean bedrock slope	0.062 (averaged over 11 km, ~10D)
Mean wind speed	8.3 m s ⁻¹

5.2.2. Borehole Measurements and Ice Core Studies

Shear strain rates determined by repeated borehole inclination measurement parallel ($\dot{\epsilon}_{xz}$) and normal ($\dot{\epsilon}_{yz}$) to surface flow are shown in Figure 5.7 (a and b) (Morgan and others, 1996). The flow direction (θ) along the entire borehole (Figure 5.7d) and the magnitude of shear strain rates ($\dot{\epsilon}_{\theta}$) in the flow direction as a function of depth (Figure 5.7c) may be calculated from the above two shear strain rate profiles by

$$\theta = \tan^{-1} \left(\frac{\dot{\epsilon}_{yz}}{\dot{\epsilon}_{xz}} \right) \quad (5.2.1)$$

$$\dot{\epsilon}_{\theta} = \sqrt{\dot{\epsilon}_{xz}^2 + \dot{\epsilon}_{yz}^2} . \quad (5.2.2)$$

The borehole temperature profile (Figure 5.7e) was measured at the site (Morgan and others, 1996). The basal temperature gradient in the ice of $0.034 \text{ }^{\circ}\text{C m}^{-1}$ at DSS is obtained.

Figure 5.8 shows some results from ice core studies (Li, 1995; Li and others, 1996; Morgan and others, 1997) which include: (a) mean crystal size, (b) the half-apex angles of the cones containing 25% of the c-axes ($\phi(1/4)$) accompanied by selected fabric diagrams, (c) normalised ratios from fabric analysis (as described below), (d) microparticle concentration (particles with diameters $\geq 0.506 \text{ }\mu\text{m}$ were counted), and (e) the smoothed oxygen isotope ratio with the age scale. C-axis crystal fabrics and crystal size were measured from crystal thin sections (about 100 crystals were measured for each section).

The borehole measurements show that the shear deformation rates are approximately parallel to the surface flow (Figure 5.7a). They increase as expected with the increase in stress and temperature down to 1000 m depth, then decrease to the bedrock presumably with decreasing shear stress due to the blocking of ice flow by surrounding bedrock hills (Figure 5.6). In the lower part of the borehole there is a narrow spike of very high shear which is associated with ice from the LGM (Last Glacial Maximum). This ice has relatively high levels of

dust (Figure 5.8d) and chemical impurities and small crystals (Figure 5.8a) with strong, vertically oriented, single maximum c-axis fabrics (Figure 5.8b).

The ice core studies have shown that in the top 300 m crystal growth is controlled mainly by temperature. Although fabric patterns are generally close to a random distribution in the upper 200 m, a small amount of central tendency is apparent by 300 m. Between the 300 and 1000 m depth crystal growth is characterised by large fluctuations around a general increase in crystal size. Crystal fabrics continue to strengthen, with strong single-maximum patterns forming between 620 and 1000 m. Below 1000 m, crystal size rapidly increases to the bottom of the core, in association with the development of multi-maximum fabric patterns.

As an indication of the fabric development towards girdle and /or single maximum pattern, the normalised ratios R_{20-30} and R_{0-15} have been used as shown in Figure 5.8c for the DSS ice core (Li, personal communication). The ratios R_{20-30} and R_{0-15} are respectively the percentage of the colatitudes within 20-30 and 0-15 degrees of the all measured c-axes normalised by the corresponding values for the randomly distributed fabric. If the fabric develops towards a girdle (or single maximum), the value of R_{20-30} (or R_{0-15}) will increase along with the fabric development. Based on the analysis of crystal orientation fabrics, the evolution of crystal c-axis orientations in the DSS core have been divided into four zones as indicated in Figure 5.8c. This Figure shows that the ice deformation is dominated by compression in the upper part of the borehole while simple shear starts to dominate at about 450 m and continues until about 1000 m. Below 1000 m the fabrics compatible with simple shear (i.e. single maximum pattern) are distorted due to the effect of variable stresses associated with the bedrock topographic.

Oxygen-isotope studies (Figure 5.8e) have shown that the DSS ice core contains 1113 m of Holocene ice, 20 m of LGM/Holocene transition ice, 54 m of ice from the Last Glacial and about 9 m of basal ice (Morgan and others, 1997).

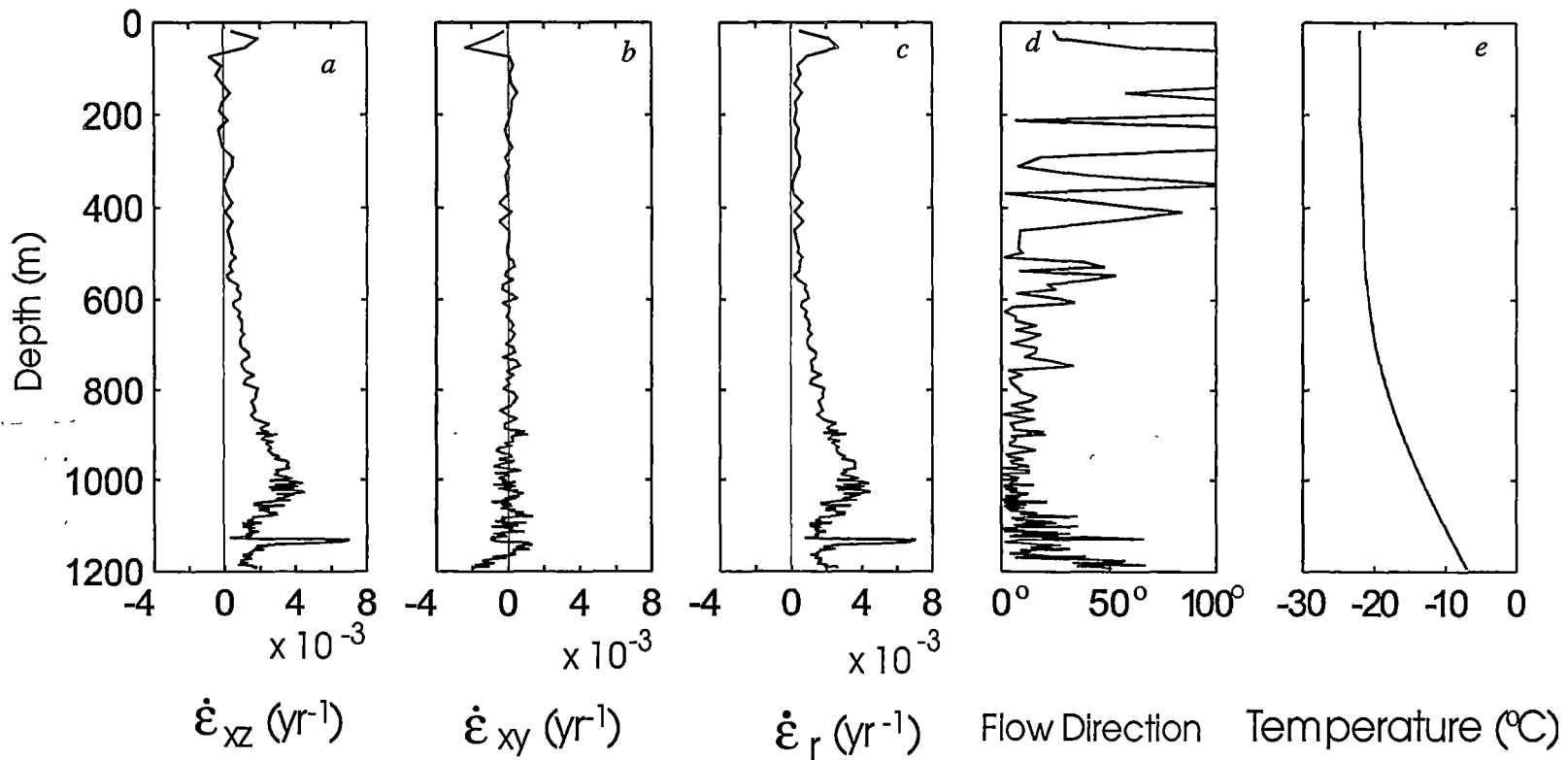


Figure 5.7. The results from the borehole measurements at the DSS borehole
 (b) horizontal shear strain rate normal to surface flow (Morgan and others, 1996);
 (a) horizontal shear strain rate parallel to surface flow (Morgan and others, 1996);
 (c) magnitude of shear strain rates a function of depth calculated from (a) and (b);
 (d) flow direction as a function of depth calculated from (a) and (b);
 (e) measured temperature profile (Morgan and others, 1996).

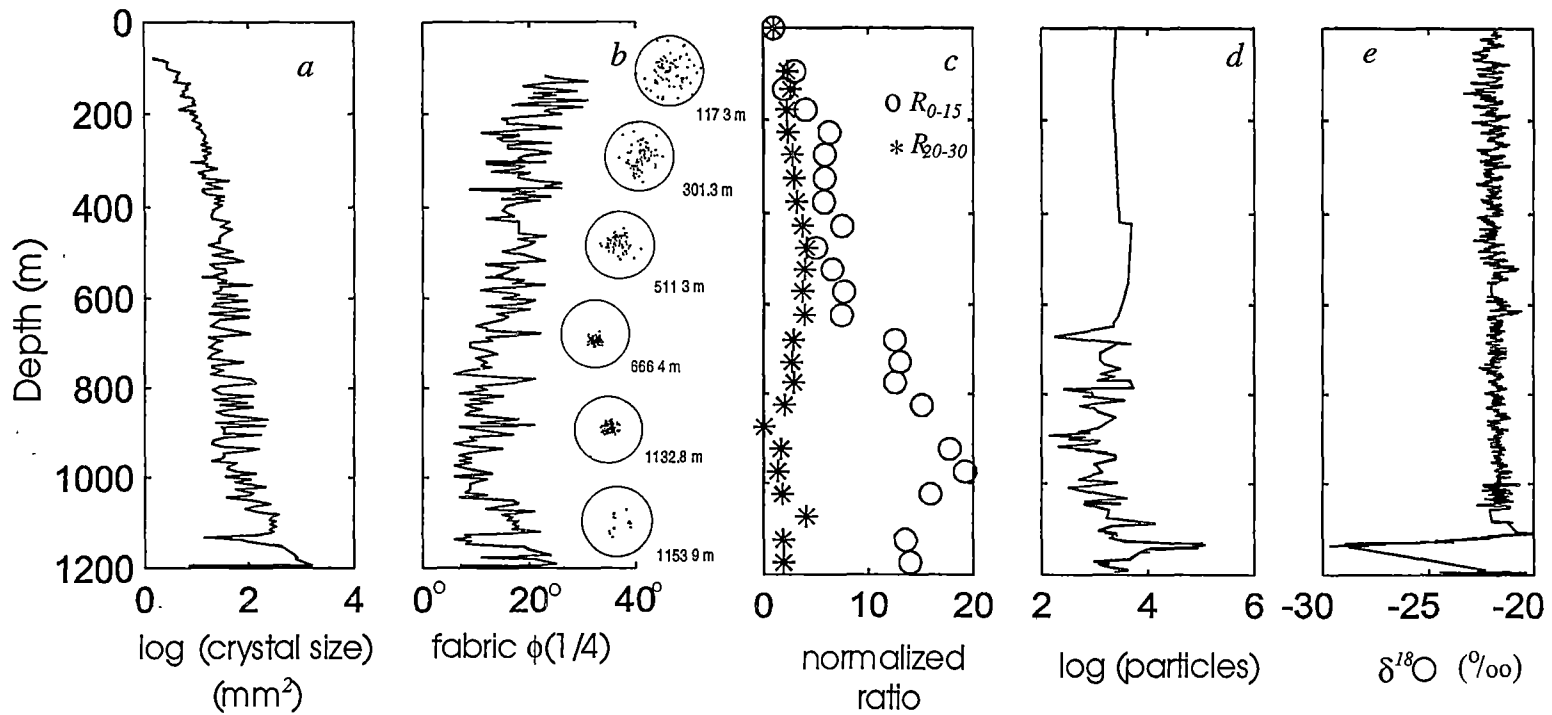


Figure 5.8. The results from the ice core studies at the DSS borehole (Li, 1995; Li and others, 1996; Morga and others, 1997).
 (a) shows the crystal size on a log scale;
 (b) fabric parameter $\phi(1/4)$, the half-apex angles of the cones containing 25% of the c-axes, and selected fabric diagrams;
 (c) the normalised ratios from fabric analysis, ratio R_{20-30} and R_{0-15} are respectively the percentage of the colatitudes within 20-30 and 0-15 degree of the all measured c-axes normalised by the corresponding values for the randomly distributed fabric;
 (d) the particles with diameters greater than $0.506 \mu\text{m}$;
 (e) smoothed oxygen-isotope.

Recently studies on the DSS ice core have also involved the measurements of seasonal cycles of the chemical species for a number of epochs spanning a total of 28 years (Curran and others, 1998). These include the total-dissolvable iron (Edwards and others, 1998), lead isotopes and some selected metals (Rosman and others, 1998). Laboratory studies involving annealing experiments on the DSS ice core samples have been carried out to investigate the relation between crystal size and microparticle variations (Li and others, 1998).

The main results from the ice core and borehole studies which are of interest here are as follows.

There appears to be a systematic variation with depth of the shear rate and ice crystal structure until the depth of the maximum shear rate at about 1 000m. Below that depth the decrease in shear strain rate is associated with a tendency for increased crystal size and a decrease in ice fabric strength favourable for horizontal shear.

The thin layer of high shear rate for the ice from the LGM is associated with a strong vertical single maximum fabric. From the intercomparison study of different ice cores by Wang (1994) it appears that the strong fabric favourable for shear is the main reason for the higher shear rate of this ice rather than the impurity content. However it appears that the preservation of the strong single maximum with small crystals in this layer is due to the retardation of the recrystallisation and crystal growth by the high level of impurities. This LGM layer is very thin and does not contribute greatly to the total shear. Therefore we focus here on the general increase in shear rate down to the maximum shear layer (at just below 1,000 m) and consider a reduction in shear strain rate and shear stress below that depth due to the general influence of large scale bedrock roughness.

5.3. The Model description

The model used here is mainly based on the model described in Chapter 4 and follows the steps as given below:

Step1: Using the measured temperature profile (T , Figure 5.9a) in the DSS borehole and the flow relation (Equation 4.3.2.7 described in Section 4.3.2) of

$$\dot{\epsilon}_{xz}^3 - \frac{2}{3} E(\lambda_c) A_o(T) \tau_{xz}^3 (\dot{\epsilon}_{xz}^2 + \dot{\epsilon}_z^2) = 0, \quad (5.3.1)$$

the shear strain rates for isotropic ice (i.e. $\dot{\epsilon}_{xz}^{iso} = \dot{\epsilon}_{xz}$, shown in Figure 5.9b by the dashed line) are calculated by assuming an enhancement of $E(\lambda_c) = 1$ and shear stress (τ_{xz}) increasing linearly with the depth all the way to the bed as

$$\tau_{xz} = \rho g \alpha Z, \quad (5.3.2)$$

where ρ is the ice density, g the gravity acceleration, α the surface slope and Z the depth of the ice from the surface at the DSS site.

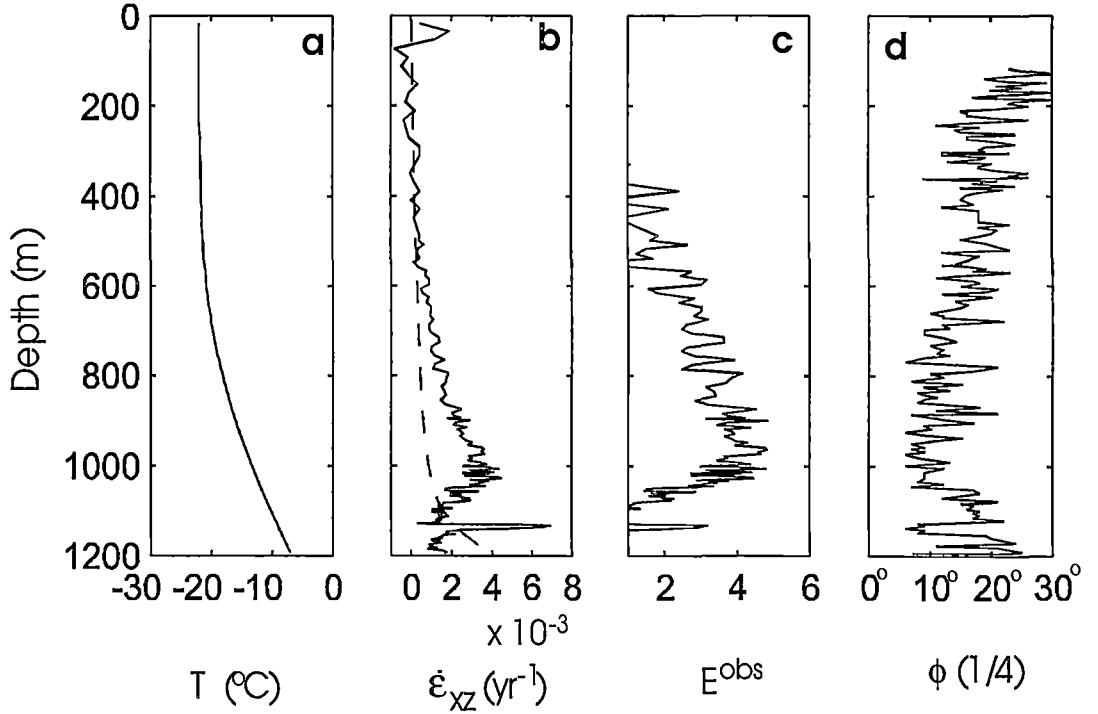


Figure 5.9. The profile of (a) temperature T , (b) shear strain rates $\dot{\epsilon}_{xz}$ (solid line from the observation and dashed line for isotropic ice calculated from the model), (c) enhancement factor E^{obs} and (d) fabric parameter $\phi(1/4)$.

Step2: The ratio of the observed shear strain rates ($\dot{\epsilon}_{xz}^{obs}$, shown in Figure 5.9b by the solid line) to the isotropic shear strain rates ($\dot{\epsilon}_{xz}^{iso}$, shown in Figure 5.9b by the dashed line) determined from **Step1** is calculated as

$$E^{obs} = \frac{\dot{\epsilon}_{xz}^{obs}}{\dot{\epsilon}_{xz}^{iso}}. \quad (5.3.3)$$

Here, E^{obs} is defined as the observed enhancement factor (Figure 5.9c).

This is the procedure followed in the determination of enhancement factors for the other Law Dome bore holes in Chapter 3.

Step3: Comparing the observed enhancement factor (E^{obs}) determined from **Step2** with the measured fabric verticality (ϕ (1/4), Figure 5.9d), Figure 5.10 shows that the enhancement factor increases with the strengthening of fabric verticality, and that for the same fabric verticality the enhancement factor below the maximum value is somewhat lower than that from above the maximum value, which indicates that the supposed linear increase of shear stress with depth overestimated the shear stresses below the depth of maximum enhancement. The enhancement reaches its maximum at about 961 m depth of the borehole which is about 40 m above the layer of maximum shear strain rate. The relationship between enhancement and verticality seen in Figure 5.10 should accordingly be regarded as more reliable above the maximum shear layer.

Step4: The enhancement factors in the lower part of the borehole (below the maximum enhancement) are recalculated, based on the relation between E^{obs} and $\phi(1/4)$ above the maximum enhancement (shown in Figure 5.10 indicated by the circle symbols), using the $\phi(1/4)$ data from Figure 5.9d. This procedure assumes that the fabric verticality remains a suitable guide to enhancement for horizontal shear, and that the variation of the shear stress with depth near the bed is the uncertain quantity.

Step5: The shear stresses below the maximum enhancement are determined by inserting the enhancements (E^{obs}) obtained from the above step and the observed shear strain rates ($\dot{\epsilon}_{xz}^{obs}$) into Equation 5.3.1, showing an

approximately linear reduction from 1003 m (the depth of the maximum shear strain rate) to 1113 m (the depth of LGM) and then nearly constant to the bed (Figure 5.11d in solid line).

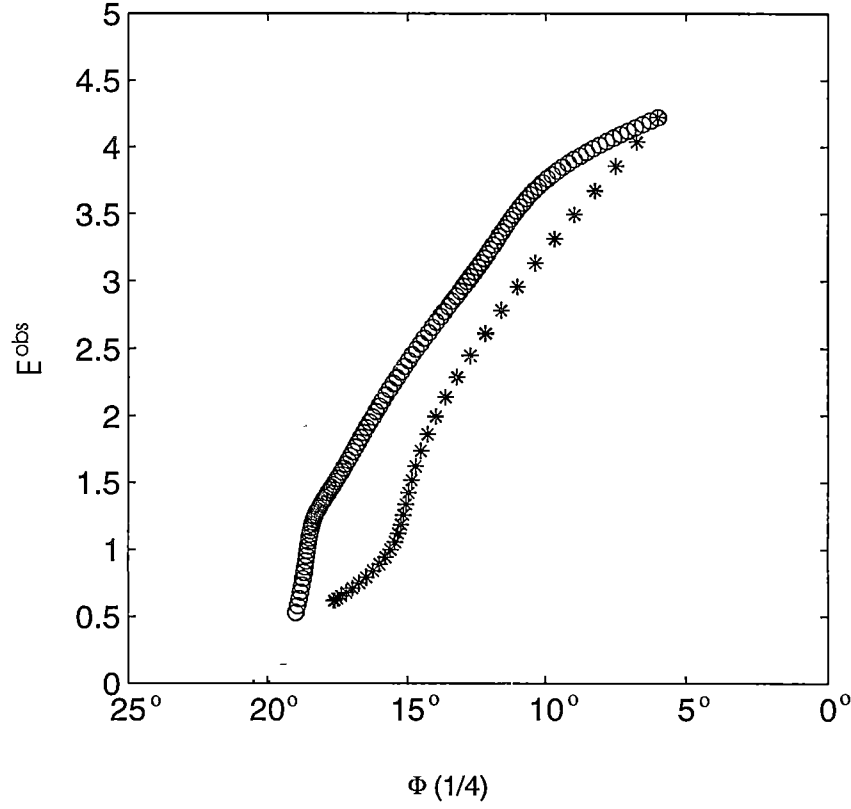


Figure 5.10. The plot of fabric parameter ($\Phi(1/4)$) as a function of the enhancement factor (E), above the maximum shear strain rate (o) and below the maximum shear strain rate (*).

Step6: Using these reduced shear stresses, and the model enhancement function

$$E(\lambda_c) = E_s (E_c/E_s)^{\lambda_c}, \quad (5.3.4)$$

where $E_s=6$ and $E_c=3$, and the compression fraction (λ_c) may be calculated as a function of the compressive ($\dot{\epsilon}_z$) and shear strain rates ($\dot{\epsilon}_{xz}$)

$$\lambda_c = \frac{\dot{\epsilon}_z}{\sqrt{\dot{\epsilon}_{xz}^2 + \dot{\epsilon}_z^2}}, \quad (5.3.5)$$

Equation 5.3.1 is iterated until the strain rate profiles converge (see Section 4.3.3). The calculated enhancement ($E(\lambda_c)$) is shown in Figure 5.11b by the dashed line and the enhanced shear strain rates are shown in Figure 5.11a by the solid thick line. The model enhancement is set to reduce linearly to unity from the depth of maximum E^{obs} to the bottom of borehole. There is a discrepancy between the model enhancement profile of $E(\lambda_c)$ (**Step6**) and the enhancement profile calculated as the ratio of the observed shear strain rate to the isotropic model shear strain rate (**Step2**). This discrepancy occurs because while both calculations use the same applied shear stress, the octahedral shear stress in the model calculations is a function of that stress, and the shear and compressive strain rates (see Section 4.3.2). The present calculations use a compressive strain-rate determined by the shape function method outlined in Section 4.4.4. The octahedral shear stress is involved in the iterative process for the calculation of enhancement, and accordingly the value in the model with enhancement differs from that of the isotropic model in regions where the compressive strain-rates cannot be neglected relative to the shear strain rates. The intention of the full model is to represent the response of anisotropic flow to the actual in situ stresses, as an enhancement over the minimum strain rates for isotropic ice under those same stresses. Clearly the estimate of the “enhancement factor” using the model with $E=1$ (**Step 2**) involves a complicating effect from overestimation of the compressive contribution to the octahedral stress. Based on the definition of the enhancement factor in the laboratory experiments as the ratio of the tertiary strain rate (anisotropic ice) to the minimum strain rate (isotropic ice) at the same temperature and stresses, a “comparable” enhancement factor ($E(\lambda_c)^{com}$) corresponding to E^{obs} can be calculated by taking out the effect of the changed octahedral shear stresses:

$$E(\lambda_c)^{com} = E(\lambda_c) \left(\frac{\tau_o^{aniso}}{\tau_o^{iso}} \right)^2 \quad (5.3.6)$$

where τ_o^{aniso} and τ_o^{iso} here denote octahedral shear stresses calculated for anisotropic ice flow (i.e. at the end of **Step 6**) and for the notional isotropic ice of (**Step 2**), respectively, at the same temperature conditions.

$E(\lambda_c)^{com}$ is indicated by the dotted line in Figure 5.11b and generally agrees with E^{obs} , although E^{obs} is somewhat larger than the expected $E(\lambda_c)^{com}$ over the interval where the strain-rates are comparable, between about 600 and 800 metres depth.

5.4. Results from the Model

The results from the model are summarised in Figure 5.11.

The shear strain rate profile computed from the model using laboratory determined rheology shows close agreement with the observations from the borehole (Figure 5.11a). When the enhancements start to reduce near the bed at the depth of 961 m the shear strain rate continues to increase with the increased shear stress and temperature until reaching its maximum (at 1003 m depth) where the shear stress starts to reduce. Below the depth of its maximum value the shear strain rates reduces under the combination of increased temperature with reduced shear stress and enhancement.

The base temperature at DSS is -6.9°C , which indicates that no significant basal sliding can be expected over the bedrock, so the integration of the shear strain rate over the ice column yields the horizontal velocity at the surface (see Section 4.5.3). The computed surface velocity (Figure 5.11c) of 2.2 m yr^{-1} is considered to be consistent with the value of $1.98 \pm 0.03 \text{ m yr}^{-1}$ obtained from the integration of the measured shear strain rate over the borehole depth and with the value of $2.04 \pm 0.11 \text{ m yr}^{-1}$ obtained by repeated GPS measurements at a surface marker.

The ratio of the depth-averaged velocity to the surface velocity is calculated from the model to be 0.73 which is close to the value of 0.74 determined from the borehole velocity measurements by Morgan and others, 1998, and their value of 0.76 calculated by assuming the local ice sheet is in mass balance (based on data

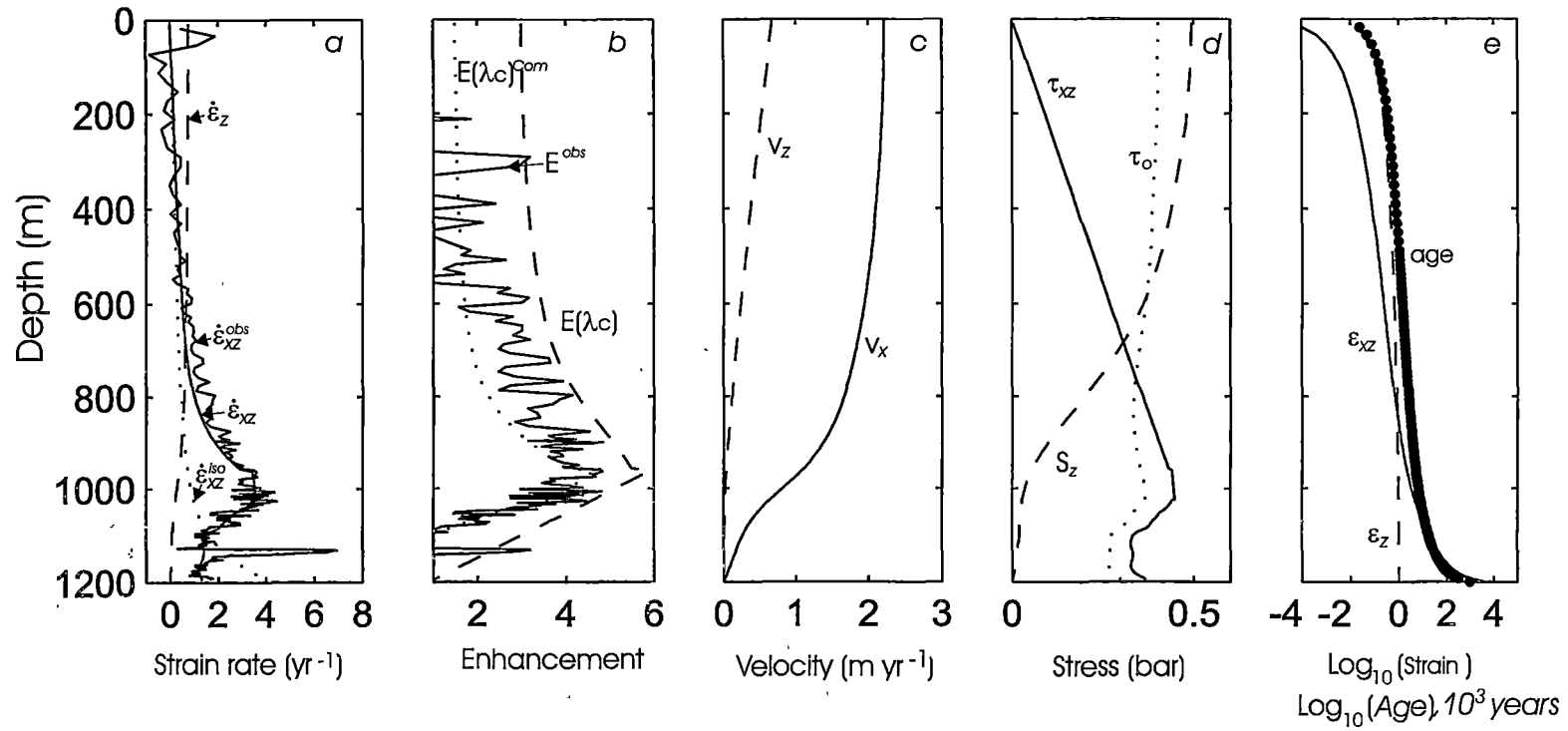


Figure 5.11. Results from the model.

- (a) the shear strain rates from the observation ($\dot{\epsilon}_{xz}^{obs}$), from the model for isotropic ice ($\dot{\epsilon}_{xz}^{iso}$) and anisotropic ice ($\dot{\epsilon}_{xz}$), and vertical compressive strain rate ($\dot{\epsilon}_z$);
- (b) enhancement calculated from observation (E^{obs}) and from the model ($E(\lambda c)$ and $E(\lambda c)^{com}$);
- (c) horizontal velocity (V_x) and vertical velocity (V_z);
- (d) shear stress (τ_{xz}), compression stress deviator (S_z) and octahedral shear stress (τ_o);
- (e) shear strain (ϵ_{xz}), compressive strain (ϵ_z) and the age in 10^3 years.

from long-term surface-elevation observations) and matching the surface accumulation rate (averaged over the last ~50 years) with the outflow around DSS determined by surface strain rate data. The ratio of the depth-averaged velocity to the surface velocity represents the relationship between the column-integrated ice flux and measurements of the ice sheet thickness and surface velocity.

To determine the state of ice sheet balance from the ice accumulation distributions and ice sheet surface topography this relationship must be considered (Budd and Warner, 1996; Wang and Warner, 1998). In areas where ice sliding can be neglected this ratio strongly reflects the rheological properties of the ice and depends on the shear strain-rate profile through the ice column, which is influenced by the profiles of stress, temperature and ice crystal fabrics (Wang and Warner, 1998) and may be strongly affected by the large scale bedrock roughness. Comparing these values with the value of 0.8 for a cubic flow law with isothermal isotropic ice (see Paterson, 1994, p.251-252), at DSS the value of 0.73 is significantly smaller. This probably involves the reduced basal shear stresses near the bed and the distortion of the fabrics, and is also complicated by the added questions of flow within a few ice thicknesses of the Dome Summit as well as the influence of quite rough bedrock topography upstream of the drilling site (see Figures 5.5 and 6).

The compressive and shear strains, and ice age are also calculated in the model and are shown in Figure 5.11e. Because the low velocities and strain rates in the basal layers, the ice at the bottom of the DSS borehole has been computed to have undergone large strains (about 10^6 % shear strain) and is approaching 10^6 years old. This model however assumes steady state and for such long times the non-steady state variations associated with the ice age cycles would need to be taken into account.

5.5. Summary

The ice flow properties at the DSS borehole have been studied in this Chapter from a combination of data including the analysis of the ice cores and observed

shear rates measured in the boreholes. The shear strain rate profile from the model based on laboratory rheology for anisotropic ice under combined compression and shear provides reasonable agreement with the observations.

In this application it was possible to argue for separate reduced enhancements and reduced shear stresses below the high shear layer, by combining the model of anisotropic flow enhancement with information about the crystal fabrics. Without such information the question of describing the flow in basal layers is more problematic, as will be seen in the application of the model of anisotropic flow enhancement to a flow line in the next Chapter.

The model presents a quantitative scheme for separating reduced enhancements and shear stresses below the high shear layer near the bed of the borehole.

We can see from Equations (5.3.1) and (5.3.2) that the results from the model are sensitive to the surface slope of the ice sheet because the shear strain rate is calculated as the third power of the surface slope. The observed surface velocity places some constraint on the effect of uncertainty in the surface slope. The relative depth profiles of the strain-rate and enhancement would not be as greatly affected by that uncertainty. In this Chapter the surface slope is chosen as a local value. The use of mean values of surface slope and ice thickness, representative of several ice thicknesses, averaged over a range of flow line scales from the Dome Summit towards and well beyond the DSS site, should also be studied for comparison.

Chapter 6

APPLICATION OF THE MODEL TO A FLOW LINE IN LAW DOME, ANTARCTICA

6.1. Introduction

The model described in Chapter 4 is applied to the Law Dome ice cap in East Antarctica along a transect from the summit to Cape Folger (see Figure 3.5), which has been the location of extensive fieldwork, and where considerable data for model inputs and for model verification are available. In particular the results from the model can be compared with the observations presented in Chapter 3 from boreholes previously drilled along this line. The calculated strain rates using the rheology model based on the laboratory studies, which includes anisotropic ice from the ice cores, agree well with strain rates determined from the borehole inclination measurements, particularly in the upper portion of the ice sheet to the maximum shear layer.

The appropriate spatial scales for smoothing the bedrock deserve further examination. Even using the envelope bedrock if it were assumed that the shear stresses continue to increase all the way to the bed we obtain surface ice velocities which are on average about 20 times larger than observed, indicating that there is a need for both the enhancement of the shear flow and the shear stress to decrease (on average) in the lower layers giving rise to a maximum shear layer at some height above the average bed. This agrees with all those borehole inclination measurements from Law Dome which reach near to the bed, but is contrary to the usual assumptions made in most simple ice sheet model formulations. However it

is also a feature seen from finite element analysis of ice flow over rough bedrock (with longitudinal stresses included) for a small portion of this flow line on Law Dome by Budd and Rowden-Rich (1985) and Budd and Jacka (1989) (see Section 6.3). In this chapter, as discussed below, this phenomenon is highlighted by simply, in the first instance, halting the vertical integrations of shear strain rate at such a depth that the flow model reproduces the observed horizontal surface velocity. Below this “rheological depth” the shear strain rate is artificially set to zero. While this is obviously an extreme and unphysical procedure, it is interesting to observe the consistency with which this depth, and the corresponding exaggerated maximum shear layer follow the envelope bedrock. Other prescriptions for a more gradual reduction in strain rates in the lower regions of the ice sheet were also examined. If an empirical prescription of sufficient generality could be devised then it can be used to calculate ice velocities throughout the Antarctic ice sheet. More extensive work, involving a wider range of ice thicknesses and temperature regimes than encountered in the present study would be required to attempt such a prescription. The application of the approach to the larger scale for the I.A.G.P flow line inland of Law Dome is described in Chapter 7.

6.2. Model Input Data

In this chapter the ice flow line model described in chapter 4 is applied to the traverse line from the summit of Law Dome to Cape Folger. This traverse line is approximately along an ice surface flow line but the ice flow direction does diverge significantly from the line along the route, primarily to the west of the traverse line direction (see Figure 3.5). The input data - surface and bedrock elevations, surface accumulation rate, surface horizontal velocity and surface temperature – used in the modelling study are shown in Figure 6.1. They are taken from the observations tabulated by Carter (1976), McLaren (1968) and Pfitzner (1980). Comparison of surface velocity measurements and borehole inclination measurements near the margin of the ice cap at BHC1 and BHC2, where the ice is relatively thin, (Etheridge, 1989) reveals that approximately half the ice motion there is due to basal sliding. These measurements have been extrapolated to

estimate the generally small sliding contribution to surface velocities along the flow line using a simple model for basal sliding velocity (see Section 4.4.3.2). This contribution is shown by the dashed curve in Figure 6.1c.

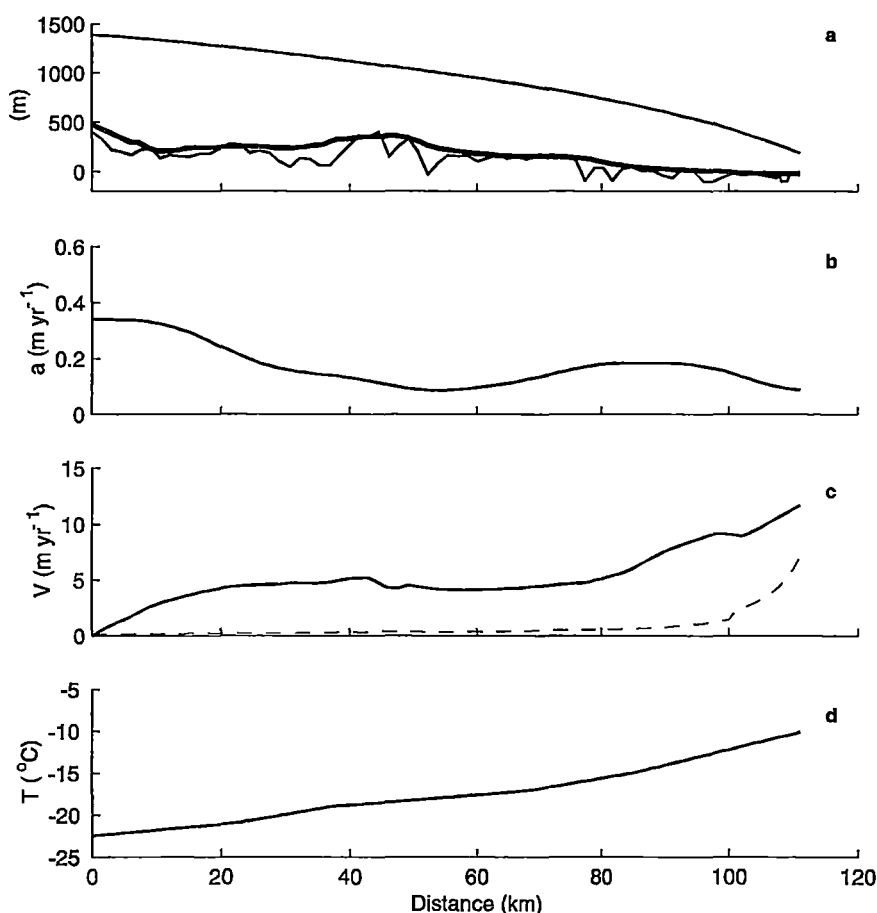


Figure 6.1. The model input data for the Law Dome flow line. (a) surface and bedrock elevation (thin lines), thick line is the envelope bed used in the model, (b) surface accumulation, (c) surface horizontal velocity (solid line) and basal sliding velocity (dashed line), and (d) surface temperature. (Carter, 1976; McLaren, 1968; Pfitzner, 1980).

All input data are interpolated so that the horizontal resolution is 1 km in the model. Vertical resolution is taken by dividing the ice thickness into 100 evenly spaced bands by use of the relative thickness coordinate.

Based on the observations from the borehole temperature profiles, a constant geothermal heat flux in the ice of 0.035 K m^{-1} (γ_g) is taken for the calculation of the basal temperature gradient in the model (Section 4.4.8.2) in the absence of basal melting and to compute the heat flux to the base of the ice when basal melting occurs. This value is equivalent to a geothermal heat flux of about 78 mWm^{-2} . Although this may be thought to be on the high side sensitivity studies have been carried out with lower values of geothermal flux but they do not give as close matches to the observed temperature profiles. It is recognised that the temperature gradient in the bedrock varies regionally and at this stage we do not have enough regional geothermal heat flux data to constrain the model values more precisely.

The enhancement factor calculated as a function of compression fraction, $E(\lambda_c)$ (Section 4.3.2.1), in the flow relations is taken to vary from 3 (i.e. $E_c=3$) near the top of ice sheet to 6 (i.e. $E_s=6$) with increasing depth of ice. As discussed in Section 4.3.2.1 these values differ from the values from the laboratory ice deformation experiments, but are consistent with the enhancement factors seen in the analyses of shear strain rates from boreholes on Law Dome in Chapters 3 and 5, and they also emerge as appropriate to the modelling in the present chapter.

The vertical strain-rates and velocities can be calculated directly from the longitudinal strain rates (Section 4.4.4a), but for this study the approximation based on steady state was used which relates them, through continuity, to the surface accumulation rate, the horizontal gradient of surface velocity, the ice sheet geometry and the shape of the depth profile of horizontal velocity at each location (Section 4.4.4b).

6.3. Treatment of Basal Layers

The discussions of both the enhancement factors in Chapter 3 and Chapter 5 showed that using ice rheology directly based on measurements forces us to address the nature of the ice flow near the bedrock. In this chapter the concept of an envelope topography, smoothing over the higher frequency bedrock roughness is used. This is based on observations, from bore-holes and radar echo sounding,

showing relatively smooth high shear layers over rough bedrock features. This smoothing is also intended to compensate for the neglect of variations in longitudinal stresses in the spirit of the shallow ice approximation.

A variety of explanations have been proposed for the discontinuities in dielectric permittivity that produce the strong internal echoes observed in radio echo soundings of ice sheets. These mechanisms include synchronous origins, such as deposits of impurities or density variations caused by surface processes, and dynamical causes such as crystal orientation fabrics, or crystal sizes (see, for example, Fujita and Mae, 1994). In shallower ice sheets the elongation of air bubbles in high shear zones also appears to cause internal reflections. During 1967 sub-surface echoes were observed (Figure 6.2) along the line treated in the present Chapter, at between 250 and approximately 400 metres depth (Carter 1976).

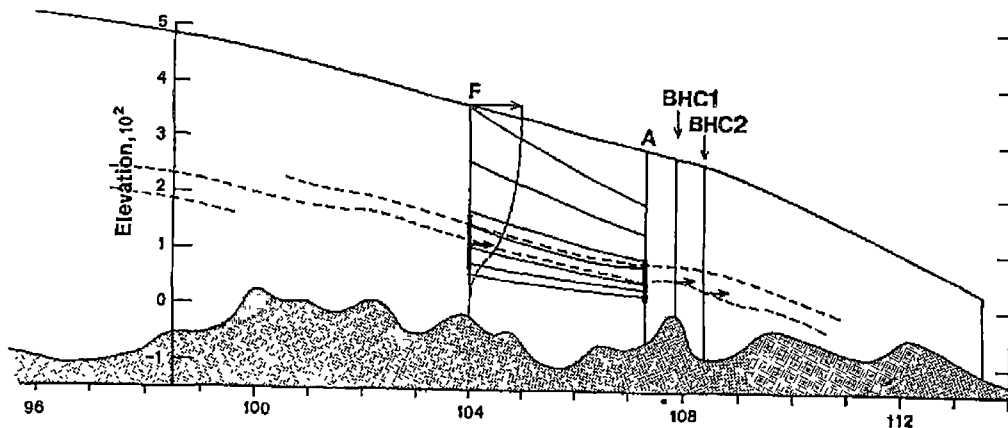


Figure 6.2. Surface and bedrock of the coastal end of the Dome – Folger line from Carter's approximately 0.25 km spacing data. The section is in the general direction of the flow and the approximate position of the boreholes on the line are shown: F, A, BHC1, BHC2. The dashed lines indicate the subsurface echoes observed by Carter (1967). Several lines from F to A are shown joining similar $\delta^{18}O$ isotope ratios at F and A. The thicker parts of the vertical lines in A and F indicate the zone of strong vertical c-axis concentrations. (from Budd and Rowden-Rich, 1985).

Correlations between these reflections and the shear strain rate profiles from boreholes near the margin of the ice cap, together with related ice dynamics modelling by Budd and Rowden-Rich (1985), (the latter is summarised in Budd and Jacka, 1989) suggests an identification with crystallographic causes, associated with a

zone of high shear. Comparison of Oxygen isotope profiles from the corresponding ice cores (Morgan and McCray, 1985) with the reflections observed by Carter (1976) indicates that in Law Dome internal reflections do not necessarily mark isochrones.

Strong reflections deep in ice sheets, above a reflection-free zone near the bedrock, are commonly seen in radar echo sounding, and are frequently suggestive of a smooth envelope over the bedrock. Fujita and others (1999) comment on the sharp transition from strong echoes which they identify with (shear) crystal orientation fabrics, overlying an echo-free basal region in studies carried out along the traverse line from Syowa station to Dome Fuji in East Antarctica.

Using the model presented in Chapter 4, the integration of the shear strain rates right down to the bedrock on Law Dome gives surface velocities much higher than the observed values shown in Figure 6.1c. This problem arises even though the shear strain rates agree well with the bore-hole inclination rates in the upper part of the ice sheet. This occurred even though the bedrock data had been replaced with a smoothed envelope topography, in anticipation of complications with the flow in the regions near the base of the ice sheet. The bedrock data were smoothed using a running mean over fifteen points (i.e. 15 km) and then adding one standard deviation of the bedrock elevation data to produce the enveloping effect. Minor tidying up was done over remaining high points. The smoothed bed is shown in Figure 6.1a by the thicker line. It should be noted that for an envelope of one standard deviation above the mean bed about one third of the above average unsmoothed points may be expected to reach above the envelope. The first and simplest response to this problem was simply to terminate the depth integration of shear strain rate at a level z_c above the bedrock, to match the observed surface velocities.

This sharp cut-off in strain rate is clearly an over-simplification, but several of the borehole inclination measurements have shown strongly reduced shear strain rates near the bedrock and maximum values of shear strain rate well above the bedrock at those locations, for example, the BHC1 and BHC2 boreholes (Figure 3.8c-d) and the DSS borehole (Figure 5.7a). As discussed in Chapter 3 this reduction is

probably due to a combination of both reduced shear stress as a consequence of the influence of longitudinal stresses (from obstruction by the higher points), and also reduced enhancement, since the strong shear fabrics in the ice cores change to large crystal multi-maximum ice with flow rates comparable to that of the random orientation ice (Russell-Head and Budd, 1979).

A 2-dimensional finite element analysis by Budd and Rowden-Rich (1985) using the isotropic flow law for a section (30 km) of the Law Dome flow line gives an illustration of the strong impact that basal irregularities can have on the stress distribution as showing the illustration from the review of Budd and Jacka (1989) presented in Figure 6.3.

The analysis was first carried out for an isotropic flow relation for ice giving the results shown in Figure 6.3a for the variation of shear stress. The bands of high shear stress could be expected to give rise to the variations in crystal anisotropy, as observed in ice from all the boreholes (Budd and Jacka, 1989, P.135).

In the investigation of the DSS borehole in Chapter 5 the detailed crystallographic measurements provided possible scheme to disentangle reduced shear stress and enhancement. In an ice sheet we generally do not know quantitatively how these different processes combine to produce the reduction in the shear strain rate. Instead, the application of a more gradual “discount” was made directly to the shear strain rates in the lower levels below the maximum shear layer. A substantial reduction in strain rates in the lower levels of the ice sheet is required to produce agreement with the observed surface velocities, compared to the simple model expectations of steadily increasing shear stress and increasing ice temperatures with depth. Such large reductions in strain rate below the maximum are also seen in the shear strain rate profiles for BHC1 and BHC2, but with considerable variability. Such high variability will be ignored for the simple approach used here. Commencing at a depth z_d the strain rates given by the model were multiplied by functions which decreased monotonically from unity at z_d , reaching 0.01 at the bedrock and the “discount depth” z_d was adjusted in each column to produce a match to the observed surface velocities. This appeared to be a reasonably simple way in which we could adjust the computed velocities to match observations without modifying the ice rheology model which also

included ice from these Law Dome ice cores. These treatments typically produce strain rate profiles with a band of high shear above the bedrock, which can be compared with observations.

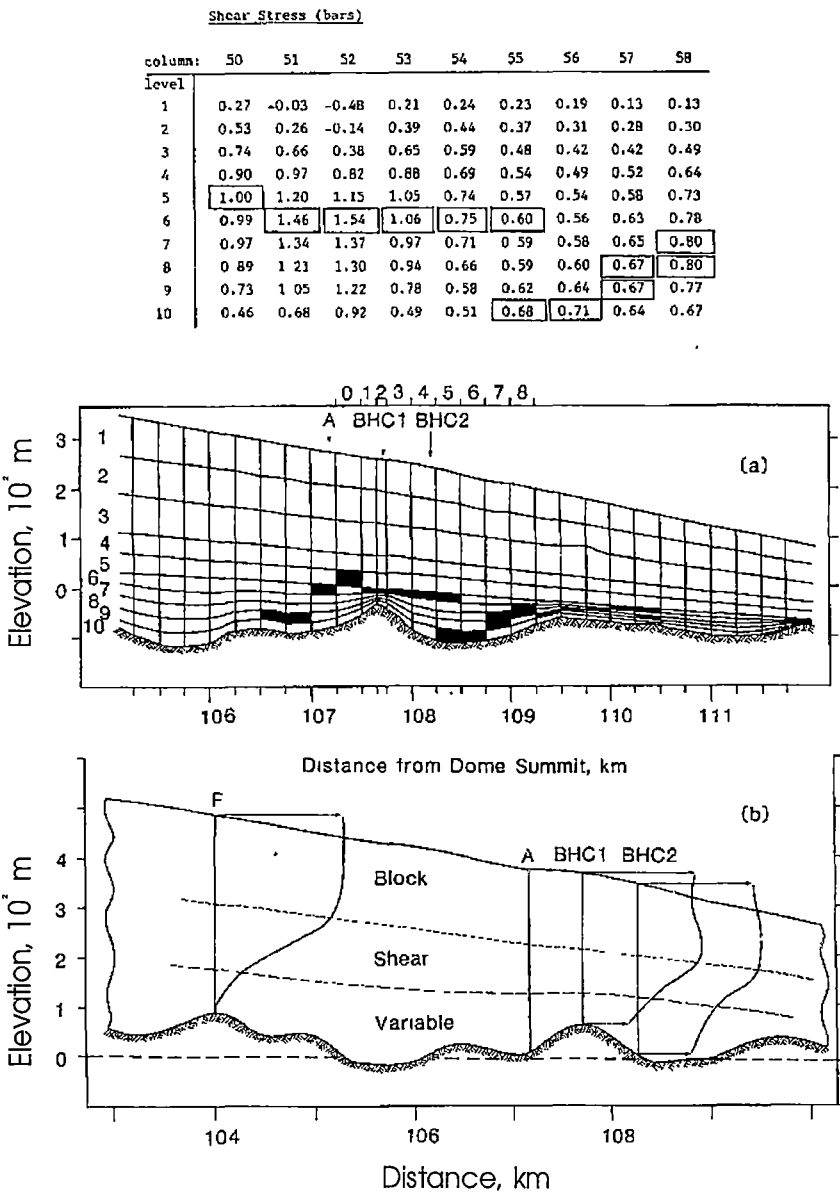


Figure 6.3. Variables stress and strain rates in ice sheets. (a) The cross-section of part of the Law Dome flow line towards Cape Folger where 3 closely spaced borehole data sets are available has been analysed using finite element analysis by Budd and Rowden-Rich (1985). For isotropic ice the pattern of development of high shear stress zones is shown by the dark shading with numerical values for the means of each element giving in the table in bars. (b) The observed velocity profiles from Russell-Head and Budd (1979) and Etheridge and McCray (1985) show the relatively stiff upper zone moving largely as a block over a high shear zone and a highly variable more mobile basal zone. The columns 0-8 in (a) correspond to 50-58 in the table. (from Budd and Jacka, 1989).

The effect is qualitatively similar to the cut-off approach, producing a band of high shear above the bedrock. Since there are still, due to the competing effect of temperature, some appreciable strain rates in the lower regions, the “discounted” shear strain rate profiles involve modifications to the strain rate reaching higher in the ice sheet, and typically produce more realistic values for the maximum shear strain rate.

6.4. Results from the Model Output

The main results from the model output include distributions of temperature, enhancement factor, stresses, strains, ice trajectories and ages, strain rates, and velocities.

As discussed in Chapter 4 the enhancement factor scheme based on the laboratory experiments with combined compression and shear $E(\lambda_c)$ represents the most rapid adjustment of enhancement possible, since it assumes that the evolution of compatible “tertiary flow” fabrics can keep pace with the changing stress regime. It was also mentioned in Chapter 4 that an earlier enhancement scheme, based on more qualitative notions of fabric development and attainment of tertiary flow, had been explored, based on the strain history of the ice sample through the simple ratio of shear strain to compressive strain ($\epsilon_{xz} / \epsilon_z$). This same scheme (Table 4.1) has also been used to calculate the enhancement factor E in the model outlined in Chapter 4, and results are presented for both schemes for comparison.

Note that in this scheme based on strain history the maximum level of shear enhancement is still taken as 10.

In Figure 7.4, the left set of graphs summarizes the output from the model using the $E(\lambda_c)$ scheme (i.e. enhancement factor E is calculated as a function of the compression fraction λ_c) and the right hand side of the figure summarizes the output from the model using the $E(\epsilon_{xz}/\epsilon_z)$ scheme (i.e. enhancement factor E is calculated as the function of the ratio of shear strain ϵ_{xz} to compressive strain ϵ_z). The features of the results are similar to those described in detail for the I.A.G.P flow line (see Section 7.4).

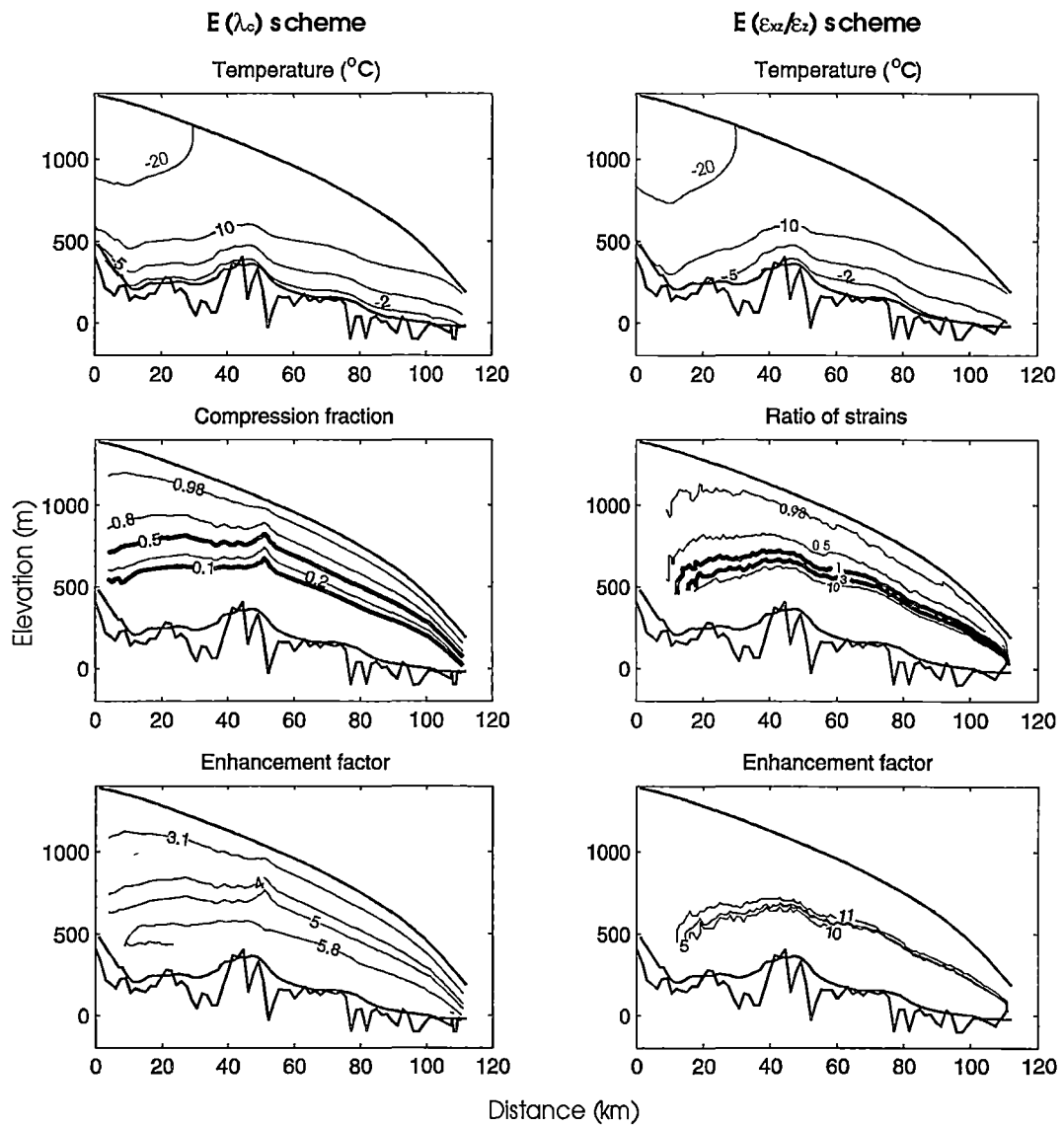


Figure 6.4a. Contour plots of temperature, compression fraction (or ratio of strains) and enhancement factor, resulting from the model based on $E(\lambda_c)$ (left side) and $E(\epsilon_{xz}/\epsilon_z)$ (right side) for the Law Dome flow line.

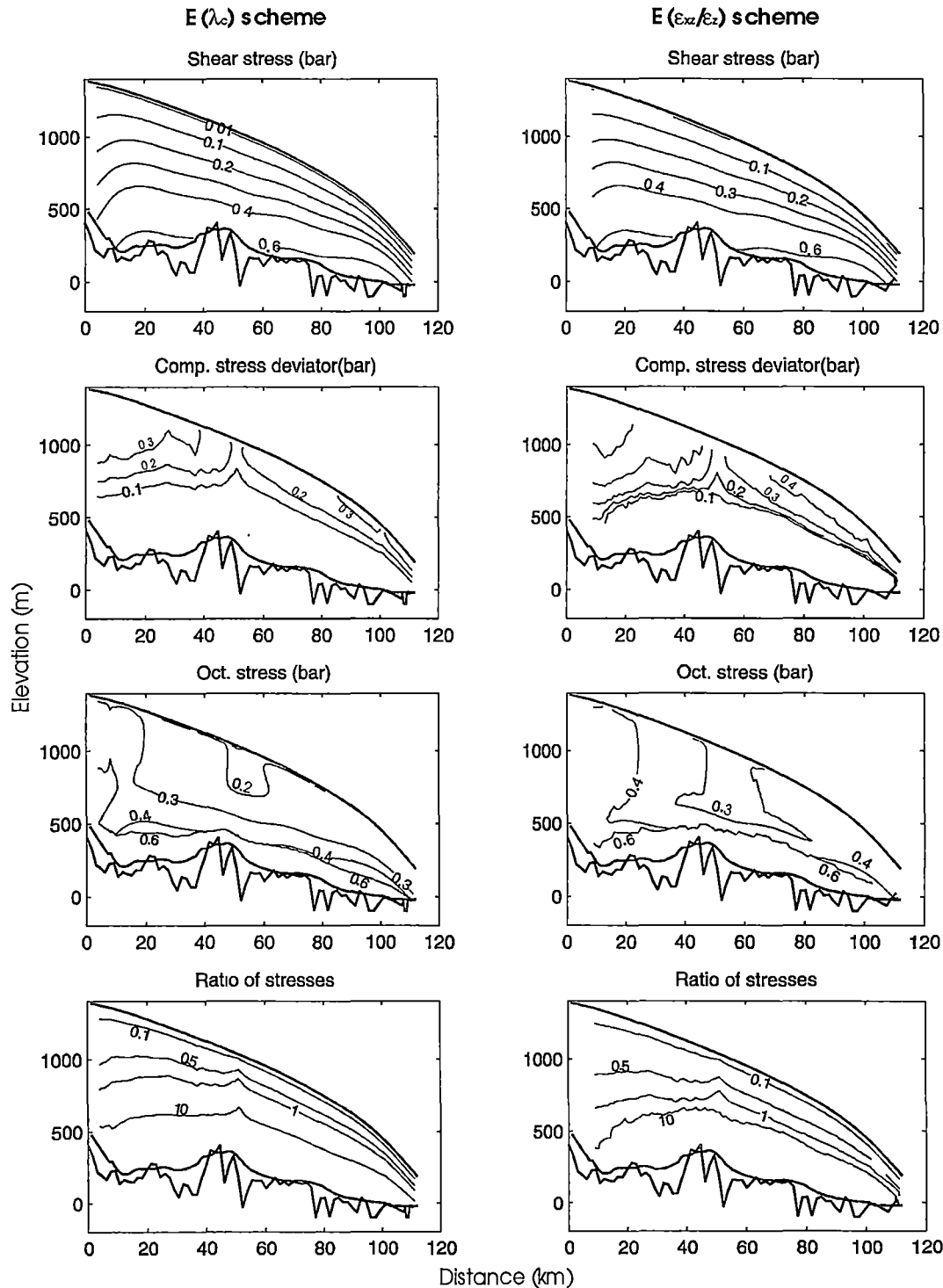


Figure 6.4b. Contour plots of shear stress, compression stress deviator, octahedral shear stress, ratio of shear stress to compression stress deviator, resulting from the model based on $E(\lambda_c)$ (left side) and $E(\epsilon_{xz}/\epsilon_z)$ (right side) for the Law Dome flow line.

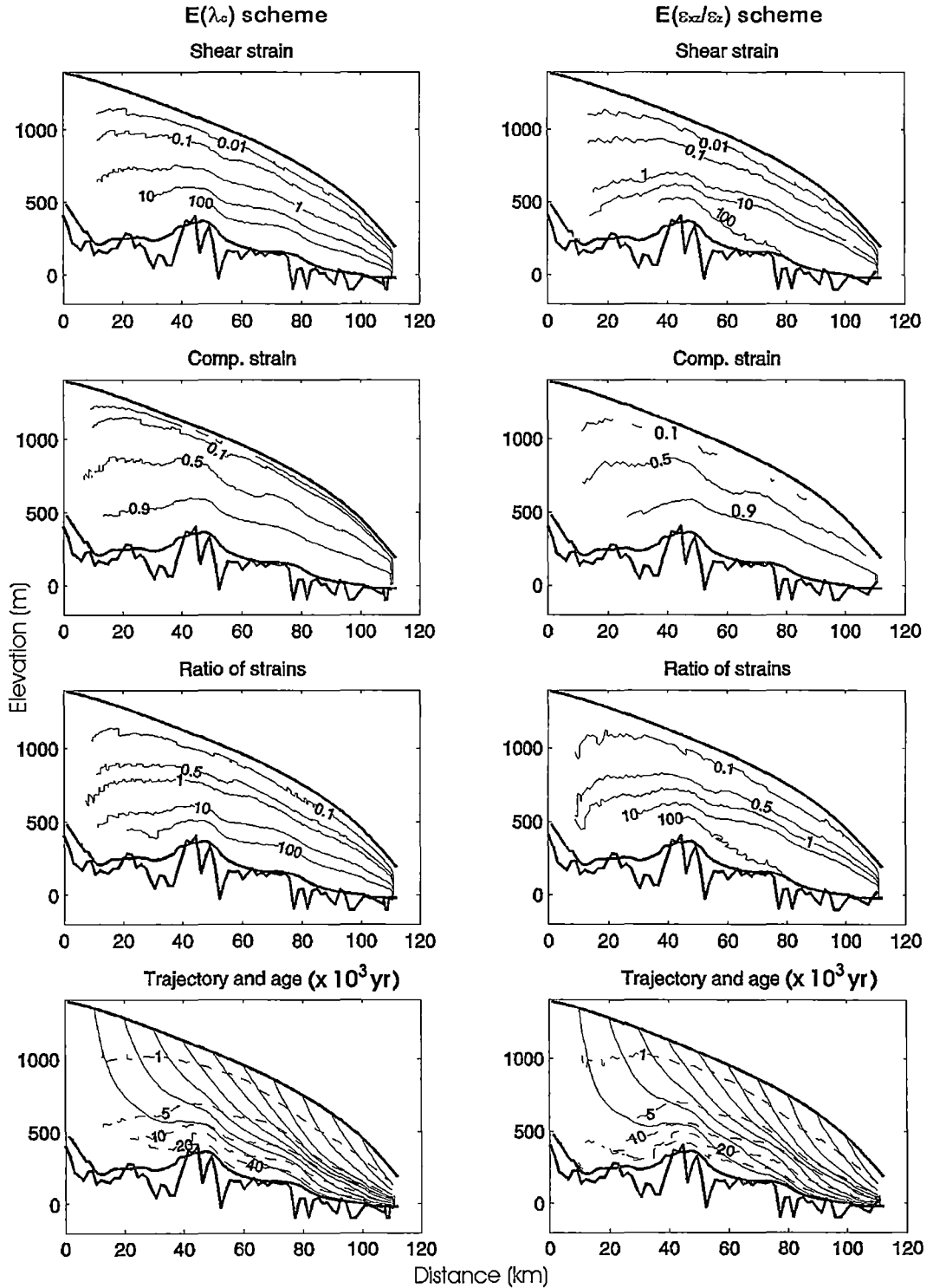


Figure 6.4c. Contour plots of shear strain, compression strain, ratio of shear strain to compression strain, trajectories and age, resulting from the model based on $E(\lambda_c)$ (left side) and $E(\epsilon_{xz}/\epsilon_z)$ (right side) for the Law Dome flow line.

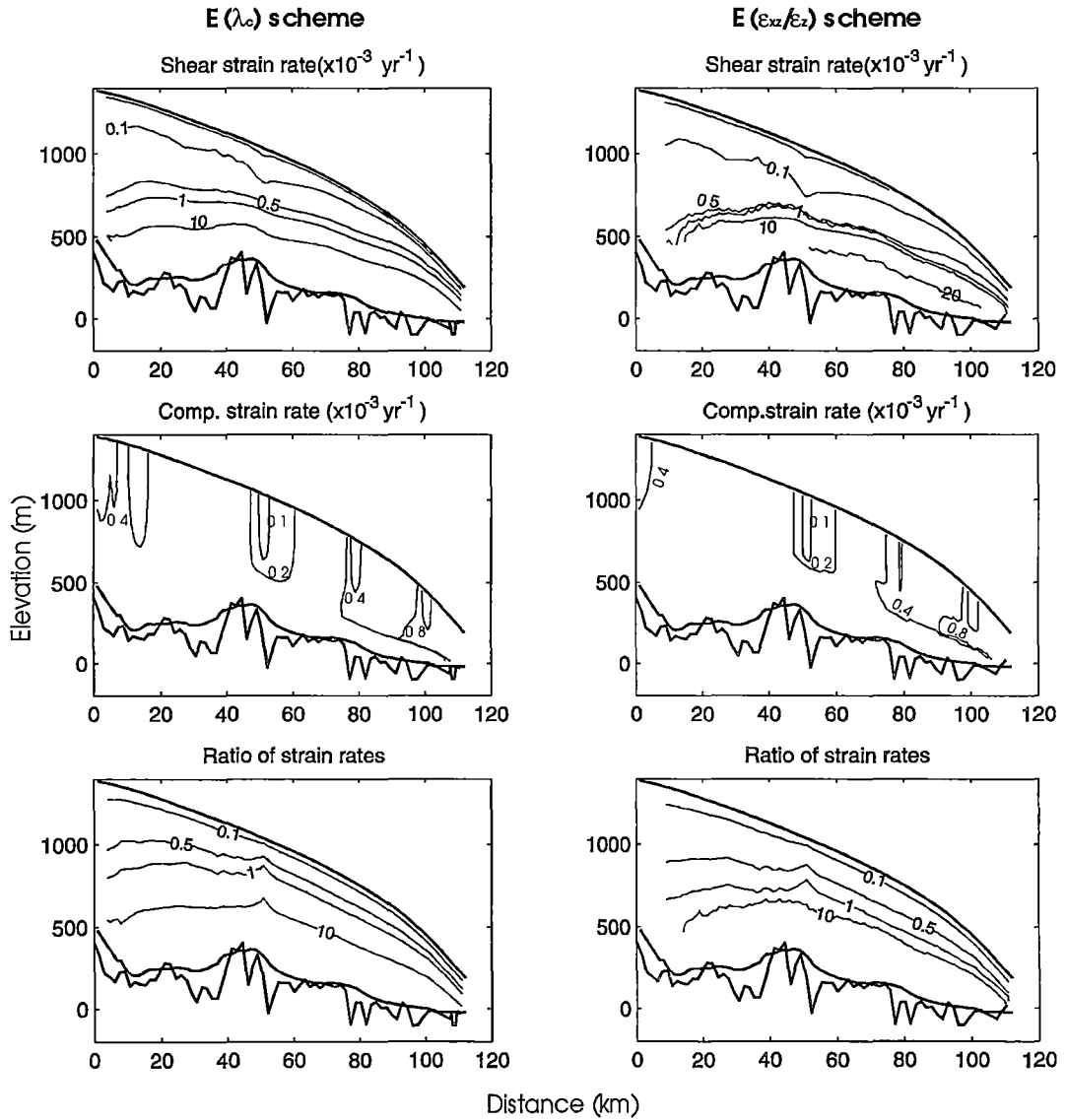


Figure 6.4d. Contour plots of shear strain rate, compression strain rate, ratio of shear strain rate to compression strain rate, resulting from the model based on $E(\lambda_c)$ (left side) and $E(\epsilon_{xz}/\epsilon_z)$ (right side) for the Law Dome flow line.

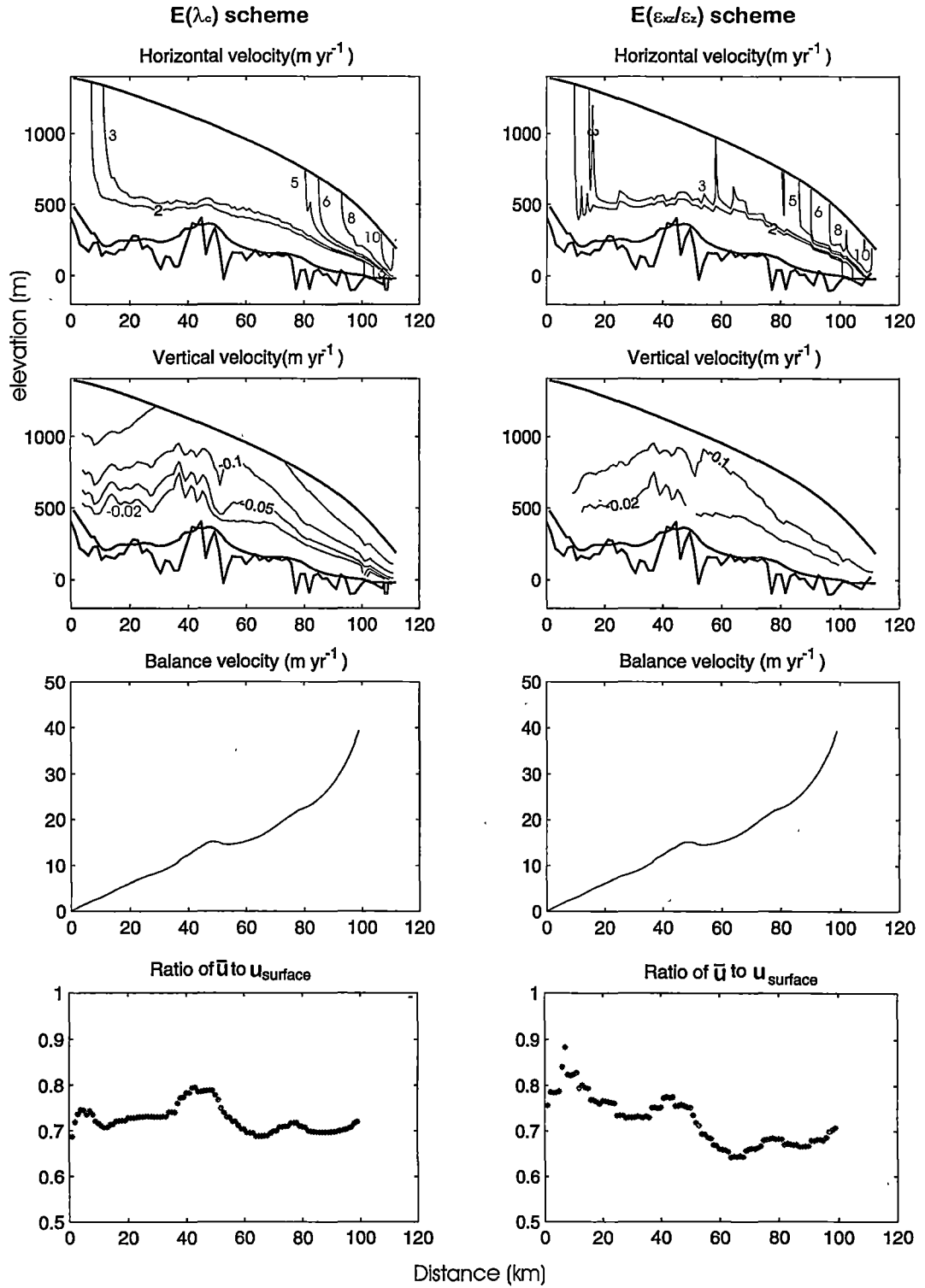


Figure 6.4e. Contour plots of horizontal and vertical velocities, and the profiles of balance velocity and the ratio of horizontal column average velocity to surface velocity (Based on the envelope bed), resulting from the model based on $E(\lambda_c)$ (left side) and $E(\epsilon_{xz}/\epsilon_z)$ (right side) for the Law Dome flow line.

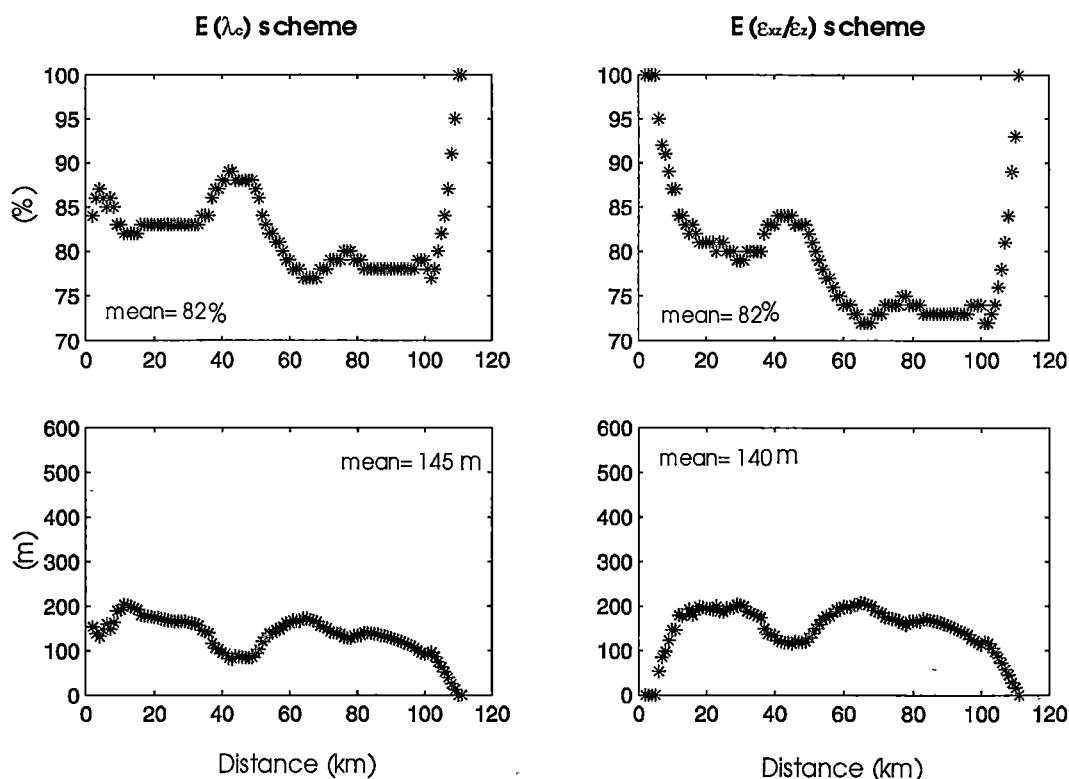


Figure 6.4f. The percentage of the ice thickness (top) and the depth above the bed (bottom) of high shear layer as a function of the envelope thickness along the Law Dome flow line.

Figure 6.5 shows the flow and strain regimes for the law Dome flow line for a comparison of a previous study (Budd and Jacka, 1989) (left side) with the current study (right side). That previous study is based on an assumption of isotropic ice flow and comparison shows that the both of compression strains (Figure 6.5b) and shear strains (Figure 6.5c) accumulate more slowly than that based on the assumption of anisotropic ice flow. For example, 10% shear strain occurs by about half way through the ice thickness for the previous study, but in the current model it occurs much higher than that and close to the surface of ice sheet which may be attributed to a number of factors including the use of the octahedral shear stress in the flow relation, the reduced shear below the high shear layer and the effect of anisotropic ice flow. A faster accumulation of vertical compression strain results in faster horizontal shear flow by the combination of stresses in the

octahedral stress and by the inclusion of an enhancement factor appropriate for tertiary flow rates.

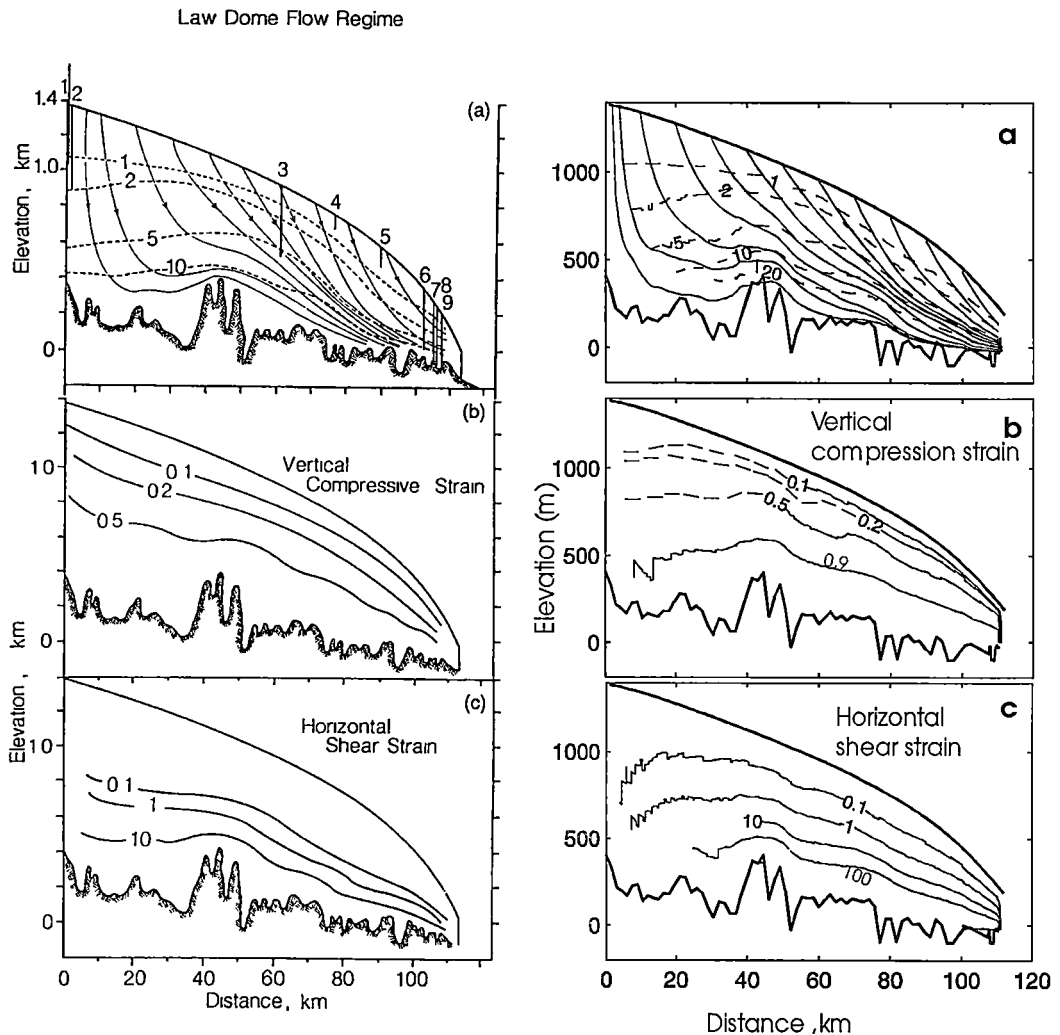


Figure 6.5. The flow and strain regimes for the law Dome flow line from the previous work (left side)(Budd and Jacka, 1989) and from the current work (right side). (a) trajectories (solid lines) and the ages(dashed lines in kyr). (b) contours of vertical compression strains. (c) contours of horizontal shear strains.

6.5. Comparison of the Model Results with Observations

6.5.1. Temperature Profiles

The computed temperature distribution (Figure 6.6a) shows that the basal temperatures along the flow line are near pressure melting point. Comparing these with the observations (Figure 6.6b), the agreement between the temperature

profiles from the model with the borehole temperature measurements (Etheridge, 1989) is reasonable. Matching temperatures has not been the central concern of the thesis, although the influence of temperature on flow rates is of course very important, and while the geothermal heat flux could probably be adjusted to improve the agreement, it is clear that the high shear stresses computed in the basal regions in the present study do not arise from overestimating the ice temperatures. This depends on the magnitude of the enhancement factor.

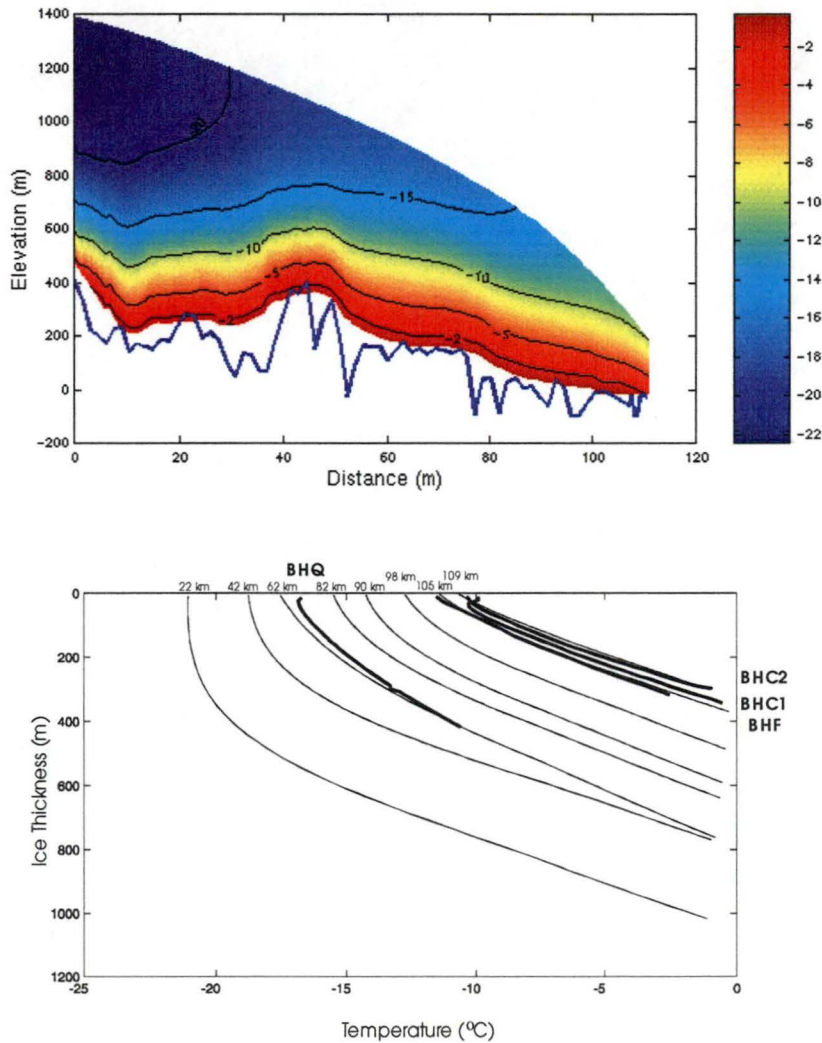


Figure 6.6. Temperatures. (a) The temperature distribution from the model. (b) The temperature profiles from the model (thin lines) and from the borehole observations (thick lines, Etheridge, 1989).

6.5.2. Shear Strain Rate Profiles

In Figure 6.7 vertical profiles of shear strain rate from borehole inclination measurements, at three drilling sites on the flow line (see Figures 3.5 and 3.7) - BHQ and BHC2 (from Etheridge, 1989), and BHF (from Russell-Head, 1979), are shown together with the corresponding profiles calculated from the two enhancement schemes modelled with the bedrock simple “cut-off” and an example applying a continuous discount function for shear strain rates the lower levels using only the $E(\lambda_c)$ scheme. At BHQ (Figure 6.7a) and BHF (Figure 6.7b) the borehole inclination logging does not extend to sufficient depth to show a maximum shear layer, although Russell-Head and Budd (1979) point out that the shear strain rate at BHF cannot continue to increase through the lower levels, given the observed surface velocity and the extent of deformational flow already accounted for. A more complete shear strain rate profile is available from BHC2 a few kilometres downstream of BHF. BHC2 is very close to the end of the flow line, and in matching the surface velocity here it becomes important to deduct the sliding motion. The BHC2 borehole is in a bedrock hollow and the smoothing of the bedrock also makes the model ice cap appreciably thinner there. With these caveats the BHC2 profile is displayed in Figure 6.7c.

Several aspects of Figure 6.7 deserve comment. Good agreement is seen between the model strain rates and the observed strain rates in the upper part of the ice sheet. Note that the strain rates at BHQ (Figure 6.7a) are approximately an order of magnitude smaller than those at BHF (Figure 6.7b) and BHC2 (Figure 6.7c). The “cut-off” strain rate profiles show the necessity for an improved treatment of dynamics in the lower regions of the ice sheet, to reconcile the agreement with the observed strain rates and agreement with the observed surface velocities. These profiles are of course unrealistic, and the dashed line profiles – examples from various experiments that smoothly discount the strain rate in the lower levels while maintaining the same surface velocities – may well be more realistic. The depths at which these strain rates diverge from the simple model are clear. Note that a substantial reduction in model strain rates in lower levels is required. We can see that for BHC2 a simple discounting gives a reasonable profile in the lower part of the ice sheet as well. It might be possible to improve the general agreement

of the lower part of the shear profiles by careful choices, but there are very few measured profiles to use for this. Generally it is clear that any smooth “discount” from declining enhancement and / or reducing shear stress will place the maxim shear layer above the simple cut-off depth.

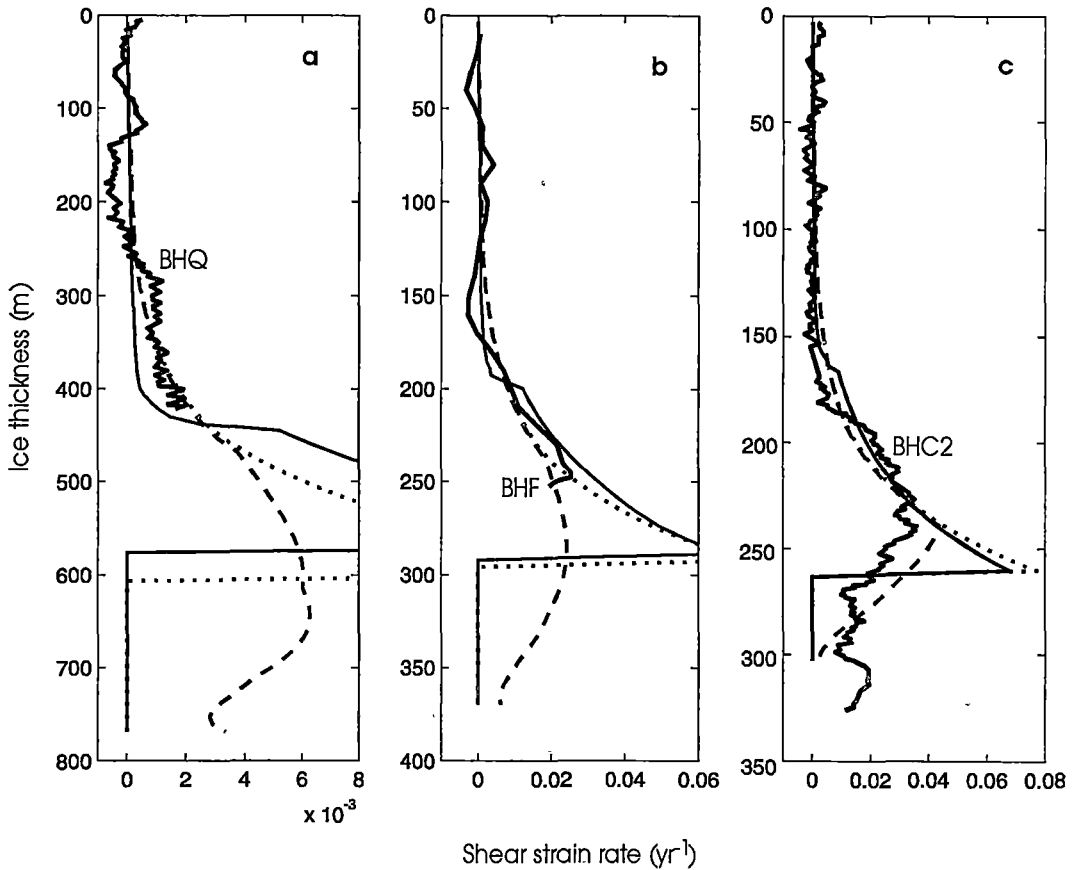


Figure 6.7. Shear strain rate profiles from borehole inclination measurements (thicker lines) at (a) BHQ borehole (Etheridge, 1989), (b) BHF borehole (Russell-Head, 1979) and (c) BHC2 borehole (Etheridge, 1989). Model profiles at these three sites are presented for the “cut-off” model (dotted line) and a “discount” model (dashed lines) applied to the $E(\lambda_c)$ enhancement scheme. The results from the enhancement scheme $E(\epsilon_{xx}/\epsilon_z)$ based on the ice history (ie. enhancement is calculated based on the ratio of shear strain to compression strain) are also shown (solid line).

Around a depth of 180 metres the measured profile from BHC2 shows a more rapid increase in shear strain-rate than the profile using the $E(\lambda_c)$ enhancement scheme. This may reflect the failure of one or other of the assumptions in that scheme. Firstly it should be noted that for ice flow over rough bedrock the shear

stress cannot be expected to simply increase linearly with depth, but rather in a more variable way as illustrated in Fig. 6.3. Secondly it is that the ice fabrics can evolve sufficiently quickly to maintain optimal fabric and tertiary flow conditions with the changing stress conditions encountered as the ice flows through the ice sheet. As previously indicated this assumption about equilibrium tertiary conditions makes the scheme a limiting case, since it models the fastest possible adjustment of the anisotropic properties of the ice to the changing stress situation. If the crystal fabric evolution tends to lag behind the changing stress conditions, until sufficient exposure to a period of shear dominated flow brings it into a compatible fabric, then the enhancement of shear flow will be delayed and concentrated over a thinner band in the ice sheet. The earlier scheme (Section 4.2), which (see Section 6.4) showed these sharper transitions, represents the other extreme in some sense, because no enhancement was applied in that model until cumulative shear strain overtook compression strain.

6.6. The Main Ice Flow Regions of the Law Dome flow line

Based on the stress configuration and the magnitudes of the strains and strain rates, resulting from the model, the ice flow regions for the Law Dome flow line are estimated in Figure 6.8. In the Law Dome flow line, a subdivision can be made into five typical ice flow regions which are the *firn zone*, the *compression zone*, the *transition zone*, the *shear zone* and the *basal ice*.

The *firn zone* is from the surface to the depth at which the surface snow has been compressed to ice for which the accumulated ice compression strain is generally below 10%. The *compression zone* is from the bottom of firn zone to the depth where shear stress overtakes the compressive deviatoric stress (or shear strain rate overtakes the compressive strain rate). The *transition zone* is between the compression and shear layers where the shear stress is approximately equal to compressive stress deviator (or the shear strain rate is about equal to the compressive strain rate) or alternatively where the shear strain becomes comparable with the compressive strain. The *shear zone* is from the bottom of transition zone to the base of the *maximum shear layer* near to the levels of the

“rheological” or “cut-off” depths, z_c . Some corresponding parameters for the general ice flow regions along the Law Dome flow line are given in Table 7.1 which also correspond in general terms to those described for the I.A.G.P flow line.

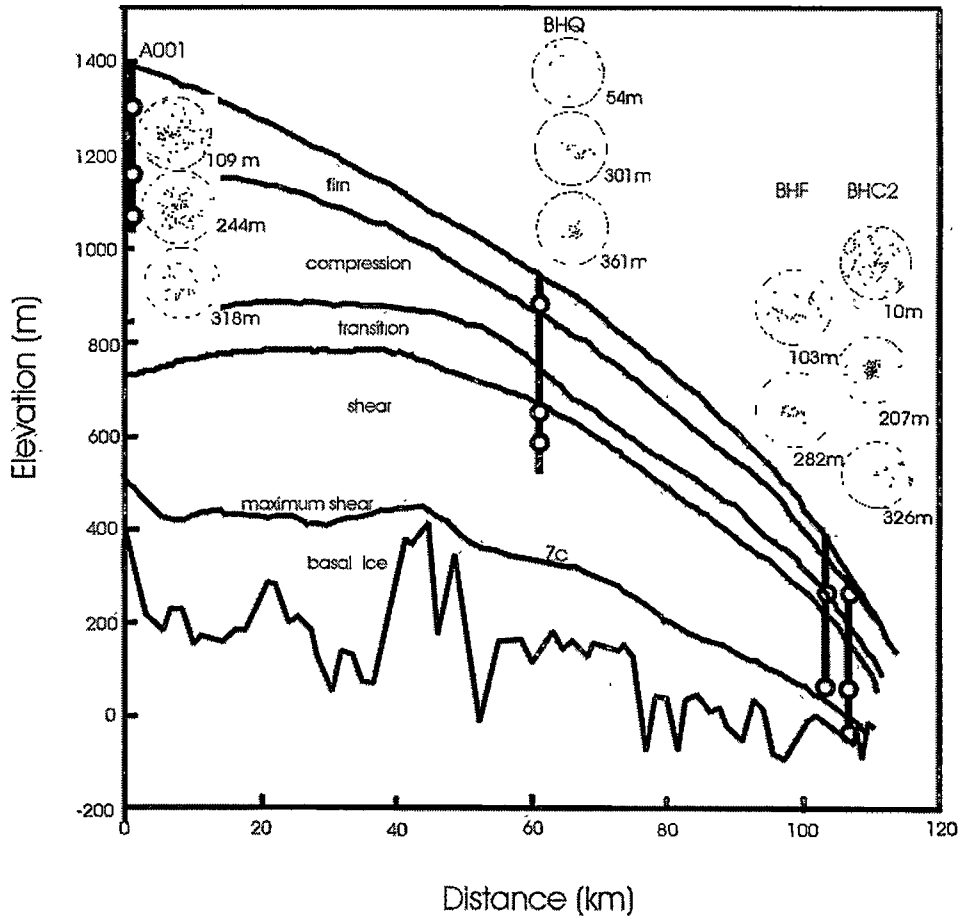


Figure 6.8. Profile of the transect from the summit of Law Dome to Cape Folger, showing the flow regions (firm, compression, transition and shear zones, and basal ice) detail in the text. Representative crystal orientation fabrics measured from ice cores from A001 (Jacka and Budd, 1989), BHQ (Li and others, 1988), BHF (Russell-Head, 1979) and BHC2 (Thwaites and others, 1984) and the locations of the boreholes are also displayed.

Comparing Figures 6.7 and 6.8 shows that the most rapid increase in shear does lie below the transition from compression to shear dominance. The “cut-off”

depth z_c lies at a fairly uniform height above the smoothed bedrock, except at the very edge of the ice cap. The mean “cut-off” depth is approximately 82 % of the ice thickness (using the smoothed envelope bedrock), with a standard deviation of 4 % (see Figure 6.4f). Naturally any smoother discounting of shear strain-rate must commence higher in the ice sheet.

The analysis of crystal orientation fabrics in the ice cores from ice sheets has shown that the fabrics develop from a random fabric near the surface to a strongly developed fabric with increasing depth. It is also known that the crystal orientation fabric pattern can be indicative of the stress configuration, i.e. a small circle girdle pattern is compatible with the uniaxial unconfined compression stress configuration, while a single maximum pattern is compatible with a simple shear stress configuration (Budd and Jacka, 1989). Thus, crystal fabrics from ice cores may provide independent evidence of the location of the transition from compression to shear dominated flow.

Some crystal orientation fabrics from ice cores drilled along our transect - A001 (Jacka and Budd, 1989), BHQ (Li and others, 1988), BHF (Russell-Head, 1979) and BHC2 (Thwaites and others, 1984) are shown in Figure 6.8 together with markers of their depths in the ice sheet. In the upper layers of the ice cap the crystal fabrics appear isotropic. The fabrics at 318 metres depth from the A001 core and at 103 metres from the BHF core, representing girdle patterns, are examples in the vertical compression zone. The single maximum fabrics from BHQ (at 361 metres), BHF (at 282 metres) and BHC2 (at 207 m) ice cores are indicative of flow domination by horizontal shear. The relationship between the locations of these fabrics and the ratio of strain rates (and hence in this model the compression fraction λ_c) is encouraging, and deserves more attention in future work. A multi-maxima fabric near the base at BHC2 is possibly due to basal effects such as higher temperature, reduced shear stress and possibly increased longitudinal and transverse stresses (Budd and Jacka, 1989).

6.7. Summary

A flow model based on ice rheology from laboratory and borehole experiments, including enhancement effects measured in combined stress experiments, gives shear strain-rate profiles that agree well with borehole inclination measurements along an Antarctic flow line, at least in the upper portion of the ice sheet. In spite of this, the simple form of the model would predict much higher surface velocities than are observed on this flow line if the computed strain rates were continued to the bed with an assumed linearly increasing shear stress. With no adjustable parameters in the flow law the question of reduced shear strain-rates in the lower levels of the ice sheet must be tackled to reconcile the situation. Explaining the details of flow in these lower levels is expected to be a difficult task, and would depend on the detailed bedrock topography at any location (among other variables). However, the present work suggests that a simpler empirical treatment may merit further investigation. This could be based on the concept of a appropriately smoothed envelope bedrock topography, together with an empirical prescription for the thickness of a basal zone of reduced strain rates depending on the large scale roughness of the bed. This prescription might depend on quantities such as the ice thickness above to the smoothed bedrock, and on distance scales associated with some characteristic wavelength and amplitude of the bedrock undulations. The comparison of the results from the analysis of the Law Dome flow line with those for the larger scale I.A.G.P flow line is expected to throw some light on this scaling problem.

Chapter 7

APPLICATION OF THE MODEL TO AN I.A.G.P. FLOW LINE, WILKES LAND, ANTARCTICA

7.1. Introduction

A model to describe the influence of anisotropy on the ice flow was developed in Chapter 4. Chapter 6 presented the application of the model to a flow line of about 100km from the Dome Summit to Cape Folger on Law Dome, East Antarctica. As described in Section 3.2.1, Law Dome is a small ice cap, separated from the ice flow of the main Antarctic ice sheet by the Vanderford and Totten glaciers. The maximum ice thickness near the centre of Law Dome is about 1200 m. The mean annual surface temperature varies linearly with elevation over a narrow range from -21°C at the Dome Summit to -9°C near the coast (Xie and others, 1989).

In this Chapter, another approximate flow line is studied, along the I.A.G.P. traverse line in the interior of East Antarctica. This flow line is the part of the southern traverse line into Wilkes Land from Law Dome Summit towards Vostok described by Budd and Young (1979) (Figure 7.1). Compared with the Law Dome flow line, this flow line is longer (~ 600 km long) with deeper (~ 4000 m deep) and colder (below -50°C at the surface) ice with faster ice flow (reaching 60 m yr^{-1}), and suitable for exploring larger scale bedrock features.

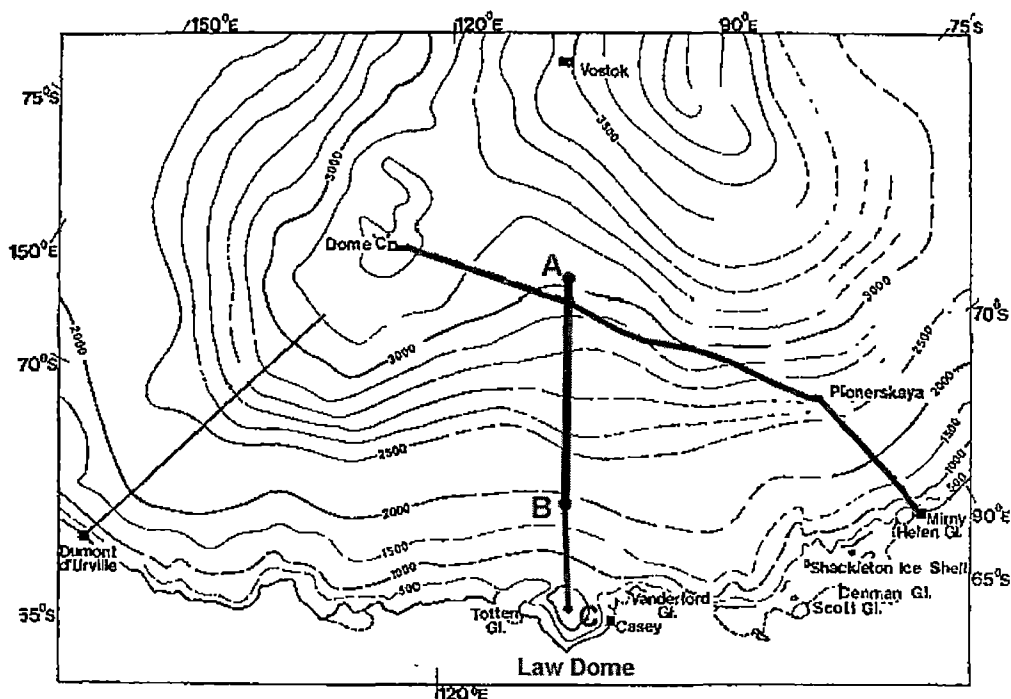


Figure 7.1. Map of region of Antarctica showing the location of the I.A.G.P line and the contours of surface elevation in meters (dashed lines). The studied flow line is the part of the traverse line from Law Dome Summit C towards Vostok and is indicated by the thick line from A to B. (modified from Young, 1979).

As described below, the part of the flow line studied here does not start from an ice divide, which was beyond the end of the traverse route. This means that the ice in the deeper part near the origin of the part of the flow line studied is coming from further upstream. This boundary condition for the start of the flow line results in a problem for the application of the scheme where the enhancement factor is based on the ice history. If the enhancement factor is based on the ice history as calculated from the accumulated strains along the flow trajectories then there is a problem with the absence of calculated ice trajectories (or strains) in the deeper part of ice near the origin of the flow line modelled. Therefore in the application of the model here only the enhancement factor scheme derived from laboratory experiments with combined stresses was used.

7.2. I.A.G.P. Flow Line

7.2.1. Background of the I.A.G.P.

The International Antarctic Glaciological Project (I.A.G.P.) was a long term program of glaciological research in East Antarctica, conceived in 1969, and involved primarily five nations: Australia, France, the United Kingdom, the U.S.A and the U.S.S.R (Anonymous, 1971; Radok, 1985).

The I.A.G.P. aimed at determining the present dynamics and state of balance of the ice sheet over a large sector of East Antarctica. It also aimed to study the history and possible future behaviour of the ice sheet in this region.

The original I.A.G.P. study area was around the Wilkes Land region (see Figure 1.2).

In past years, the I.A.G.P gathered a vast amount of data, mostly from oversnow traverses, airborne echo-sounding and ice core drilling (e.g. Black and Budd, 1964; Budd and Young, 1979; Drewry, 1975; Drewry and Jordan, 1980; Hamley, 1987; Lorius and Vaugelade, 1972, 1973; Radok, 1977, 1985; Raynaud and others, 1979; Robin and others, 1977; Walker, 1966, 1976; Young, 1979; Young and others, 1989).

7.2.2. The I.A.G.P. Flow Line

As part of the I.A.G.P, some longer overland traverse routes were carried out such as shown in Figure 7.1: from Dumont d'Urville to 800 km towards Vostok; from Law Dome to Vostok; from Mirny to Pionerskaya which is approximately along a flowline, and then from Pionerskaya to Dome C, which crosses the general flow direction, rising to an approximate elevation of over 3000 m.

Glaciological data from these traverses include ice velocity and ice thickness, surface levelling from barometric altimetry, gravity, magnetics and snow accumulation. These data (for the deep interior region of Antarctica) have already been used in accordance with the I.A.G.P. aims, to investigate the state of balance of the Antarctic ice sheet (Young, 1979; Hamley and others, 1985; Budd and Warner, 1996). Based on the observed data a map of accumulation rate in the

Wilkes Land area has been generated by Young (1982, Figure2), showing a general decrease from Law Dome towards Vostok.

According to the smooth flow lines (Figure 7.2) drawn from orthogonals to the elevation contours in Figure 7.1, it appears that part of the traverse route between Vostok and Law Dome, corresponding to the line from point A to point B is approximately along a flow line. It is therefore reasonable to apply our flow line model to this section of the traverse line.

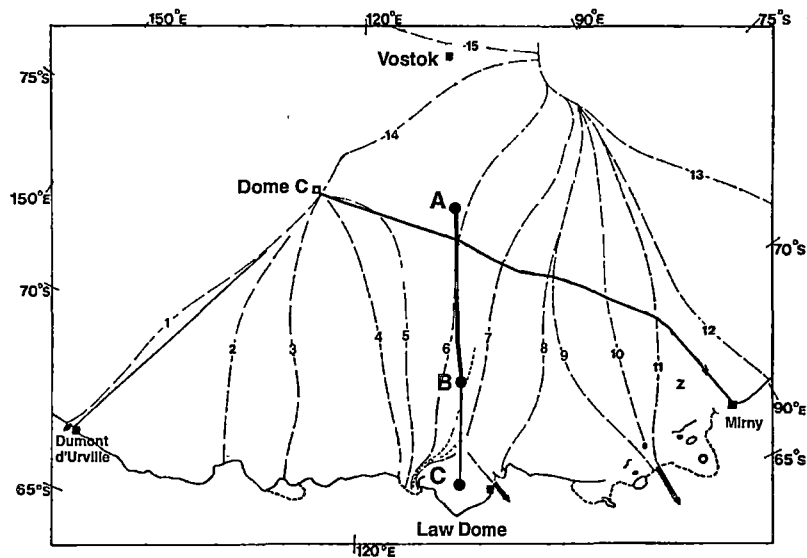


Figure 7.2. Map showing smooth flow lines in the study area. The studied line from A to B is approximately along a flow line. (modified from Young, 1979).

7.3. Model Input Data

The flow line for the modelling studies in this Chapter was chosen to represent the region from point A to point B along the traverse route (Hamley, 1987) from Law Dome Summit towards Vostok, where the data required for model input, which include relatively detailed surface and bedrock data, are available (approximate 2 km intervals) and are shown in compact form in Figure 7.3a. The model input

data also include surface accumulation (Figure 7.3b), horizontal velocity (Figure 7.3c) and temperature (Figure 7.3d). They were taken from the observations from a number of the over snow traverses. The surface and bedrock elevations, and surface velocity were taken from Hamley (1987, Table 3.3 and Table 5.1), while surface accumulation and temperature were taken from Qin (1988, Table 1). According to the contours of accumulation generated by Young (1982, Figure 2), showing a general decrease from Law Dome towards Vostok, the measured accumulation rates were smoothed along the flow line and used in the model as shown in Figure 7.3b.

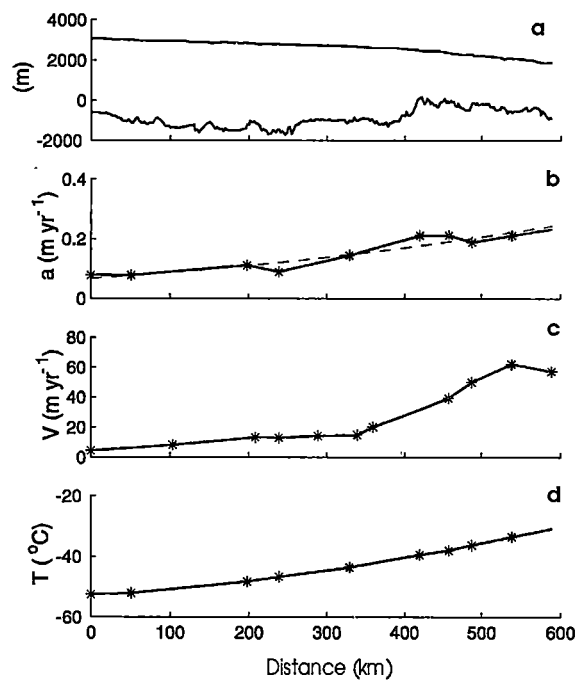


Figure 7.3. The model input data (solid line) for the I.A.G.P flow line. Symbol * indicates the data from field measurements (Hamley, 1987; Qin, 1988). (a) surface and bedrock elevation, (b) surface accumulation rate, dashed line shows the smooth data used in the model, (c) surface horizontal velocity and (d) surface temperature.

As described in Section 4.3.4, the concept of an envelope topography, smoothing over the higher frequency bedrock roughness, was used in the model to reduce the effect of bedrock undulations. The bedrock topography along the I.A.G.P line also has large undulations of up to about 30% of the ice thickness which are still represented by the smoothed bed. The results of different scales of bedrock

smoothing are illustrated in Figure 7.4. Using a running mean over a certain number points (or distance) and then adding one (or two) standard deviations of the bedrock variations about the means to the mean produced a smooth envelope bedrock above the mean smoothed bed. Comparing these various results, the bedrock chosen for this study was the envelope bedrock formed by a running mean over 63 km, which is about 15 times the maximum ice thickness in this flow line, and raising it by one standard deviation of the bedrock data calculated over each corresponding 63 km band of the running mean.

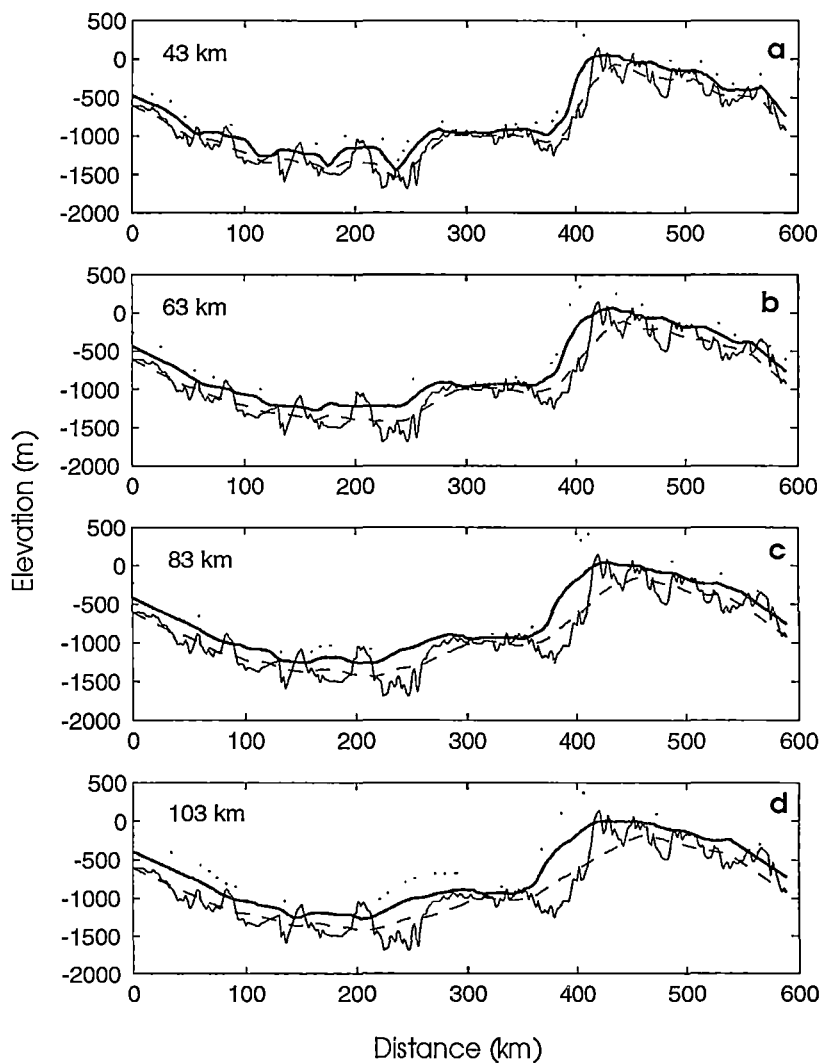


Figure 7.4. Bedrock smoothing along the I.A.G.P flow line. The thin solid line is the real bedrock from the observations (Hamley, 1987). The dashed line is the mean bed calculated from the running mean over the indicated distance. The thick solid line (respectively dotted line) is the mean bed adding one (respectively two) standard deviations of the bedrock variations about the means to the mean.

In similar fashion to the studies for the Law Dome flow line in Chapter 6, all input data in this study were interpolated so that the horizontal resolution is 1 km and vertical resolution was set by dividing the ice thickness into 100 evenly spaced bands. The basal geothermal heat flux gradient for the temperature calculations was taken as 0.035 K m^{-1} similar to that used for Law Dome. It was assumed that basal sliding is negligible along this flow line. The enhancement factor used was the function of compression fraction, $E(\lambda_c)$ (Section 4.3.2.1) varying as in Chapter 6 from 3 (i.e. $E_c=3$) near the top of ice sheet to 6 (i.e. $E_s=6$) with increasing depth of ice. Assuming that the vertical profile of horizontal velocity varies very slowly in the horizontal direction along the flow line, vertical strain rates and velocities were once again calculated by use of the shape function as described in Section 4.4.4b, along with the assumption of steady state.

As already mentioned, the modelled section of the flow line (thick line in Figure 7.2) does not start from an ice divide, indicating that the ice in the deeper part near the origin of the flow line is coming from further upstream. Similarly the observed surface velocity (Figure 7.3c) shows that the horizontal velocity at the origin of the flow line is not equal to zero while it would be equal to zero at an ice divide. This boundary condition for the origin of the flow line requires a different scheme for treating the term for the horizontal advection in the heat Equation 4.4.8.6 at the first column of the flow line. This scheme is described in Appendix II in detail.

The method of application of the model in this Chapter was the same iterative approach as that for the Law Dome flow line (Chapter 6). To consider the combined reduction of shear stress and enhancement near the bed the depth integration of shear strain rate was simply terminated at a level above the bed selected to match the observed surface velocity (see Section 6.4 for details).

7.4. Results from the Model Output

The main results from the model output include temperature, enhancement factor, stresses, strains, ice trajectories and ages, strain rates, and velocities. For comparison, the right hand side of the graphs of the computed variable (Figures 7.6 – 7.10) shows the results from the same model, but using a very smoothed bedrock obtained by the repeated averaging of three neighbouring points (i.e. over

a 3 km interval) 2000 times, which has a similar effect to smoothing with a moving gaussian filter with a full width at half maximum of 85 km, and then raising the mean by one standard deviation for the whole line. The more smoothed bedrock gives more smoothed contours of the results which may be easier to be read, but this may also over smooth the results and neglect some of the important bedrock features, especially near the high bumps (Budd and Carter, 1971). The profiles of temperature, stresses, strain rates and velocities through the ice column are plotted as an example in Figure 7.5 at a distance of 300 km from the origin of the flow line.

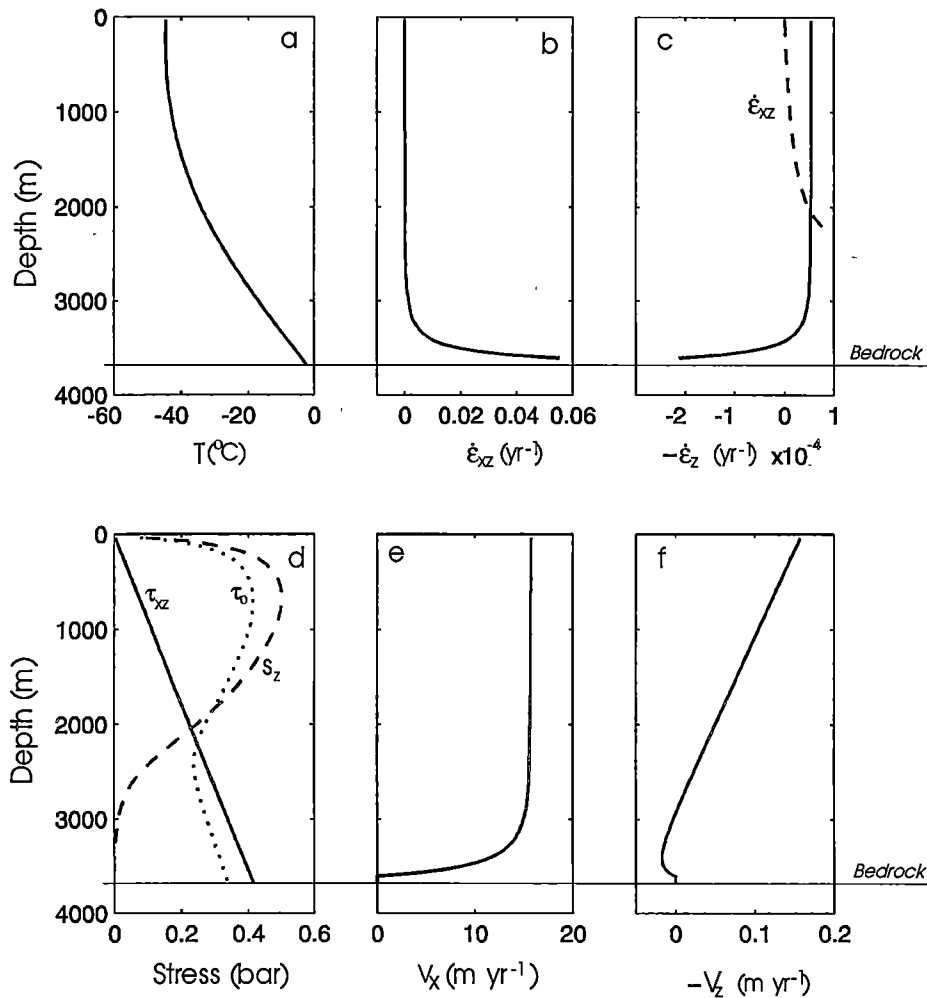


Figure 7.5. Vertical profiles of (a) temperature (T), (b) shear strain rate ($\dot{\epsilon}_{xz}$), (c) vertical strain rate ($\dot{\epsilon}_z$) with part of the shear strain rate profile (dashed line) plotted for contrast, (d) shear stress (τ_{xz}), compression stress deviator (S_z) and octahedral shear stress (τ_o), (e) horizontal velocity (V_x) and (f) compression velocity (V_z) at a distance of 300 km from the origin of the I.A.G.P. flow line.

7.4.1. Temperature and Enhancement

The temperature distribution (Figure 7.6a) shows that the ice is nearly isothermal near the top, and then warms rapidly near the bed. The ice at the bed is near the pressure melting point, indicating that some sliding could occur near the bed and may need to be taken into account in the model.

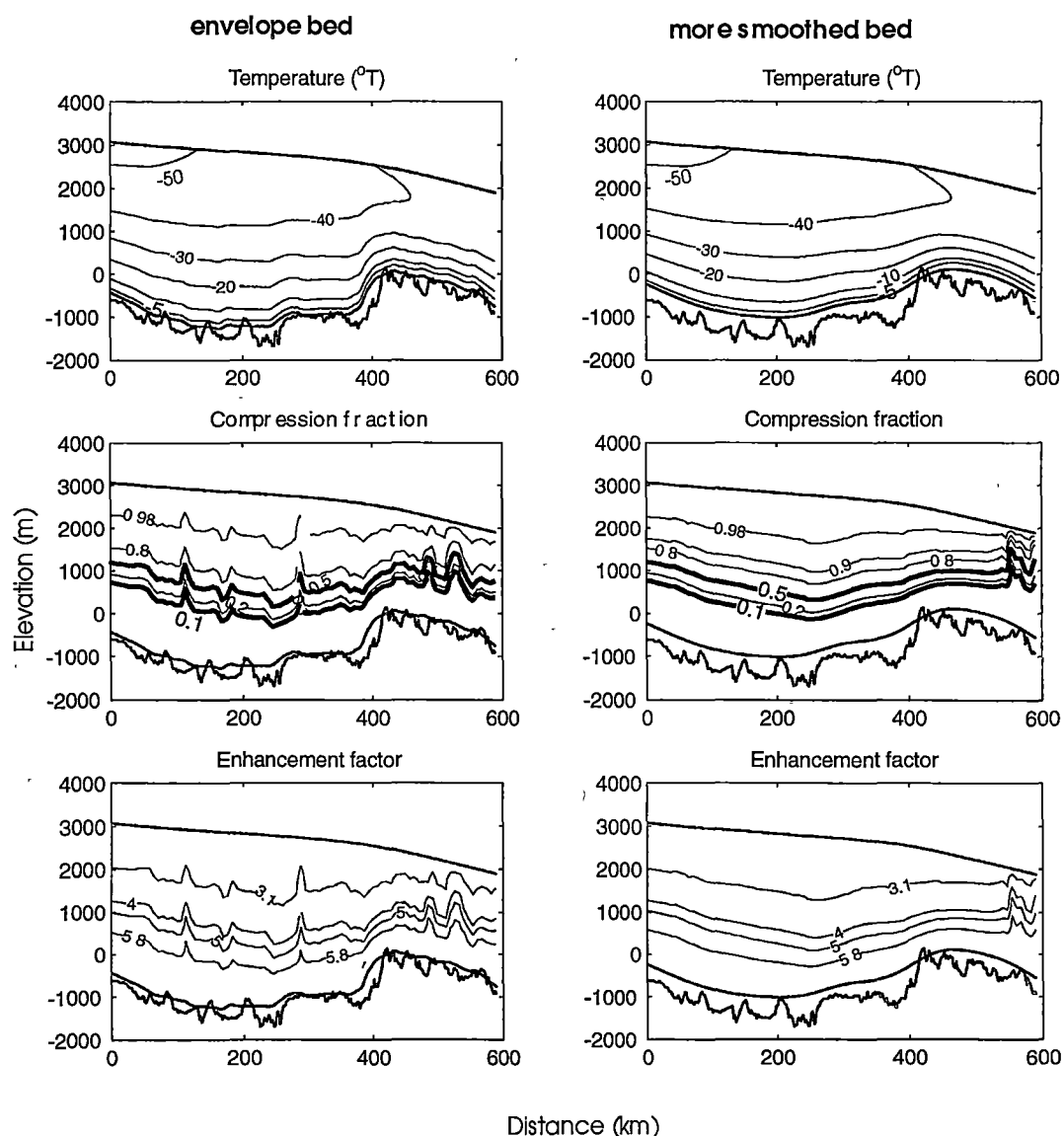


Figure 7.6. Contour plots of temperature, compression fraction and enhancement, resulting from the model based on the envelope bed (left side) and the more smoothed bed (right side).

The enhancement factor (Figure 7.6c) calculated as a function of the compression fraction (λ_c) (Figure 7.5b) varies from 3 for compressive deformation ($\lambda_c=1$) to near 6 for shear deformation ($\lambda_c=0$).

7.4.2. Stresses

Shear stress (Figure 7.7a) generally increases with the depth and towards the margin of the flow line. In the upper part of the flow line the stress contours are more flat while they become steeper along the flow line, which shows the maximum shear stresses occurring in the deeper part of the ice and near the margin of the flow line, even though the ice becomes thinner there. By contrast, the compression stress deviator (Figure 7.7b) decreases with the depth. Octahedral shear stress (Figure 7.7c) as a combination of shear and compression deviatoric stresses (see Section 2.2.1.3) decreases in the upper part of the ice sheet and increases in the deeper part (also see Figure 7.5d).

The ratio of the shear stress to the compressive stress deviator is shown in Figure 7.7d. It is considered that above the layer where the shear stress overtakes the compressive stress deviator the ice flow is dominated by compression while it is dominated by shear below that layer.

The relation between the stress configurations and the preferred crystal orientation fabrics has been discussed in Chapter 3 in detail. Based on the stress configurations the fabric development in an ice sheet should be predictable (for example, Budd and Jacka, 1989; Azuma, 1994).

7.4.3. Strains and Age

In the upper part of the ice sheet compression strain (Figure 7.8b) is accumulated faster than shear strain (Figure 7.8a). The layer where shear strain overtakes compression strain (Figure 7.8c) is in the middle to lower part of the ice sheet and close to the layer where shear strain rate overtakes compression strain rate, or shear stress overtakes compressive stress (in octahedral terms).

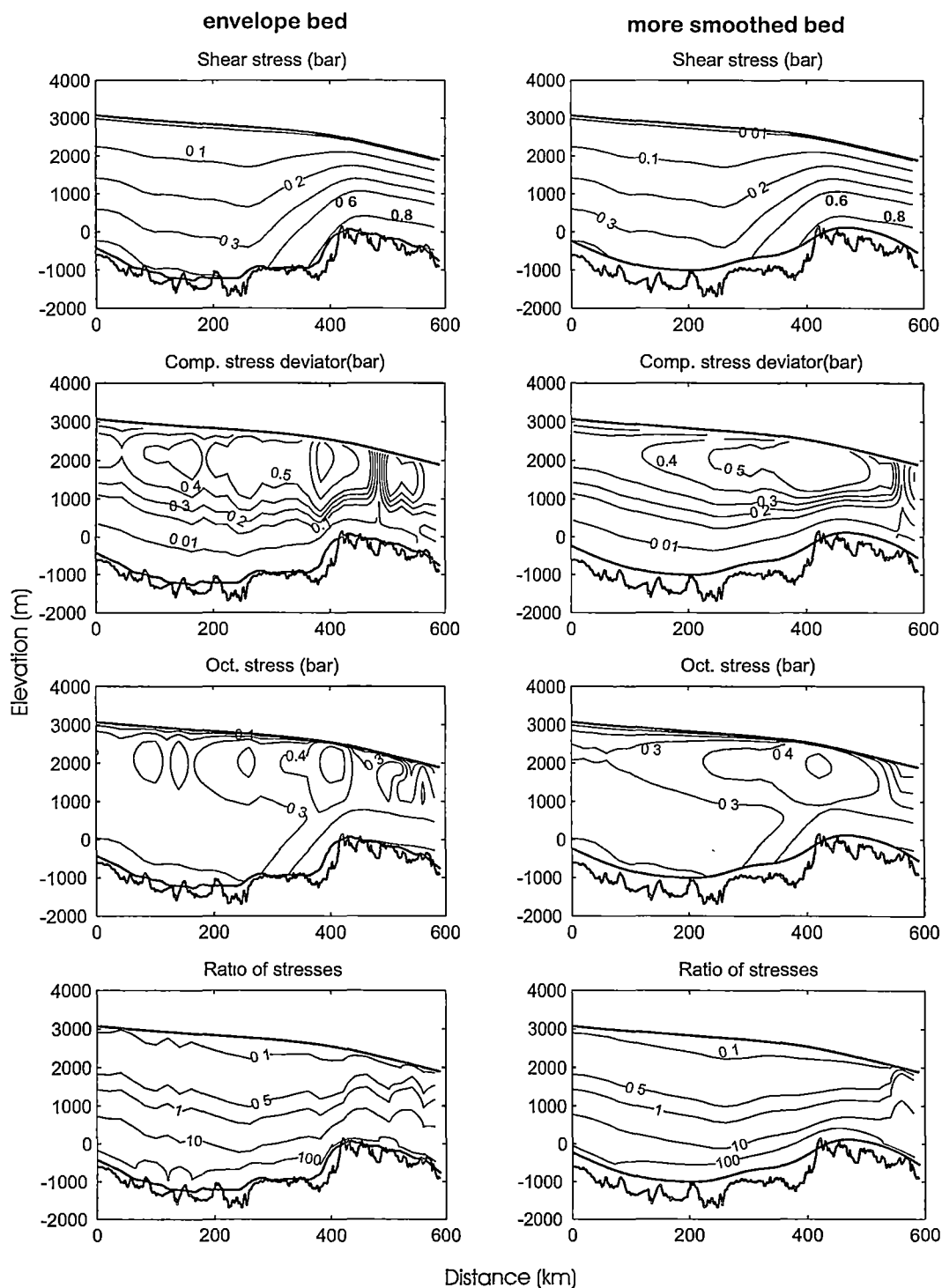


Figure 7.7. Contour plots of shear stress, compression stress deviator, octahedral shear stress and the ratio of shear stress to compression stress deviator, resulting from the model based on the envelope bed (left side) and the more smoothed bed (right side).

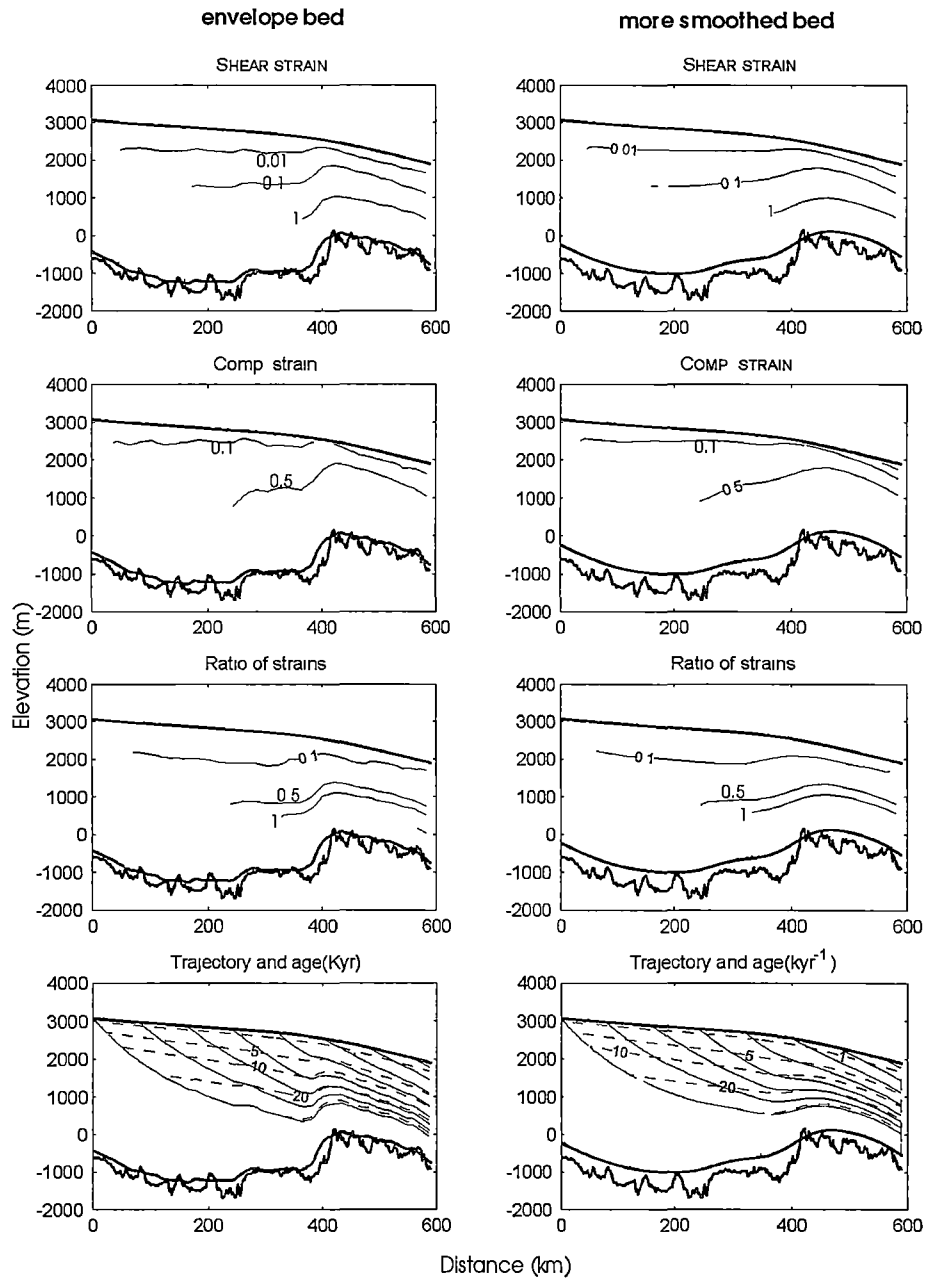


Figure 7.8. Contour plots of shear stain, compression strain, the ratio of shear strain to compression strain, trajectories and age, resulting from the model based on the envelope bed (left side) and the more smoothed bed (right side).

7.4.4. Strain Rates

Shear strain rate (Figure 7.9a) increases with depth and overtakes the compression strain rate (Figure 7.9b) near the middle of the depth of the ice sheet (Figure 7.9c), where the enhancement factor (Figure 7.6c) shows a substantial increase. The ratio of shear strain rate to compressive strain rate is similar in pattern to that of the ratio of shear stress to the compressive stress deviator because the model uses a similar form of flow relation for the shear and compression components (see Equations 4.3.2.2 and 4.3.2.3).

7.4.5. Velocities

The horizontal velocities increase along the ice flow towards the margin of the ice sheet. Over the high bump of the bedrock the vertical velocities change sign, indicating that the ice deformation at that location changes from compression to extension.

The ratio of column averaged velocity (\bar{V}) to surface velocity (V_{surface}) along the flow line based on an envelope bedrock (Figure 7.10d) varies between 0.85 and 0.93 with an average of 0.89.

If λ_e and λ_m are the ratios of \bar{V} to V_{surface} based on the envelope bed and on the mean bed, and D_e and D_m are the corresponding ice thicknesses, they have the relation as (Wang and Warner, 1996):

$$F = \lambda_e V_{\text{surface}} D_e = \lambda_m V_{\text{surface}} D_m, \quad (7.1)$$

where F is balance flux and V_{surface} is surface horizontal velocity, so the ratio based on the mean bed can be obtained by

$$\lambda_m = \lambda_e \frac{D_e}{D_m}, \quad (7.2)$$

which varies from 0.72 to 0.92 with an average of 0.85, corresponding to a mean value for D_e/D_m of 0.95.

These later values tend to be somewhat lower than the suggested values of between 0.85 and 0.92 given by Budd and others (1971, p.161), 0.9 by Young

(1979) and 0.89 by Hamley and others (1985) estimated by comparing the observed surface flux with calculated balanced flux.

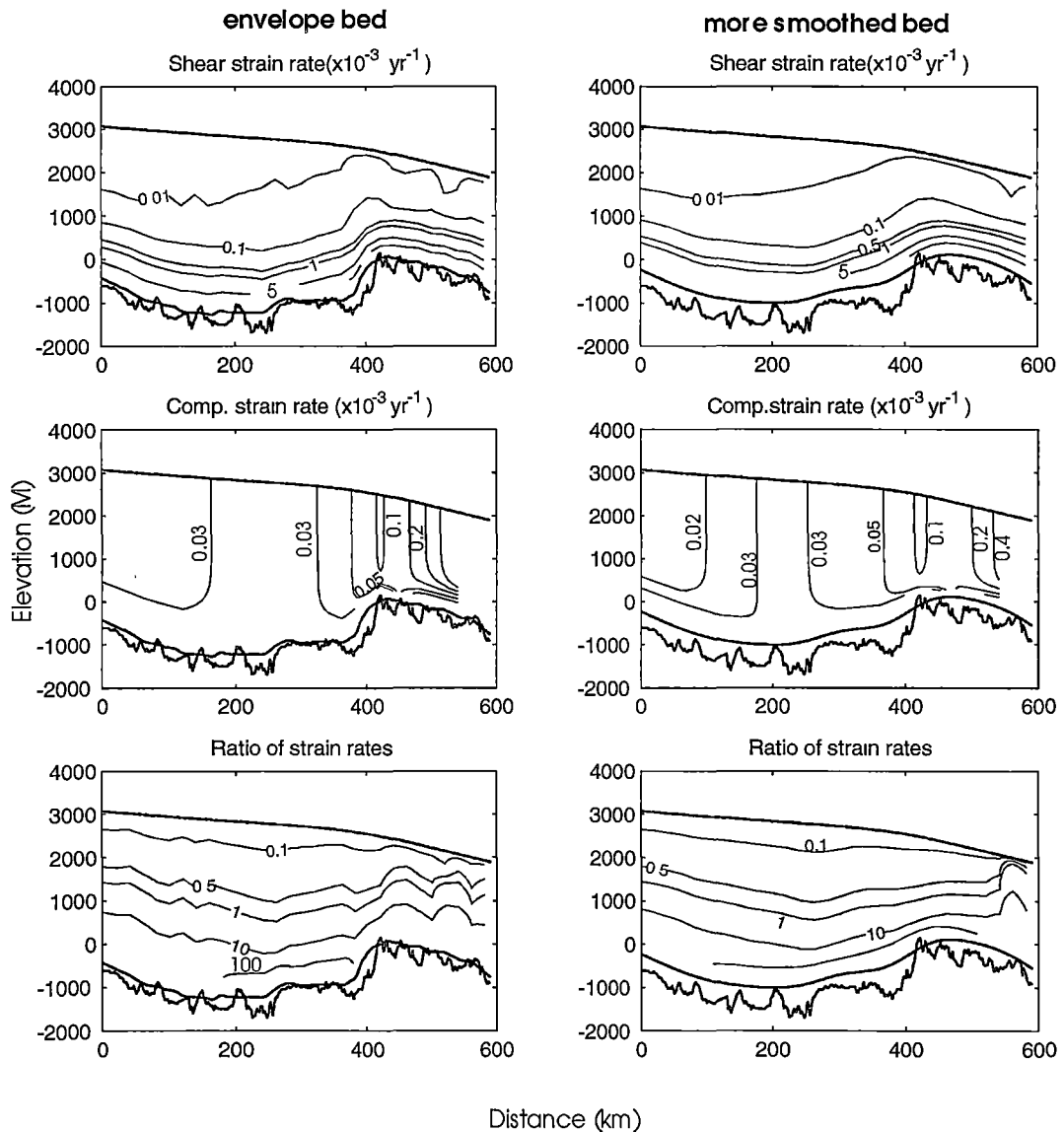


Figure 7.9. Contour plots of shear strain rate, compression strain rate and the ratio of shear strain rate to compression strain rate, resulting from the model based on the envelope bed (left side) and the more smoothed bed (right side).

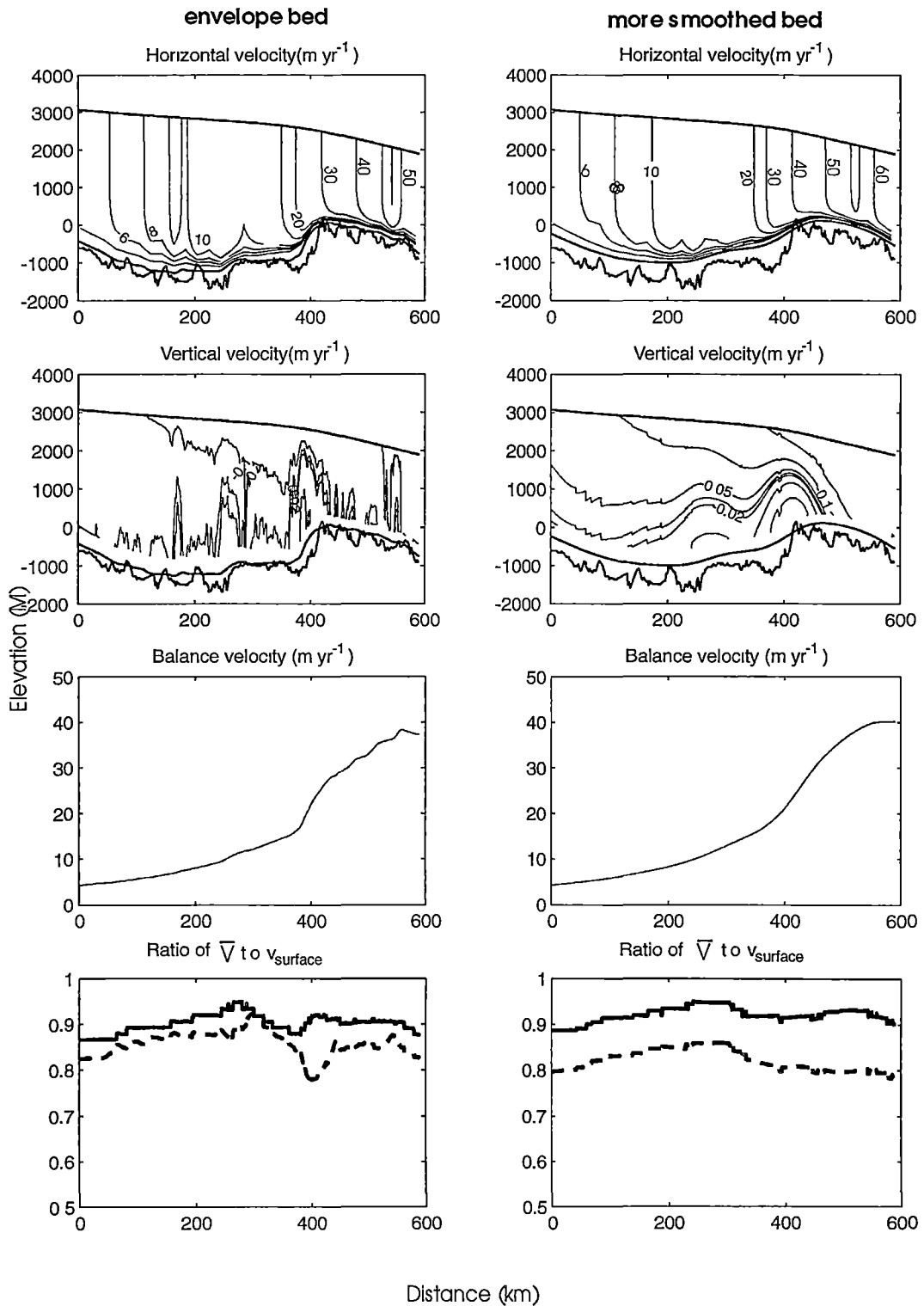


Figure 7.10. Contour plots of horizontal and vertical velocities, and the profiles of balance velocity and the ratio of horizontal column average velocity to surface velocity (solid line for envelope bed upper and dashed line lower for mean bed), resulting from the model based on the envelope bed (left side) and the more smoothed bed (right side).

7.5. High Shear Layers

Figure 7.11a is a radio-echo profile (Robin and others, 1977) showing internal layering in the Antarctic ice sheet. The layers conform to the large-scale features of the bedrock and the amplitude of the undulations decreases with increasing distance above the bed. A zone above the bedrock occurs in which internal layers failed to be recorded despite apparently adequate radar system performance. This 'echo-free basal zone' (EFBZ) is thought to be due possibly to high shear strain above the lowermost ice layers which combined with complex flow and ice intermixing over bed undulations destroys the contiguity of layers below. The high shear layers along the I.A.G.P line which resulted from our model are about 310 m above the mean bed (about 150 m above the envelope bed) (Figure 7.12a) and occur at about the depth of 91% of the ice thickness (95% for the envelope bedrock) (Figure 7.12c). A more smoothed high shear layer can be seen in Figure 7.11c which is obtained based on the more smoothed bedrock. At the high shear layer the temperature is near -5°C (Figure 7.6a). The high shear layers in the model exhibit anisotropy which enhances the flow as discussed previously.

Comparing the results here with those from the modelling of the Law Dome flow line (Chapter 6), it is found that the high shear layers along the flow line from the Dome Summit to Cape Folger also occurred at about 150 m above the envelope bedrock (see Figure 6.4f). This distance above the envelope bedrock is similar to that in the I.A.G.P. flow line, even though the ice thickness in the Law Dome flow line is only about one quarter on average of the ice thickness in the I.A.G.P. flow line. This may imply that the high shear layers in the ice sheet can be found based on an envelope bedrock computed from the variance of the bedrock elevations around a running mean bed for a range of ice thicknesses. Although the ice thickness influences the scales chosen for the smoothing and the calculation of variance it appears that the height of the envelope above the bed depends more on the amplitude of the bedrock variations rather than the ice thickness.

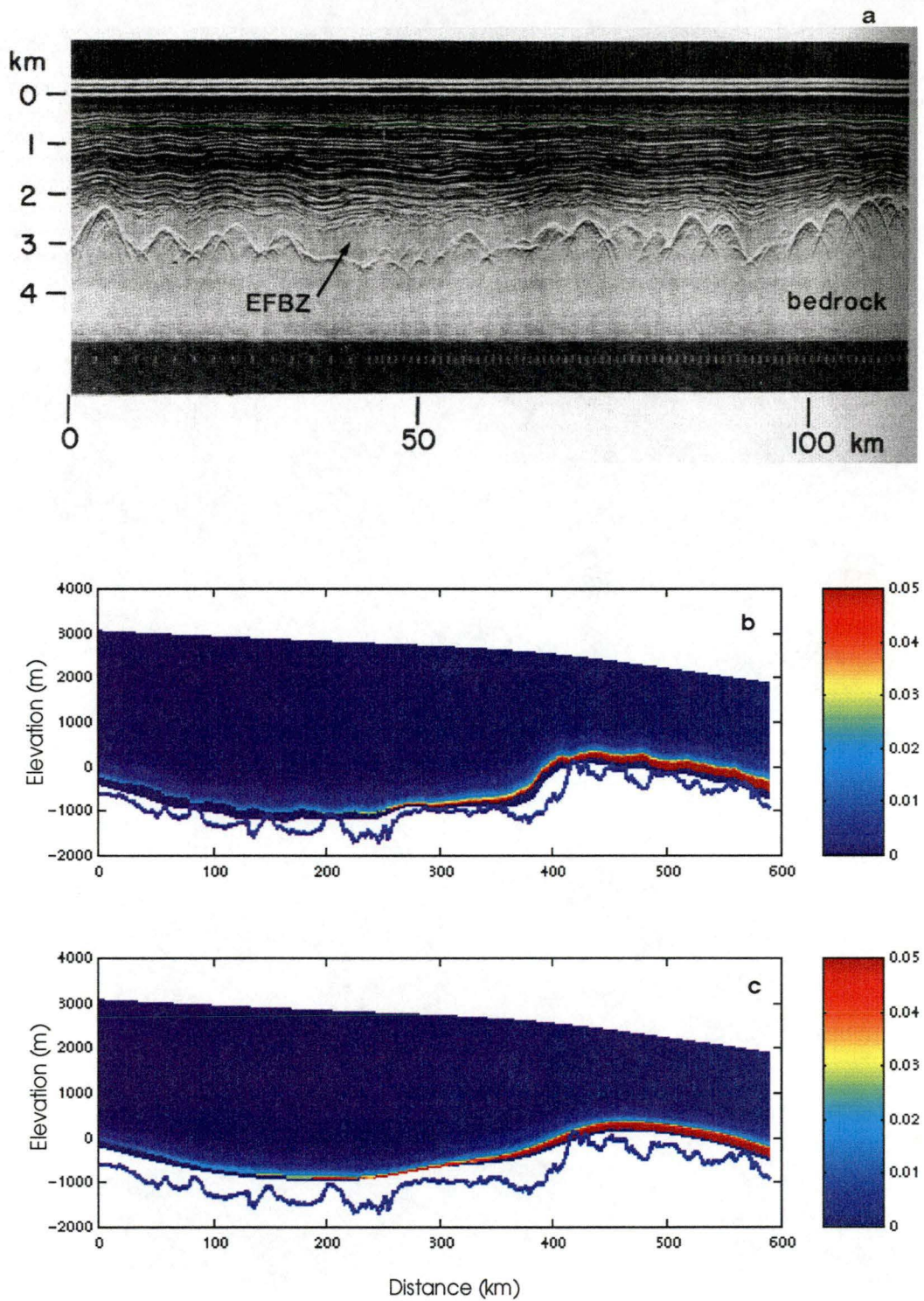


Figure 7.11. Comparison of the high shear layers. (a) is a radio-echo profile (Robin and others, 1977), (b) and (c) are shear strain rate distributions (yr^{-1}) based on the running mean bed and more smooth bed, respectively, and show the high shear layer occurring at about the depth of 95% of the ice thickness for the envelope bed.

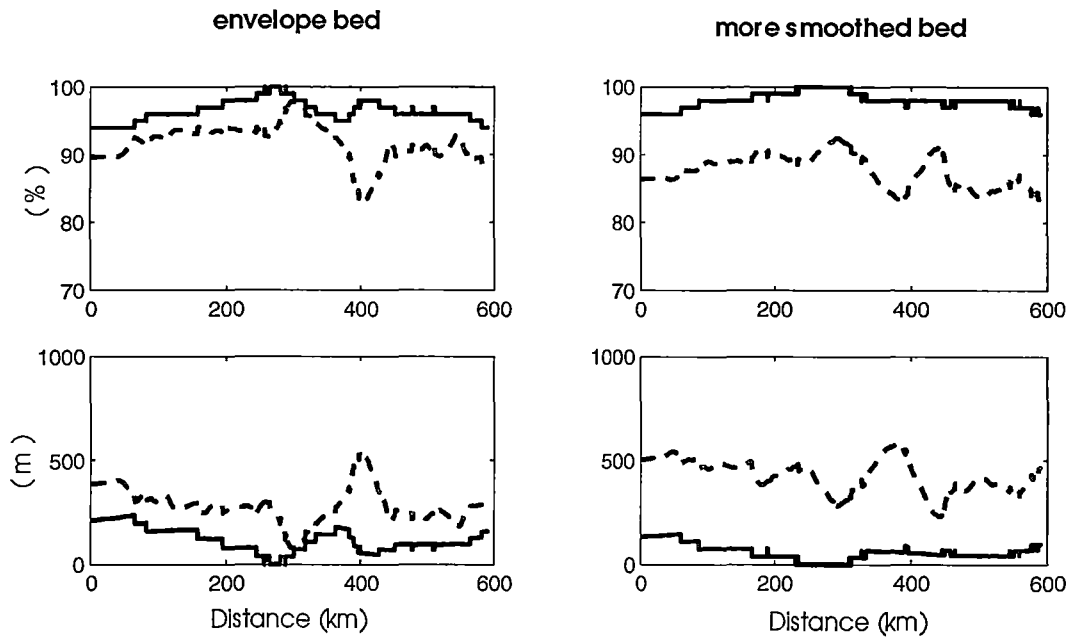


Figure 7.12. The percentage of ice thickness (top) and the depth above the bed (bottom) of the high shear layer as a function of the envelope thickness (full line) and mean thickness (dashed line) along the I.A.G.P flow line.

7.6. The Main Ice Flow Regions of the I.A.G.P Flow Line

Based on the stress configuration and the magnitudes of the strains and strain rates, resulting from the model, the ice flow regions for the I.A.G.P. line (analogous to those discussed for Law Dome in Section 6.6) are estimated and the corresponding predicted evolution of the fabric development is presented in Figure 7.13. Some related parameters are summarised in Table 7.1.

In the version of the model used in this chapter the basic assumption for the treatment of the enhancement factor is that the ice is always in tertiary flow, with the ice crystal fabric always compatible with the current stress configuration. This assumption ignores any delay in the crystal fabric responding to (becoming compatible with) the changing applied stresses, it therefore represents the most rapid response possible of the ice flow to the stress conditions. In practice the crystal structure adjustment to a new stress regime becomes accomplished in a large part by an additional 10-20% strain under the new regime. If the stress

configuration remains the same and only the magnitude of stresses changes there is relatively little change to the resulting crystal orientation fabric.

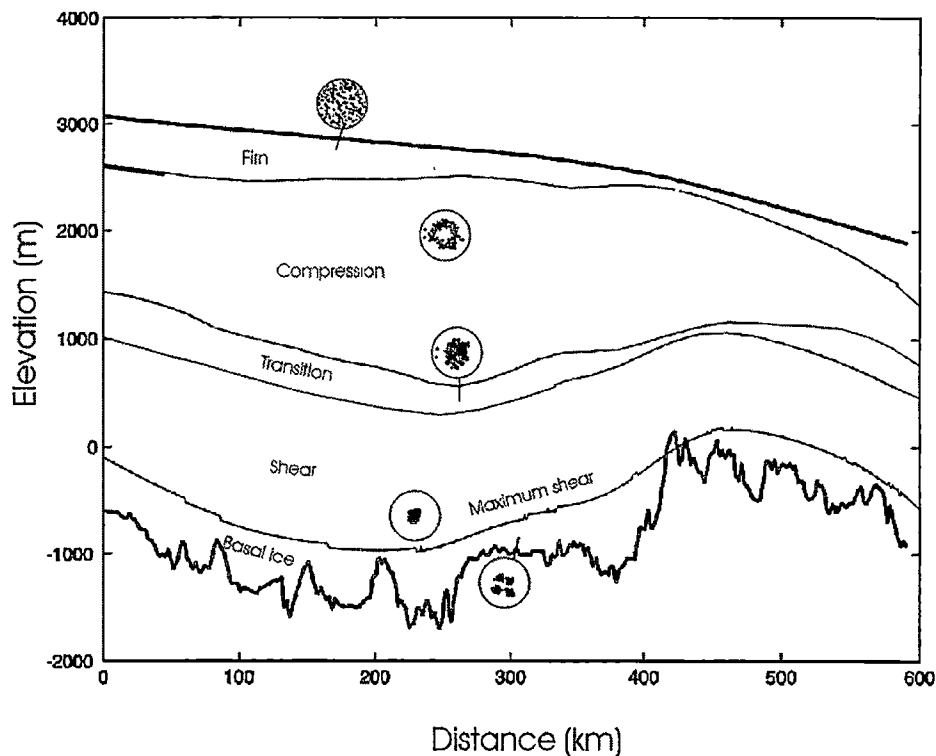


Figure 7.13. The ice flow regions for the I.A.G.P flow line. Also shown the predicted evolution of the crystal orientation fabric development, represented by suggested characteristic fabrics.

In the I.A.G.P flow line, a subdivision can be made into five typical ice flow regions which are the firn zone, the compression zone, the transition zone, the shear zone and the basal ice. The top region labelled the *firn zone* is identified by the accumulated snow and ice compression with strain less than 10% (of ice equivalent strain). In this region snow deposited on the surface undergoes a complicated compaction and densification process to form firn and eventually polycrystalline ice under its own weight. The ice is under little or no shear stress and the accumulated shear strain is only about 0.5% or less. Although the compressive stress deviator is higher, a preferred c-axis orientation fabric is not developed due to a small compressive strain usually much (less than 10%) and the partial accommodation of the compressive strain by the densification. The fabric

in this region is still expected to show an approximately random pattern. The thickness of the firm zone increases towards the inland of Antarctica, probably because of the lower accumulation rates and the lower temperatures giving a lower strain rate and a slower rate of densification with depth.

	Firm Zone	Compression zone	Transition Zone	Shear zone	Maximum Shear	Basal Zone
Temperature	surface temperature	<-30 °C	~-30 °C	30°C- -5°C	~-5 °C	near pressure melting point
Shear Strain ϵ_{xz}	<0.5%	<50%	~50%	50 - >100%	-	-
Compressive Strain ϵ_z	<10%	10-50%	~50%	>50%	-	-
Ratio of Strains $\epsilon_{xz} / \epsilon_z$	~0.03	<1	~1	1->10	>100	-
Ratio of Stresses τ_{xz} / S_z	~0.05	0.05-1	~1-2	2->100	>100	-
Enhancement Factor $E(\lambda_c)$	<3	3	3-5	5-6	~6	<6
Predicted Fabric Pattern	random	girdle	central trend or weak single maximum	single maximum	strong single maximum	multi maximum

Table 7.1. The parameters in the ice flow regions for the I.A.G.P. flow line. The general pattern for the corresponding parameters in the ice flow regions for the I.A.G.P flow line model as shown in Figure 7.13.

Below the firm layer, with the accumulating compressive strain, the ice flow is dominated by compression until shear stress overtakes the compressive stress (or shear strain rate overtakes the compressive strain rate). This is labelled the *compression zone*. In this region, the deformation of ice is mainly under the

compressive stress configuration and the compatible fabric with unconfined compressive stress configuration is a girdle pattern. The enhancement factor increases slightly with the depth to reach up to about 3 to 4. The compression zone in the I.A.G.P line contains nearly half of the ice thickness and is much thicker than that in the Law Dome flow line (see Figure 6.8).

It is well known that in an ice sheet the ice flow is dominated by compression in the upper part and by shear in the deep parts. The region where the ice flows from compression domination to shear domination is called here the *transition zone*. The boundaries of the transition zone are defined between the two layers where the shear stress is about equal to the compressive stress deviator (or the shear strain rate is equal to the compressive strain rate) or alternatively where the shear strain is equal to the compressive strain (in this case the line from the middle of the flow line to the origin is estimated). In this region, shear strain starts to accumulate faster than the compressive strain accumulation and overtakes the compressive strain at about 50% strain, the magnitude of shear stress increases to a value twice as high as the compressive stress deviator. Under this combination of shear and compressive stress configuration the fabric develops towards a single maximum (compatible with the shear stress configuration). The enhancement factor is about 4. The transition zone is a very narrow region which implies that the ice flow transforms quickly from compression domination to shear domination.

The *Shear Zone* contains the most ice deformation in an ice sheet. In this region, with a high shear stress (between 10 and 100 times higher than the compressive stress) and shear strain (larger than 100%) the ice flows faster than anywhere else. The crystals are oriented to provide the greatest amount of basal glide therefore allowing the ice to flow at a higher rate. This easy glide crystal fabric is a strong vertical single maximum pattern. The strength of this single maximum fabric increases with the depth in the ice sheet until reaching the *Maximum shear*, at a certain distance above the smoothed bedrock, where the preferred crystal orientation fabric is developed into a very strong single maximum pattern and shear strain rate reaches its maximum.

Below the maximum shear layer, the deformation of the *basal ice* is disturbed and constrained by obstruction from the higher bedrock peaks giving a reduction in the effective shear stress and strain rate. The ice is often under annealing conditions, associated with higher temperature and reduced stress. As the ice moves from high to low stress zones the stress release gives rise to extensive crystal growth together with the formation of typical multi-maximum fabrics. As well as in Law Dome (Chapter 6), these multi-maximum crystal orientation fabrics have been found near the base of ice sheets, particularly at locations where the basal ice temperature is warmer than -10°C by Gow and Williamson (1976) and Matsuda and Wakahama (1978). The thickness of basal ice in the I.A.G.P line derived from the model is similar to that found in the Law Dome flow line from both the model and the observations from the ice cores.

7.7. Summary

The application of the model based on the laboratory determined ice rheology to the I.A.G.P. line in Eastern Antarctica, has been studied in this Chapter.

The ratio of averaged column velocity to surface velocity along the I.A.G.P line is between 0.82 and 0.95 with a mean value of 0.9 for the envelope bedrock and between 0.72 and 0.92 with a mean value of 0.85 for the mean bedrock.

Based on the stress configuration and the magnitudes of strains and strain rates, resulting from the model, the ice flow regions for the I.A.G.P. line are divided into five typical and crystallographic flow regions which are the firn zone, the compression zone, the transition zone, the shear zone and the basal ice. The predicted evolution of the fabric development is shown in each ice flow region. These zones are analogues to the similar zones depicted for Law Dome where the ice cores and borehole deformation studies provide reasonable confirmation of the general pattern depicted here.

The transition zone from compression domination to shear domination along the I.A.G.P line occurs in about the middle of ice depth.

The high shear layer is at the depth containing about 91% ice thickness (95% for envelope bedrock) and about 310 m above the bed (150 m above envelope bedrock) at the temperature of about -5°C .

The thickness of basal ice in the I.A.G.P line is similar to the amount found in the Law Dome flow line. The ice at the bed over most of the I.A.G.P. flow line appears to be near to the pressure melting point, indicating some loss of ice by melting may be occurring which also may need to be taken into account in the model.

Chapter 8

INCORPORATION OF ANISOTROPIC RHEOLOGY INTO THE WHOLE ANTARCTIC ICE SHEET MODEL

The aim of the work in this Chapter is to apply the same description of the flow of ice as used for the flow lines (Chapter 6 and Chapter 7) to the whole Antarctic ice sheet, again assuming (in the first instance) that everything is in steady state.

The scheme for including the effect of octahedral stress in the shear flow law, and for calculating the enhancement effect of anisotropic ice flow developed in Chapter 4, and the simple cut-off treatment of flow in the basal regions used in Chapters 6 and 7, were reformulated as new subroutines in a three dimensional steady state thermomechanical model of the whole Antarctic ice sheet, currently being developed by Roland Warner at the Antarctic CRC. This model was then applied to provide the first indications of the effect of this anisotropic rheology scheme over the whole continent at 20 km resolution.

8.1 Model Input Data Sets

For ice sheet modelling four basic data fields are usually required for input: the surface elevation, bedrock elevation, surface accumulation and the surface temperatures. In addition, for modelling such as that carried out in Chapter 6 and 7, surface velocity data was required in order to check that the rheology was appropriate or, more correctly, that the model ice flow could be brought into agreement by modifying the flow in basal regions.

For the present study the surface elevation, bedrock elevation, surface accumulation grids and a grid classifying each grid point as grounded ice, floating

ice, bare rock or at the grounding line, have been taken from a recent compilation of data sets by Huybrechts and others (in press), with surface temperature grids from Budd and Smith (1982). These data grids of the entire Antarctic are 281x281 points with even grid spacing of 20 km and are shown in Figure 8.1.

8.2 The Running of the Model and the Results

The surface elevation data set was further smoothed by a weighted average of each grid point with its eight nearest neighbours, covering a horizontal scale of approximately 10 times the maximum ice thickness, to better reflect the large scale slopes appropriate for ice dynamics.

Since observed surface velocities are not available for a comprehensive coverage of the whole continent, the “cut-off” or rheological depth was adjusted to give a match to the balance fluxes (the depth integrated ice flow that would keep the present shape of Antarctica unchanged for the present accumulation) instead. The balance fluxes can be calculated from the assumption of a steady state balanced ice sheet using the continuity equation (A1.1). In this study the balance fluxes (Figure 8.2) were obtained using the computer program developed at the Antarctic CRC by Roland Warner which is developed from the scheme for rapid calculations of balance-flux distribution presented in Budd and Warner (1996).

Even if the ice sheet is not in fact in balance this overall coverage of balance flux provides a suitable target for choosing an effective cut-off depth of ice with the prescribed laboratory based flow law including anisotropic enhancement to give the required dynamics based flux. The aim of the study here is thus to use the model of ice flow developed in the thesis (Chapter 4) in a steady state thermomechanical ice sheet model, with an effective cut-off depth adjusted to match the ice dynamics flux to solve for the effective ice thickness. The effective bedrock or cut-off surface can then be compared with the input data. As incorporation of basal sliding into a steady state thermodynamics model can present some difficulties, and as there are various opinions about the dynamical form of the relation that is appropriate to describe sliding, it was decided to neglect sliding in this first investigation and to concentrate on the effects of enhanced deformation flow.

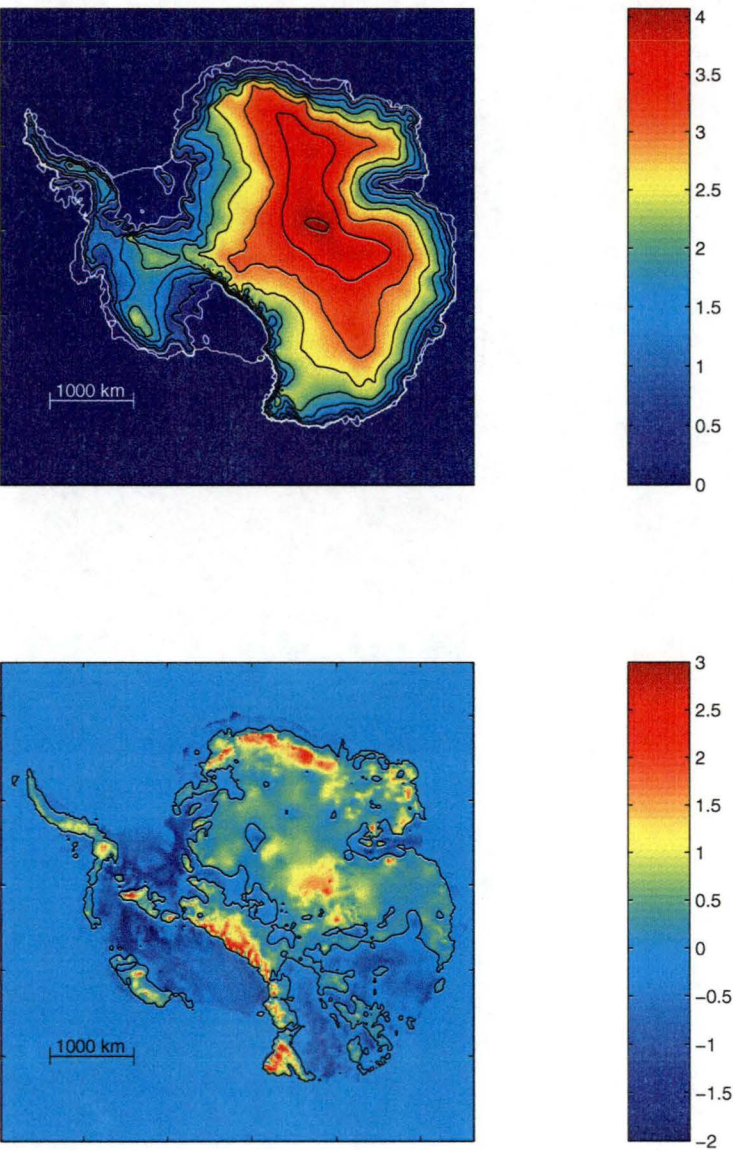


Figure 8.1. Map of surface elevation (km)(top) with 500 metre contours and Bedrock elevation (km)(bottom) over the whole Antarctic, with the sea level contour in black. Data from Huybrechts and others (in press).

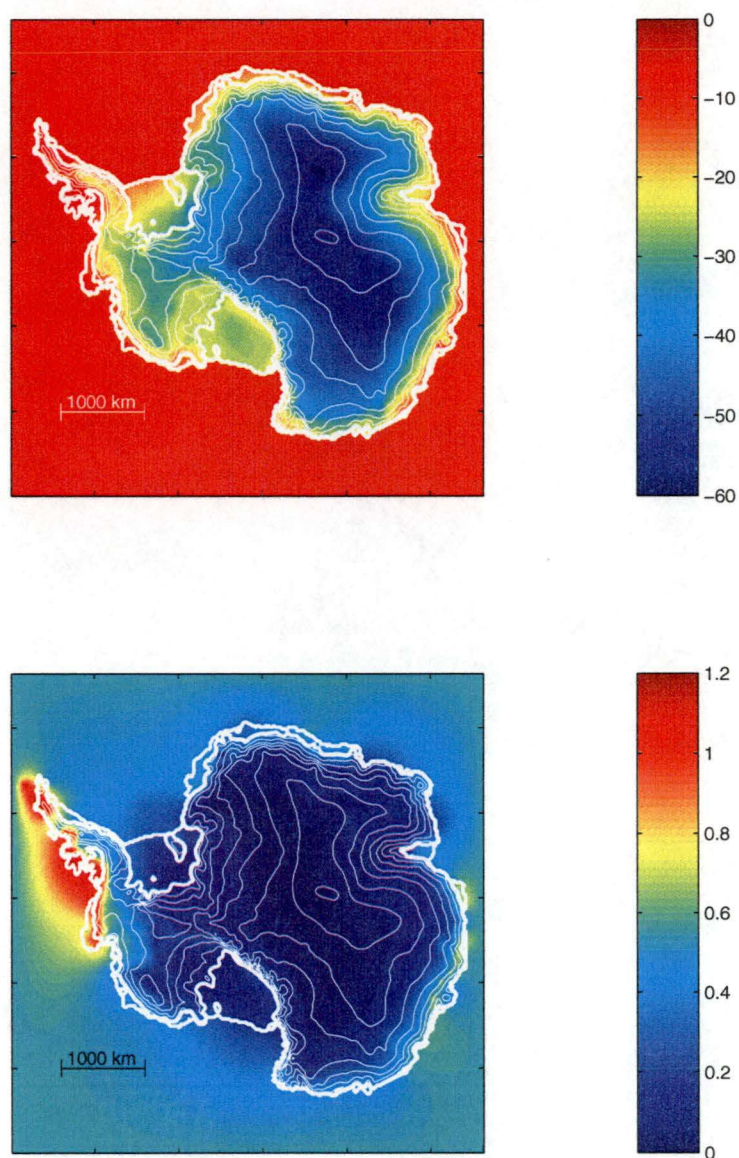


Figure 8.1. (continued). Map of surface temperature ($^{\circ}\text{C}$, data set from Budd and Smith, 1982) (top) and surface accumulation rate (m yr^{-1} ice, data set from Huybrechts and others, in press) (bottom) over the whole Antarctic ice sheet showing the contours of surface elevation at 500 metres interval.

The program calculates the steady state temperature distribution for the whole Antarctic ice sheet. It includes vertical diffusive heat flux with horizontal and vertical advection and internal mechanical heating. The heat equation was solved iteratively (see Section 4.3.3 and Figure 4.4) with the temperature dependent anisotropic ice flow relation (Equation 4.3.2.8), allowing for the feedback of temperature and mechanical heating, and also of the vertical strain rate, in calculating the shear strain rate as in the previous flow line model (Chapter 4). As in the flow line model this is alternated with iterative treatment of the enhancement factor and vertical strain rate, with the whole procedure being repeated to bring the system to equilibrium.

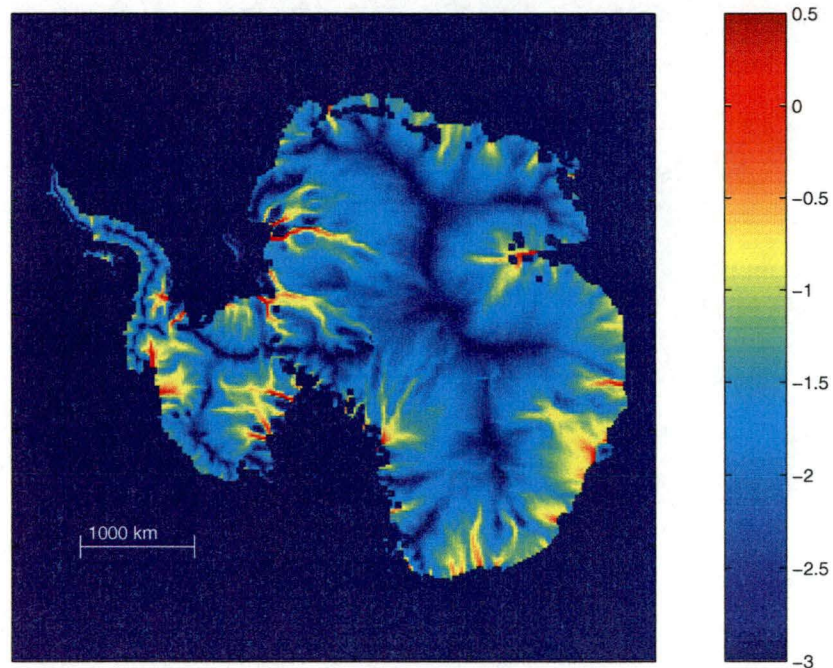


Figure 8.2. The distribution of balance fluxes ($\text{km}^2 \text{yr}^{-1}$) over the whole Antarctic grounded ice sheet, displayed on a logarithmic scale, with the bare rock mask of Huybrechts and others (in press) applied.

As in the studies for the flow lines (Chapter 6 and Chapter 7) vertical resolution was set by dividing the ice thickness into evenly spaced bands in this case 30 bands were used. The basal geothermal heat flux for the temperature calculations

was taken as 54 mW m^{-2} close to the value suggested by Huybrechts (1992) from his studies of Antarctica. This is lower than the value 78 mW m^{-2} used in Chapters 6 and 7 which was chosen because it matched the observed gradients well for the Law Dome temperature profiles. The enhancement factor calculated as a function of compression fraction, $E(\lambda_c)$ (Section 4.3.2.1), in the flow relations varies from 3 (i.e. $E_c=3$) near the top of ice sheet to 6 (i.e. $E_s=6$) with increasing depth of ice. By assuming the vertical profile of horizontal velocity with depth varies very slowly in the horizontal direction, vertical strain rates and velocities were calculated by use of the shape function described in Section 4.4.4b, along with the assumption of steady state.

Figure 8.3a shows the cut-off depth as a fraction of ice thickness, representing the depth at which the shear strain rates reach their maximum, over the whole Antarctic ice sheet. The cut-off surface is placed at the bedrock for about 30% of the grounded ice. Except where a near match occurs right at the bed this failure to generate dynamically the balance ice flux may be due to the lack of sliding or possibly due to the bedrock data set being not sufficiently deep to enable sufficiently warm ice and high shear stresses in the deeper layer of the ice sheet. Where a cut-off depth above the bedrock was obtained in matching the balance fluxes, the cut-off was located at more than 90% of the depth at 50% of the grid points and at more than 70% of the depth at 95% of grid points. Figure 8.3b shows that the cut-off layer typically lies a few hundred meters above the bedrock (50% lies within 250 meters), but in some small areas the thickness of the layer is considerably larger, reaching values of over 500 meters in approximately 10% of locations.

In some regions the cut-off depth reaches the bed. In Figure 8.4 the surface corresponding to the cut-off (high shear) layer is compared with the bedrock input data set. Note that the present scheme can only suggest a higher elevation for a “rheological” bedrock.

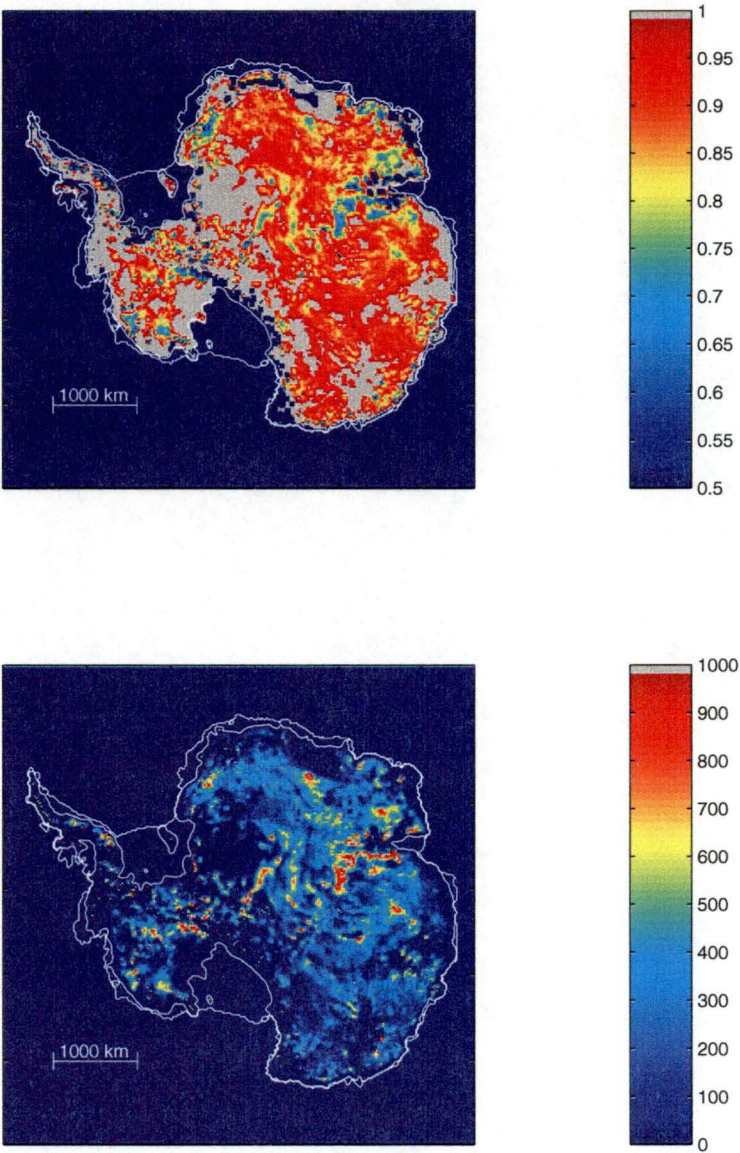


Figure 8.3. The cut-off depth (top) as a function of ice thickness and the height (m) of the cut-off layer (bottom) above the bedrock data set over the whole grounded Antarctic ice sheet. The grey band in (b) denotes values of 1000 meters or greater.

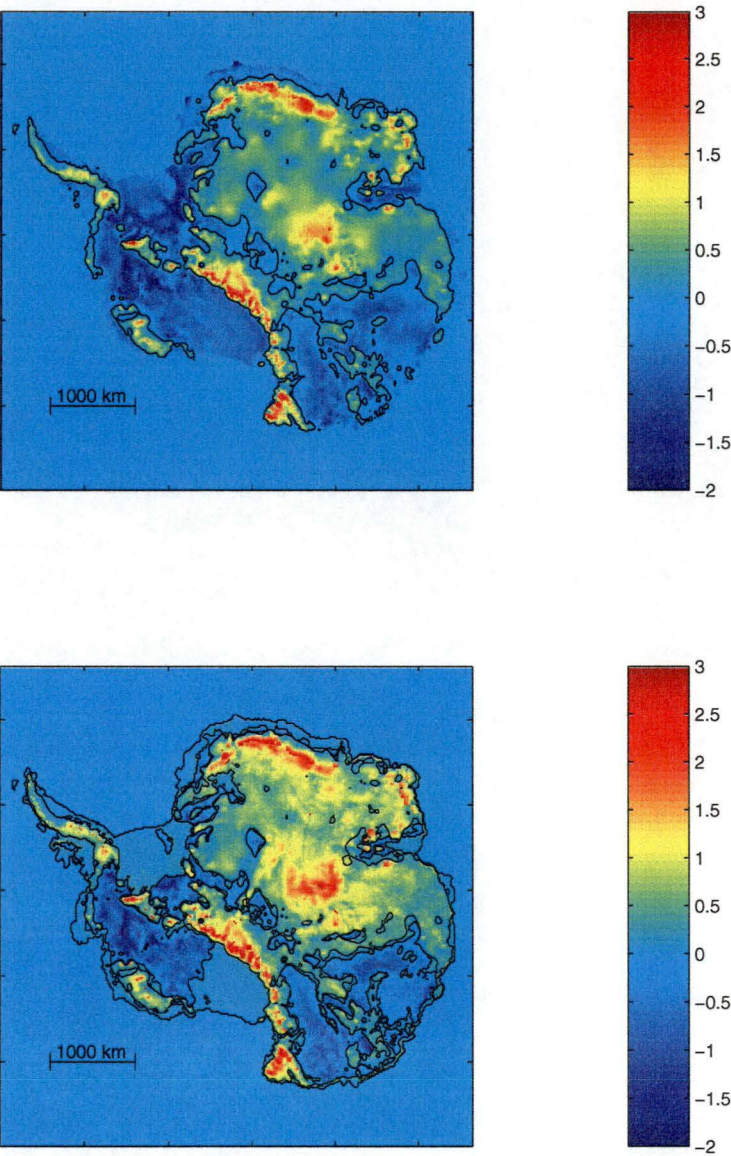


Figure 8.4. Elevations (km) of bedrock data set (top) and of cut-off layer (bottom) over the whole Antarctic ice sheet.

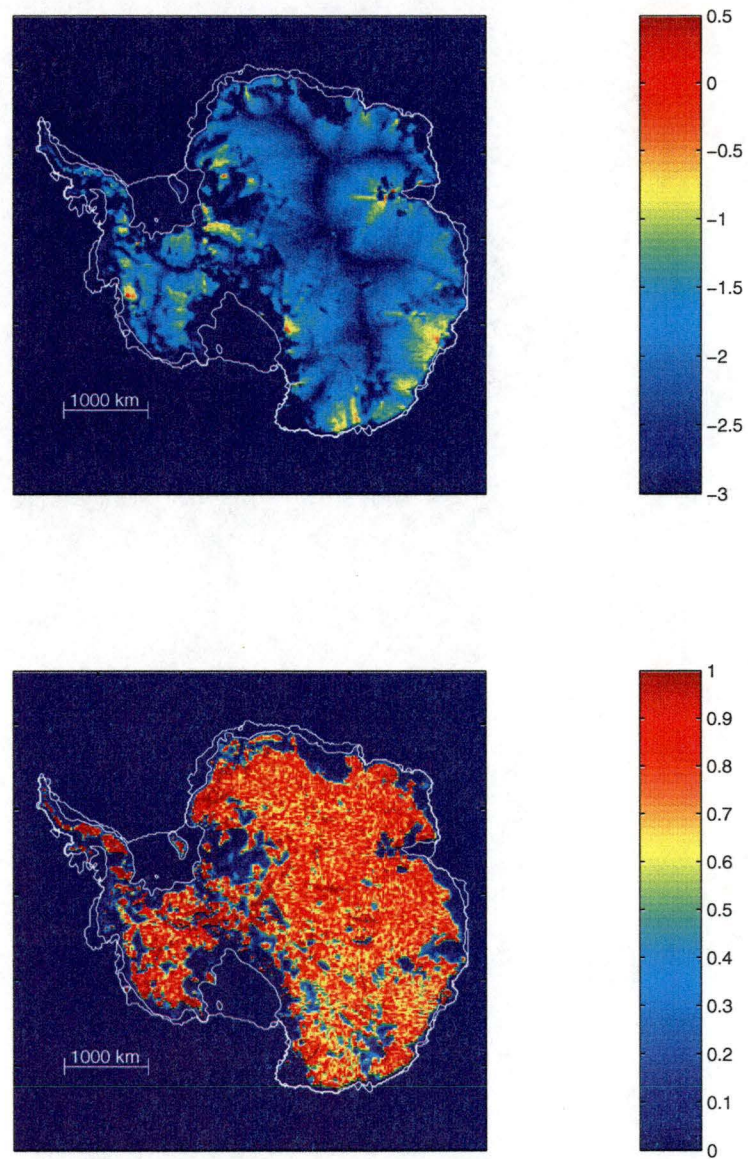


Figure 8.5. The dynamics flux ($\text{km}^2 \text{yr}^{-1}$) (top) and the ratio (bottom) of the dynamics flux to balance flux over the whole Antarctic ice sheet.

A similar procedure, using standard ice dynamics, balance fluxes and surface shape information to estimate the effective bedrock topography was recently presented by Warner and Budd (1999). A more comprehensive bedrock data set is expected to come from the international collaborative compilation of ice thickness data by the BEDMAP project of SCAR soon (Warner, personal communication).

The dynamic ice fluxes calculated by the model are presented in Figure 8.5a for comparison with the balance fluxes (Figure 8.2). In Figure 8.5b the ratio of the dynamics flux to the balance flux is presented to indicate what fraction of the balance is being explained by the deformation flow using the enhanced ice rheology. In areas where ice sliding would be important, in the ice stream regions of the West Antarctic ice sheet and the other major outlet glaciers the contribution from deformation is very small.

8.3 Comparison with the Results from the Flow Line Model along the I.A.G.P Flow Line

The I.A.G.P. flow line has sufficient extent to make it possible to interpolate from the 20 km grid of the 3-D model and make comparison with the detailed flow line modelling of Chapter 7 and the observed bedrock data. Figure 8.6 shows bedrock from observations (blue line), from the smoothed bed used in the modelling in Chapter 7 (red dashed line) and from interpolating the 3-D data set (red solid line) to the I.A.G.P. line.

Comparing the bedrock from the 20 km data set with the observations it is clear that in the region for 400 - 600 km of the I.A.G.P. line, the data set bedrock which is apparently based here on the Drewry Folio (1983), completely misses the rise in the actual bed which is captured quite well by the envelope and dynamics scheme used here. Further inland in the first half of the figure the data set resembles the envelope bed over the rough topography.

The close agreement between the two cut-off layers (black lines in Figure 8.6) in spite of the different bedrock inputs used in the two models further suggests that a very high cut-off layer may be a sign of deficiencies in the bedrock data,

especially when this happens away from deep bedrock depressions where it might genuinely indicate a high shear layer above a thick layer of stagnant ice. General agreement also can be seen in some other output results, as shown in Figure 8.7, including temperature, enhancement factor, shear strain rate and the ratio of shear strain rate to compressive strain rate, from the 3-D model (right side) in this chapter and from the flow line model in Chapter 7 along the I.A.G.P. flow line.

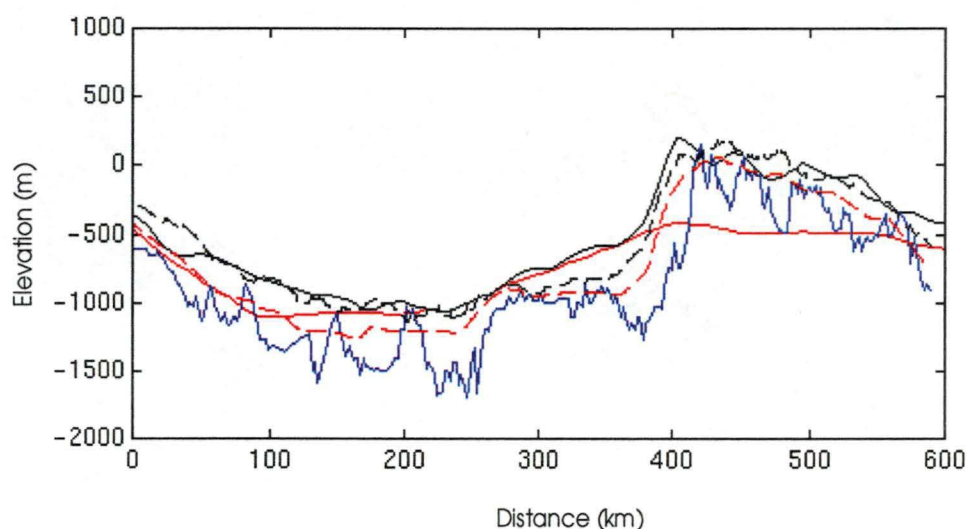


Figure 8.6. The bedrock comparison along the I.A.G.P flow line. Red solid line indicates the bedrock from the data set used in this study, blue line the bedrock from the observations (Chapter 7), black solid line the cut-off layer in this study, black dashed line and red dashed line the cut-off layer and the envelope bed, respectively, from the study of the flow line model in Chapter 7.

Even though the geothermal heat fluxes are different in the whole Antarctic ice sheet model compared with the I.A.G.P. flow line model (see Figure 7.3a), the temperature distributions from the 3-D model and from the flow line model are similar, which may indicate that if the basal temperatures are near to the pressure melting point then different geothermal heat fluxes may not have much influence on the temperature profiles. The section extraction from the 3-D model appears to contain some colder ice advected from the interior of the continent.

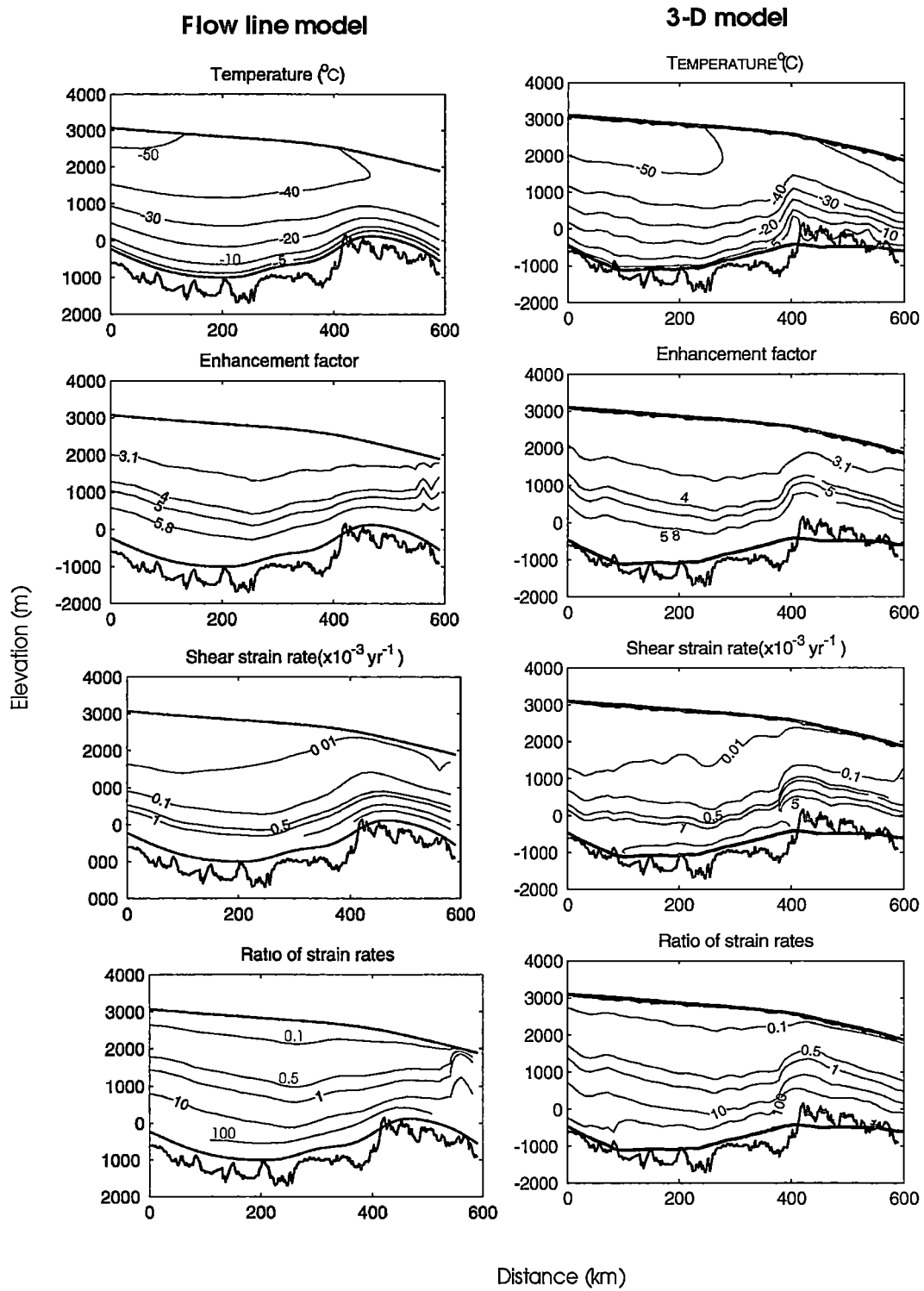


Figure 8.7. Contour plots of temperature, enhancement factor, shear strain rate and the ratio of shear strain rate to compression strain rate from the flow line model (left side) based on the more smoothed bed and 3-D model (right side).

8.4. Concluding Remarks

This application of the anisotropic rheology in the 3-D model, incorporating the estimate of the octahedral stress, and including the enhancement of shear flow, has provided reasonable flow rates for a steady state simulation of the Antarctic ice sheet, if one is prepared to accept the adjustments made to shear strain rates in the basal layers. This suggests again that more attention needs to be paid to flow in these deep regions of the ice sheet. As the present bedrock data is quite uncertain over a considerable of part of Antarctica, this cut-off adjustment is perhaps a more reasonable approach to estimating the form of the large scale smooth bed topography in regions of poor data coverage than by using simple interpolation, and where the cut-off layer lies far above the bedrock, the bedrock input data itself may be called into question. Other inputs such as the geothermal heat flux are also not well determined, and there is scope to explore other values.

Chapter 9

CONCLUSION AND FURTHER OUTLOOK

9.1. Summary and Conclusions

In this thesis a model for anisotropic ice flow in a polar ice sheet was developed. The scheme for developing the anisotropic flow rates is based on the combination of laboratory measurements of ice rheology and shear deformation rates measured in boreholes through the ice. Although the model is set up as a steady state dynamic and thermodynamic flow line model there is no fundamental restriction on its application to time varying flow.

To incorporate the effect of ice fabric anisotropy on the flow of ice into an ice sheet model an “enhancement factor” is applied to the relationship between stress and strain rate (i.e. the constitutive relation for ice) as the ice passes through a range of stress regimes from predominantly vertical compression in the upper layers to predominantly shear stress, as it flows down through the ice sheet towards the bed. The enhancement factor represents the increased flow rate of anisotropic ice, in steady state tertiary flow, relative to that of isotropic ice at minimum strain rate under the same stress and temperature conditions. The laboratory experiments and the analysis of the borehole measurements give information about the magnitude of shear enhancement. The transition from minimum creep to tertiary flow and the concept of development of compatible crystal fabrics related to the stress situation, initially motivated the formulation of an enhancement factor based on the ice history, using a simple description in terms of the ratio of shear strain to compressive strain, in an attempt to take

account of the considerable compressive strain accumulated in natural ice sheets before the shear zone is reached. (It would be possible to investigate a more complicated dependence on shear and compressive strains).

The combined stress experiments, and the assumption of maintaining a compatible fabric that developed in step with the changing stress situation, provided the basis for the second enhancement scheme, based on the compressive stress fraction λ_c which was modelled by using strain rate ratios.

To test this model two different flow lines in the Antarctic ice sheet have been studied. One flow line is in the Law Dome Ice Cap near the margin of the Antarctic ice sheet. The second one is from an I.A.G.P traverse line in the interior of the Antarctic ice sheet in Wilkes Land. The model was also applied to a study of the shear strain rate profile from the borehole at Dome Summit South on Law Dome.

Modifications of the simple model predictions for high shear strain rates in the lower layers of the ice sheet were required in order to match the observed surface velocities and the observed borehole shear rates. In these lower regions reductions in the enhancement of shear flow and also in the shear stress are required to produce good agreement with surface velocities. For Law Dome, where inclination measurements are available for several boreholes, the shear strain rate profiles from the field observations and the model are in good agreement in the upper part of the ice sheet, emphasizing that more attention needs to be given to the dynamics deep within ice sheets, near the bed.

Based on the stress configurations and the magnitude of strains and strain rates, resulting from the model, the ice flow regions for those two flow lines were divided into five typical ice flow regions. These different flow regions are expected to have distinctive crystallographic structures with the estimated preferred crystal orientation fabric in each zone as follows: the firn zone with a random fabric pattern, the compression zone with a girdle (or two maxima) fabric pattern, the transition zone with a central trend or weak maximum fabric pattern, the shear zone with a strong single maximum fabric pattern and the variable basal ice with often a multi-maximum fabric pattern and large crystals. This general

picture is in consistent agreement with the observations from the Law Dome ice cores and boreholes.

From the model the transition zone from compression domination to shear domination along the I.A.G.P line occurs in the middle of the ice depth, proportionately lower than where it appears for the Law Dome flow line, indicating that towards the interior of the Antarctic ice sheet the compression zone becomes thicker and contains more ice.

The high shear layers along the I.A.G.P line resulting from the model are about 150 m above the envelope bedrock which represents a depth of about 95% of the ice thickness based on the envelope bedrock. Comparing this with the Law Dome flow line, it was found that the high shear layers along the flow line from the Dome Summit to Cape Folger also occur at about 150 m above the envelope bedrock, even though the ice thickness in the Law Dome flow line is only on average about one quarter of the ice thickness in the I.A.G.P. flow line. This may imply that the high shear layers in the ice sheet can be found at consistent levels above an envelope bedrock computed from the variance of the bedrock topographic variations about the mean bed over appropriate distance scales.

It was found here that an envelope bed about 1 SD (Standard Deviation) of the roughness above the smoothed mean bed appeared to give a reasonable representation of an “effective bed” for ice dynamics. The apparent high shear layer was found to be a similar distance above that effective bed i.e. about 2 SD above the mean bed. This may be interpreted as follows. Above 2 SD from the mean bed, where less than about 5% of the above average bedrock peaks protrude, the shear flow is sufficiently undisturbed by the bedrock irregularities to allow the formation of a practically continuous layer of high shear anisotropic ice with strong vertical single maximum c-axis fabrics. Between 1 SD and 2 SD, which is penetrated by about one third of the above mean bedrock peaks, the ice flow may be sufficiently disturbed to prevent such a near continuous high shear layer of anisotropic ice from forming. These irregularities could also reduce the average horizontal shear stress in this layer and replace it by drag from longitudinal and transverse stresses associated with the ice flow over and around the higher bedrock protrusions.

Since the shallow ice approximation for ice flow only holds for horizontal scales of the order of 10 ice thickness or more it seems appropriate that the bed and ice thickness should be smoothed on about that same scale. The smaller scale variations can be regarded as roughness and can be treated by the approach taken here using an envelope bed of 1 SD above the mean bed and with an anisotropic high shear layer above about 2 SD from the mean bed.

Where the sub-ice topography is smooth on these scales (in the line of flow) it can be expected that the envelope bed will coincide with the mean bed and in that case the strong crystal anisotropy and the maximum shear rate can also be expected to occur right at the real bed. This may be the typical situation for the fast flowing ice streams and outlet glaciers where the bed has been deepened and smoothed by erosion.

The relationship between enhancement factors based on the borehole inclinations for several boreholes in Law Dome and the ice deformation tests and fabric parameter, $\phi(1/4)$ (the half-apex angle of the cone containing 25% of the c-axis crystals) was also investigated. The general feature is that the enhancement factor increases with the fabric strengthening. When the fabric parameter $\phi(1/4)$ reduces from about 37° (near the theoretical value for a random fabric pattern) to its minimum at about 9° (a strong single maximum fabric pattern) the enhancement factor increases generally (non-linearly) from 1 to about 6. These relations have been used to help depict the evolution of the fabric development in the I.A.G.P flow line. However since there are still some uncertainties regarding the enhancement factors, particularly for the individual strain rate components in combined stress situations, further studies were carried out with the enhancement in shear varying from 3 to 10.

The ratio of the depth-averaged velocity to the surface velocity represents the relationship between the column-integrated ice flux and the flux computed from the measurements of ice sheet thickness and the surface velocity. To determine the state of ice sheet mass balance from the ice accumulation distributions and ice sheet surface topography this relationship must be considered. This ratio has been calculated in the present work. Along the I.A.G.P line it is between 0.72 and 0.92 with a mean value of 0.85 which is somewhat lower than the suggested values of

between 0.85 and 0.92 given by Budd and others (1971, p.161), 0.9 by Young (1979) and 0.89 by Hamley and others (1985) estimated from modelling with isotropic ice flow properties and used for comparing the observed surface flux with calculated balanced flux. On the Law Dome flow line this ratio is computed from the present model to range between 0.65 and 0.82 with a mean value of 0.75. At the DSS site it is computed to be 0.73 which is close to the value of 0.74 determined by the borehole measurements, and 0.76 (Morgan and others, 1998) calculated by assuming the local ice sheet is in mass balance and matching accumulation with the outflow around DSS determined by surface strain data. Compared with the value of 0.8 for a cubic flow law with isothermal isotropic ice (see Paterson, 1994, p.251-252), this ratio is usually expected to be increased by the effect of warmer, more deformable ice deeper in the ice sheet, an effect which would be expected to be further increased by enhanced flow. The lower values at DSS and along the Law Dome flow line reflect the large proportion of basal ice below the maximum shear layer, with reduced basal shear stresses and variable ice fabrics tending to contribute smaller shear strain rates in spite of the relatively higher temperature. The ice flow at DSS may also be complicated by the role of longitudinal stresses within a few ice thicknesses of the Dome Summit and the influence of the quite rough bedrock topography in that region.

The incorporation of anisotropic rheology into the whole Antarctic ice sheet model was studied by applying the same description for the anisotropic ice flow used for the flow lines (Chapter 6 and Chapter 7) to a model of the whole Antarctic ice sheet. Ice thickness cut-off layers appropriate for high shearing over rough bedrock topography along the I.A.G.P flow line shows good agreement between the 3-D model and the flow line model.

The comparison of the 3-D model with the flow line model and the field data for the I.A.G.P flow line suggested that the anisotropic enhancement of ice flow was able to provide an acceptable match to the balance flux. It also gave an indication that particularly thick “cut-off” layers in the model might be indicative of discrepancies in the bedrock dataset, which can now be re-examined in relation to the actual observations. In some regions the high shear layer was placed right at the bedrock and the model dynamic flux did not reach the target balance fluxes. In some regions such as the ice stream regions of West Antarctica and other outlet

glaciers this may be due to the neglect of basal sliding in the present formulation. In some other regions it might also reflect places where the bedrock data set underestimates the thickness of the ice sheet.

9.2. The Need for Further Studies

As mentioned above, in this thesis the effect of ice fabric anisotropy on the flow of ice was incorporated into an ice sheet model via the derivation of a variable prognostic “enhancement factor” in the ice flow relations (i.e. relation between stress and strain rate). The functional relation for the enhancement factor with position was based on the laboratory studies of the development of anisotropic tertiary flow rates for different stress configurations and the modelling of the stresses, strain rates and strains through the ice sheet as a function of position in the ice sheet. For comparison, it is worth examining further the potential of some other suggested ice flow relations for anisotropic ice flow, for example, Azuma’s model (Azuma and Goto-Azuma, 1996). However it would be important to first show that such a scheme can be used to match the laboratory determined anisotropic flow rates and crystallographic evolution and can also generate the ice fabrics and shear rate development in the ice sheet as observed in the ice cores and boreholes.

The relationship (Figure 3.10) of enhancement factor to fabric parameter $\phi(1/4)$, based on the borehole inclinations and ice core measurements in Law Dome and on laboratory experiments, has also been studied in this thesis. The possibility of using this relation for a given fabric, along with the more explicit evolution of the fabric with strain, to obtain the enhancement factor for the present ice dynamics model also deserves further study, and a comparison with predictions of models relating anisotropic flow to crystal fabrics, such as Lliboutry (1993), Azuma (1994) and Van der Veen and Whillans (1994), would be interesting.

Based on the analysis that the ratio of shear enhancement to compressive enhancement is of order unity (see Section 4.3.2 for details), the current model took the same enhancement factors for the shear and the compression components as for the enhancement of the octahedral strain rate. The laboratory data and further analysis by Warner and others (1999) shows that different influences of

increasing compression on the shear rate compared with the effect of increasing shear on the compression rate, may need to be considered in the model by using different enhancements for shear and compression components individually.

In the present model the ice dynamics was driven by the shallow ice approximation for the shear stress, with the influence of vertical compression on the horizontal shear strain rate being estimated through the flow relations and a model for the vertical strain rate. It would be appropriate to apply a more complicated set of component flow relations to a solution of the complete stress equilibrium equations for the flow line.

The flow lines in the Law Dome Summit area have also been generated in this thesis (Figure 5.4). This gives us the possibility to apply the current model to a flow line from the Dome Summit through the DSS site. Recent work by Morgan and others (personal communication) has now established a more accurate time scale for the DSS core. The comparison of the results from such a flow line study with the observations from the borehole will provide more information about the internal dynamics of the ice in Law Dome.

Basal sliding needs to be studied more extensively in the model. Surface velocity measurements and borehole inclination measurements near the margin of the Law Dome at the BHC1 and BHC2 boreholes, where the ice is relatively thin, (less than 300 m, Etheridge, 1989) reveal that approximately half the ice motion there is due to basal sliding. The temperature distribution in the I.A.G.P line also indicates that the ice near the bed may be near the pressure melting point. In the study for the Law Dome flow line, the form of the equation to calculate sliding velocity was adopted from Budd and others (1984) using the observations from the regions of the BHC1 and BHC2 boreholes. It is still not well known how such a sliding relation performs for the much thicker ice of the interior or for the fast flowing ice streams as they approach floating. The model including an appropriate sliding formulation needs to be tested in a region where comprehensive data sets including ice thickness and surface velocity are available. In such regions the transverse shear strain rates may also need to be taken into account including the possible development of strong shear enhancement fabrics

at the margins of the ice streams (e.g. Echelmeyer and others, 1994; Whillans and Van der Veen, 1997).

For the I.A.G.P flow line the detailed information from the field observations including bedrock, surface elevation and velocity also provides the possibility to determine the state of balance by comparing the balance fluxes with the actual fluxes.

With the envelope orography the match between the observed surface velocities and the computed surface velocities from the model implies compatibility with the laboratory based flow properties of ice including anisotropy. The model also provides a value for the ratio of the average column velocity to the surface velocity which is required to obtain the column average flux for the assessment of the mass balance.

References

- Alley, R.B. 1988. Fabrics on polar ice sheets: development and prediction. *Science* **240** (4851), 493-495.
- Alley, R.B. 1992. Flow law hypotheses for ice-sheet modeling. *Journal of Glaciology* **38** (129), 245-256.
- Anonymous. 1971. International Antarctic Glaciological Project. *Polar Record*. Vol. **15**, No. 98, 829-833.
- Azuma, N. and Higashi, A. 1984. Mechanical properties of Dye 3 Greenland deep ice cores. *Annals of Glaciology* **5**, 1-8.
- Azuma, N. and Higashi, A. 1985. Formation processes of ice fabric pattern in ice sheets. *Annals of Glaciology* **6**, 130-134.
- Azuma, N. 1994. A flow law for anisotropic ice and its application to ice sheets. *Earth and Planetary Science letters*, **128**, 601-614.
- Azuma, N. 1995. A flow law for anisotropic polycrystalline ice under uniaxial compressive deformation. *Cold Regions Science and Technology* **23**, 137-147.
- Azuma, N. and K. Goto-Azuma. 1996. An anisotropic flow law for ice-sheet ice and its implications. *Annals of Glaciology* **23**, 202-208.
- Azuma, N. 1997. The evolution of fabric and flow property of ice predicted by an anisotropic flow law. *Report of the workshop on rheology and anisotropy (EISMINT), Grindelwald, switzerland*. (abstract).
- Baker, R. W. 1981. Texture and crystal fabric anisotropies and flow of ice masses. *Science* **211**, 1043-1044.
- Baker, R. W. 1982. A flow equation for anisotropic ice. *Cold Regions Science and Technology* **6**(2), 141-148.

References

- Baker, R. W. 1987. Is the creep of ice really independent of the third deviatoric stress invariant? IUGG General Assembly of Vancouver, Aug.1987, *IAHS Publication* **170**, 7-16.
- Bamber, J.L. 1994. A digital elevation model of the Antarctic ice sheet derived from ERS-1 altimeter data and comparison with terrestrial measurements. *Annals of Glaciology* **20**, 48-54.
- Bindschadler, R. 1983. The importance of pressurized subglacial water in separation and sliding at the glacier bed. *Journal of Glaciology* **29**(101), 3-19.
- Bouchez, J.L. and P. Duval. 1982. The fabric of polycrystalline ice deformed in simple shear: experiments in torsion, natural deformation and geometrical interpretation. *Textures and Microstructures*. **5**, 171-190.
- Budd, W.F. 1966. Glaciological studies in the region of Wilkes, eastern Antarctica, 1961: *ANARE Scientific Report, Series A (IV) Glaciology*, Publication No. **88**, 152 pages.
- Budd, W.F. 1968 The longitudinal velocity profile of large ice masses. *IAHS Publication* **79**, 58-77.
- Budd, W.F. 1969. The dynamics of ice masses. *ANARE Scientific Report, Series A (IV) Glaciology*, Publication No. **108**, 216 pages.
- Budd, W.F. 1970a. Ice flow over bedrock perturbations. *Journal of Glaciology* **9**(55), 29-48.
- Budd, W.F. 1970. The Wilkes ice cap project. *IAHS Publication* **86**, 414-429.
- Budd, W.F. 1971. Stress variations with ice flow over undulations. *Journal of Glaciology* **10**(59), 177- 195.
- Budd, W.F. 1972. The development of crystal orientation fabrics in moving ice. *Zeitschrift fr Gletscherkunde und Glazialgeologie*, **8** (1-2), 65-105.
- Budd, W.F. 1975. Numerical modelling of glacier systems. *IAHS Publication* **104**, 257-291.

References

- Budd, W.F. 1976. Ice sliding and friction experiments. *Journal of Glaciology* **16** (74), 279-280.
- Budd, W.F., D. Jenssen and U. Radok. 1971 Derived physical characteristics of the Antarctic ice sheet. *ANARE Scientific Report, Publication No.120*, 178p + maps.
- Budd, W.F., and Matsuda, M. 1974 Nijiku-kuripu asshuka ni okeru takesshohyo no sentaku-hoisei ni tsuite [On preferred orientation of polycrystalline ice by biaxial creep]. *Teion-kagaku: Low Temperature Science Series A* (32), 261-265.
- Budd, W.F., N.W. Young and C.R. Austin. 1976. Measured and computed temperature distribution in the Law Dome ice cape, Antarctica. *Journal of Glaciology* **16** (74), 99-110.
- Budd, W.F. and V.I. Morgan. 1977. Isotopes, climate and ice sheet dynamics from core studies on Law Dome, Antarctica. *IAHS Publication* **118**, 312-321.
- Budd W.F., Keage, P.L. and Blundy, N.A. 1979. Empirical studies of ice sliding. *Journal of Glaciology* **23**(89), 157-170.
- Budd W.F. and N.W. Young. 1979. Results from the I.A.G.P. flow-line study inland of Casey, Wilkes Land, Antarctica. *Journal of Glaciology* **24** (90), 89-101.
- Budd, W.F., T.H. Jacka, D. Jenssen, U. Radok and N.W. Young. 1982. Derived physical characteristics of the Greenland ice sheet. *The University of Melbourne Meteorology Department, Publication No. 23*, 103 pages.
- Budd W.F. and Smith, I.N. 1982. Large-scale numerical modeling of the Antarctic ice sheet. *Annals of Glaciology* **3**, 42-49.
- Budd W.F., Jenssen, D. and Smith, I.N. 1984. A three dimensional, time dependent model of the West Antarctic Ice Sheet. *Annals of Glaciology* **5**, 29-36.

References

- Budd, W. F., and R. J. M. Rowden-Rich, 1985. Finite element analysis of two-dimensional longitudinal section flow on Law Dome. *ANARE Research Notes*, **28**, 153-161.
- Budd, W.F. and D. Jenssen. 1989. The dynamics of the Antarctic ice sheet. *Annals of Glaciology* **12**, 16-22.
- Budd, W.F. and T.H. Jacka. 1989. A review of ice rheology for ice sheet modelling. *Cold Regions Science and Technology* **16** (2), 107-144.
- Budd, W.F. and I.N. Smith. 1985. The state of balance of the Antarctic ice sheet. *Glaciers, ice sheets, and sea level: effect of a CO₂-induced climatic change, Report of Workshop held in Seattle, Washington, September 13-15, 1984*. Washington, DC, US Department of Energy. Office of Energy Research, 172-177. (Attachment 9, Report DOE/ER/60235-1)
- Budd, W.F. and R.C. Warner. 1996. A computer scheme for rapid calculations of balance-flux distributions. *Annals of Glaciology* **23**, 21-27.
- Budd, W.F., T.H. Jacka, Li Jun and R.C. Warner. In preparation. Ice flow relations for individual components in combined shear and compression.
- Cameron, R.L. 1964. Glaciological studies at Wilkes station, Budd Coast, Antarctica. *Antarctic Research series* **2**. 1-36. American Geophysical Union.
- Carter, D. 1976. Wilkes ice cap project 1967. M.Sc. Thesis, *Department of Meteorology, The University of Melbourne*.
- Castelnau, O. and P. Duval. 1994. Simulations of anisotropy and fabric development in polar ices. *Annals of Glaciology* **20**, 277-282.
- Castelnau, O., Th. Thorsteinsson, J. Kipfstuhl, P. Duval and G.R. Canova. 1996a. Modelling fabric development along the GRIP ice core, central Greenland. *Annals of Glaciology* **23**, 194-201.
- Castelnau, O., P. Duval, R.A. Lebensohn and G.R. Canova. 1996b. Viscoplastic modelling of texture development in polycrystalline ice with a self-consistent approach: comparison with bound estimates. *Journal of Geophysics research* **101** (B12), 13851-13868.

References

- Curran, M.A.J., T.D. Van Ommen and V.I. Morgan. 1998. Seasonal characteristics of the major ions in the high-accumulation Dome Summit South ice core, Law Dome, Antarctica. *Annals of Glaciology* **27**, 385-390.
- Dahl-Jensen, D. 1985. Determination of the flow properties at Dye 3, south Greenland, by bore-hole-tilting measurements and perturbation modeling. *Journal of Glaciology* **31** (108), 92-98.
- Dahl-Jensen, D. and Gundestrup, N.S. 1987. Constitutive properties of ice at Dye 3, Greenland. IUGG General Assembly of Vancouver, Aug.1987, *IASH Publication* **170**, 31- 43.
- Dahl-Jensen, D. 1997. Anisotropic flow law. *Report of the workshop on rheology and anisotropy (EISMINT), Grindelwald, switzerland.* (abstract).
- Dahl-Jensen, D. and L.W. Morland. 1997. *Report of the workshop on rheology and anisotropy (EISMINT), Grindelwald, switzerland.* 27pages.
- Dahl-Jensen, D, T. Thorsteinsson, R. Alley and H. Shoji. (in press). Flow properties of the ice from the GRIP ice core – the reason for folds? *Journal of Geophysics research*
- Donoghue, S. 1999. A profile through Law Dome, of stress patterns based on c-axis orientation fabric patterns and crystal size. Honours Thesis, *Institute of Antarctic and Southern Ocean Studies (IASOS), University of Tasmania.*
- Drewry, D.J. 1975. radio-echo sounding map of Antarctica, (~90°E – 180°). *Polar Record* **17** (109), 359-374.
- Drewry, D.J. (ed). 1983. Antarctic glaciological and geophysical folio. *Scott Polar Research Institute.* Cambridge.
- Drewry, D.J. and S.R. Jordan. 1980. Compilation of an Antarctic glaciological and geophysical folio. *Polar Record* **20** (126), 228.
- Drewry, D.J., S.R. Jordan and E. Janowski. 1982. Measured properties of the Antarctic ice sheet: Surface configuration, ice thickness, volume and bedrock characteristics. *Annals of Glaciology* **3**, 83-91.

References

- Duval, P. and Lorius, C. 1980. Crystal size and climatic record down to the last ice age from Antarctic ice. *Earth and Planetary Science Letters* **48** (1), 59-64.
- Duval, P., and Le Gac, H. 1980. Does the permanent creep rate of polycrystalline ice increase with crystal size? *Journal of Glaciology* **25** (91), 151-157.
- Duval, P., and Le Gac, H. 1982. Mechanical behaviour of Antarctic ice. *Annals of Glaciology* **3**, 92-95.
- Echelmeyer, K.A., W.d. Harrison, C. Larsen and J.E. Mitchell. 1994. The role of the margins in the dynamics of an active ice stream. *Journal of Glaciology* **40** (136), 527-538.
- Edwards, R, P.N.Sedwick, Vin Morgan, C.F. Boutron and S. Hong. 1998. Iron in ice cores from Law Dome, East Antarctica: implications for past deposition of aerosol iron. *Annals of Glaciology* **27**, 365-370.
- Etheridge, D.E. 1985. Gas extraction and analysis from Antarctic ice cores. *ANARE Research Notes* **28**, 32-35.
- Etheridge, D.E. and A.P. McCray. 1985. Dynamics of the Law Dome ice cap from borehole measurements. *ANARE Research Notes* **28**, 10-17.
- Etheridge, D.E. 1989. Dynamics of the Law Dome ice cap, Antarctica, as found from bore-hole measurements. *Annals of Glaciology* **12**, 46-50.
- Etheridge, D.M. 1990. Scientific plan for deep ice drilling on Law Dome. *ANARE*. **76**, 41p.
- Fisher, D. A. and Koerner, R. M. 1986. On the special rheological properties of ancient microparticle-laden northern hemisphere ice as derived from bore-hole and core measurements. *Journal of Glaciology* **32** (112), 501-510.
- Fujita, S., M. Nakawo and S. Mae. 1987. Orientation of the 700-m Mizuho core and its strain history. *Proceedings of the NIPR Symposium on Polar Meteorology and Glaciology* **1**, 122-131.

References

- Fujita, Shuji and Shinji Mae, 1994. Causes and nature of ice-sheet radio-echo internal reflections estimated from the dielectric properties of ice. *Annals of Glaciology* **20**, 80-86.
- Fujita, Shuji, Hideo Maeno, Seiho Uratsuka, Teruo Furukawa, Shinji Mae, Yoshiyuki Fuji and Okitsugu Watanabe, 1999. Nature of radio echo layering in the Antarctic ice sheet detected by a two-frequency experiment. *Journal of Geophysics research* (in press).
- Fung, Y. C. 1965. Foundations of Solid Mechanics. *Prentice-Hall, Englewood Cliffs, New Jersey*.
- Funk, M., K. Echelmeyer and A. Iken. 1994. Mechanisms of fast flow in Jakobshavns Isbre, West Greenland: Part II. Modeling of englacial temperatures. *Journal of Glaciology* **40** (136), 569-585.
- Gao, X.Q. 1989. Laboratory studies of the development of anisotropic crystal structure and flow properties of ice. Ph. D. Thesis, *Department of Meteorology, The University of Melbourne*.
- Gao, X.Q. and Jacka, T.H. 1987 The approach to similar tertiary creep rates for Antarctic core ice and laboratory prepared ice. *Journal de Physique Colloque C1*, **48** (Supplement to No. 3), 289-296.
- Gao, X.Q. and Jacka, T.H. and Budd, W.F. 1989 The development of ice crystal anisotropy in shear and comparisons of flow properties in shear and compression. *Proceedings of the International Symposium on Antarctic Research*. China Ocean Press, 32-40.
- Glen, J.W. 1952. Experiments on the deformation of ice. *Journal of Glaciology* **2** (12), 111-114.
- Glen, J.W. 1953a. *Mechanical properties of ice and their relation to glacier flow*. Dissertation. Cambridge, 1953.
- Glen, J.W. 1953b. Rate of flow of polycrystalline ice. *Nature* **172** (4381), 721-722.
- Glen, J.W. 1955. The creep of polycrystalline ice. *Proceedings of the Royal Society, Series A* **228** (1175), 519-538.

References

- Glen, J.W. 1958. The flow law of ice: a discussion of the assumptions made in glacier theory, their experimental foundation and consequences. *International Association of Scientific Hydrology Publication* **47** (Symposium at Chamonix 1958 - Physics of the Movement of the Ice), 171-183.
- Glen, J.W. 1974. The physics of ice. In Johnson, T.C. (ed.), *cold Regions Science and engineering, Part II-C2a*, CRREL, Hanover, New Hampshire, 1-77.
- Glen, J.W. 1975. The mechanics of ice. In Johnson, T.C. (ed.), *cold Regions Science and engineering, Part II-C2b*, CRREL, Hanover, New Hampshire.
- Glen, J.W. and Jones, S. 1967. The deformation of ice single crystals at low temperatures. *Proceedings of International Conference on Low Temperature Science*. Vol.1, Pt. 1. Int. of Low Temperature Science, Hokkaido University, Sapporo, 267-275.
- Gow, A.J. and Williamson, T. 1976. Rheological implications of the internal structure and crystal fabrics of the West Antarctic ice sheet as revealed by deep core drilling at Byrd Station. *CRREL Report* 76-35.
- Gundestrup, N.S. and Hansen, B.L. 1984. Bore - hole survey at dye 3, South Greenland. *Journal of Glaciology* **30** (106), 282-288.
- Haltiner, G.J. and R.T. Williams. 1980. Numerical prediction and dynamic meteorology. 2nd edition. *John Wiley and Sons, USA*.
- Hamley, T.C. 1985. Glaciological measurements on the 1983-84 Soviet traverse from Mirny to Dome C. *ANARE*. **28**, 180-184.
- Hamley, T.C., I.N. Smith and N.W. Young. 1985. Mass-balance and ice-flow-law parameters for East Antarctica. *Journal of Glaciology*, **31**(109), 334-339.
- Hamley, T.C. 1987. The east Antarctic ice from ice sheet flow to iceberg dissolution. Ph. D. Thesis, *Department of Meteorology, The University of Melbourne*.

References

- Hamley, T.C., V.I. Morgan, R.J. Thwaites and X.Q. Gao. 1986. An ice-core drilling site at Law Dome Summit, Wilkes Land, Antarctica. *ANARE*. **37**, 34p.
- Hammer, C.U. 1980 Acidity of polar ice cores in relation to absolute dating, past volcanism, and radio echoes. *Journal of Glaciology* **25** (93), 359-372.
- Han, J.K. and Young, N.W. 1988. Ice structure, bubble properties and stratigraphy in the BHC1 ice core from Law Dome, Antarctica. *Studies on Glaciology*, No. 5, A collection of Antarctic scientific exploration. 153 - 163.
- Hansen, B.L. and N.S. Gundestrup. 1988. Resurvey of bore-hole at Dye 3, south Greenland. *Journal of Glaciology*, **34** (117), 178-182.
- Herron, S.L. and C.C. Langway. 1982. A comparison of ice fabrics and textures at Camp Century, Greenland and Byrd Station, Antarctica. *Annals of Glaciology* **3**, 118-124.
- Herron, S.L. and Langway, C.C. 1985 Ulhl chloride, nitrate, and sulfate in the Dye 3 and Camp Century, Greenland ice cores. In: *Greenland Ice Core Geophysics, Geochemistry and the Environment* (ed. by C.C. Langway, H. Oeschger and W. Dansgaard), 77-84. Geophysical Monograph No.33, American Geophysical Union, Washington, D.C., USA.
- Herron, S.L., Langway, C.C. and Brugger, K.A. 1985 Ultrasonic velocities and crystalline anisotropy in the ice core from Dye 3 Greenland. In: *Greenland Ice Core Geophysics, Geochemistry and the Environment* (ed. by C.C. Langway, H. Oeschger and W. Dansgaard), 23-31. Geophysical Monograph No.33, American Geophysical Union, Washington, D.C., USA.
- Higashi, A. 1969. Mechanical properties of ice single crystals. *Physics of Ice*, N. Riehl, B. Bullemer, H. Engelhardt, (Eds), Plenum Press, 197-212.
- Homer, D.R. and Glen, J.W. 1978. The creep activation energies of ice. *Journal of Glaciology* **21** (85), 429-444.
- Hooke, R. LeB., B.B. Dahlin and M.T. Kauper. 1972. Creep of ice containing dispersed fine sand. *Journal of Glaciology* **11** (63), 327-336.

References

- Hooke, R. LeB. and Hudleston, P.J. 1980 Ice fabrics in a vertical flow plane. Barnes Ice Cap, Canada. *Journal of Glaciology* **25** (92), 195-214.
- Hooke, R. LeB. 1981 Flow law for polycrystalline ice in glaciers: comparison of theoretical predictions, laboratory data and field measurements. *Reviews of Geophysics and Space Physics* **19** (4) : 664-672.
- Hopkins, W. 1845. On the motion of glaciers. *The London, Edinburgh, and Dublin Philosophical Magazine and Journal of Science*, Third Ser., **26** (170), 1-16.
- Hopkins, W. 1849. On the motion of glaciers. *Transactions of the Cambridge Philosophical Society*, Vol. **8**, Pt.1, P. 50-74.
- Huang, M.H., W.T. Wang, J. Li, G. Li and Z.C. Xie. 1988. Repeated compression-annealing experiments for the ice from Antarctica. *Studies on Glaciology*, No. 5, A collection of Antarctic scientific exploration. 141 - 152.
- Hutchinson, J.W. 1976. Bounds and self-consistent estimates for creep of polycrystalline materials. *Proc. R. Soc. London, Ser. A*, **348**, 101-127.
- Hutter, K. 1983. Theoretical glaciology: material science of ice and the mechanics of glaciers and ice sheets. Dordrecht, D. Reidel Publishing Co./Tokyo, Terra Scientific Publishing Co.
- Huybrechts, P. 1992. The Antarctic ice sheet and environmental change: a three-dimensional modelling study. *Reports on Polar Research* **99**. 241 pages.
- Huybrechts, P., T. Payne and The EISMINT Intercomparison Group. 1996. The EISMINT benchmarks for testing ice-sheet models. *Annals of Glaciology* **23**, 1-12.
- Huybrechts, P., D. Steinhage, F. Wilhelms and J. Bamber. 2000. Balance velocities and measured properties of the Antarctic ice sheet from a new compilation of gridded data for modelling. *Annals of Glaciology* **30**. in press.
- Jacka, T.H. 1983. A computer data base for Antarctic sea ice extent. *ANARE Research Notes* **13**. 54 pages.

References

- Jacka, T.H. 1984. Laboratory studies on relationships between ice crystal size and flow rate. *Cold Regions Science and Technology* **10** (1), 31-42.
- Jacka, T.H. and Maccagnan, M. 1984. Ice crystallographic and strain rate changes with strain in compression and extension. *Cold Regions Science and Technology* **8** (3), 269-286.
- Jacka, T.H. 1987. Experiment investigations of the flow of ice. Ph. D. Thesis, *Department of Meteorology, The University of Melbourne*.
- Jacka, T.H. and W.F. Budd. 1989. Isotropic and anisotropic flow relations for ice dynamics. *Annals of Glaciology* **12**, 81-84.
- Jacka, T.H. and X. Gao. 1989. Ice crystal orientation fabrics and related glaciological parameters from neighbouring Antarctic core sites. *Proceedings of the International Symposium on Antarctic Research (Chinese Committee on Antarctic Research)*. China Ocean Press. 41-52.
- Jacka, T.H. and Li, J. 1994. The steady state crystal size of deforming ice. *Annals of Glaciology* **20**
- Jacka, T.H. and Li Jun. 1999 (in press). Flow rates and crystal orientation fabrics in compression of polycrystalline ice at low temperatures and stresses.
- Jaeger, J.C. 1969. Elasticity, Fracture and Flow: With Engineering and Geological Applications. Third edition, Methuen, London.
- Jenssen, D. 1977. A three-dimensional polar ice-sheet model. *Journal of Glaciology* **18** (80), 373-389.
- Jenssen, D. 1988. Note on modelling the thermodynamics and dynamics of large ice masses. *Unpublished*.
- Johnson, A.F. 1977. Creep characterization of transversely-isotropic metallic materials. *J. Mech. Phys. Solids*, **25**, 117-126.
- Jones, D.J. and E. Davis. 1985. The Vanderford glacier topographic survey. *ANARE Research Notes*, **28**, 185-190.
- Jones, S.J. and J.W. Glen. 1968. The mechanical properties of single crystals of ice at low temperatures. *IASH Publication* **79**, 326- 340.

References

- Jones, S.J. and J.W. Glen. 1969. The effect of dissolved impurities on the mechanical properties of ice crystals. *Phil. Mag., Ser. 8*, 19, 13-24.
- Jones, S.J. and H.A.M. Chew. 1981. On the grain-size dependence of secondary creep *Journal of Glaciology* **27** (97), 517-518.
- Jones, S.J. and H.A.M. Chew. 1981. Effect of sample and grain size on the compressive strength of ice. *Annals of Glaciology* **4**, 129-132.
- Kamb, B. and K.A. Echelmeyer. 1986. Stress-gradient coupling in glacier flow: I. Longitudinal averaging of the influence of ice thickness and surface slope. *Journal of Glaciology* **32** (111), 267-284.
- Kamb, W.B. and Shreve, R.L. 1963. Texture and fabric of ice at depth in a temperate glacier. *Transactions of the American Geophysical Union* **44** : 103. (Abstract).
- Kamb, W.B. 1972. Experimental recrystallization of ice under stress. In: (Heard, H.C., Borg, I.Y. Carter, N.L. and Raleigh, C.B. eds.) *Flow and Fracture of Rocks* American Geophysical Union, Geophysical Monograph **16**, 211-241.
- Kostecka, J.M. and I.M. Whillans. 1988. Mass balance along two transects of wide side of the Greenland ice-sheet. *Journal of Glaciology* **34** (), 31-39.
- Langway, C.C. Jr. 1958. Ice fabrics and the Universal Stage. *SIPRE Technical Report* **62**.
- Langway, C.C. jr, Shoji, H. and Azuma, N. 1988. Crystal size and orientation patterns in the Wisconsin - age ice from Dye 3, Greenland. *Annals of Glaciology* **10**, 109-115.
- Lebensohn, R.A. and C.N. Tome. 1993. A self-consistent anisotropic approach for the simulation of plastic deformation and texture development of polycrystals: application to zirconium alloys. *Acta Metaal.* **41**, 2611-2624.
- Lebensohn, R.A. and C.N. Tome. 1994. A self-consistent viscoplastic model: prediction of rolling textures of anisotropic polycrystals. *Mater. Sci. Eng., Ser. A.*, **175**, 71-82.

References

- Legrand, M. and Delmas, R.J. 1986. Relative contributions of tropospheric and stratospheric sources to nitrate in Antarctic snow. *Tellus* **38B** (3-4), 236-249.
- Legrand, M. and Delmas, R.J. 1988. Soluble impurities in four Antarctic ice cores over the last 30000 years. *Annals of Glaciology* **10**, 116-120.
- Li, Jun, Xie Zichu and M. Huang. 1988a. Study of the structure of ice core from BHQ borehole on Law Dome, Antarctica. *Studies on Glaciology*, No. 5, A collection of Antarctic scientific exploration. 119 - 131.
- Li, Jun, Xie Zichu and M. Huang. 1988b. Fabrics of the ice cores from BHQ on Law Dome ice cap, Antarctica. *Kexue Tongbao*, **33**(3), 216-220.
- Li, Jun. 1995. Interrelation between flow properties and crystal structure of snow and ice. Ph. D. Thesis, *Department of Meteorology, The University of Melbourne*.
- Li, Jun and T.H. Jacka. 1996. Isotropic ice flow rates derived from deformation tests in simultaneous shear and compression. *IASH Proceeding of the 13th International Symposium on Ice. Beijing, 27-31 August 1996*. **3**, 937- 947.
- Li, Jun, T.H. Jacka and W.F. Budd. 1996. Deformation rates in combined compression and shear for ice which is initially isotropic and after the development of strong anisotropy. *Annals of Glaciology* **23**, 247-252.
- Li, Jun, T.H. Jacka and V.I. Morgan. 1998. Crystal-size and microparticle record in the ice core from Dome Summit South, Law Dome, East Antarctica. *Annals of Glaciology* **27**, 343-348.
- Li, Jun and T.H. Jacka. 1998. Horizontal shear rate of ice initially exhibiting vertical compression recrystallization fabrics. *Journal of Glaciology* **44** (148), 670-672.
- Lile, R.C. 1978. The effect of anisotropy on the creep of polycrystalline ice. *Journal of Glaciology* **21** (85), 475-483.
- Lile, R.C. 1984 The flow law for isotropic and anisotropic ice at low strain rates. *ANARE Report* **132**

References

- Lliboutry, L. 1979. Local friction laws for glaciers: a critical review and openings. *Journal of Glaciology* **23** (89), 67-95.
- Lliboutry, L. 1987a. Sliding of cold ice sheets. *IAHS Publ. No.* **170**, 131-143.
- Lliboutry, L. 1987b. Very slow flows of solids: basics of modeling in geodynamics and glaciology. *Martinus Nijhoff Publishers, Dordrecht*.
- Lliboutry, L. 1993. Anisotropic, transversally isotropic nonlinear viscosity of rock ice and rheological parameters inferred from homogenization. *Int. J. plasticity*, **9**, 619-632.
- Lliboutry, L. and P. Duval. 1985. Various isotropic and anisotropic ices found in glaciers and polar ice caps and their corresponding rheologies. *Annales Geophysicae* **3** (2), 207-224.
- Lorius, C. and J. Vaugelade. 1972. 800-km traverse from Dumont d'Urville toward Vostok Station. *Antarctic Journal of the United States*, **7** (5), 154-155.
- Lorius, C. and J. Vaugelade. 1973. International Antarctic Glaciological Project traverse, Dumint d'Urville to Vostostok. *Antarctic Journal of the United States*, **8** (4), 171-172.
- MacAyeal, D.R. 1996. EISMINT: Lessons in Ice-Sheet modelling. *Department of Geophysical Sciences, University of Chicago, Chicago, Illinois*, 392pages.
- Mangeney, A., F. Califano and O. Castelnau. 1996. Isothermal flow of an anisotropic ice sheet in the vicinity of an ice divide. *Journal of Geophysics research* **101**, 28,189-28,204.
- Mangeney, A., F. Califano and K. Hutter. 1997. A numerical study of anisotropic, low Reynolds number, free surface flow for ice sheet modeling. *Journal of Geophysics research* **102**, 22,749-22,764.
- Mangeney, A. and F. Califano. 1998. The shallow ice approximation for anisotropic ice: formulation and limits. *Journal of Geophysics research* **103**, 691-705.

References

- Matsuda, M. and Wakahama, H. 1978. Crystallographic structure of polycrystalline ice. *Journal of Glaciology* **21** (85), 607-620.
- Mavrakis, E. 1989. Derived physical characteristics of the Wilkes-Vostok region. Honours Thesis, *University of Melbourne*.
- Mavrakis, E. 1992. Time dependent, three-dimensional, modelling of the dynamics and thermodynamics of large ice masses. M.Sc. Thesis, *University of Melbourne*.
- McLaren, W.A. 1968. A study of the local ice cap near Wilkes, Antarctica. *ANARE Scientific Report, Series A (IV) Glaciology, Publication No. 103*.
- McWhirter, N.D. (ed) 1986 The Guinness Book of Records. *Jarrols Printing, Norwich*. 352 pages.
- Mellor, M. and Smith, J.H. 1966. Creep of snow and ice. U.S. Army CRREL Research Report **220** (also Sapporo Conference, 1966, Physics of Snow and Ice, Part 2).
- Meyssonier, J. and A. Philip. 1996. A model for the tangent viscous behaviour of anisotropic polar ice. *Annals of Glaciology* **23**, 253-261.
- Miyamoto, A., H. Narita, T. Hondoh, H. Shoji, K. Kawada, O. Watanabe, D. Dahl-Jensen, N.S. Gundestrup, H.B. Clausen and P. Duval. (In press). Ice sheet flow conditions deduced from mechanical tests of ice core. *Annals of Glaciology* **30**
- Molinari, A., G.R. Canova and S. Ahzy. 1987. A self-consistent approach of the large deformation polycrystal viscoplasticity. *Acta. Metall.*, **35** (12), 2893-2994.
- Morgan, V. I. 1985. Snow accumulation and oxygen isotope records in two adjacent ice cores. *ANARE Research Notes*, **28**, 25-31.
- Morgan, V. I., and A. P. McCray, 1985. Enhanced shear zones in ice flow - implications for ice cap modelling and core dating. *ANARE Research Notes*, **28**, 4-9.

References

- Morgan, V.I., C.W. Wookey, J. Li, T.D. Van Ommen, W. Skinner and M.F. Fitzpatrick. 1997. Site information and initial results from deep ice drilling on Law Dome, Antarctica. *Journal of Glaciology* **43** (143), 3-10.
- Morgan, V.I., T.D. Van Ommen, A. Elcheikh and J. Li 1998. Variations in shear deformation rate with depth at Dome Summit South, Law Dome, East Antarctica. *Annals of Glaciology* **27**, 135-139.
- Morland, L.W. 1984. Thermomechanical balances of ice sheet flows. *Geophys. Astrophys. Fluid Dyn.*, **29**, 237-266.
- Nye, J.F. 1953. The flow law of ice from measurements in glacier tunnels, laboratory experiments and the Jungfraufirn bore hole experiment. *Proceedings of the Royal Society Series A* **219** (1139), 477-489.
- Paterson, W.S.B. and W.F. Budd. 1982. Flow parameters for ice-sheet modelling. *Cold Regions Science and Technology* **6**, 175-177.
- Patterson, W.S.B. 1994. The Physics of Glaciers. Third edition, Pergamon Press. ISBN 0-08-037944 3.
- Petit, J.R., J.Jouzel, D. Raynaud, N.I. Barkov, J.-M. Barnola, I. Basile, M. Bender, J.Chappellaz, M. Davis, . Delaygue, M. Delmotte, V.M. Kotlyakov, M.Legrand, V.Y. Lipenkov, C. Lorius, L. Pepin, C. Ritz, E. Saltzman and M. Stievenard. 1999. Climate and atmospheric history of the past 420,000 years from the Vostok ice core, Antarctica. *Nature* **399**, 429-435.
- Pfützner, M.L. 1980. The Wilkes Ice Cape Project, 1966. *ANARE Scientific Report, Series A (IV) Glaciology, Publication No. 127*.
- Phillips, N.A. 1957. A coordinate system having some special advantages for numerical forecasting. *Journal of meteorology* **14** (2), 184-185.
- Qin, D.H. 1988. Research on the stratigraphy of shallow snow/firn core in Wilkes Land, Antarctica. In: (Xie, Z.C. ed) *A Collection of ANTARCTIC Scientific Explorations: Studies on Glaciology*, Science press, Beijing, (5), 22-35 (in Chinese with English abstract).
- Radok, U. 1977. International Antarctic glaciological Project: past and future. *Antarctic Journal of the United states*. Vol.**12**, Nos. 1-2, 32-38.

References

- Radok, U. 1985. The Antarctic ice. *Scientific American*. **253** (2), 98-105.
- Radok, U., R.G. Barry, D. Jenssen, R.A. Keen, G.N. Kiladis and B. McInnes. 1982. Climatic and physical characteristics of the Greenland ice sheet, Parts I & II. Cooperative Institute for Research in Environmental Sciences, University of Colorado, Boulder, Colorado. (Report CO 80309).
- Raynaud, D, C. Lorius, W.F. Budd and N.W. Young. 1979. Ice flow along an I.A.G.P. flow line and interpretation of data from an ice core in Terre Adelie, Antarctica. *Journal of Glaciology* **24** (90), 103-115.
- Reeh, N. 1988. A flow-line model for calculation the surface profile and the velocity, strain-rate and stress fields in an ice-sheet. *Journal of Glaciology* **34** (116), 46-54.
- Rigsby, G.P. 1958. Effect of hydrostatic pressure on velocity of shear deformation of single ice crystals. *Journal of Glaciology*, **3** (24), 273-278.
- Robin, G de Q, D.J. Drewry and D.T. Meldrum. 1977. International studies of ice sheet and bedrock. *Philosophical Transactions of the Royal. Society of London. Ser. B* **279**, 185-196.
- Rosman, K.J.R., W. Chisholm, C.F. Boutron, S. Hong, R. Edwards, Vin Morgan and P.N. Sedwick. 1998. Lead isotopes and selected metals in ice from Law Dome, Antarctica. *Annals of Glaciology* **27**, 349-354.
- Russell-Head, D.S. and W.F. Budd. 1979. Ice-sheet flow properties derived from bore-hole shear measurements combined with ice-core studies. *Journal of Glaciology*, **24** (90), 117-130.
- Russell-Head, D.S. 1979. Ice sheet flow from borehole and laboratory studies. M. Sc. Thesis, *Department of Meteorology, The University of Melbourne*.
- Sachs, G. 1928. Zur Ableitung einer Fließbedingung. *Z. des Vererins Deutscher Ingenienre*, **72** (8), 734-736.
- Schott, C., E.D. Waddington and C.F. Raymond. 1992. Predicted time-scales for GISP2 and GRIP boreholes at Summit, Greenland. *Journal of Glaciology* **38** (128), 162-168.

References

- Schott, C., and others. 1996 (in press). Ice flow between the GRIP and GISP2 boreholes in Central Greenland. *Journal of Geophysics research*
- Sheehy, D.E. 1981. The dynamics of undulation ice flow. MSc. Thesis, *Department of Meteorology, The University of Melbourne.*
- Shoji, H. and C.C. Langway. 1984. Flow behaviour of basal ice as related to modelling considerations. *Annals of Glaciology* **5**, 141-148.
- Shoji, H. and Langway, C.C. 1987. Flow velocity profiles and accumulation rates from mechanical tests on ice core samples. IUGG General Assembly of Vancouver, Aug.1987, *IASH Publication* **170**: 67 -77.
- Shoji, H. and C.C. Langway. 1988. Flow-law parameters of the Dye 3, Greenland, deep ice core. *Annals of Glaciology* **10**, 146-150.
- Shumskiy, P.A. 1964. Principles of structural glaciology. *Pergamon Press.*
- Steinemann, S. 1954. Flow and recrystallization of ice. *IAHS Publication* **39**, 449-462.
- Steinemann, S. 1958. Experimentelle Untersuchungen zur Plastizitat von Eis. *Beitrage zur Geologie der Schweiz, Geotechnische Serie, Hydrologie* (**10**), 1-72.
- Svendsen, B. and K. Hutter. 1996. A continuum approach for modelling induced anisotropy in glaciers and ice sheets. *Annals of Glaciology*, **23**, 262-269.
- Taylor, G.I. 1938. Plastic strain in metals. *J. Inst. Met.*, **62**, 307-324.
- Thompson, L.G. 1977. Variations in microparticle concentration, size distribution and elemental composition found in Camp Century, Greenland, and Byrd Station, Antarctica deep ice cores. IUGG General Assembly of Vancouver, Aug./Sept. 1975, *IASH Publication* **118**, 351 - 364.
- Thompson, L.G. and Mosley-Thompson, E. 1981 Microparticle concentration Variations linked with climatic change: evidence from pole ice cores. *Science* **212** (4496): 812 - 815.

References

- Thorsteinsson, T. 1996. Textures and fabrics in the GRIP ice core, in relation to climate history and ice deformation. *Reports on Polar Research* **96**. 146 pages.
- Thorsteinsson, T. 1997. Can anisotropy alone explain enhanced shear strain rates in the Greenland ice sheet? *Report of the workshop on rheology and anisotropy (EISMINT), Grindelwald, switzerland*. (abstract).
- Thorsteinsson, T, E.D. Waddington, K.C. Taylor, R.B. Alley and D.D. Blankenship. 1999. Strain-rate enhancement at Dye 3, Greenland. *Journal of Glaciology*, **45** (105), 338-345.
- Thwaites, R.J., C.J.L. Wilson and A.P. McCray. 1984. Relationship between bore-hole closure and crystal fabrics in Antarctic ice core from Cape Folger. *Journal of Glaciology*, **30** (105), 171-179.
- Van der Veen, C.J. and I.M. Whillans. 1990. Flow laws for glacier ice: comparison of numerical predictions and field measurements. *Journal of Glaciology*, **36** (124), 324-339.
- Van der Veen, C.J. and I.M. Whillans. 1994. Development of fabric in ice. *Cold Regions Science and Technology* **22** (2), 171-195.
- Van Ommen, T.D. and V.I. Morgan. 1997. Calibrating the ice core paleothermometer using seasonality. *Journal of Geophysics research* **102** (D8), 9351-9357.
- Wakahama, G. 1967. On the plastic deformation of single crystal of ice. *Physical of Snow and Ice (H. Oura, ed). Institute of Low Temperature Science, Hokkaido University, Sapporo*, 291-311.
- Wakahama, G. 1974. Studies of fabrics and texture in deep layers from Dome Summit, Cape Folger and The Amery Ice Shelf. *Physical and chemical studies on ices from glaciers and ice sheets*. 99-108. (in Japanese).
- Walker, D.J. 1966. Wilkes geophysical surveys, Antarctica 1962. *Bureau of Mineral Resources, Geology and Geophysics, Canberra*. (Record No. 1966/129).

References

- Walker, D.J. 1976. Glaciological and geophysical studies in Wilkes Land, Antarctica 1962/63. M.Sc. Thesis, *Department of Meteorology, The university of Melbourne*.
- Wang, W.L. 1994. Laboratory studies of flow properties and associated crystal structure in Holocene and Wisconsin ice. M.Sc. Thesis, *I.A.S.O.S, The University of Tasmania*.
- Wang, W.L. and R.C. Warner. 1998. Simulation of the influence of ice rheology on velocity profiles and ice-sheet mass balance. *Annals of Glaciology* **27**, 194-200.
- Wang, W.L. and R.C. Warner. 1999. Modelling of the anisotropic ice flow in Law Dome, Antarctica. *Annals of Glaciology* **29**, in press.
- Warner, R.C., T.H. Jacka, Li Jun and W.F. Budd. 1999. Tertiary flow relations for compression and shear components in combined stress tests on ice. *Advances in Cold-Region Thermal Engineering and Sciences: Technological, Environmental, and Climatological Impact* (ed. By K. Hutter, Y. Wang and H. Beer), 259-270.
- Warner, R.C. and W.F. Budd. 1999. Derivation of ice thickness and bedrock topography in data gap regions over Antarctica. International Symposium on the Verification of Cryospheric Models: Bringing data and modelling scientists together. Zurich, Switzerland. 28 (abstract).
- Weertman, J. 1963. The Eshelby-Schoeck viscous dislocation damping mechanism applied to the steady-state creep of ice. In: (W.D. Kingery, ed.) *Ice and Snow* MIT Press, Cambridge, Massachusetts, U.S.A., 28-33.
- Weertman, J. 1964. The theory of glacier sliding. *Journal of Glaciology* **5** (39), 287-303.
- Weertman, J. 1983. Creep deformation of ice. *Annu.Rev. Earth Planet.Sci.* **11**, 215-240.
- Whillans, I.M. and C.J. van der Veen. 1997. The role of lateral drag in the dynamics of ice stream B, Antarctica. *Journal of Glaciology* **43** (144), 231-237.

References

- Xie, Z.C. 1985. Ice formation and ice structure on Law Dome, Antarctica. *Annals of Glaciology* **6**, 150-153.
- Xie, Z.C. 1988. Ice crystallographic studies on Law Dome, Antarctica. Studies on Glaciology, No. 5, A collection of Antarctic scientific exploration. 93-118.
- Xie, Z.C., Li Jun and N.W. Young. 1989. Physical characteristics of the snow and ice cover of Law Dome, East Antarctica. *Proceedings of the International Symposium on Antarctic Research (Chinese Committee on Antarctic Research)*. China Ocean Press. 8-22.
- Young, N.W. 1979. Measured velocities of interior East Antarctica and the state of mass balance within the I.A.G.P. area. *Journal of Glaciology* **24** (90), 77-87.
- Young, N.W., D. Sheehy and T.C. Hamley. 1982. Ice flow along an IAGP flow line, Wilkes Land, Antarctica. (Abstract). *Annals of Glaciology* **3**, 346.
- Young, N.W., M. Pourchet, V.M. Kotlyakov, P.A. Korelev and M.B. Dyugero. 1982. Accumulation distribution in the IAGP area, Antarctica. *Annals of Glaciology* **3**, 333-338.
- Young, N.W., Z.C. Xie and D.H. Qin. 1985. Multilayer crystallographic structure of Law Dome from ice core analysis. *ANARE Research Notes*, **28**, 18-24.
- Young, N.W., I.D. Goodwin, N.W.J. Hazelton and R.J. Thwaites. 1989. Measured velocities and ice flow in Wilkes Land, Antarctica. *Annals of Glaciology* **12**, 192-197.

Appendix I: Ice Dynamics and Thermodynamics Equations

In an ice sheet, theoretically, its size, the distributions of stress and velocity throughout, and how these quantities change with time for any given bedrock configuration and time-dependent variation of mass balance, can be calculated (Paterson, 1994). The basic equations for the calculations are the continuity equation, equation of motion (the stress equilibrium equations) and the flow law (relation between strain rate and stress). The flow law has been described in the thesis in detail (Section 2.3). This section will describe the continuity equation, the equation of motion and the equation for heat transfer.

AI.1. Continuity Equation

The continuity equation expresses the law of mass conservation of a moving continuum. The change in ice thickness with time ($\frac{\partial D}{\partial t}$) over a fixed point of the bedrock, has the relation with the net of accumulation and ablation (M), the ice thickness (D) and depth averaged horizontal velocity (V) of the form of

$$\frac{\partial D}{\partial t} = -\nabla \cdot (\bar{V} D) + M \quad (\text{AI.1})$$

where the ∇ -operator is

$$\nabla = \frac{\partial}{\partial x} \hat{i} + \frac{\partial}{\partial y} \hat{j} + \frac{\partial}{\partial z} \hat{k} \quad (\text{AI.2})$$

where \hat{i} , \hat{j} and \hat{k} are unit vectors in x , y , and z directions, with z in the vertical. If all the parameters on the right hand side are known over an ice sheet the change in shape can be calculated. The change in ice thickness with time can also be computed by numerical methods. The net surface mass balance M is treated in ice equivalent units and 20m is subtracted from the surface elevation and ice thickness to account for the firn and to give the ice equivalent elevation and thickness. The ice density is then taken as constant and the ice as incompressible.

AI.2. Equations of Motion

The dynamical behaviour of ice deforming under its own weight is governed primarily by Newton's equations of motion and its rheological properties. As the ice flow in an ice sheet is sufficiently slow that the acceleration term in Newton's Second Law can be neglected. The equations of motion then reduce to equations of static equilibrium expressing the balance between the surface forces (stresses) and the body forces (gravity in this case) that act on all its parts. The forces on a block of size $dx dy dz$ are shown in Figure AI.1 for an arbitrarily oriented Cartesian coordinate system.

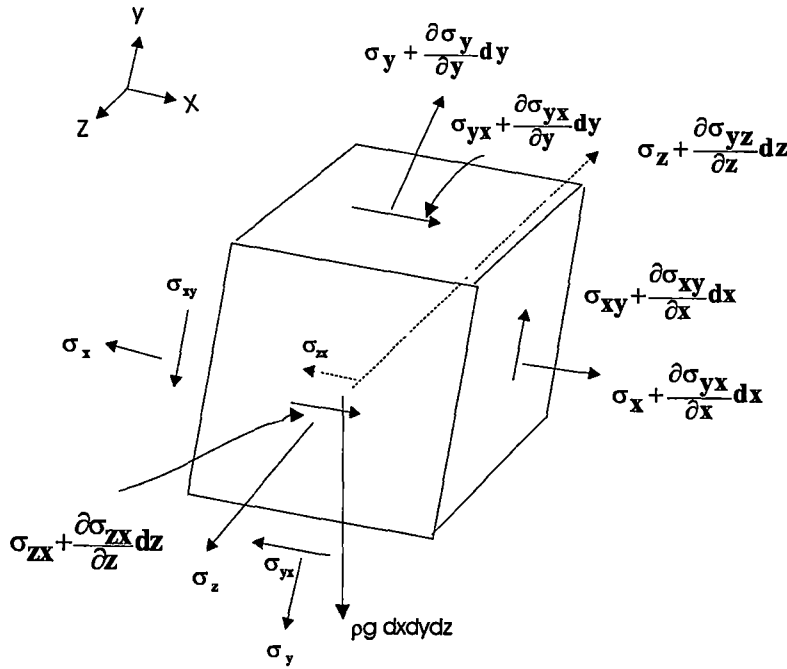


Figure AI.1. The forces on a block of size $dx dy dz$.

Here, $\sigma_x, \sigma_y, \sigma_z, \tau_{xy}, \tau_{yx}, \tau_{yz}, \tau_{zy}, \tau_{xz}, \tau_{zx}$ are the nine components of stress (see section 2.2.1); g is the gravitational acceleration with three components g_x, g_y and g_z in x, y and z directions, respectively; and ρ is the density (usually assumed to be constant). Taking the stresses to vary smoothly across the infinitesimal block the total force in the x -direction on a block of size $dx dy dz$ is

$$\begin{aligned} \sum F_x = & -\sigma_x dy dz + \left(\sigma_x + \frac{\partial \sigma_x}{\partial x} dx \right) dy dz - \tau_{yx} dx dz + \left(\tau_{yx} + \frac{\partial \tau_{yx}}{\partial y} dy \right) dx dz \\ & - \tau_{zx} dx dy + \left(\tau_{zx} + \frac{\partial \tau_{zx}}{\partial z} dz \right) dx dy + \rho g_x dx dy dz = 0 \end{aligned} \quad (A1.3)$$

The first two terms on the right hand side are the normal forces on the faces of the block that are normal to the x-axis. The next four terms are the shear forces in the x direction on faces normal to the y and z axes, respectively. The last term is the body force, g_x , which represents the component of the gravitational acceleration in x direction. Cancelling like terms with opposite sign and dividing each of the remaining terms by the volume $dx dy dz$, we obtain the equation of motion in the x direction

$$\frac{\partial \sigma_x}{\partial x} + \frac{\partial \tau_{xy}}{\partial y} + \frac{\partial \tau_{xz}}{\partial z} = -\rho g_x \quad (A1.4)$$

Similar equations of motion in y and z directions are

$$\frac{\partial \tau_{yx}}{\partial x} + \frac{\partial \sigma_y}{\partial y} + \frac{\partial \tau_{yz}}{\partial z} = -\rho g_y \quad (A1.5)$$

$$\frac{\partial \tau_{zx}}{\partial x} + \frac{\partial \tau_{zy}}{\partial y} + \frac{\partial \sigma_z}{\partial z} = -\rho g_z. \quad (A1.6)$$

A1.3. Equation of Heat Transfer

When the mechanical equivalent of heat is omitted (it is unity in S.I. units) the equation of conservation of energy in a deforming medium can be written (Fung, 1965, p.346; Paterson, 1994)

$$\rho \frac{dE}{dt} = f - \nabla \cdot \bar{q}, \quad (A1.7)$$

where, $\frac{dE}{dt}$ is the change of specific internal energy (E) with time (t), ρ the density, f the rate of internal heat production per unit volume and \bar{q} the heat flux

vector. The ∇ Operation in Cartesian coordinate system is shown in Equation AI.2.

In an ice sheet, the forms of internal energy other than deformational heating are negligible, so that

$$E = \int_0^T c(T') dT', \quad (\text{AI.8})$$

where T denotes temperature and c is specific heat capacity. Thus

$$\frac{dE}{dt} = c \frac{dT}{dt}. \quad (\text{AI.9})$$

The heat flux due to conduction is

$$\bar{q} = -k \nabla T, \quad (\text{AI.10})$$

where, k is thermal conductivity and varies with density and temperature. Thus

$$-\nabla \cdot \bar{q} = \nabla \cdot (k \nabla T) = k \nabla^2 T + \nabla k \cdot \nabla T \quad (\text{AI.11})$$

The internal deformation (and possible heat released by freezing of water in the firm) are sources of internal heating, thus

$$f = \dot{\epsilon}_x \sigma_x + \dot{\epsilon}_y \sigma_y + \dot{\epsilon}_z \sigma_z + 2(\dot{\epsilon}_{xy} \sigma_{xy} + \dot{\epsilon}_{xz} \sigma_{xz} + \dot{\epsilon}_{yz} \sigma_{yz}) + w \quad (\text{AI.12})$$

where, $\dot{\epsilon}$ are components of strain rate (see Section 2.2.2), σ and τ are stress components (see Section 2.2.1), w is the rate of release of latent heat per unit volume and is taken to be zero due to assuming density is constant. Further if it is assumed that internal heating is mainly from the shear deformation, f can be reduced to

$$f = 2 \dot{\epsilon}_{xz} \tau_{xz}. \quad (\text{AI.13})$$

Substituting (AI.9), (AI.11) and (AI.13) to (AI.7), we have

$$\begin{aligned} \frac{dT}{dt} &= \frac{1}{\rho c} (k^2 T + \nabla k \cdot \nabla T + f) \\ &= K \nabla^2 T + \bar{K}' \nabla T + F \end{aligned} \quad (\text{AI.14})$$

where, thermal diffusivity $K = \frac{k}{\rho c}$, and $\bar{K}' = \frac{1}{\rho c} \nabla k$ and $F = \frac{f}{\rho c}$.

Expanding the total derivative $\frac{dT}{dt}$ into partial derivatives, we have

$$\begin{aligned}\frac{\partial T}{\partial t} &= \frac{dT}{dt} + \bar{V} \cdot \nabla T \\ &= K \nabla^2 T + (\bar{K}' - \bar{V}) \cdot \nabla T + F\end{aligned}\tag{AI.15}$$

where \bar{V} is velocity vector $\{V_x, V_y, V_z\}$. This is the general equation for heat transfer in the ice sheet to be used here. To solve it, boundary and initial conditions are needed which are described in detail in Chapter 4.

Appendix II: Iterative Scheme for Calculation of Steady State Temperatures

For any column of ice the temperature distribution can be calculated from Equation 4.4.8.10 as following (Equation 4.4.8.11):

$$a (T_{j+1} - 2T_j + T_{j-1}) + b (T_{j+1} - T_{j-1}) + c T_j = d \quad (\text{AII.1})$$

where the subscript refers to points in the column: $j=1$ at the ice surface and $j = N_z$ at the bedrock, N_z is the number of vertical levels formed by dividing ice thickness into evenly spaced bands of with $D\Delta\zeta$ (see Section 4.4.1), and

$$a = \frac{K}{(D \Delta\zeta)^2} \quad (\text{AII.2})$$

$$b = \frac{K'}{(2D \Delta\zeta)^2} (T_{j+1} - T_{j-1}) - \frac{\omega}{2\Delta\zeta} \quad (\text{AII.3})$$

$$c = \frac{U}{\Delta x} \quad (\text{AII.4})$$

$$d = -F - \frac{U}{\Delta x} T_j^{\text{upstream}}. \quad (\text{AII.5})$$

Rearranging Equation (AII.1) gives

$$(a + b)T_{j-1} + (c - 2a)T_j + (a + b)T_{j+1} = d. \quad (\text{AII.6})$$

Equation AII.6 is easy to be solved because it is of the tridiagonal form (Press and others, 1986). Since K , K' and b are all functions of T , an iterative scheme is needed to reach the solutions of the steady state temperatures is following:

- (i) Suppose a guess, θ^n is available. In the study here the first guess is obtained taking the upstream profile.
- (ii) Compute K , K' , b from $T=\theta^n$.
- (iii) Solve the tridiagonal system (Equation AII.2) for T_j and set $\theta^{n+1}=T_j$.

- (iv) If $|\theta^{n+1} - \theta^n| < \delta$ for all the points (where δ is some arbitrary number), the process has reached a solution. Otherwise return to step (ii) until convergence is attained.

This scheme has been used to determine the temperature profiles along the flow lines from the second column of the ice to the end.

The temperature profile at the first column of the flow line is determined similarly to the above iterative scheme, except (i) the first guess is made to take the temperature profile increasing linearly with the depth from the surface temperature to the bed, (ii) the heat horizontal advection term ($U \cdot \nabla T$) in the heat Equation 4.4.8.10 is treated as:

- (1) if the first column is at the ice divide (i.e. the Law Dome line in Chapter 6), the term c (Equation AII.4) and term d (Equation AII.5) are equal to zero since the horizontal velocity (U) is zero;
- (2) if the first column is not at the ice divide (i.e. the I.A.G.P line in Chapter 7), which means that the horizontal velocity is not equal to zero and that temperature is being advected from upstream, the following scheme is used:

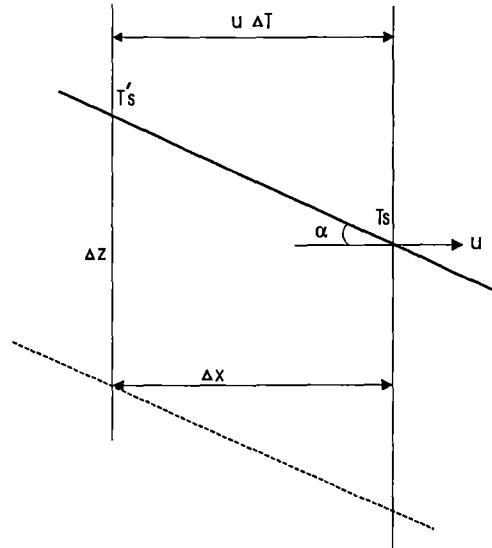


Figure AII.1. The scheme showing the heat horizontal advection.

in Figure AII.1, if T_s is the surface temperature and U is horizontal velocity at the column and prime T_s' is the temperature upstream, we have the relation

$$\nabla T = \frac{T_s - T_s'}{\Delta x} = \frac{\Delta T}{\Delta z} \frac{\Delta z}{\Delta x} = \gamma_s \alpha, \quad (\text{AII.7})$$

where α is surface slope and γ_s is the vertical gradient of surface temperature or the “lapse rate” and is taken as $\gamma_s = 0.01$ °C/m.

If it is supposed that γ_s is a constant through the whole column the heat horizontal advection may be calculated by

$$U \cdot \nabla T = U \gamma_s \alpha, \quad (\text{AII.8})$$

this is represented as the term c (Equation AII.4) which is equal to zero and the term d (Equation AII.5) is replaced by

$$d = -F - U \gamma_s \alpha. \quad (\text{AII.9})$$